Application of machine learning approach in solving materials science problems

Thesis submitted for the degree of

Doctor of Philosophy (Science)

in

Physics (Theoretical)

by

Aishwaryo Ghosh

Department of Physics

University of Calcutta

2025

Contents

Dedicated to my parents, whose unwavering support has guided me through this journey.

Acknowledgments

As this chapter of my life comes to a close, I find myself deeply indebted, both intellectually and emotionally, to several people for shaping the path.

First and foremost, I would like to express my sincere gratitude to Prof. Tanusri Saha-Dasgupta, for her constant guidance and constructive criticism. Her passion for science, problem-solving mindset, and systematic approach to critical challenges have been a source of inspiration for me. Her critical comments and suggestions throughout the drafting of this dissertation have been invaluable.

I also thank Dr. Amitava Moitra, Dr. Anita Halder, Dr. Biswajit Pabi, Dr. Soumendu Datta, and Dr. Samir Rom for their collaborative efforts and insightful contributions across various projects. Their expertise and support have been instrumental to my work.

I would like to especially thank Dr. Atindra Nath Pal for his guidance and providing experimental data towards our collaboration.

I feel truly fortunate to have been part of a research group filled with such dynamic and supportive colleagues. My sincere acknowledgment goes to Samir, Shiladitya'da, Rajdeep, Koushik, Manoj, Arnab, Prosanta, Sweta, Sourav, and Arun'da for their unwavering support and camaraderie. I would especially like to thank Samir for being my first friend here. From sharing an office space to spending Saturday evenings deep in conversation, his company has made this journey more joyful.

I heartily regard the S.N. Bose National Centre for Basic Sciences for hosting me throughout these years and providing an excellent environment for learning and research. There are several individuals, starting from professors to administrative and non-teaching staff, to thank in connection to this place. Although I cannot name them all here for reasons of brevity, my appreciation to them is heartfelt.

My time here has gifted me the friendship of some truly remarkable people who have helped navigate the recurring trials and tribulations of life, both within and beyond academia. Together, we have shared the common dejection known to most PhD students, often over countless cups of tea, coffee, and more. Krishnendu's wry humor and quiet perseverance, Manodip's diligence and tireless work ethic, Anirban's practicality and enthusiasm, and Samir's calm determination and levelheadedness have been both recuperative and inspiring. Their presence has made this journey not only endurable, but truly meaningful.

When I had started this journey, I was unsure how meandering it would turn out to be. But I

was sanguine about a few pit stops that would never fail me. I owe hugely to each of them. To my friend, my counselor, my brother, Jeet - it'd be futile to attempt penning any note of gratitude that'd suffice. Thank you for being the back-propagation to my neural net. To my didi, who has always been my guardian angel. She has tended the perfect concoction of utmost kindness and practical advice during unfavorable times. Our online sessions, spanning from philosophy to k-drama, have been greatly energizing : no existential or fictional crisis went undiscussed!

A massive shout-out to Rahul for defying timezones to keep me entertained with his endless quirks and wit. I owe him for being a pillar of support during my academic visit to Dresden. From showing me around to helping me settle in, he made it remarkably comfortable to navigate a new city far from home.

I also wholeheartedly appreciate my friend Anusuya, for being an ardent supporter and often more optimistic about the fate of my PhD than myself. Thanks for delivering both motivation and magically-timed food parcels from miles away!

Finally, and most importantly, my infinite love and gratitude to my Maa and Baba, without whose unstinted support I might have never dared to embark on this herculean exercise. Thank you for the quiet sacrifices, endless patience, and unconditional love that have formed the very foundation of this course. Every page of this thesis bears the imprint of your encouragement and warmth. I am who I am because of you.

Abstract

Machine learning(ML) enables extraction of information and unearthing of hidden patterns from often complex and multidimensional data and making predictions or decisions based on it. This holds promise in complementing the traditional methods of materials' research which are bottlenecked by their long development cycles, high costs etc. In fact, ML has lately emerged as a transformative tool in materials science, enabling rapid and accurate analysis of complex material properties, prediction of new materials with targeted functionalities, optimization of fabrication processes, to name a few. In this thesis, various techniques of ML have been implemented in addressing a range of materials science problems, given in the following.

- We established a machine learning model for prediction of types of semiconductor heterostructures using features that describe the constituent semiconductors, and trained on a known dataset of binary semiconductor heterostructures. Using this, we theoretically predicted the types of 872 previously unknown semiconductor heterostructures formed from combinations of elemental and binary semiconductors. Out of the predicted heterostructures, several are experimentally realizable given the acceptable lattice mismatch. Interestingly, the developed scheme also was found to be extendable to heterojunctions involving semiconductor quantum dots.

- We studied binary-alloyed metallic nanoparticles composed of a wide range of alkali, alkaline earth, basic, 3d, 4d, and 5d transition metals, as well as p-block elements, to determine core–shell preferences by calculating the segregation energies of single-atom alloy clusters using density functional theory (DFT). Applying machine learning to this extensive database, constructed from features characterizing the constituent metals, reveals the primary factors governing core-to-shell preference. Interestingly, we find that the dominant factor varies with the metal type. The analysis further reveals the conditions under which nanoparticles tend to favour mixed or Janus structures over the core-shell configuration.

- The influence of component concentration and cluster size on ordering was further investigated in terms of detailed first-principles calculations for Pd-based binary nanoalloys. These are particularly relevant as potential alternatives to Pt-based electrocatalysts, which are both scarce and costly. We then elaborated on the catalysis effect of such nanoclusters.

- We developed a hybrid machine learning framework that integrates both unsupervised and supervised learning models, trained on experimentally measured conductance traces,

to gain microscopic insight into the process of formation of gold atomic wires in mechanical break junction experiments. Using two independent data sets of conductance-displacement traces of single-atomic junctions, we first determined the optimal conditions of bias voltage and stretching rate required to form atomic chains longer than 4 Å. We then applied a deep learning model to classify individual breaking traces, successfully identifying key trace features associated with long-chain formation. Ab-initio molecular dynamics simulations were then conducted, offering a detailed molecular-level understanding of the mechanisms behind chain formation.

- We adopted a data-driven approach to develop a machine-learning interatomic potential for the MAX compound Ti_2AlC following the moment tensor potential protocol and validated against several physical properties. Finally, the potential is applied in classical molecular dynamics, providing a faithful representation of the experimentally observed nonlinear elasticity. We also find the effects of common defects, such as Al vacancies, in its stress-strain behavior.

List of Publications

1. *"Prediction of the Properties of the Rare-Earth Magnets $Ce_2Fe_{17-x}Co_xCN$: A Combined Machine-Learning and Ab-Initio Study."*, Anita Halder, Samir Rom, **Aishwaryo Ghosh**, Tanusri Saha-Dasgupta, Phys. Rev. Applied 14, 034024 (2020).

2. *"Machine learning classification of binary semiconductor heterostructures"*, Samir Rom*, **Aishwaryo Ghosh***, Anita Halder*, and Tanusri Saha-Dasgupta (*These authors contributed equally to this work), Phys. Rev. Materials 5, 043801 (2021).[Included in the thesis]

3. *"Understanding the trend in core–shell preferences for bimetallic nanoclusters: A machine learning approach"*, **Aishwaryo Ghosh**, Soumendu Datta, and Tanusri Saha-Dasgupta, The Journal of Physical Chemistry C 126.15 (2022). [Included in the thesis]

4. *"First principles insights into the relative stability, electronic and catalytic properties of core–shell, Janus and mixed structural patterns for bimetallic Pd–X nano-alloys (X = Co, Ni, Cu, Rh, Ag, Ir, Pt, Au)"*,Soumendu Datta, **Aishwaryo Ghosh** and Tanusri Saha-Dasgupta, Physical Chemistry Chemical Physics 25.6 (2023). [Included in the thesis]

5. *"Machine-learning prediction of the formation of atomic gold wires by mechanically controlled break junctions"*, **Aishwaryo Ghosh***, Biswajit Pabi*, Atindra Nath Pal and Tanusri Saha-Dasgupta (*These authors contributed equally to this work), Nanoscale 15.42 (2023). [Included in the thesis]

6. *"Ab-initio trained machine learning potential for MAX compound Ti_2AlC: Construction, validation, and study of non linear elasticity"*,**Aishwaryo Ghosh**, Amitava Moitra and Tanusri Saha-Dasgupta, Journal of Physics: Materials 8, 025001(2025). [Included in the thesis]

List of Figures

List of Tables

1

Introduction

"*Science no longer is in the position of observer of nature, but rather recognizes itself as part of the interplay between man and nature. The scientific method ... changes and transforms its object: the procedure can no longer keep its distance from the object.*"

- Werner Heisenberg

As human beings came into existence, their trajectory of treading through time became essentially embodied in the materials utilized by them. So much has been the latter's impact in progressing human civilization that the ages of history have been synopsized in terms of the concurrent predominant materials. During the course of the Stone age, the archaic human used their first tools shaped from stones to facilitate hunting, scavenging, etc., eventually leading up to the remarkable revolution of agriculture. This juncture of Neolithic history became the linchpin for the forthcoming organized society. The Bronze Age further reinforced the integrity of the growing social fabric through the transmission and trade of expertise, information, and utensils. Out of the womb of the Bronze Age emerged the Iron Age , driven by the advent of new metallurgical techniques. The invention of electronic components such as silicon semiconductors and optical amplifiers in the 20^{th} century brought an enormous shift from traditional industries to the information technology-based paradigm. The Information age allowed for the functioning of technologies in digital format; substantially metamorphosing communications,research & development, entertainment, transport and healthcare. To keep this wheel of technological revolution rolling in the 21^{st} century, new materials with targeted properties play a pivotal role. This includes but are not limited to lightweight durable materials, energy materials, polymers, materials for harsh environments, and biomaterials for tissue engineering. In order to satiate the exponentially increasing consumption, mankind has to bolster its resource base by tactfully implementing present unutilized materials or inventing novel functional materials. But for most of human civilization, the pace of innovation has been so slow that it has not been before decades

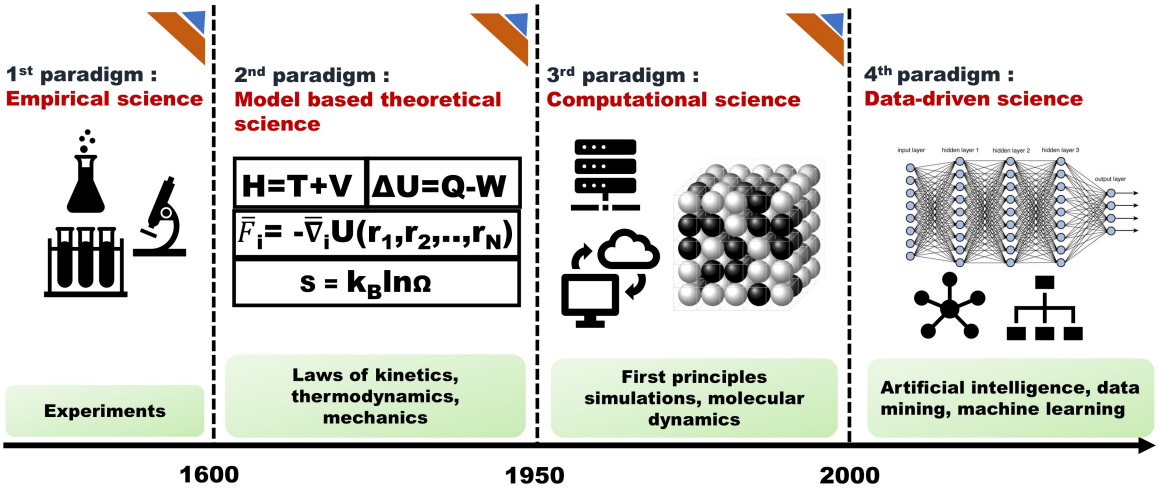

Figure 1.1: *A walk-through across the four paradigms of science: empirical, theoretical, computational, and data-based.*

that materials' discovery would influence the lives of people. The key bottleneck is the extensive trial and error approach towards materials engineering, which is time-consuming, high-cost, and arduous. Moreover, until recently, the lack of real-time databases of such efforts have been amiss; making the cycles of materials development further redundant and drawn out.

The progression of the field of materials science has closely followed the tracks of evolution in the overall fields of science and technology(c.f. Figure 1.1). Throughout most of the ages, it has been empirical - based on metallurgical inspection. Gradually, it shifted to the paradigm of theoretical models a few centuries ago, characterized by the various "laws" in the form of mathematical equations. However, for complex systems, analytical solutions tended to be infeasible. The next breakthrough came as we delved into the domain of computers a few decades ago. A third paradigm of computational science opened its doors, allowing complex numerical simulations based on a theoretical framework already developed. Density functional theory (DFT) and molecular dynamics (MD) are such excellent examples.

Today we, as has been told, are experiencing the fourth industrial revolution characterized by sophisticated technologies that "span the digital, physical and biological worlds.."[1] affecting "nearly the entire gamut of human development.."[1]. So,in order to alleviate the pressing issue of limited pace and efficacy in materials discovery, a large scale collective and interdisciplinary approach towards the sequence of design, development and implementation of materials and workflow can be adapted by capitalizing on these current state-of-the-art computational and information technologies. Generally speaking, tools and theories derived from the growing fields of data science & machine learning, big-data analytics, internet of things(IOT), computer science, digital and cloud technologies are ex-

ploited. This latest holistic approach comes under the purview of materials informatics[2], often considered the fourth scientific research paradigm[3]. Major momentum to this field was provided by the materials genome initiative[4] proposed by the US government in 2011 with the overarching goal of curtailing the developmental cost while substantially accelerating the process via the engagement of high-throughput prediction models and experiments, and a systematic repository and sharing platform. The aim of this emerging field lies in combinatorial materials design and synthesis, modeling, data management, product impact and life cycle assessment and so on. Furthermore, there has been much advancement in expanded data storage facilities. For example, CERN holds over 200 petabytes of data while the European Bioinformatics Institute stores tentatively 20 petabytes[5]. The material informatics community can also greatly benefit from such large repositories of relevant materials data.In fact, presently, several databases of both hypothetical and synthesized compounds, such as OQMD[6], Materials Project[7], AFLOWLib[8], ICSD[9] etc., have been made available to the community.

Machine learning, a branch of Artificial Intelligence, is one of the crucial components of materials informatics. Proposed by Arthur Samuel in the 1950s[10], it is the capability of a computer to interpret and model the inherent pattern(s) within data.This data-to-knowledge strategy has already been successfully administered to the fields of pattern recognition (facial[11] or fingerprint recognition[12]), bioinformatics[13], event forecasting[14], cognitive game theory[15] etc. It is also making great strides within materials research with the rise of materials informatics. Particularly, it finds great use in problems where fashioning specific algorithms can be cumbersome or non-viable. In these cases, rather than looking for solutions over a high-dimensional phase space, computers are able to progressively learn and infer directly from samples.

This capability of machine learning to scheme through multidimensional data, extract information, and unearth hidden laws makes it apt for assisting research in materials discovery, property prediction, and data interpretation, to name a few. Broadly, machine learning can be classified as supervised learning, unsupervised learning, and reinforcement learning. Supervised learning aims at connecting known inputs to unknown outputs based on patterns inferred from labeled training data. More often than not, the tasks assigned to such learning schemes are regression and classification. While the former forecasts continuous numerical output, the latter groups instances into discretized classes. On the other hand, unsupervised learning works with unlabeled data either by clustering them based on similarity,or by discovering association rules among them, or by reducing their dimensionality. Reinforcement learning aims to discover the most optimal result at a task by mimicking a trial-and-error approach. It is often used in learning representations[16]. Using the techniques discussed

above, some of the broader applications of machine learning in solving materials science problems and congruent examples from the literature have been briefly described in the following paragraphs.

- **Discovering new materials** : About 35 years back, the then general view towards materials discovery was well encapsulated by John Maddox, editor of Nature : "One of the continuing scandals of physical science is that it remains in general impossible to predict the structure of even the simplest crystalline solids from a knowledge of their chemical composition"[17]. The route through first principles based calculations has been almost insurmountable since the combinatorial space is extensive with convoluted energy surfaces[18]. Nowadays, this "classical" approach towards structure prediction has found some relevance owing to advances in structure selection and generational algorithms like minima hoping[19], random sampling[20, 21], evolutionary algorithms[22, 23] and metadynamics[24]. Nonetheless, these techniques demand substantial amount of resource intensive force and energy calculations and the issue regarding computational feasibility persists. However, search for modern high-functional materials remains incomplete without scheming through large structural and compositional spaces. The advances in data-driven approaches have assisted in challenging this notion. Machine learning can be used to address this problem in multifaceted ways. One of them is to hasten the force/energy evaluations by replacing first principles calculations by machine learned force fields. Another prominent approach is by component prediction[25] where the component space is scrutinized to find fitting stable materials to a prototype structure. This is achieved by either predicting the formation energies, convex hull calculations or simply computing the probability of a compound existing in a definite phase. For example, Ward et al.[26] employed standard Random Forest model to predict formation energies. Similarly, Kim et.al[27] have identified 53 novel quaternary Heusler compounds. Faber et al.[28] trained on a set of 10^4 compositions to compute formation energies of 2 million elpasolites crystals, out of which 90 stoichiometries are suggested to be lying on the convex hull. Machine learning has also been implemented in structure prediction. Early attempts include prediction of probability of a specific binary crystal structure[29], classification of binary crystal structures[30] and ternary compounds[31], classification between perovskite and non-perovskite structures[32] and so on. A somewhat different approach has been adopted by Park et.al.[33], where unlike using chemical composition and structure as descriptors, X-ray diffraction patterns are used to distinguish crystal system and space group of inorganic compounds. A similar approach has been utilized for crystal structure classification using an algorithm optimized on a simulated 2D diffraction fingerprint[34]. A neural network based architecture has

been employed to conjure stable ternary structures by drawing insights from binary hydrides[35].

- **Materials property prediction** : Machine learning methods have been successfully put to test in predicting various materials properties. Classification and regression algorithms can be employed to map system descriptors to targeted properties, revealing structure-property relationships. Various technological implementation of materials require a precise knowledge of bandgap, however, standard exchange correlation functionals are infamous for their systematic underestimation of bandgaps when compared with experimental values. Other more involved approaches, like using hybrid functionals or many-body GW approximations, are also computationally expensive. This issue has been attempted to be overcome using direct ML prediction of bandgaps based on experimental or theoretical training data. Zhuo et. al.[36] have used a two-pronged approach characterized by elemental properties of sample constituents,first to classify materials as metals or non-metals using a classifier and then a regressor to predict the bandgaps. Weston et.al[37] have taken the route of classification to distinguish between direct and indirect bandgaps in semiconducting materials. Rajan et.al[38] have predicted high-fidelity G_0W_0 bandgaps of MXENES by using varied regression methods. With the rekindled interest in the topic of topological states in condensed matter owing to the discovery of topological insulators[39, 40], the ML ansatz has made inroads in the research of this field. Neural Networks have been deployed to predict the topological invariants of 1D and 2D topological insulators[41–43]. In another work, taking advantage of the capability of neural networks in processing images, a representative image of the Hamiltonian derived from Monte Carlo simulations have been used to determine the topological phase of the system[44]. ML has been widely applied in the exploration of superconductive properties in materials, particularly their critical temperature T_C. Isayev et. al.[45] have segregated superconductors with T_C above and below 20K. Further, they used partial least squared regression and a forest-based regression scheme to model the transition temperature. Stanev et.al[46] have used a relatively larger dataset of 14000 materials in classifying materials with T_C below and above 10K with an accuracy of 92%. They have also observed that crucial descriptors are the average number of valence electrons, the metallic electronegativity differences, and orbital radii differences. Ziatdinov et al. have applied clustering algorithms to scanning tunneling microscopy data to derive insights into electronic interactions, expecting to throw light upon the illusive domain of unconventional superconductivity[47].

- **Interpretation of experimental data** : ML has also been utilized in the interpreta-

tion and processing of experimental data. Neural network-based pattern recognition systems have been used to characterize complex surface reconstructions[48]. Electrochemical impedance spectroscopy (EIS) data can be interpreted with ML, as exhibited by Bongiorno et. al[49]. X Ray Diffraction patterns have been analyzed using various ML workflow, including XRD classification,lattice analysis, detection of defects, etc[50]. In the same spirit, information can also be retrieved from neutron scattering data under the purview of ML[51]. Phase transition in ferroelectrics has been determined by implementing ML on multidimensional datasets depicting relaxation to voltage and thermal stimuli, without construction of an explicit Hamiltonian[52]. Interestingly, on the other end of the spectrum, the information from failed experiments has been found to be beneficial in training a ML model capable of predicting the crystallization of vanadium selenites[53].

- **Machine learning force fields**: First principle calculations can mostly provide accurate accurate descriptions of systems at a high computation cost. But Monte Carlo simulations, atomistic and molecular dynamics simulations or other techniques requiring frequent evaluations of forces,energies or stresses on larger systems or for longer simulation times cannot possibly afford to pay this price. In molecular dynamics, for example, simulations are based on classical force fields. Machine learned force fields, in this context, can describe the potential energy surface with high accuracy. They are reported to be as accurate and versatile as quantum mechanics based methods while being as fast as classical force fields. The underlying hypothesis for this class of force fields is that the force acting on an atom depends solely on the arrangement of its surrounding atoms. With a dataset containing sufficient arrangement vs force/energy examples, one can train an algorithm to learn the relationship between them and make future enumerations based purely on atomic arrangement information. The seminal work of Blank et.al.[54] on surface diffusion of Co/Ni(111) based on a neural network potential connected the energy of a system to its structure, specifically to the angle of the molecular axis relative to the surface normal and the location of the center of mass. The learning set has been generated from first principle calculations. One of the popular approaches in literature for representing the potential energy surface using machine learning can be accredited to Behler and Parrinelo [55], who suggested that the total energy of a system can be divided into their atomic contributions. Every atomic neighborhood, represented by a set of symmetric functions, and their corresponding energies/forces serve as input. Several different force fields have been built based on this principle, for example, the spectral neighbor analysis potential[56], moment tensor potential[57], neural network potentials[58] etc. Another family of highly explored potentials is the Gaussian approximation potentials

(GAPs)[59], interpolating atomic energies using Gaussian Process Regression[60]. The application of such potentials has been made to phases like bcc ferromagnetic iron[61], boron[62] and graphene[63] with great accuracy. Some other linear models worth mentioning are the works of Seko et.al[64] who have generated force fields for Na and Mg l[65].

In this thesis, we focus on different systems, starting from atomic scale to bulk limit, and attempt to address open questions germane to them. The systems studied in this thesis are:

- **Semiconductor Heterostructures**: Fabrication of semiconductor heterostructures with targeted characteristics involves scheming through a large number of combinations of the constituent semiconductors. A high-throughput search of this configurational space is restrictive in terms of conventional simulations. In our study, we focus on suggesting novel heterostructures formed by the joining of elemental and binary semiconductors; thus belonging to the branch of machine learning that aids discovering new materials. We first demonstrate that the type of heterostructure can be accurately predicted based on the band structure of the constituent semiconductors. We then train our algorithm, utilizing features that describe these semiconductors, on a known dataset of binary semiconductor heterostructures. Using the trained model, we theoretically predict the types of a large number of unknown heterostructure semiconductors, involving both elemental and binary semiconductors. Notably, the developed method is found to be extendable to heterojunctions of semiconductor quantum dots.

- **Bimetallic nanoalloys, particularly, core-shell configuration**: The factors driving the core-shell segregation of bimetallic nanoalloys is an interesting research problem. There is a dearth of experimental efforts in synthesizing and identifying the ordering in binary nanoclusters. Alternatively, we leverage a machine learning algorithm's capability of detecting underlying patterns in complex data. It is trained on first-principles data to identify chemical ordering in core-shell nanostructures. The key factors belonging to the constituent elements and their relative importance in ordering are elucidated. The influence of component concentration and cluster size on ordering is further investigated in terms of detailed first-principles calculations for Pd-based binary nanoalloys. These are particularly relevant as potential alternatives to Pt-based electrocatalysts, which are both scarce and costly. We then elaborate on the catalysis effect of such nanoclusters.

- **Gold atomic 1D-chains**: A mechanically-controlled break junction can be utilized in forming monoatomic 1D atomic chains of reasonable length. The impact of external

stimuli such as stretching rate and bias voltage is critical in their mechanical stability and transport properties. The combined influence of the electric field and the stretching rate on optimizing atomic chain formation has not been thoroughly investigated. Additionally, the widely used histogram analysis is unable to precisely identify the trace characteristics affected by the nanoscale structure of the metal electrode prior to the rupture of the point contact. In our work, machine learning model has been built based on large dataset obtained from inhouse experimental facility. In particular, a combination of unsupervised and supervised machine learning models are utilized to achieve a deeper microscopic understanding of Au chain formation. Particularly, we find optimal conditions of bias and the stretching rate for the formation of chains of length > 4 Å and detect trace features linked to these long-chain formation.

- **Layered, crystalline, MAX compounds, particularly, Ti_2AlC**: MAX phase compounds, which are layered crystalline solids, exhibit an intriguing nonlinear elastic behavior inspite of being mechanically stiff. Theoretical investigations of this curious feature have been challenging due to the length and time scales involved in these phenomena. In this study, we employ a data-driven approach to develop a machine-learned interatomic potential for the MAX compound Ti_2AlC. The effectiveness of the model is validated against various physical properties and finally applied in reproducing the non-linear elastic behavior in a classical molecular dynamics simulations scenario. The study uncovers the ripplocation as the underlying mechanism.

A brief background and pertinent theories of each of the aforementioned systems are described in the next section.

1.1 Material Background and Phenomena

1.1.1 Semiconductor heterostructures

The discovery and implementation of semiconductors have brought about a sea change in the domain of electronics and have permanently altered the course of human history. The research and development of semiconductor heterostructures, constructed by interfacing dissimilar semiconductors with unequal bandgaps, further widened their impact in many areas of human life. Semiconductor heterostructures have such an all-encompassing acceptance and attention owing to the potential of tuning their fundamental parameters like bandgap width, refractive index, effective masses and mobilities of carriers, and the electron energy spectrum. Double heterostructure lasers in telecommunications systems, high-electron-mobility transistors applied in high-frequency devices like satellite television

systems, light-emitting diodes and bipolar transistors, and solar cells with heterostructure components are just a few examples of practical applications of heterojunctions.

1.1.1.1 Classification and designing of heterostructures

When a heterojunction is formed by joining two semiconductors of dissimilar band gaps, discontinuities emerge between their valence band maxima or conduction band minima at their interface, and the consequent band bending modifies the electronic properties. These properties depend greatly on the nature of valence(conduction) band offsets VBOs(CBOs), viz. the discontinuity in valence bond maxima(conduction band minima) between two interfacing semiconductors, and the condition of the interface with respect to roughness and interfacial defects[66]. The structural integrity of the heterostructures can be achieved by choosing constituents with comparable lattice constants and crystal structure, or atleast, symmetry. For example, in Figure 1.2, the direct band gap and lattice constant of the various III-V and II- VI compounds are plotted. Few binaries, like GaAs/AlAs, InSb/CdTe, InAs/GaSb and InAs/AlSb have nearly the same lattice constants but different bandgaps and have been synthesized as a result of their clean crystalline interfaces. Ternaries can be derived by combining two binaries, with different band gap and lattice constant. The line joining the binaries in Figure 1.2 gives the values of the ternary compounds that may be made by consolidating them. It will have an identical lattice constant if the combining binaries have comparable lattice constant. The bandgap can lie between the two extreme values, depending on the percentage of the binaries. For instance, $Al_xGa_{1-x}As$ has similar lattice lattice constant as AlAs and GaAs, but the direct bandgap can range between 1.51 ev and 2.79 eV based on value of x. Moreover, combination of binaries with dissimilar lattice constants can give rise to a ternary with lattice constant comparable to a third binary. For example, $Al_{0.45}In_{0.52}As$ and $Ga_{0.47}In_{0.53}As$ are ternaries whose lattice match to InP. Heterostructures of good crystalline quality can also be obtained with non-matched lattices, but for lower dimensions. The strain generated from the lattice mismatch can be accommodated upto a thickness of around 4 nm[68]. The larger thickness can cause stacking faults due to the strain. The heterojunction interfaces are mostly devoid of crystal defects and interfacial charge density. Thus, the potential profile arising from the disparity in the bandgap is solely responsible for altering the electron states in the heterostructures as compared to the bulk states.

The aforementioned band alignment distinguishes the heterostructures into three classes, as schematically shown in Figure 1.3:(i) type-I (straddling gap), (ii) type-II (staggered gap), and (iii) type -III (broken gap)[69]. In type-I heterostructures, the valence bond maxima(VBM) and conduction band minima(CBM) of one material lie entirely within the

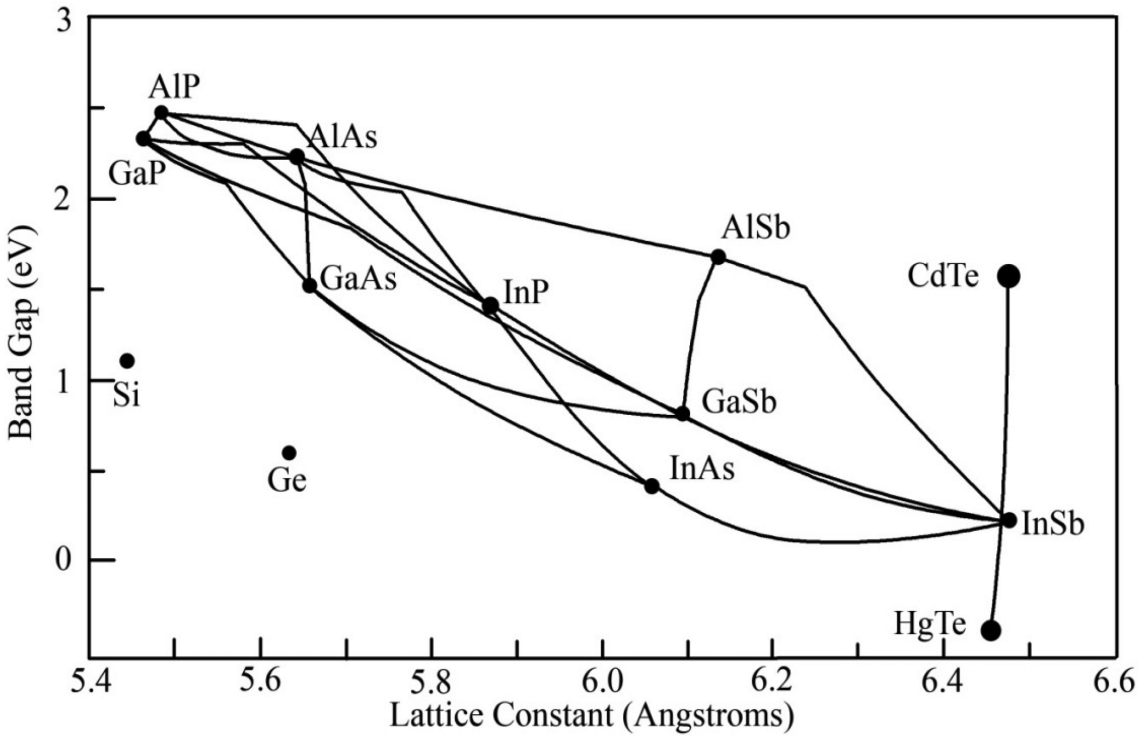

Figure 1.2: *Lattice constant of various III-V and II-VI semiconductors against their direct band gap E_g. The figure is taken from Ref [67].*

bandgap of the other, and consequently, VBM and CBM of the system lie in the same layer. The conduction band offset E_c and the valence band offset E_v can be represented as :

$$\Delta E_c = E_{c1} - E_{c2} = f(E_{g1} - E_{g2}) = f\Delta E_g$$

$$\Delta E_v = E_{v1} - E_{v2} = (1-f)(E_{g1} - E_{g2}) = (1-f)\Delta E_g$$

It is considered that $E_{g1} > E_{g2}$ and ΔE_g is the bandgap difference. The factor f gives the ratio $\frac{\Delta E_c}{\Delta E_g}$ and is determined by the pair of materials across the heterojunction with magnitude lying between 0 and 1. In type-I heterostructures, the narrower bandgap constitutes a well-like structure, while the wider bandgap acts as a barrier structure. This confines the electrons and the holes to the lower bandgap material in these heterostructures. $Al_{0.48}In_{0.52}As/Ga_{0.47}In_{0.53}As$, $InP/Ga_{0.47}In_{0.53}As$ and $Al_x\ Ga_{1-x}As/GaAs$ are some type-I heterostructures. This kind of heterostructures find application in light-emitting diodes and lasers, etc.

In type-II heterostructures, the bandgaps of the constituents partially overlay each other with one's CBM situated inside the bandgap of the other, and resultingly, the CBM and VBM of the complex lie in different layers. In these, $E_{v1} > E_{v2}$ and E_c may or may not

be greater than E_{g1}. In contrast to type-I, E_{g1} is not necessarily greater than E_{g2} and $\Delta E_c < E_{g1}$. Holes and electrons are confined in separate components of the heterostructure. InAs/$Al_{0.4}Ga_{0.6}$ is an instance of type-II heterostructure. These are implemented in photovoltaic devices and photodetectors. In the literature, Type-II has sometimes been referred to as Type-II staggered.

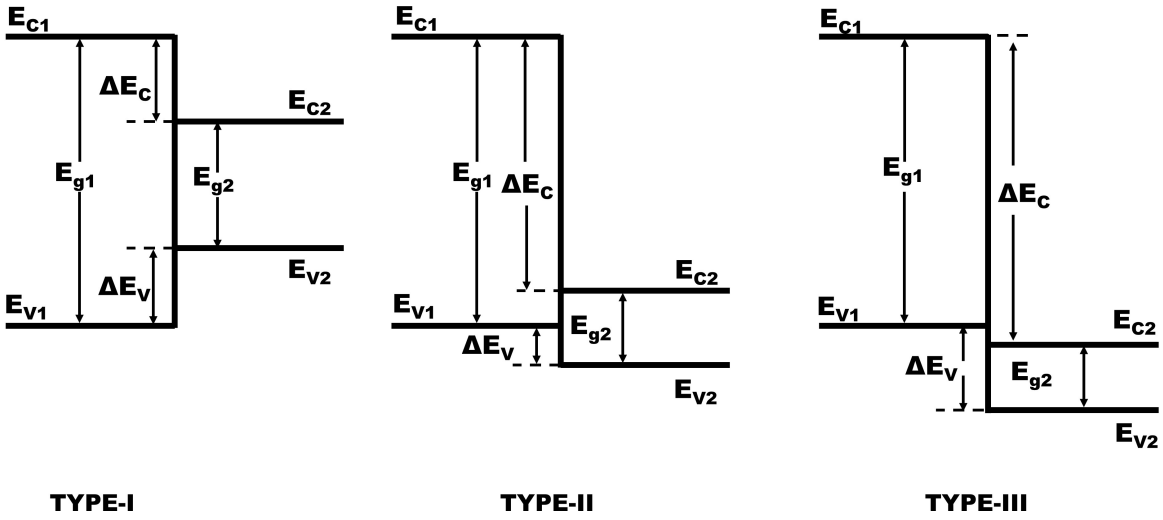

Figure 1.3: *Types of semiconductor heterojunctions based on band alignment of its components.*

Type-III heterostructures are devoid of any overlap in the bandgaps. Here also the electrons and holes are limited to separate materials. But, the valence band of the material containing the holes overlays the material with the electrons, leading to some unusual phenomena. They are utilized in tunneling devices such as negative differential resistance (NDR) devices and chemical sensors, as they enable the formation of p-n junctions without the need for external chemical doping. InAs/GaSb belongs to this class of heterostructure. In the literature, Type-III has sometimes been referred to as Type-II misaligned.

Effective designing of the band offsets is a crucial requirement relevant to all electronic devices exploiting semiconductor heterostructures.Two empirical rules[70–73] have been historically used in estimation of band offsets before the arrival of more complete theoretical methods. The oldest approach is due to Anderson[70, 71]. He stated that the difference in conduction band edges is equivalent to the difference in electron affinities of the constituents, i.e, the conduction band offset is :

$$\Delta E_c = x_1 - x_2,$$

where x_1 and x_2 are the electron affinities of the two materials across the junction. Despite the criticism of this simplistic model[68], it has been used extensively in the past and had

closely matched experimental results in some cases.

The other empirical rule, called the common anion rule[72, 73], stands on the empirical results derived from Schottky contacts[74] in III-V and II-VI compounds.When interfaced with gold, the Schottky barrier for the valence band of these compounds has been observed to remain consistent across different compounds that share the same anion. The theoretical bandstructure calculations present that the valence band is majorly contributed by the p-levels of the anions with minimal contributions from the cations. Consequently, the VBM position with respect to some reference level should rely only on the anion's electronegativity. The valence band offset between compounds sharing common anion should be zero, while the offset for different anions can be determined from the Schottky barrier valence-band offsets. However, experimentally the band offsets are seen to vary in the order of 0.2-0.4 eV between compounds with common anion. Thus, the rule cannot be strictly implemented, but considered as a guiding tool.

Several theoretical approaches have been used in the context of predicting band offsets at heterojunctions[75, 76]. These comprise the model solid theory[77], the dielectric midgap energy[78], the branch point energy or the charge neutrality level[79, 80] and the self-consistent dipole theory[81], generally in conjugation to first principles calculations.

A heterostructure can also be classified on the basis of arrrangement and interface of its constituent materials : (i) spherical zero dimensional (0D); (ii) cylindrical one dimensional (1D); (iii) planar two dimensional (2D); and (iv) cubic three dimensional (3D). 0D heterostructures have garnered much interest owing to their unique properties. Some notable examples are nanoclusters, quantum dots, quantum wells and core-shell structures[82, 83]. 1D nanoscaled heterostructures like nanowires[84], nanosheets[85] , nanorods[86] and nanotubes[87] have found extensive application for their physical and chemical properties. 2D heterostructures such as thin films are widely used in the electronics industry. 3D nanostructured materials comprise powders and polycrystalline materials in which 0D,1D and 2D elements are brought together to form heterostructure interfaces.

A substantial research endeavor has been put into type-II nanostructures composed of III and V direct bandgap semiconductor materials. This is because they offer relatively large bandgap energies and enable coverage of the entire mid- and far-infrared optical ranges for photoelectric devices. In nanoparticles/quantum-dots, the energy levels are discrete due to the confined carriers in all dimensions and electronic properties are dominated by their geometric size and shape. This quantum confinement in individual nanoparticles, combined with the unique balance of electronic properties from the parent semiconductors, offers exotic functionalization in heterostructures at the nanoscale. In this context, heterostructures

constructed of two different semiconductor quantum dots (QDs) are of interest because they allow for band offset engineering by tuning the QD-relevant structural characteristics. For example, the GaSb/GaAs quantum dot, which exhibits giant valence band offset, can find application in light emitting devices in the spectral range of 1 to approximately 1.5 μm, such as in neurology, ophthalmology, and endoscopy [88].

1.1.1.2 Applications

Catalytic applications: Heterostructure semiconductors have found recent applications in photocatalytic hydrogen evolution in photocatalysis. Various structures that enhance the hydrogen evolution rate have been synthesized and characterized. Heterostructures based on sulfide have found ubiquitous interest in this regard. Although transition metal sulfides have the necessary characteristics of a narrow bandgap and an appropriate valence band structure, they are unstable to some extent. Hence, they are usually combined with other semiconductor materials to alleviate this issue. Some example are : Cds/Nb_2CT_x Schottky heterojunctions formed by growing 1D Cds nanorods on 2D Nb_2CT_x, CdS-MoS_2 heterojunctions, 2D/2D $Ti_3C_2T_x$/$ZnIn_2S_4$ nanosheets etc. Another variant is the heterojunctions based on graphitic carbon nitride (g-C_3N_4). The limited photochemically active surface area of pure g-C_3N_4 and its inadequate solar energy utilization result in photocatalytic activity that falls short of optimal performance. Hence heterostructures such as g-C_3N_4/rGO/perylene diimide, cyano-modified graphitic carbon nitride (CGCN)/Cds etc. have been explored.

Electronics applications: Semiconductor heterostructures exhibit multifaceted applications in electronics.

- Semiconductor lasers : Semiconductor distributed-feedback laser, IR type-II heterostructure lasers,vertical surface emitting lasers.
- High-efficiency LEDs and low-noise, high-electron-mobility transistors(HEMTs) utilized in high-frequency devices
- Solar cells and photodetectors, relying on wide-gap window effect. Space station Mir has been equipped with heterostructure solar cells.
- Bipolar wide-gap transistors, high-power diodes and thyristors.

1.1.2 Bimetallic nanoalloys

In recent times, bimetallic nanoalloys have attracted both academic and industrial interest for their unusual properties, which can be different from pure metal clusters of their constituents and bulk alloy configurations, and for their miscellaneous applications in optics[89,

90], catalysis[91, 92], biomedicine[93, 94] etc. The interesting part of these alloys is that their properties depend not only on their size, as evident in pristine nanoclusters, but also on their chemical composition and stoichiometry. A rich variety of phases and structures are possible, and regulating them can be the stepping stones towards custom-made cluster-assembled materials[95].

The structural motifs of nanoparticles are varied and can change with size in a complex manner. Moreover, the constraint of alloy formation imposes additional caveats. Broadly, structural motifs can be divided into two classes: the crystalline and the noncrystalline motifs. The crystalline motifs are the segments of bulk crystals, viz,portions of the body-centered cubic (bcc), hexagonal close-packed (hcp), and face-centered cubic (fcc) lattices. The noncrystalline motifs are made possible by the absence of the constraint of translational symmetry in clusters and nanoparticles, which can acquire shapes unlike fragments of crystal lattices. For pure metal nanoparticles the icosahedron (Ih) and the decahedron (Dh) are common motifs while nanoalloys can assume other structures like the polyicosahedra.

1.1.2.1 Crystalline structures

In order to obtain energetic stability, cut is made to expose only low surface energy orientations. In most metals, these coincide to surfaces with densest atomic packing.

Face-centered cubic (fcc) nanoparticles: In FCC, (111) surfaces are closed packed with maximum possible 6 nearest neighbors to each atom. To obtain a nanoparticle with surfaces strictly made of (111) facets, an octahedral or a tetrahedral fragment can be cut. Structures based on regular octahedron (Oh) is more ubiquitous than the tetrahedron. To optimize the relatively larger surface-to-volume ratio in them, tactful truncation can be performed at the vertices giving rise to the truncated octahedron (TO) or the cuboctahedron (COh).

Body-centered cubic (bcc) nanoparticles: In BCC lattice, the densest packed surface is of (110) type. A fragment exposing these surfaces can be cut in an octahedral form, albeit not a regular one. The triangular facets are isosceles triangles. Truncation are preferable here too, by removing atoms from the common vertices of the two pyramids, forming a rhombic dodecahedron (RD). It can additionally be truncated at its six more acute vertices, uncovering (110) facets.

Hexagonal close-packed (hcp) nanoparticles: HCP lattice cannot be fragmented to exclusively reveal close-packed facets. Facets of type $(10\bar{1}1)$ offer good compactness, with each atom having five nearest neighbors in the surface plane. A hexagonal bipyramid with

surfaces made of 12 $(10\bar{1}1)$ facets can be an option. It can be truncated at the top and bottom vertex to yield a truncated hexagonal bipyramid.

1.1.2.2 Non-crystalline structures

Decahedra: The decahedron has a five-fold rotational axis which is not a permitted symmetry of a Bravais lattice. Evidently, it is noncrystalline. The regular decahedron is built by joining two pentagonal pyramids at their bases. It can hold 10 close-packed (111)-like facets, but also have a large surface-to-volume ratio. This can be compensated by forming the ino-decahedron[96] with five (100)-like facets by the removal of atoms from the edges surrounding the common base. Moreover, Marks decahedron[97] can be constructed by inserting re-entrances separating the (100)-like facets- providing further energetic gain.

Mackay Icosahedra: The mackay icosahedron[98] is a noncrystalline structure formed of concentric atomic layers. It features 20 triangular close-packed (111)-like facets and 12 vertices. Several surface reconstructions are possible, which form the foundation of the well-known low-symmetry structures initially introduced by Garzon et al.[99] as the lowest energy isomers of pure Au_{55} clusters. Reconstructions can happen by a series of *Rossette*[100] restructering of its vertices. Further structures like the Chui icosahedron[101] and the Mackay icosahedron with a central vacancy[102] are also possible.

Beyond the above mentioned structures, several other configurations like the anti-mackay[103], polyicosahedra[104], leary tetrahedra[105] and pentadodecahedra[106] are also found.

1.1.2.3 Chemical ordering

Chemical ordering denotes how different elements are arranged within a nanoparticle. There can be two main types of ordering : mixing patterns and non mixing patterns.

1.1.2.3.1 Mixing patterns

The mixing chemical ordering patterns are generally differentiated by their degree of ordering. These can cover from perfectly ordered phases, as in fragments of bulk ordered phases(Figure 1.4 (A)), to entirely random solid solutions(Figure 1.4 (B)). Real systems are composed of both of these orderings. However, all ordered phases contain defects at finite temperature, while true randomness is unachievable due to presence of finite short range correlation. Systems exhibiting ordered phases for some specific compositions are Au-Pd, Au-Cu, Fe-Pt and Co-Pt. FCC lattice form the basis of these compositions. Example of systems that exhibit random mixing are Ag-Au and Ag-Pd. In fact, a long-range

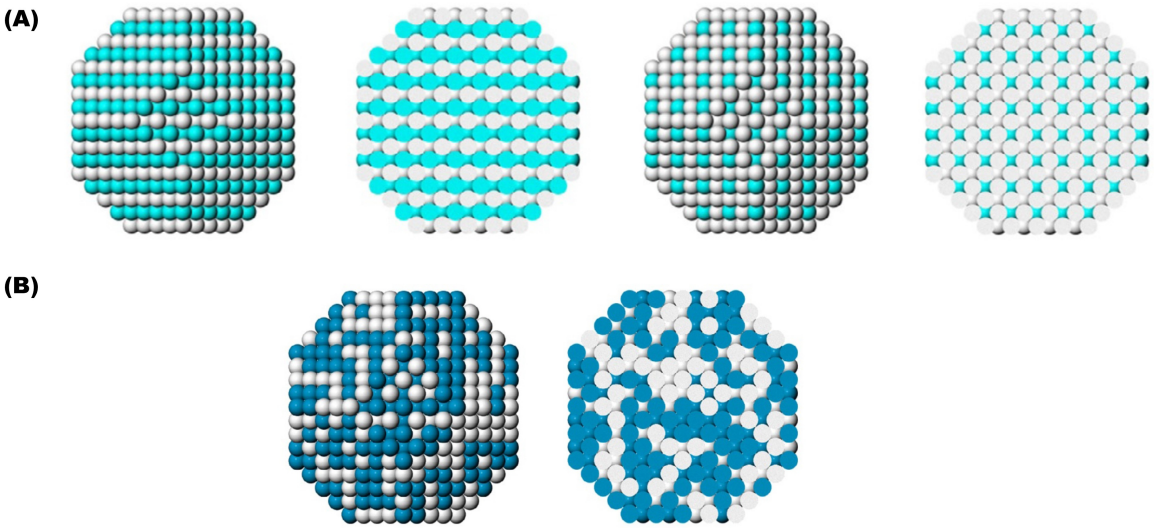

Figure 1.4: *Schematic representation of mixing configurations,taken from[107].(A) FCC-based ordered phases in a regular truncated octahedron. Nanoalloy surfaces and cross-sections are shown. (B) Randomly mixed disordered phase.*

order parameter is often employed to investigate whether an alloy is in ordered or disordered state. In reality, the mixing patterns are further complicated by the tendency of one of the components to segregate to surface(the component with lower surface energy). This can exhaust the nanoalloy interior,forming patterns between mixed and core-shell, or even completely core-shell(see section 1.1.2.3.2). This segregation trend can be the natural tendency of the element, or induced by the environment of the nanostructure: for example,ligands binding strongly to a component can pull it to the surface.

1.1.2.3.2 Non-mixing patterns

A motley of nonmixing patterns have been observed, as portrayed schematically in Figure 1.5. A frequent pattern is the core-shell pattern, characterized by a core of one type of atoms A covered by shell of another type of atoms B, often represented as A@B (Figure 1.5 (A)). A phase-separated form called Janus pattern, nomenclatured after the two-headed god of ancient Roman mythology, is also seen, shown schematically in Figure 1.5(D). Here the nanoalloy is occupied by two species at opposite sides. Other probable arrangements include multishell(Figure 1.5 (B)),quasi-Janus(Figure 1.5 (E)), ball-and-cup pattern(Figure 1.5 (C)) and multi-shell patchy[109–113]. In a three-shell configruation, a core of species B is surrounded by an intermediate shell of species A which, in turn, is again coated by an outer shell of B, as represented by B@A@B. In a quasi-Janus setup, we can consider the A part being engulfed by atoms of B type forming a very thin layer of A, or an asymmtrically placed core in a core-shell nanoparticle. In a ball-and-cup configuration, the shell incompletely covers the core in one of its sides. A unique multi-shell ordering with patchy nature

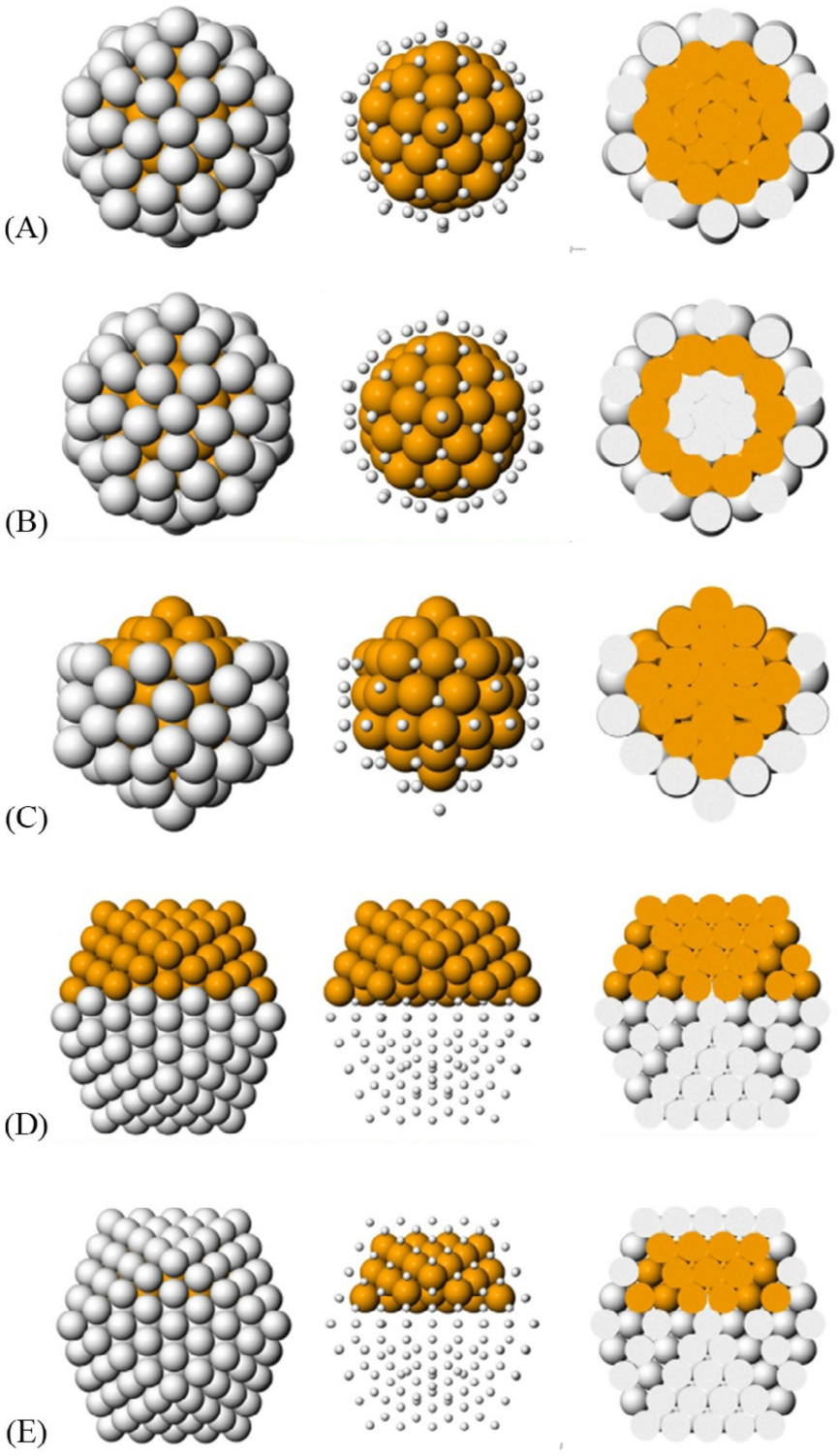

Figure 1.5: *Schematic representation of non-mixing configurations,adapted from[108].Two types of atoms A and B are shown in orange and gray,respectively.Each pattern is presented from three views: external structure(left),cross-section(middle) and B atoms drawn as small spheres(right).From top to bottom: (A)Core-shell A@B; (B)Multi-shell B@A@B; (C)Ball-and-cup A@B; (D)Janus; (E)quasi-Janus A@B.*

has been observed in nanoalloys like Pd-Pt, where component species have negligible lattice mismatch. Each shell is constructed by conglomeration of atoms of the two species but

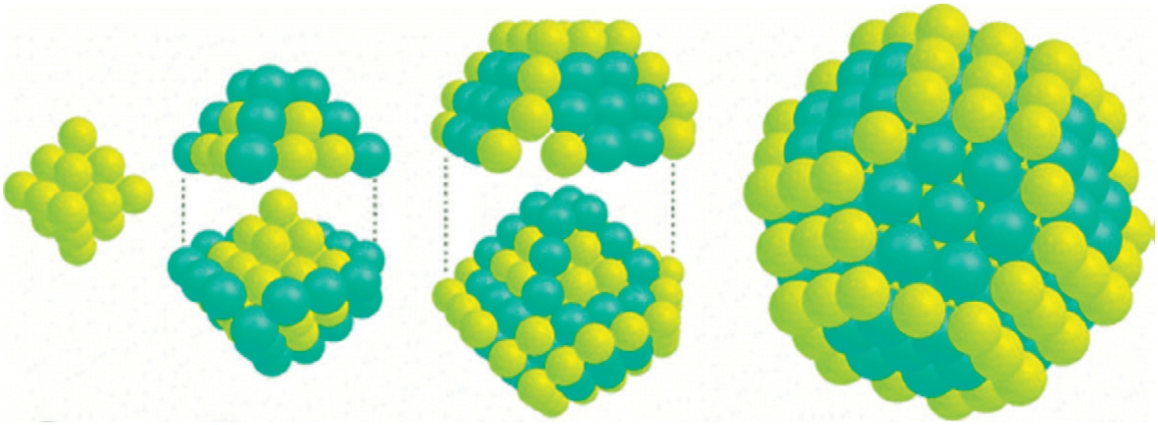

Figure 1.6: *Patchy multishell ordering in Pd-Pt nanoalloy,taken from[109].The distinct shells are shown. In each shell two species, shown in two different colors, are aligned in patches.*

their order are reversed in alternative shells, see Figure 1.6.
The important driving forces behind the non-mixing behavior can be briefly noted as follows[104, 114]:

- Poor likelihood of elements mixing at bulk limit.
- Element with lower surface energy segregates to the surface. Generally, surface energy correlates to cohesive energy.
- Atomic size mismatch forces larger atoms to surface to reduce internal stress.

Size mismatch and surface energy difference can cooperate if species with larger atoms has lower surface energy(e.g, in Au-Co, Ag-Co, Au-Pt,Ag-Ni etc). Conversely, if the larger atoms possess a higher surface energy, these two effects can be counteractive. Furthermore, the geometric structure of the nanoalloy plays a crucial role in chemical ordering in a complex way[115].Thus,the segregation trend in nanoalloys is highly nontrivial, due to the interplay of multiple factors.

1.1.2.4 Applications

Biomedical applications: Nanomaterials have found wide usage in biomedicine. This capability can be ascribed to the advantages of their high surface- to-volume ratio. However, physical properties that are suitable for the purpose of the application are the most crucial parameters to consider. Moreover, the selected system should *a priori* be ”safe” throughout the duration of its use. The spectrum of application can be divided into two flavors : in-vivo and in-vitro. The former includes therapeutic techniques such as hyperthermia and targeted drug delivery, and diagnostic aspects such as bioimaging. Nanoalloys such as Fe-Co and Cu-Ni have been prescribed for hyperthermic treatment. Fe_3O_4 nanoparti-

cles with varied coated systems have been suggested for drug delivery to cancer cells. In MRI, core-shell nanoparticles, for instance Fe-Co, Fe-Ni, Fe-Pt, etc., have been suggested as contrast agents. The latter is mainly implemented in diagnostic purposes like magneto-relaxometry[116].

Catalysis: Nanoalloys can find utilization as catalysts in some of the most critical industrial chemical processes. In three way catalysis(TWC) CO, hydrocarbons(HC) and NO_x in automobile exhaust are congruently converted. CO and HC are oxidised to Co_2 and H_20 while NO_x are reduced to oxygen. Pt-Rh nanoalloys have been employed in NO_x decomposition. Au-Ag nanoparticles have been reported for oxidation of CO[117]. Au-Cu bimetallic nanoparticles have also been inspected as a catalyst for CO oxidation[118]. Effective catalysts for the Fischer–Tropsch[119] process is another challenge and bimetallic systems like PtCo, CuCo,RuCo are found to be promising. Catalytic reforming is an indispensable part of refinery industry. Pt-Re and Pt-Sn bimetallic systems have shown exciting headway in this regard. Optimized activity is of utmost importance in electrocatalysis. Activity of dendrimer-encapsulated Pt nanoclusters has been reported to be substantial. Other candidates include Pt-Ir, Pt-Pd, MnCo etc.

Energy applications: The disbursement and storage of energy in an effective and sustainable manner is an ongoing research requirement. Conventionally, expensive and rare metals have been an essential component to reach peak performance in terms of catalytic performance in hydrogen evolution reaction and the oxygen evolution reaction[120]. For oxygen evolution reaction, the usage of Pt-shell@M-core nanoalloys, where M is transition metals like Fe,Co,Cu,Ni, has been explored. For ethanol oxidation reactions, Sn/Pt nanoparticles have been found useful. The use of nanosystems have also being attempted in batteries, specifically in nanostructuring the electrodes. Most of the success in cathode engineering has come from carbon nanostructures, with some examples of nanoporous metallic systems of Au,Pt,Pd and Ag and their combinations. For anode, Cu-Li systems are found to be encouraging. Nanoparticles like AuCu are used in photocatalysis. Metallic nanoparticles such as Au, Al and Ag are used to manufacture photovoltaic devices.

1.1.3 Atomic gold 1D chain

The metallic nanowires fashioned by mechanically controlled break junction or scanning tunneling microscopy techniques, being a one-dimensional system, have emerged as a unique testbed for electronic transport phenomenon in the atomic limit. They are projected to play a significant role in future generations of electronic devices. The observation of step-like conductance during the formation of these wires has generated increasing interest in this field since the last decade[121, 122]. The invention of the Scanning Tunneling Microscope (STM) greatly impacted the panorama of this field. Gimzewski and

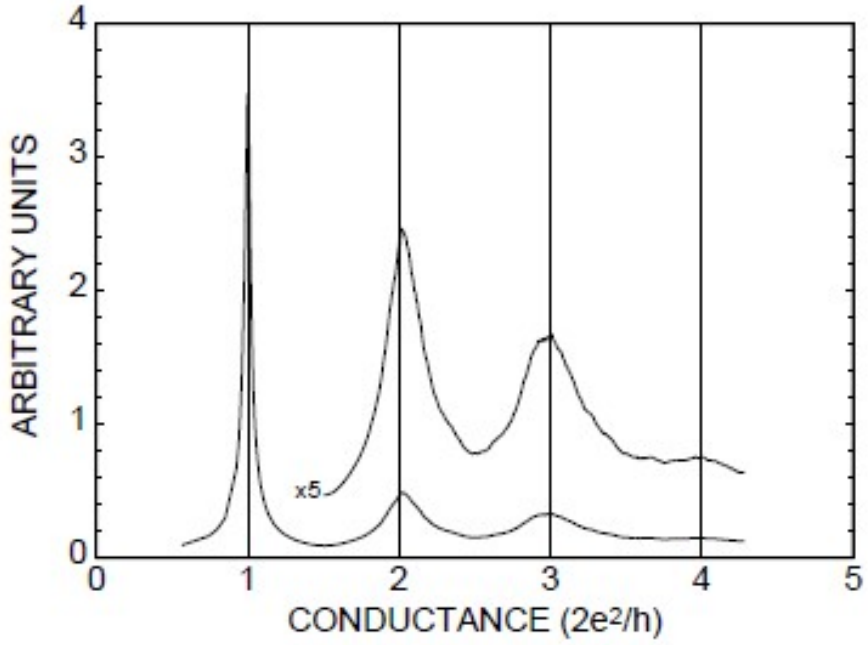

Figure 1.7: *Conductance histogram of Au contacts at room temperature combining several thousands independent measurements, taken from [130].*

Möller[123] first used the STM to investigate the conductance in atomic sized contacts and Dürig et.al[124] measured the forces using an Atomic Force Microscope (AFM). Secondly, the quantization of conductances was observed in 2D electron gas devices[125]. Finally, the mechanical properties of atomic-sized metallic contacts were elucidated in two seminal papers [126, 127]. It was shown using molecular dynamics simulations of contact between an atomic scale STM tip and a flat surface that the contact underwent a series of elastic deformations and abrupt atomic rearrangements. These three activities imparted inertia to developments in the early 1990s. Around this time, Muller et al.[128] came up with the technique of the mechanically controllable break junction (MCBJ) to make and break atomic contacts - establishing the quantized behavior of the conductance with steps of $G_0=2e^2/h$[129]. Such phenomenon was attributed to atomic structural reconfigurations[126, 127]. This subtle interplay of structure and conductance has been closely observed under the purview of several experimental results. In the experiments, atomic-sized contacts are stretched till breakage, and the conductance across them is measured. The conductance falls stepwise with steps of order of G_0. Each curve displays a unique profile due to the different possible atomic configurations the contact can assume.. For objective analysis, conductance histograms based on multiple such curves are made. The presence of conductance plateaus, preferably at nG_0 values, has been observed for various metals under different conditions.

1.1.3.1 Gold contacts and morphologies

Gold contacts have been extensively investigated by the histogram method. Many characteristics of the histograms, observed in experiments performed at wildly varied conditions, seem to coincide. The low reactivity of the gold surfaces and capability of excellent surface reconstructions might be the underlying cause. In general, peaks slightly shifted to lower values from 1,2 and $3G_0$ are recorded, and the shift can be accredited to electron backscattering at impurities or defects near the contacts. The first peaks are always the most pronounced, whereas the latter peaks decrease in height with increasing conductance, as shown in Figure 1.7. The first peak can survive upto 2V of bias voltage, analogous to impressive current densities of the order of $2\times\ 10^{15}$A/m^2. The other features also remain unchanged upto 500 mV. No qualitative changes are observed in the histograms between helium and room temperatures[131]; however, the relative height of the first peak increases as the temperature decreases. Although no significant change is observed depending on the retraction rate ranging from 30 to 4000 nm/s, at very slow limit[132] the shape of the histogram can alter substantially owing to the surface diffusion of gold atoms.
Two typical morphologies of gold atomic contacts are single-atom contacts and chains. This has been explored in ref [133] in some detail, using a combination of molecular dynamics simulations and tight-binding calculations. In Figure 1.8, taken from the above reference, the forces, the conductance, the radius of the minimum cross section, and the transmissions of the different conduction channels are presented for the evolution of a starting configuration of central gold wire connected to two banks. The decrease in conductance on the stretching of the wire is closely aligned with the changes in the minimum cross section. However, at some points, the conductance jumps in spite of the smooth evolution of the cross section. This can be attributed to the atomic rearrangements further away from the narrowest part of the wire. The force evolution in the upper panel also corroborates this. If jumps in conductance are not supplemented by sudden toggles in the minimum cross section, abberations in the forces can be observed. This suggests that plastic deformations in the regions of the wire far from its thinnest part also affect the conductance. The most interesting part of the evolution of a gold nanocontact is the region before its breaking, i.e., around $1G_0$. A glance at the MD snapshots at the bottom panel would convince that a single conduction channel dominates. This is because the number of channels is determined by the number of valence orbitals at the tip of the contact[134]. For Au, the density of states at the Fermi level is dominated by the 6s band, meaning that there is only a single valence orbital. During the stretching exercise, the channels are removed consecutively as the Au atoms leave the narrowest part of the constriction.

In certain cases, the contacts do not break, but rather form a chain of atoms pulling atoms

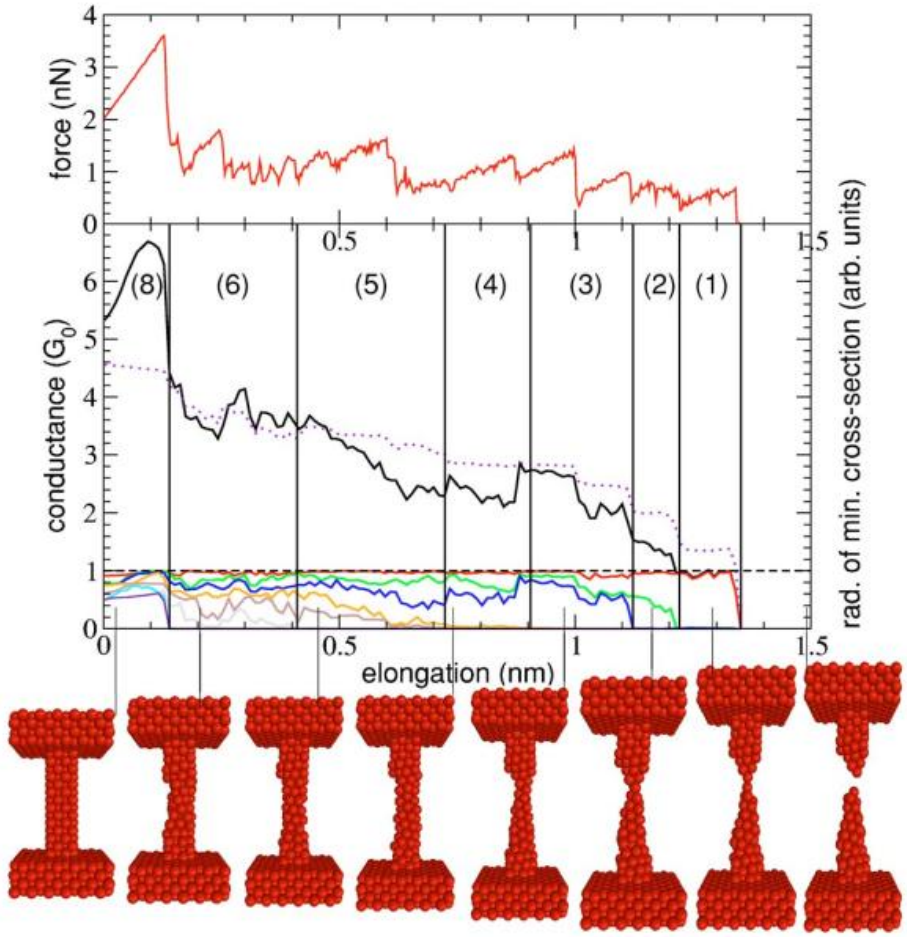

Figure 1.8: *Formation of single-atomic contacts of Au. The top panel exhibits the forces with contact stretching. The lower panel shows the conductance and minimum cross section. The image below the graphs are snapshots from MD simulation of stretching of the Au wire. Taken from [133].*

from the bank. The formation of chains has been suggested in different simulations and experiments[135, 136].Bahn and Jacobsen have explained the mechanism in terms of many-body effects in metals. The crux is that it is typical that the binding strength increases as the coordination number decreases. Thus, the force required to break bonds in a linear chain is larger than the force needed to break the bulk bond. The conductance can range from $0.6G_0$ to $1.1G_0$, with a flat plateau around $1G_0$. The conductance is again dominated by a single channel, which is a consequence of Au being a monovalent atom. At the final stages of elongation, in some cases, multiple channels are observed. Figure 1.9 shows that the structural variations in conductance during chain formation are followed by sudden shifts in forces, indicating plastic deformations. These deformations are understood to correspond to the addition of another atom to the chain.

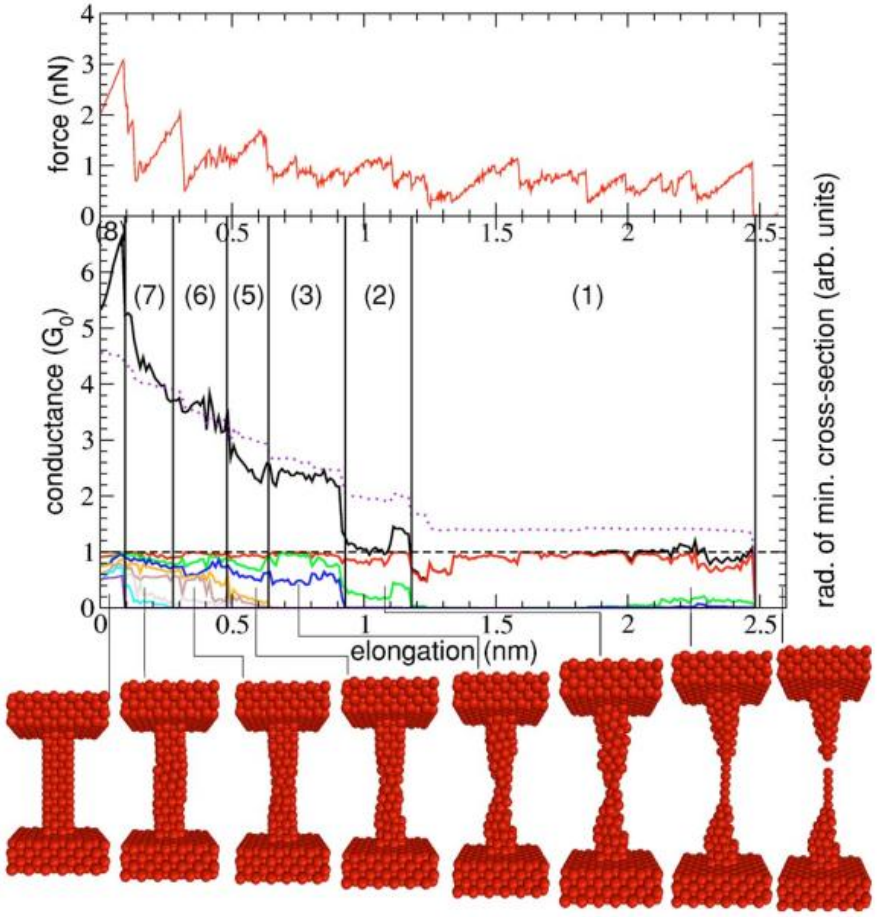

Figure 1.9: *Formation of Au chain. The top panel exhibits the forces with contact stretching. The lower panel shows the conductance and minimum cross section. The image below the graphs are snapshots from MD simulation of formation of chain and its subsequent breaking. Taken from [133].*

1.1.3.2 Effect of bias voltage and stretching rate

External parameter like bias voltage is found to affect the atomic contacts. Bias voltage is applied to measure the conductance. In particular, the stabilization of these nanowires and the relevant geometries at higher bias has been reported[137, 138]. The nanowires because of their size are ballistic, but high bias can lead to a finite probability of inelastic electron-phonon scattering. Energy dissipation has been shown to occur when the applied bias voltage exceeds the characteristic zone-boundary phonon energy. Scattering events per volume will be predominant within the atomic wire, owing to the high current density. Thus, the average lattice vibration energy will contribute towards increasing the local effective temperature. This increased temperature can lead to thermal rupture of the wire, and hence a significant parameter. It is also found that the maximum voltage sustained decreases as chain length increases. The first peak can shift to higher conductance values as the chains are transformed into single-atom contacts at higher bias voltages. Another

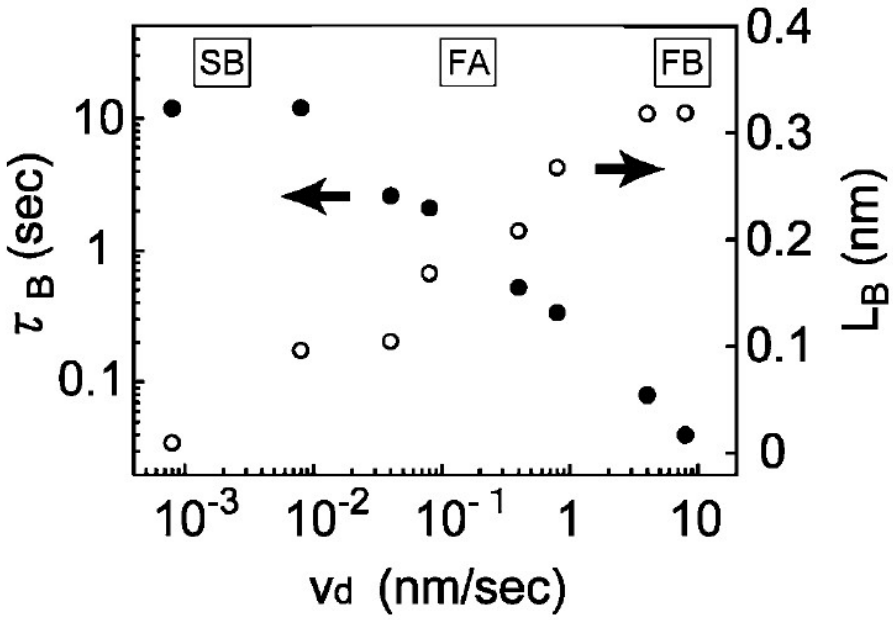

Figure 1.10: *Semilogarithmic plot of contact breaking length and contact lifetime versus stretching rate clearly illustrating three distinct regions: the force-breaking regime, the force-accelerated spontaneous breakdown regime, and the self-breaking regime. Taken from [139].*

factor that impacts chain formation is the breaking speed/stretching rate while using a setup like MCBJ. It is the rate at which the bending mechanism of the MCBJ separated the electrodes, thus thinning the wire, breaking it at its weak point, and relaxing again to reestablish contact. A study[139] of gold junctions at room temperature has revealed that the peak of single atomic contact lifetime(τ_B) shifts monotonically to higher values as the stretching rate(v_d) decreases. It is anticipated that during mechanical elongation at low stretching rates, sufficient relaxation of the contact structure will occur, given the relative mobility of gold atoms at room temperature. Consequently, stable contacts with specific configurations are more likely to form. The characteristic contact breaking length L_B is calculated from τ_B, assuming that that the contacts are elongated at a uniform rate v_d, and is plotted as a function of v_d alongside τ_B in Figure 1.10. The plot reveals three distinct regions : the self-breaking (SB) regime, where L_B tends to zero and τ_B saturates, the force-accelerated spontaneous breaking (FA) regime, where L_B falls monotonically while v_d decreases, and the force-breaking (FB) regime, where L_B is a constant independent of v_d. In the SB region, the stretching rate is comparable to the atomic diffusion speed, and there is sufficient contact structure relaxation at the banks compensating for the induced strains. The stretching rate thus plays almost no role in the breakdown of contact, and is mediated solely by thermal activity. At the other extremity in the FB region, mechanical loading dominates the breaking mechanism. Stress accumulation effectively lowers the energy barrier for thermally activated contact breakdown. At sufficiently high loading rate, the energy barrier can

quickly drop to zero, leaving little room for thermal fluctuations to play a significant role. As a result, contacts tend to break at a specific length. In the intermediate region, spontaneous breakdown might occur as contacts rupture at a level of external force at which thermal dissociation is also viable.

1.1.3.3 Way forward from atomic chains

The fabrication of nanoscale atomic contacts and chains and understanding of their dynamics are the stepping stones toward the actualization of molecular electronics. In contrast to silicon-based electronics, they have the following advantages:
Size: The reduced size of small molecules mean higher packing density of the devices, consequently curtailing cost, increasing efficacy and power dissipation.
Speed: While most molecules have low conductivity, well-engineered molecular wires could decrease the transit time of typical transistors, thereby shortening the time required for operations.
Synthetic customization: By manipulating the geometry and composition, it is possible to tune a molecule's binding, transport, optical and structural properties.
Novel functionalities: Unique molecular properties, such as the presence of distinct stable geometric structures or isomers, could enable new electronic functions that cannot be achieved with conventional solid-state devices.

1.1.4 MAX compounds

MAX compounds are layered ternary nitrides and carbides with the general formula $M_{n+1}AX_n$ where M is an early transition metal, A is an A-group element (a subset of group 13–16 elements); X is C or N and n =1,2,3. The possible elements present in reported MAX compounds so far is represented in Figure 1.11. First synthesized by Nowotny et.al[140, 141] in powder form, Barsoum and El-Raghy[142] finally purified the phase-pure bulk Ti_3SiC_2 rekindling the interest in this class of compounds. This interest is chiefly rooted in their unusual and unique properties due to their diverse atomic bonding and structural characteristics.

1.1.4.1 Crystal structure, atomic bonding and defects

Most MAX unit cells are hexagonal and belong to the space group P63/mmc with two formula units per unit cell. Layers of edge-sharing M_6X octahedra are interspersed with layers of pure A atoms, located at the center of trigonal prisms (Figure 1.11). The value of 'n' determines the number of M-X layers between two consecutive A-layers. So far, different compositions have been discovered that exceed 150 in number. More are being added

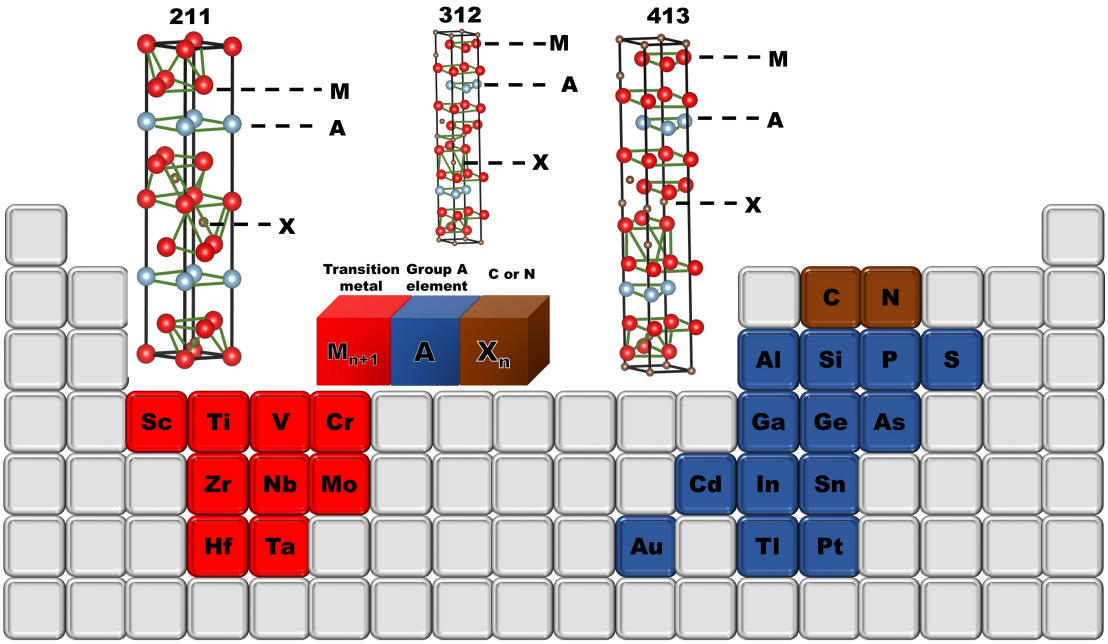

Figure 1.11: *Elements from the periodic table present in the reported MAX phases, along with the crystal structures for the 211, 312, and 413 phases, are also illustrated.*

because of theoretical and experimental work. However, not all possible combinations are stable thermodynamically. For instance, Ti_2AlC(n=1) and Ti_3AlC_2(n=2) belonging to the Ti-Al-C system are stable over an extended temperature range, but in other systems such as Cr-Al-C and Ti-Si-C only combinations corresponding to n =1 and 2 are stable,respectively. At the same time, solid solutions can be prepared by subsitutions on "M", "A" or/and "X" sites. However, the immense number of possible permutations limits the definition of compositions of stable solid solutions. Curiously,in some cases, solid solutions are found to be stable, although their parent compositions are not.

Crystal defects remain a constant challenge for any material with scope for practical applications, as the advancement of materials development inevitably relies on understanding these defects. For example, a crucial step in utilizing MAX phases as high-temperature structural materials is to have superior resistance to oxidation and mechanical degradation. These properties are primarily influenced by A-site vacancies and basal dislocations. MAX phases have been reported to accommodate various defects. These defects can be classed as point defects, line defects, planar defects and bulk defects in 0,1,2 and 3 dimensions respectively. Point defects include vacancies and solid solutions; line defects include dislocation and disclination; and planar defects include stacking faults, grain boundaries, domain boundaries, and so on. Effect of vacancies on elastic behavior has been explored in this thesis. MAX phases like Ti_2AlC, Ti_3SiC_2 and Ta_4AlC_3 can remarkably support upto 50% A site vacancies, beyond which the Ti-Al antibonding levels are occupied, diminishing the bonding between M-X and A layers and undermining structural stability. A site vacancy

formation energy are of the order of $\approx$ 2 eV. The vacancy migration energies along the basal plane are found to be less than 1 eV for Ti-Al-C systems. This exceptional capacity of Al vacancy formation and migration are crucial in forming protective Al_2O_3 layers at high temperature. While the X site vacancy formation energy is comparable to that of A sites, their migration energies are 3-4 times larger and are found to destabilize the hexagonal structure. It is more difficult to migrate C vacancies. For MAX phases where n $>$ 2, there exists multiple crystallographically non-equivalent X sites with different capacities of accommodating X vacancies. Structures with ordered C vacancy stabilizes at low temperature. With increasing temperature, vacancies start to become disordered. The incomplete order-disorder transformation leads to the formation of nanometer-sized domains. Various electronic, mechanical and deformation characteristics are bound to the extent and structure of these domains, however such studies are limited. A vacancies are reported to increase dielectric property, X vacancies can diminish the superconductivity transition temperature while enhancing electronic conductivity.

The bonding picture in MAX compounds are quite appealing, with a combination of metallic,covalent and ionic bonds. The M and X atoms form strong, directional covalent bonds by the overlap of p levels of X atoms and d levels of M atoms. The Fermi level, with substantial density of states, is dominated by M-d/M-d metallic bonds. The M-A bonds are generally weaker than M-X bonds, and are partly covalent and partly ionic. In the M_2AlC phases, charge is transferred from the A atoms to the X atoms[143].

1.1.4.2 Properties

Many properties are found to be intermediate to those of metals and ceramics. Akin to their corresponding binary carbides and nitrides, the MAX phases exhibit elastic stiffness, excellent thermal and electrical conductivity, are resistant to chemical corrosion, and have relatively low thermal expansion coefficients. Several MAX phases, including Ti_3SiC_2, exhibit very low thermoelectric or Seebeck coefficients. The optical properties of the MAX phases are mainly influenced by delocalized electrons. Most of them are Pauli paramagnets, with susceptibility being moderate and independent of temperature. Thermally, MAX phases are good thermal conductors with conductivity ranging between 12-60 W/(m.K) at room temperature. At high temperatures, the MAX phases undergo peritectic decomposition rather than congruent melting, forming A-rich liquids and $M_{n+1}X_n$ carbides or nitrides. Some MAX phases are resistant to oxidation, making them suitable for practical purposes. Consequently, they are being considered for high temperature applications because of their appreciable electrical, mechanical, and high temperature properties. In spite of the similarity in physical properties between the MX and MAX phases, they are quite different

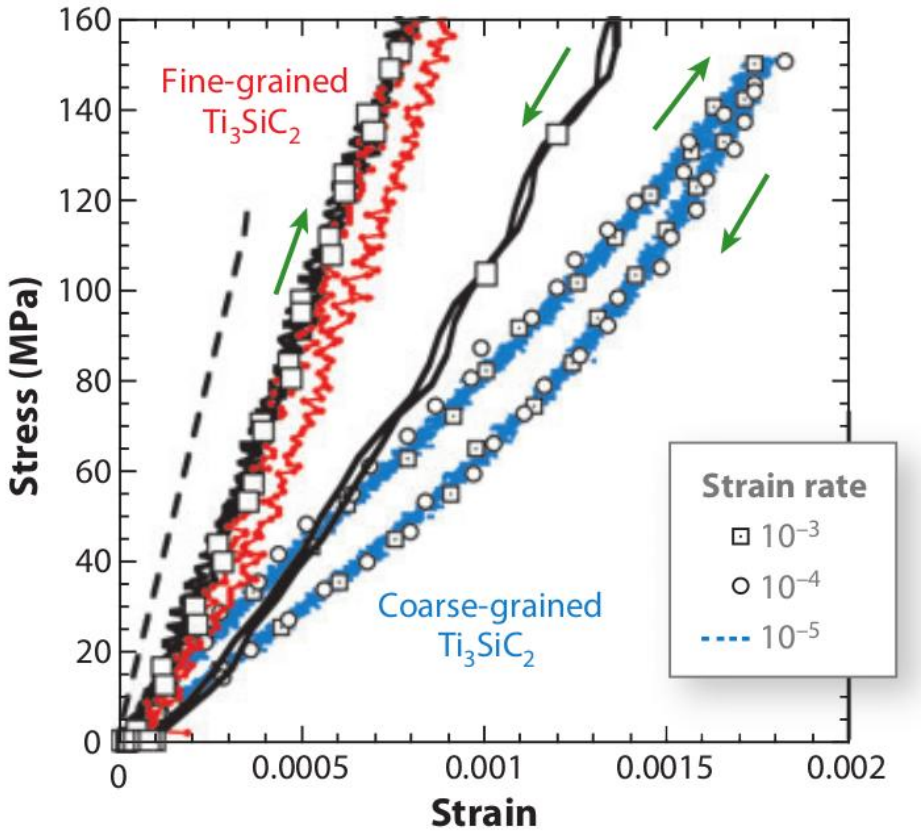

Figure 1.12: *Ti_3SiC_2 samples demonstrate a significant difference in behavior between coarse-grained (CG) samples (blue loops) and fine-grained (FG) samples (black and red loops). The small loops represent three different tests conducted at strain rates varying by an order of magnitude each. Within the resolution of the measurement, all three loops exhibit identical shape and area. Plot taken from [144].*

mechanically. They demonstrate superior damage tolerance compared to other ceramics. This can be validated by Vickers indentation. Rather than cracking and its propagation, alternative mechanisms like delamination, grain kinking, and grain pullout are set in the vicinity of the indentation. They are also not vulnerable to thermal shock. MAX phases have been tested against different corrosive agents, with positive outcomes. Interestingly, they are easily machinable, resulting from their thermal shock and damage resistance and can be machined by electrically owing to their high electrical conductivity.

One of the widely explored areas are the elastic properties of the MAX phases, which present nonlinear, hysteretic, and elastic behavior that is puculiar for stiff compounds. Spontaneously reversible hysteretic loops can be seen on cyclic loading (compression or tension) of the MAX phases. The shapes and sizes of such loops closely relate to the grain size. Figure 1.12 shows cyclic stress-strain curves for Ti_3SiC_2 with two different grain sizes. Although initially it was thought that incipient kink bands(IKBs) - oppositely signed basal dislocation walls- were responsible for this behavior, certain evidence has been re-

ported against it. The most critical one is the presence of c-axis strain as evident from delaminations after nanoindentation - basal dislocations cannot give rise to c-axis strain. Another strike is the strong dependence of confining pressure on compressive strengths of the crystals. An alternative explanation of the non-linear behavior has been offered in literature in terms of *ripplocations* - atomic scale ripples- and has been explored in this thesis.

1.1.4.3 Potential applications

Many potential applications have been proposed and tested, including replacing graphite in high-temperature environments, heating elements, high-temperature foil bearings, gas burner nozzles, tooling for dry concrete drilling, ignition devices, and electrical contacts. However, these applications have not yet been commercialized. The only product currently in use is Cr_2AlC pantographs for electric high-speed trains in China, which have successfully replaced carbon-based alternatives. This lack in commercial application can be ascribed to certain reasons: lack of high-quality powders on a commercial scale, complexity of the family and long time needed before being accepted for nuclear or aerospace applications. However, some potential applications are discussed below.

High temperature tolerant structural materials: MAX phases that develop Al_2O_3 scales can find application in high temperature environments for extended period of time. Along with heating elements and gas nozzles, Ti_2AlC, Ti_3AlC_2, and Cr_2AlC are promising candidates to replace Ni/Co superalloys in the hottest sections of gas turbine engines, enabling higher operating temperatures and improved efficiency. Moreover, Ni/Co superalloys are doped with strategic elements that might be sparse in supply or toxic to environment but elements such as Ti,Al and C are abundant, non toxic and cheap. MAX phase coatings are also being explored as protective layers for refractory alloys and as bond coats.

Nuclear purpose: Phases that are characterized by radiation tolerance and oxidation and corrosion resistance and chemical stability can be considered as potential accident tolerant fuel (ATF) claddings in third-generation light-water reactors (LWRs) and future fourth-generation fission plants.

Concentrated solar power: Concentrated Solar Power (CSP) systems generate electricity from solar energy without producing greenhouse gas emissions and provide the potential for thermal energy storage. CSP systems use mirrors to focus solar radiation onto a receiver, where the heat is transferred by a heat transfer fluid (HTF) to a steam turbine, generating electricity. MAX phases can be implemented in the solar reciever or the storage tank. The former requires oxidation resistance, low thermal emission in the IR region and good absorptance in UV-vis-NIR region. MAX phases seem to fit this bill. Moreover, they can

also serve as the storage tank providing compatibility with moten salts.

Catalysis: MAX phases can function both as catalysts and as catalyst supports. Cr_2AlC powders have been tested as solid catalysts to reduce carbon monoxide formation in catalytic wet peroxide oxidation (CWPO) processes. Additionally, Ti_3SiC_2, Ti_2AlC, and Ti_3AlC_2 exhibit outstanding chemoselectivity, achieving 100% selectivity for the hydrogenation of organic compounds even with low palladium content.

Joining: Joining is a crucial technology for producing large, complex assemblies by carefully integrating smaller, simpler parts. This process is especially challenging for ceramic components. Strong joining can be achieved by solid state difuusion of Ti_3SiC_2/Ti_3SiC_2, Ti_3AlC_2/Ti_3AlC_2, and Ti_3SiC_2/Ti_3AlC_2.

Electrical contacts: Ti_3SiC_2 has been suggested as an ohmic contact for 4H-SiC because of its linear current-voltage characteristics. Additionally, Ti_3SiC_2 can be easily fabricated in a single step by sputter-depositing titanium onto SiC substrates. This method offers the potential to directly synthesize oxygen-barrier capping layers after depositing the main contact, eliminating exposure to air and preventing oxidation, contamination, or the need for a cleaning step, thereby enhancing the device's long-term stability. Additionally, Ti_2AlN has been considered as an ohmic contact for GaN-based devices due to its ohmic behavior.

1.2 Overview of present thesis

This thesis explores different systems with varied properties and applications to address pertinent open questions assisted by modern tools of machine learning. The contents of different chapters discussed in this thesis can be summarized as follows:

Chapter 2 : This chapter introduces the theoretical and computational methods used in the thesis. It covers the machine learning methodology, particularly the different algorithms of supervised and unsupervised learning used in our work. It also discusses the ab-initio technique used via Density Functional Theory (DFT), and ab-initio molecular dynamics. Additionally, the concepts of classical molecular dynamics and machine-learned interatomic potentials are introduced.

Chapter 3 : In this chapter, we explore the semiconductor heterostructures using a data-driven approach. They have immense technological relevance in fabricating solar cells, LEDs, photovoltaic cells etc. At the interface of such heterostructures, the bulk bandstructures merge into one another leading to an electronic transition region characterized by band-edge discontinuities. They can be classified as type I or type II, depending on the signs of these discontinuities in valence and conduction bands. The prediction and design-

ing of semiconductor heterostructures of a specific type is a difficult materials science problem given the numerous combinations possible between different semiconductors. In our work, we suggest that the type of heterostructure can be accurately predicted based on the band structures of the constituent semiconductors. Building on this, we establish a machine learning model for this purpose, using features that describe the constituent semiconductors, and trained on a known dataset of binary semiconductor heterostructures. Using this, we theoretically predict the types of 872 previously unknown semiconductor heterostructures formed from combinations of elemental and binary semiconductors. Interestingly, the developed scheme also proves to be extendable to heterojunctions involving semiconductor quantum dots.

Chapter 4: In this chapter, we concentrate on bimetallic nanoclusters, which often feature a core–shell structure characterized by the enrichment of one metal in the shell over the other. They are highly significant due to their enhanced catalytic, biomedical, magnetic, and optical properties. Finding out factors that drive such core-shell segregation between atoms of different types are pertinent in this context. In our work,we study binary-alloyed metallic nanoparticles composed of a wide range of alkali, alkaline earth, basic, 3d, 4d, and 5d transition metals, as well as p-block elements, to determine core–shell preferences by calculating the segregation energies of single-atom alloy clusters using density functional theory (DFT). Applying machine learning to this extensive database,constructed from features characterizing the constituent metals, reveals the primary factors governing core-to-shell preference. Interestingly, we find the dominant factor varies with metal type. The analysis further reveals the conditions under whuch nanoparticles tend to favor mixed or Janus structures over the core-shell configuration.

Chapter 5: This chapter builds on the work presented in the previous chapter. In the previous work, segregation energies were calculated using single-atom alloys modeled as 55-atom icosahedral clusters. However, the influence of component concentration and cluster size on ordering was not investigated. In this chapter, we explore how these factors impact cluster stability by examining (a) two compositional extremes—one element in excess and vice versa (b) two cluster sizes: 55 and 147 atoms. We also identify key microscopic properties that change in tandem with variations in the relative stability of the three structural motifs across the composition limits. While a machine learning approach would ideally require a large dataset from high-throughput calculations across diverse structures and compositions, such a task is computationally intensive. Therefore, we focus instead on detailed first-principles calculations for Pd-based binary nanoalloys. These are particularly relevant as potential alternatives to Pt-based electrocatalysts, which are both scarce and costly. We then elaborate on the catalysis effect of such nanoclusters.

Chapter 6: This chapter deals with the analysis of gold-atomic chain formation in mechanically controlled break junction (MCBJ) experiments. Atomic chains formed at cryogenic temperature in break-junction experiments offer a unique testing ground for different phenomenon of mesoscopic physics. One of the key challenges in such experiments is the formation of stable monoatomic chains of sufficient length. To address this, we develop a hybrid machine learning framework that integrates both unsupervised and supervised learning models, trained on experimentally measured conductance traces, to gain microscopic insight into the process. Using two independent datasets of conductance–displacement traces of single-atomic junctions, we first determine the optimal conditions of bias voltage and stretching rate required to form atomic chains longer than 4 Å. We then apply a deep learning model to classify individual breaking traces, successfully identifying key trace features associated with long-chain formation. Ab-initio molecular dynamics simulations are then conducted, offering a detailed molecular-level understanding of the mechanisms behind chain formation.

Chapter 7: In this chapter we explore MAX phase compounds, which are layered ternary carbides or nitrides, exhibit non-linear elastic behavior despite being elastically stiff. Although insights have been given for the micromechanism behind such phenomenon from the experimental point-of-view, theroetical probing remains a challenge due to the associated length and time scales of the phenomena. In the present work, we adopt a data driven approach to develop a machine learned interatomic potential for the MAX compound Ti_2AlC following the moment tensor potential protocol and validated against several physical properties. Finally, the potential is applied in classical molecular dynamics, providing a faithful representation of the experimentally observed nonlinear elasticity. We also find the effects of common defects like Al vacancies in its stress-strain behavior.

Chapter 8: In this chapter, the key findings of our studies are summarized, and potential directions of expanding on them are discussed.

Bibliography

[1] Thomas Philbeck and Nicholas Davis. The fourth industrial revolution: Shaping a new era. Journal of International Affairs, 72(1):17–22, 2018.

[2] Rajan Jose and Seeram Ramakrishna. Materials 4.0: Materials big data enabled materials discovery. Applied Materials Today, 10:127–132, 2018.

[3] Ankit Agrawal and Alok Choudhary. Perspective: Materials informatics and big data: Realization of the "fourth paradigm" of science in materials science. Apl Materials, 4(5), 2016.

[4] David L McDowell and Surya R Kalidindi. The materials innovation ecosystem: a key enabler for the materials genome initiative. Mrs Bulletin, 41(4):326–337, 2016.

[5] Seeram Ramakrishna, Tong-Yi Zhang, Wen-Cong Lu, Quan Qian, Jonathan Sze Choong Low, Jeremy Heiarii Ronald Yune, Daren Zong Loong Tan, Stéphane Bressan, Stefano Sanvito, and Surya R Kalidindi. Materials informatics. Journal of Intelligent Manufacturing, 30:2307–2326, 2019.

[6] Scott Kirklin, James E Saal, Bryce Meredig, Alex Thompson, Jeff W Doak, Muratahan Aykol, Stephan Rühl, and Chris Wolverton. The open quantum materials database (oqmd): assessing the accuracy of dft formation energies. npj Computational Materials, 1(1):1–15, 2015.

[7] Anubhav Jain, Shyue Ping Ong, Geoffroy Hautier, Wei Chen, William Davidson Richards, Stephen Dacek, Shreyas Cholia, Dan Gunter, David Skinner, Gerbrand Ceder, et al. Commentary: The materials project: A materials genome approach to accelerating materials innovation. APL materials, 1(1), 2013.

[8] Stefano Curtarolo, Wahyu Setyawan, Shidong Wang, Junkai Xue, Kesong Yang, Richard H Taylor, Lance J Nelson, Gus LW Hart, Stefano Sanvito, Marco Buongiorno-Nardelli, et al. Aflowlib. org: A distributed materials properties repository from high-throughput ab initio calculations. Computational Materials Science, 58:227–235, 2012.

[9] Dejan Zagorac, H Müller, S Ruehl, J Zagorac, and Silke Rehme. Recent developments in the inorganic crystal structure database: theoretical crystal structure data and related features. Journal of applied crystallography, 52(5):918–925, 2019.

[10] A. L. Samuel. Some studies in machine learning using the game of checkers. IBM Journal of Research and Development, 44(1.2):206–226, 2000.

[11] Sudha Sharma, Mayank Bhatt, and Pratyush Sharma. Face recognition system using machine learning algorithm. In 2020 5th International Conference on Communication and Electronics Systems (ICCES), pages 1162–1168. IEEE, 2020.

[12] JKPS Yadav, Zainual Abdin Jaffery, and Laxman Singh. A short review on machine learning techniques used for fingerprint recognition. J Crit Rev, 7, 2020.

[13] Pedro Larranaga, Borja Calvo, Roberto Santana, Concha Bielza, Josu Galdiano, Inaki Inza, José A Lozano, Rubén Armananzas, Guzmán Santafé, Aritz Pérez, et al. Machine learning in bioinformatics. Briefings in bioinformatics, 7(1):86–112, 2006.

[14] Manish Kumar, Deepak Kumar Gupta, and Samayveer Singh. Extreme event forecasting using machine learning models. In Advances in Communication and Computational Technology: Select Proceedings of ICACCT 2019, pages 1503–1514. Springer, 2021.

[15] Iead Rezek, David S Leslie, Steven Reece, Stephen J Roberts, Alex Rogers, Rajdeep K Dash, and Nicholas R Jennings. On similarities between inference in game theory and machine learning. Journal of Artificial Intelligence Research, 33:259–283, 2008.

[16] Hai Nguyen, Shinichi Maeda, and Kenta Oono. Semi-supervised learning of hierarchical representations of molecules using neural message passing. arXiv preprint arXiv:1711.10168, 2017.

[17] John Maddox. Crystals from first principles. Nature, 335(6187):201–201, 1988.

[18] Artem R Oganov. Modern methods of crystal structure prediction. John Wiley & Sons, 2011.

[19] Stefan Goedecker. Minima hopping: An efficient search method for the global minimum of the potential energy surface of complex molecular systems. The Journal of chemical physics, 120(21):9911–9917, 2004.

[20] Bouke P Van Eijck and Jan Kroon. Structure predictions allowing more than one molecule in the asymmetric unit. Acta Crystallographica Section B: Structural Science, 56(3):535–542, 2000.

[21] Chris J Pickard and RJ Needs. Ab initio random structure searching. Journal of Physics: Condensed Matter, 23(5):053201, 2011.

[22] Dieter Gottwald, Gerhard Kahl, and Christos N Likos. Predicting equilibrium structures in freezing processes. The Journal of chemical physics, 122(20), 2005.

[23] TS Bush, C Rchard A Catlow, and PD Battle. Evolutionary programming techniques for predicting inorganic crystal structures. Journal of Materials Chemistry, 5(8):1269–1272, 1995.

[24] Roman Martoňák, Alessandro Laio, and Michele Parrinello. Predicting crystal structures: the Parrinello-Rahman method revisited. Physical review letters, 90(7):075503, 2003.

[25] Yue Liu, Tianlu Zhao, Wangwei Ju, and Siqi Shi. Materials discovery and design using machine learning. Journal of Materiomics, 3(3):159–177, 2017.

[26] Logan Ward, Ruoqian Liu, Amar Krishna, Vinay I Hegde, Ankit Agrawal, Alok Choudhary, and Chris Wolverton. Including crystal structure attributes in machine learning models of formation energies via voronoi tessellations. Physical Review B, 96(2):024104, 2017.

[27] Kyoungdoc Kim, Logan Ward, Jiangang He, Amar Krishna, Ankit Agrawal, and C Wolverton. Machine-learning-accelerated high-throughput materials screening: Discovery of novel quaternary heusler compounds. Physical Review Materials, 2(12):123801, 2018.

[28] Felix A Faber, Alexander Lindmaa, O Anatole Von Lilienfeld, and Rickard Armiento. Machine learning energies of 2 million elpasolite (ABC_2D_6) crystals. Physical review letters, 117(13):135502, 2016.

[29] Tohru Morita. Cluster variation method of cooperative phenomena and its generalization ii. quantum statistics. Journal of the Physical Society of Japan, 12(10):1060–1063, 1957.

[30] Anton O Oliynyk, Lawrence A Adutwum, James J Harynuk, and Arthur Mar. Classifying crystal structures of binary compounds AB through cluster resolution feature selection and support vector machine analysis. Chemistry of Materials, 28(18):6672–6681, 2016.

[31] Anton O Oliynyk, Lawrence A Adutwum, Brent W Rudyk, Harshil Pisavadia, Sogol Lotfi, Viktor Hlukhyy, James J Harynuk, Arthur Mar, and Jakoah Brgoch. Disentangling structural confusion through machine learning: structure prediction and polymorphism of equiatomic ternary phases ABC. Journal of the American Chemical Society, 139(49):17870–17881, 2017.

[32] Prasanna V Balachandran, Benjamin Kowalski, Alp Sehirlioglu, and Turab Lookman. Experimental search for high-temperature ferroelectric perovskites guided by two-step machine learning. Nature communications, 9(1):1668, 2018.

[33] Woon Bae Park, Jiyong Chung, Jaeyoung Jung, Keemin Sohn, Satendra Pal Singh, Myoungho Pyo, Namsoo Shin, and K-S Sohn. Classification of crystal structure using a convolutional neural network. IUCrJ, 4(4):486–494, 2017.

[34] Angelo Ziletti, Devinder Kumar, Matthias Scheffler, and Luca M Ghiringhelli. Insightful classification of crystal structures using deep learning. Nature communications, 9(1):2775, 2018.

[35] Asma Nouira, Nataliya Sokolovska, and Jean-Claude Crivello. Crystalgan: learning to discover crystallographic structures with generative adversarial networks. arXiv preprint arXiv:1810.11203, 2018.

[36] Ya Zhuo, Aria Mansouri Tehrani, and Jakoah Brgoch. Predicting the band gaps of inorganic solids by machine learning. The journal of physical chemistry letters, 9(7):1668–1673, 2018.

[37] L Weston and C Stampfl. Machine learning the band gap properties of kesterite I 2-II-IV-V 4 quaternary compounds for photovoltaics applications. Physical Review Materials, 2(8):085407, 2018.

[38] Arunkumar Chitteth Rajan, Avanish Mishra, Swanti Satsangi, Rishabh Vaish, Hiroshi Mizuseki, Kwang-Ryeol Lee, and Abhishek K Singh. Machine-learning-assisted accurate band gap predictions of functionalized MXene. Chemistry of Materials, 30(12):4031–4038, 2018.

[39] Jing Wang and Shou-Cheng Zhang. Topological states of condensed matter. Nature materials, 16(11):1062–1067, 2017.

[40] Joel E Moore. The birth of topological insulators. Nature, 464(7286):194–198, 2010.

[41] Pengfei Zhang, Huitao Shen, and Hui Zhai. Machine learning topological invariants with neural networks. Physical review letters, 120(6):066401, 2018.

[42] Matthew JS Beach, Anna Golubeva, and Roger G Melko. Machine learning vortices at the Kosterlitz-Thouless transition. Physical Review B, 97(4):045207, 2018.

[43] Ning Sun, Jinmin Yi, Pengfei Zhang, Huitao Shen, and Hui Zhai. Deep learning topological invariants of band insulators. Physical Review B, 98(8):085402, 2018.

[44] Yi Zhang and Eun-Ah Kim. Quantum loop topography for machine learning. Physical review letters, 118(21):216401, 2017.

[45] Olexandr Isayev, Denis Fourches, Eugene N Muratov, Corey Oses, Kevin Rasch, Alexander Tropsha, and Stefano Curtarolo. Materials cartography: representing and

mining materials space using structural and electronic fingerprints. Chemistry of Materials, 27(3):735–743, 2015.

[46] Valentin Stanev, Corey Oses, A Gilad Kusne, Efrain Rodriguez, Johnpierre Paglione, Stefano Curtarolo, and Ichiro Takeuchi. Machine learning modeling of superconducting critical temperature. npj Computational Materials, 4(1):29, 2018.

[47] Maxim Ziatdinov, Artem Maksov, Li Li, Athena S Sefat, Petro Maksymovych, and Sergei V Kalinin. Deep data mining in a real space: separation of intertwined electronic responses in a lightly doped $BaFe_2As_2$. Nanotechnology, 27(47):475706, 2016.

[48] Maxim Ziatdinov, Artem Maksov, and Sergei V Kalinin. Learning surface molecular structures via machine vision. npj Computational Materials, 3(1):31, 2017.

[49] V. Bongiorno, S. Gibbon, E. Michailidou, and M. Curioni. Exploring the use of machine learning for interpreting electrochemical impedance spectroscopy data: evaluation of the training dataset size. Corrosion Science, 198:110119, 2022.

[50] Vasile-Adrian Surdu and Romuald Győrgy. X-ray diffraction data analysis by machine learning methods—a review. Applied Sciences, 13(17):9992, 2023.

[51] Mathieu Doucet, Anjana M Samarakoon, Changwoo Do, William T Heller, Richard Archibald, D Alan Tennant, Thomas Proffen, and Garrett E Granroth. Machine learning for neutron scattering at ornl. Machine Learning: Science and Technology, 2(2):023001, 2020.

[52] Linglong Li, Yaodong Yang, Dawei Zhang, Zuo-Guang Ye, Stephen Jesse, Sergei V Kalinin, and Rama K Vasudevan. Machine learning–enabled identification of material phase transitions based on experimental data: Exploring collective dynamics in ferroelectric relaxors. Science advances, 4(3):8672, 2018.

[53] Paul Raccuglia, Katherine C Elbert, Philip DF Adler, Casey Falk, Malia B Wenny, Aurelio Mollo, Matthias Zeller, Sorelle A Friedler, Joshua Schrier, and Alexander J Norquist. Machine-learning-assisted materials discovery using failed experiments. Nature, 533(7601):73–76, 2016.

[54] Thomas B Blank, Steven D Brown, August W Calhoun, and Douglas J Doren. Neural network models of potential energy surfaces. The Journal of chemical physics, 103(10):4129–4137, 1995.

[55] Jörg Behler and Michele Parrinello. Generalized neural-network representation of

high-dimensional potential-energy surfaces. Physical review letters, 98(14):146401, 2007.

[56] Aidan P Thompson, Laura P Swiler, Christian R Trott, Stephen M Foiles, and Garritt J Tucker. Spectral neighbor analysis method for automated generation of quantum-accurate interatomic potentials. Journal of Computational Physics, 285:316–330, 2015.

[57] Ivan S Novikov, Konstantin Gubaev, Evgeny V Podryabinkin, and Alexander V Shapeev. The mlip package: moment tensor potentials with mpi and active learning. Machine Learning: Science and Technology, 2(2):025002, 2020.

[58] Lukáš Kỳvala and Christoph Dellago. Optimizing the architecture of behler–parrinello neural network potentials. The Journal of Chemical Physics, 159(9), 2023.

[59] Albert P Bartók, Mike C Payne, Risi Kondor, and Gábor Csányi. Gaussian approximation potentials: The accuracy of quantum mechanics, without the electrons. Physical review letters, 104(13):136403, 2010.

[60] Christopher KI Williams and Carl Edward Rasmussen. Gaussian processes for machine learning, volume 2. MIT press Cambridge, MA, 2006.

[61] Daniele Dragoni, Thomas D Daff, Gábor Csányi, and Nicola Marzari. Achieving dft accuracy with a machine-learning interatomic potential: Thermomechanics and defects in bcc ferromagnetic iron. Physical Review Materials, 2(1):013808, 2018.

[62] Volker L Deringer, Chris J Pickard, and Gábor Csányi. Data-driven learning of total and local energies in elemental boron. Physical review letters, 120(15):156001, 2018.

[63] Patrick Rowe, Gábor Csányi, Dario Alfè, and Angelos Michaelides. Development of a machine learning potential for graphene. Physical Review B, 97(5):054303, 2018.

[64] Atsuto Seko, Akira Takahashi, and Isao Tanaka. Sparse representation for a potential energy surface. Physical Review B, 90(2):024101, 2014.

[65] Hui Zou and Trevor Hastie. Regularization and variable selection via the elastic net. Journal of the Royal Statistical Society Series B: Statistical Methodology, 67(2):301–320, 2005.

[66] John Robertson. High dielectric constant gate oxides for metal oxide Si transistors. Reports on progress in Physics, 69(2):327, 2005.

[67] Chandler Downs and Thomas E Vandervelde. Progress in infrared photodetectors since 2000. Sensors, 13(4):5054–5098, 2013.

[68] Biswaranjan R Nag. Physics of quantum well devices, volume 7. Springer Science & Business Media, 2001.

[69] Simon M Sze, Yiming Li, and Kwok K Ng. Physics of semiconductor devices. John wiley & sons, 2021.

[70] DW Niles and G Margaritondo. Heterojunctions: Definite breakdown of the electron affinity rule. Physical Review B, 34(4):2923, 1986.

[71] Richard L Anderson. Experiments on ge-gaas heterojunctions. Solid-State Electronics, 5(5):341–351, 1962.

[72] JO McCaldin, TC McGill, and CA Mead. Correlation for III-V and II-VI semiconductors of the Au Schottky barrier energy with anion electronegativity. Physical review letters, 36(1):56, 1976.

[73] Su-Huai Wei and Alex Zunger. Role of d orbitals in valence-band offsets of common-anion semiconductors. Physical review letters, 59(1):144, 1987.

[74] Winfried Mönch. On the present understanding of schottky contacts. Festkörperprobleme 26: Plenary Lectures of the Divisions "Semiconductor Physics""Dynamics and Statistical Mechanics""Low Temperature Physics""Magnetism""Metal Physics""Thin Films""Surface Physics""Vacuum Technology" of the German Physical Society (DPG) Freudenstadt, April 7-11, 1986, pages 67–88, 1986.

[75] Alfonso Franciosi and Chris G Van de Walle. Heterojunction band offset engineering. Surface Science Reports, 25(1-4):1–140, 1996.

[76] John Robertson. Band offsets, schottky barrier heights, and their effects on electronic devices. Journal of Vacuum Science & Technology A, 31(5), 2013.

[77] Chris G Van de Walle and Richard M Martin. Theoretical study of band offsets at semiconductor interfaces. Physical Review B, 35(15):8154, 1987.

[78] Manuel Cardona and Niels E Christensen. Acoustic deformation potentials and heterostructure band offsets in semiconductors. Physical Review B, 35(12):6182, 1987.

[79] Jerry Tersoff. Theory of semiconductor heterojunctions: The role of quantum dipoles. Physical Review B, 30(8):4874, 1984.

[80] F Flores and C Tejedor. Energy barriers and interface states at heterojunctions. Journal of Physics C: Solid State Physics, 12(4):731, 1979.

[81] WRL Lambrecht, B Segall, and OK Andersen. Self-consistent dipole theory of heterojunction band offsets. Physical Review B, 41(5):2813, 1990.

[82] Asha Kumari and Ragini Raj Singh. Encapsulation of highly confined cdse quantum dots for defect free luminescence and improved stability. Physica E: Low-dimensional Systems and Nanostructures, 89:77–85, 2017.

[83] Hong-Ying Zang, Ya-Qian Lan, Zhong-Min Su, Guang-Sheng Yang, Guang-Juan Xu, Dong-Ying Du, Lei Chen, and Li-Kai Yan. Construction of a series of 0d, 2d and 3d inorganic–organic hybrid coordination polymers based on octamolybdate and 2-(2-pyridyl) imidazole and its derivative. Inorganica Chimica Acta, 363(1):118–126, 2010.

[84] C.N.R Rao, F.L Deepak, Gautam Gundiah, and A Govindaraj. Inorganic nanowires. Progress in Solid State Chemistry, 31(1):5–147, 2003.

[85] SV Prabhakar Vattikuti, Chan Byon, Ch Venkata Reddy, B Venkatesh, and Jaesool Shim. Synthesis and structural characterization of MoS2 nanospheres and nanosheets using solvothermal method. Journal of Materials Science, 50:5024–5038, 2015.

[86] SV Prabhakar Vattikuti, Chan Byon, Ch Venkata Reddy, Jaesool Shim, and B Venkatesh. Co-precipitation synthesis and characterization of faceted MoS_2 nanorods with controllable morphologies. Applied Physics A, 119:813–823, 2015.

[87] SV Prabhakar Vattikuti, Chan Byon, and Ch Venkata Reddy. Synthesis of MoS_2 multi-wall nanotubes using wet chemical method with H_2O_2 as growth promoter. Superlattices and Microstructures, 85:124–132, 2015.

[88] Peter H Tomlins and Ruikang K Wang. Theory, developments and applications of optical coherence tomography. Journal of Physics D: Applied Physics, 38(15):2519, 2005.

[89] Uwe Kreibig and Michael Vollmer. Optical properties of metal clusters, volume 25. Springer Science & Business Media, 2013.

[90] Pannaree Srinoi, Yi-Ting Chen, Varadee Vittur, Maria D Marquez, and T Randall Lee. Bimetallic nanoparticles: enhanced magnetic and optical properties for emerging biological applications. Applied Sciences, 8(7):1106, 2018.

[91] Alvise Benedetti, L Bertoldo, Patrizia Canton, G Goerigk, Francesco Pinna, Pietro

Riello, and Stefano Polizzi. ASAXS study of Au, Pd and Pd–Au catalysts supported on active carbon. Catalysis today, 49(4):485–489, 1999.

[92] Manoj B Gawande, Anandarup Goswami, Tewodros Asefa, Huizhang Guo, Ankush V Biradar, Dong-Liang Peng, Radek Zboril, and Rajender S Varma. Core–shell nanoparticles: synthesis and applications in catalysis and electrocatalysis. Chemical Society Reviews, 44(21):7540–7590, 2015.

[93] Dongshi Zhang, Bilal Gokce, and Stephan Barcikowski. Laser synthesis and processing of colloids: fundamentals and applications. Chemical reviews, 117(5):3990–4103, 2017.

[94] David Medina-Cruz, Bahram Saleh, Ada Vernet-Crua, Alfonso Nieto-Argüello, Diana Lomelí-Marroquín, Lydia Yerid Vélez-Escamilla, Jorge L Cholula-Díaz, José Miguel García-Martín, and Thomas Webster. Bimetallic nanoparticles for biomedical applications: A review. Racing for the Surface: Antimicrobial and Interface Tissue Engineering, pages 397–434, 2020.

[95] Pablo Jensen. Growth of nanostructures by cluster deposition: Experiments and simple models. Reviews of Modern physics, 71(5):1695, 1999.

[96] Shozo Ino. Stability of multiply-twinned particles. Journal of the Physical Society of Japan, 27(4):941–953, 1969.

[97] Laurence D Marks. Experimental studies of small particle structures. Reports on progress in physics, 57(6):603, 1994.

[98] Alan L Mackay. A dense non-crystallographic packing of equal spheres. Acta Crystallographica, 15(9):916–918, 1962.

[99] IL Garzón, K Michaelian, MR Beltrán, A Posada-Amarillas, P Ordejón, E Artacho, D Sánchez-Portal, and JM Soler. Lowest energy structures of gold nanoclusters. Physical review letters, 81(8):1600, 1998.

[100] Edoardo Apra, Francesca Baletto, Riccardo Ferrando, and Alessandro Fortunelli. Amorphization mechanism of icosahedral metal nanoclusters. Physical review letters, 93(6):065502, 2004.

[101] AS Barnard, George Opletal, IK Snook, and SP Russo. Ideality versus reality: Emergence of the chui icosahedron. The Journal of Physical Chemistry C, 112(38):14848–14852, 2008.

[102] Kari Laasonen, Emanuele Panizon, Davide Bochicchio, and Riccardo Ferrando. Competition between icosahedral motifs in AgCu, AgNi, and AgCo nanoal-

loys: a combined atomistic–DFT study. The Journal of Physical Chemistry C, 117(49):26405–26413, 2013.

[103] IA Harris, RS Kidwell, and JA Northby. Structure of charged argon clusters formed in a free jet expansion. Physical review letters, 53(25):2390, 1984.

[104] Giulia Rossi, Arnaldo Rapallo, Christine Mottet, A Fortunelli, F Baletto, and Riccardo Ferrando. Magic polyicosahedral core-shell clusters. Physical review letters, 93(10):105503, 2004.

[105] Lauro Oliver Paz-Borbon, Thomas V Mortimer-Jones, Roy L Johnston, Alvaro Posada-Amarillas, Giovanni Barcaro, and Alessandro Fortunelli. Structures and energetics of 98 atom Pd-Pt nanoalloys: potential stability of the leary tetrahedron for bimetallic nanoparticles. Physical Chemistry Chemical Physics, 9(38):5202–5208, 2007.

[106] Dora J Borbón-González, Alessandro Fortunelli, Giovanni Barcaro, Luca Sementa, Roy L Johnston, and Alvaro Posada-Amarillas. Global minimum $Pt_{13}M_{20}$ (M= Ag, Au, Cu, Pd) dodecahedral core–shell clusters. The Journal of Physical Chemistry A, 117(51):14261–14266, 2013.

[107] Riccardo Ferrando. Structure and properties of nanoalloys. Elsevier, 2016.

[108] Riccardo Ferrando. Symmetry breaking and morphological instabilities in core-shell metallic nanoparticles. Journal of Physics: Condensed Matter, 27(1):013003, 2014.

[109] Giovanni Barcaro, Alessandro Fortunelli, Micha Polak, and Leonid Rubinovich. Patchy multishell segregation in Pd- Pt alloy nanoparticles. Nano letters, 11(4):1766–1769, 2011.

[110] F Baletto, C Mottet, and R Ferrando. Growth of three-shell onionlike bimetallic nanoparticles. Physical review letters, 90(13):135504, 2003.

[111] F Calvo, E Cottancin, and M Broyer. Segregation, core alloying, and shape transitions in bimetallic nanoclusters: Monte carlo simulations. Physical Review B—Condensed Matter and Materials Physics, 77(12):121406, 2008.

[112] Cyril T Langlois, Tetsuo Oikawa, Pascale Bayle-Guillemaud, and Christian Ricolleau. Energy-filtered electron microscopy for imaging core–shell nanostructures. Journal of Nanoparticle Research, 10:997–1007, 2008.

[113] I Parsina and F Baletto. Tailoring the structural motif of AgCo nanoalloys: core/shell versus janus-like. The Journal of Physical Chemistry C, 114(3):1504–1511, 2010.

[114] Riccardo Ferrando, Julius Jellinek, and Roy L Johnston. Nanoalloys: from theory to applications of alloy clusters and nanoparticles. Chemical reviews, 108(3):845–910, 2008.

[115] Davide Bochicchio and Riccardo Ferrando. Morphological instability of core-shell metallic nanoparticles. Physical Review B—Condensed Matter and Materials Physics, 87(16):165435, 2013.

[116] Karrina McNamara and Syed AM Tofail. Nanosystems: the use of nanoalloys, metallic, bimetallic, and magnetic nanoparticles in biomedical applications. Physical chemistry chemical physics, 17(42):27981–27995, 2015.

[117] Alberto Sandoval, Antonio Aguilar, Catherine Louis, Agnès Traverse, and Rodolfo Zanella. Bimetallic Au-Ag/TiO_2 catalyst prepared by deposition–precipitation: High activity and stability in co oxidation. Journal of Catalysis, 281(1):40–49, 2011.

[118] Xiaoyan Liu, Aiqin Wang, Lin Li, Tao Zhang, Chung-Yuan Mou, and Jyh-Fu Lee. Structural changes of Au-Cu bimetallic catalysts in CO oxidation: In situ XRD, EPR, XANES, and FT-IR characterizations. Journal of catalysis, 278(2):288–296, 2011.

[119] Franz Fischer and Hans Tropsch. The preparation of synthetic oil mixtures (synthol) from carbon monoxide and hydrogen. Brennst. Chem, 4:276–285, 1923.

[120] Long Zhao, Ming Wen, Yakun Tian, Qingsheng Wu, and Yongqing Fu. A novel structure of quasi-monolayered nico-bimetal-phosphide for superior electrochemical performance. Journal of Energy Chemistry, 74:203–211, 2022.

[121] C J_ Muller, JM Van Ruitenbeek, and LJ De Jongh. Conductance and supercurrent discontinuities in atomic-scale metallic constrictions of variable width. Physical review letters, 69(1):140, 1992.

[122] N Agrait, JG Rodrigo, and S Vieira. Conductance steps and quantization in atomic-size contacts. Physical Review B, 47(18):12345, 1993.

[123] JK Gimzewski and R Möller. Transition from the tunneling regime to point contact studied using scanning tunneling microscopy. Physical Review B, 36(2):1284, 1987.

[124] U Dürig, O Züger, and DW Pohl. Observation of metallic adhesion using the scanning tunneling microscope. Physical review letters, 65(3):349, 1990.

[125] BJ Van Wees, H Van Houten, CWJ Beenakker, J Gr Williamson, LP Kouwenhoven, D Van der Marel, and CT Foxon. Quantized conductance of point contacts in a two-dimensional electron gas. Physical Review Letters, 60(9):848, 1988.

[126] Uzi Landman, WD Luedtke, Nancy A Burnham, and Richard J Colton. Atomistic mechanisms and dynamics of adhesion, nanoindentation, and fracture. Science, 248(4954):454–461, 1990.

[127] AP Sutton and JB Pethica. Inelastic flow processes in nanometre volumes of solids. Journal of Physics: Condensed Matter, 2(24):5317, 1990.

[128] CJ Muller, JM Van Ruitenbeek, and LJ De Jongh. Experimental observation of the transition from weak link to tunnel junction. Physica C: Superconductivity, 191(3-4):485–504, 1992.

[129] C J_ Muller, JM Van Ruitenbeek, and LJ De Jongh. Conductance and supercurrent discontinuities in atomic-scale metallic constrictions of variable width. Physical review letters, 69(1):140, 1992.

[130] Mads Brandbyge, J Schio, MR So, Per Stoltze, Karsten Wedel Jacobsen, JK No, L Olesen, Erik Lægsgaard, Ivan Stensgaard, Flemming Besenbacher, et al. Quantized conductance in atom-sized wires between two metals. Physical Review B, 52(11):8499, 1995.

[131] C Sirvent, JG Rodrigo, N Agrait, and S Vieira. Stm study of the atomic contact between metallic electrodes. Physica B: Condensed Matter, 218(1-4):238–241, 1996.

[132] CJ Muller, JM Krans, TN Todorov, and MA Reed. Quantization effects in the conductance of metallic contacts at room temperature. Physical Review B, 53(3):1022, 1996.

[133] Markus Dreher, Fabian Pauly, Jan Heurich, Juan Carlos Cuevas, Elke Scheer, and Peter Nielaba. Structure and conductance histogram of atomic-sized au contacts. Physical Review B—Condensed Matter and Materials Physics, 72(7):075435, 2005.

[134] Elke Scheer, Nicolás Agraït, Juan Carlos Cuevas, Alfredo Levy Yeyati, Bas Ludoph, Alvaro Martín-Rodero, Gabino Rubio Bollinger, Jan M Van Ruitenbeek, and Cristián Urbina. The signature of chemical valence in the electrical conduction through a single-atom contact. Nature, 394(6689):154–157, 1998.

[135] Mads Brandbyge and R Mads. Sorensen, and Karstn W. Jacobsen. Phys. Rev. B, 56(14):956, 1997.

[136] V Rodrigues and D Ugarte. Real-time imaging of atomistic process in one-atom-thick metal junctions. Physical Review B, 63(7):073405, 2001.

[137] SK Nielsen, Yves Noat, Mads Brandbyge, RHM Smit, K Hansen, LY Chen, AI Yanson, Flemming Besenbacher, and JM Van Ruitenbeek. Conductance of single-atom

platinum contacts: Voltage dependence of the conductance histogram. Physical Review B, 67(24):245411, 2003.

[138] RHM Smit, Carlos Untiedt, and JM Van Ruitenbeek. The high-bias stability of monatomic chains. Nanotechnology, 15(7):S472, 2004.

[139] Makusu Tsutsui, Kohei Shoji, Masateru Taniguchi, and Tomoji Kawai. Formation and self-breaking mechanism of stable atom-sized junctions. Nano Letters, 8(1):345–349, 2008.

[140] Von Hans Nowotny. Strukturchemie einiger verbindungen der übergangsmetalle mit den elementen C, Si, Ge, Sn. Progress in Solid State Chemistry, 5:27–70, 1971.

[141] Hans Nowotny, Peter Rogl, and Julius C Schuster. Structural chemistry of complex carbides and related compounds. Journal of Solid State Chemistry, 44(1):126–133, 1982.

[142] Michel W Barsoum and Tamer El-Raghy. Synthesis and characterization of a remarkable ceramic: Ti_3SiC_2. Journal of the American Ceramic Society, 79(7):1953–1956, 1996.

[143] M Jaouen and MW Barsoum. X-ray absorption spectroscopy, eels, and full-potential augmented plane wave study of the electronic structure of Ti_2AlC, Ti_2AlN, Nb_2AlC, and $(Ti_{0.5}Nb_{0.5})_2AlC$. PHYSICAL REVIEW B Phys Rev B, 71:024105, 2005.

[144] Michel W Barsoum and Miladin Radovic. Elastic and mechanical properties of the max phases. Annual review of materials research, 41(1):195–227, 2011.

2

Methodology

2.1 Introduction

This chapter outlines the methodologies used in this thesis. The specific approaches and techniques employed are as follows:

- **Machine Learning Technique**: Different machine learning schemes have been extensively implemented in the problems addressed in this thesis. In particular, two broad divisions of ML algorithms have been used, supervised and unsupervised learning.
- **Ab Initio Technique**: First-principles density functional theory(DFT) calculations are performed at T = 0 K and under Born-Oppenheimer approximation to analyze different properties of the materials studied. Also ab-initio molecular dynamics simulations are carried out at different finite temperatures.
- **Force field and Classical molecular dynamics technique**: Classical molecular dynamics simulations using ML-generated interatomic potential have been used.

The following sections provide an overview of the methods.

2.2 Machine learning

Within the last few decades, machine learning have pervaded almost every sector of human lives. For instance, ML is adapted in health and clinical care to assist in drug discovery, medical diagnosis, record-keeping etc. Similarly, in pharmaceuticals, ML can help in keeping the supply chain intact for life-saving drugs by analyzing demand and supply data. In farming, ML is employed to classify and assess the quality of harvested grains and enable

automatic adjustment systems for harvesters. ML has also found extensive usage in fraud detection across the fields of banking, insurance and retail. In the oil and gas sector, ML can provide data analytics and virtual sensors to detect leak and corrosion detection, geological feature characterization etc. Recently, ML is being used in the real estate industry for property evaluation based on economy,location and neighborhood statistics.

Machine learning is gradually making its way into materials science research and discovery. Unlike most of the above mentioned applications in different fields, the integration of ML to this field is often challenged by the lack of sufficient quantity of reliable data. Hence, the entire workflow needs to be designed to circumnavigate this issue.

A machine learning algorithm is known to detect or "learn" inferences from data. To define this 'learning', Mitchell[1] uses a concise definition: "A computer program is said to learn from experience E with respect to some class of tasks T and the performance measure P, if its performance in tasks in T, as measured by P, improves with experience E." An assortment of tasks T, experience E and performance measures P are at our disposal to handle a particular problem.

Machine learning tasks are typically defined by how the learning system should process an example, also called an **instance**. An example consists of a set of **features** that characterize it. An example is represented as a vector $\mathbf{x} \in \mathbb{R}^n$, where each entry x_i of the vector corresponds to a different feature. There are several types of tasks that can be solved using machine learning, for eg:

- **Classification:** In this kind of task, the computer program attempts to determine the category of given input from the set of categories **k**. To do that, a learning algorithm usually generates a function $f : \mathbb{R}^n \to \{1,\ldots,k\}$. When an input, represented as the vector x, is given, the model assigns it a category, or rather, an index of this category, such as the numeric code $y = f(x)$. There exist some variations of the classification task, such as those where f produces a probability distribution over the possible classes rather than a single categorical label.

- **Regression:** In regression tasks, the algorithm aims to predict a continuous numerical value for some supplied inputs. This is performed by defining a function $f : \mathbb{R}^n \to \mathbb{R}$. In a sense, this kind of task is akin to a classification task, only the output format is different.

- **Structured output:** Structured output tasks refer to any task where the output is a vector or a more complex data structure containing multiple values, with meaningful relationships between its elements. This task outputs values that are interlinked and are a compendious description of the input.

- **Synthesis and sampling:** In this type of task, the machine learning algorithm is tasked with creating new examples that resemble those found in the training data. This is a kind of structured output task, except that there is no one output that is uniquely correct for every input. In other words, high output variation is desired in order to give the appearance of more realism with respect to input samples. This is implemented in generating synthetic samples,

The learning system performs a quantitative measure of the performance (P) of a machine learning algorithm for a specific task (T).

For classification, a confusion matrix helps in evaluating the performance. Considering two classes, positive and negative, the confusion matrix can be written as : 5 Certain per-

Actual \ Predicted	**Positive (P)**	**Negative (N)**
Positive (P)	True Positive (TP)	False Negative (FN)
Negative (N)	False Positive (FP)	True Negative (TN)

Table 2.1: *Confusion Matrix for Binary Classification*

formance measures can be defined using the confusion matrix:

- **Accuracy** = $\frac{(TP+TN)}{(TP+TN+FP+FN)}$. It denotes how often the classifier is correct.
- **Precision**=$\frac{TP}{(TP+FP)}$. It denotes ratio of positive cases classified correctly to all predicted positive cases.
- **Recall**=$\frac{(TP)}{(TP+FN)}$. It denotes the ratio of correctly classified positive cases to all positive cases.
- **F1-score**= 2 * $\frac{(Precision*Recall)}{(Precision+Recall)}$. This denotes the harmonic mean of precision and recall - often a better indicator for a classifier's fidelity.

For regression tasks, some commonly used measures are :

- **Root mean squared error(RMSE)**=$\sqrt{\frac{1}{N}\sum_{i=1}^{N}(y_i-\hat{y}_i)^2}$
- **Mean absolute error(MAE)**= $\frac{1}{N}\sum_{i=1}^{n}|y_i-\hat{y}_i|$

  where $\hat{y}$ and y are predicted and actual values. N is the total number of instances.
- **Coefficient of determination, R^2** = 1 - $\frac{\sum_{i=1}^{n}(y_i-\hat{y}_i)^2}{\sum_{i=1}^{n}(y_i-\bar{y})^2}$

  where $\bar{y}$ is the mean of actual values.

However, the training and evaluation on the same data is methodologically wrong, since in that case the model 'memorizes' the labels of the training samples to produce perfect

scores but fail to make meaningful predictions on new, unseen data. This is called overfitting. Hence, it should be assessed against data not used during training to obtain an impartial evaluation of its capacity. The original data set is divided into a training set and a test set. With regard to the tuning of various settings, so-called hyperparameters of the algorithm, there is still a risk of overfitting to the test set. In striving for best performance on the test data, these hyperparameters can be selected in such a way that the model learns about the test set. Evaluation metrics may then no longer reflect the true ability of the model to generalize to new data. A still better approach is to split the data into three segments: a training set for training the model, a validation set to evaluate the model and tweak its parameters iteratively, and the test set to get the error metrics of the final model. However, dividing the available data into three sets significantly reduces the number of samples available for training the model. Additionally, the results may vary depending on the specific random selection of the training and validation sets. Alternatively, a procedure called cross-validation(CV) can be used, where a separate validation set is not necessary. In the standard approach known as k-fold CV, the training data is divided into k smaller subsets. For each of the folds, the process follows these steps:

- A model is trained using k-1 of the folds as training data.
- The trained model is then evaluated on the remaining fold, using an appropriate performance metric.

The final performance measure from k-fold cross-validation is obtained by averaging the results across all folds. This workflow has been schematically shown in Figure 2.1.

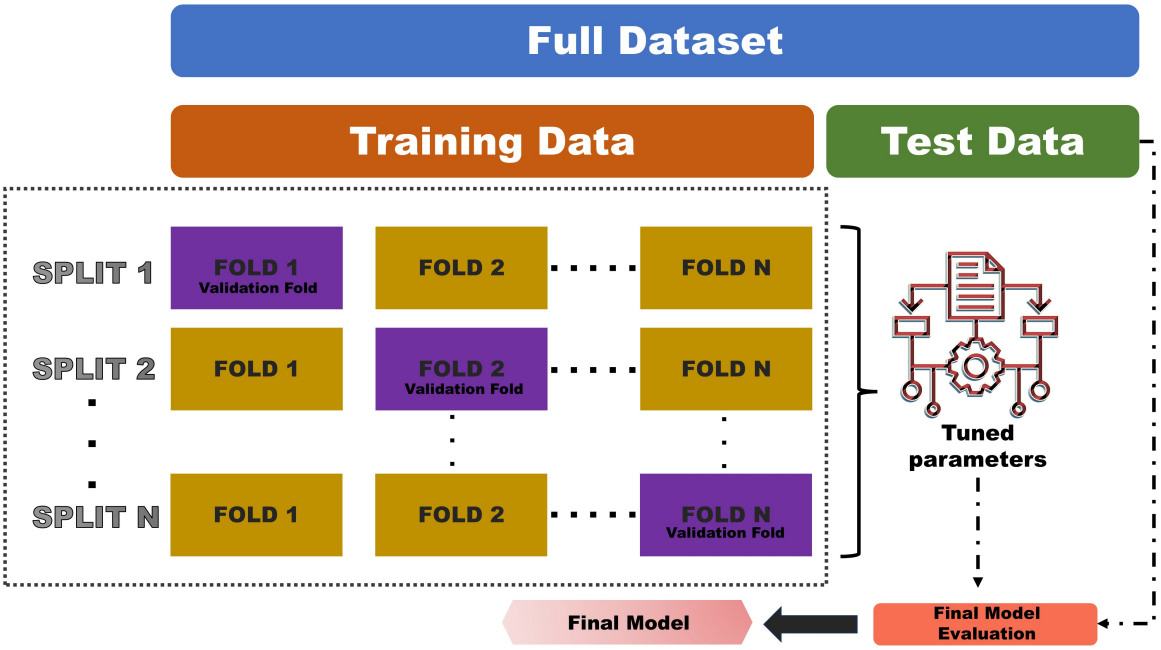

Figure 2.1: *The cross-validation workflow for estimating model performance.*

Machine learning algorithms can broadly be classified as either **unsupervised** or **supervised** or **reinforcement learning** depending on the experience they have during the learning process.

Supervised learning algorithms work with datasets that contain features, where each data point is paired with a corresponding label or target. There are two main types of supervised learning : *Regression* and *classification*. **Unsupervised learning** algorithms analyze datasets with multiple features to uncover meaningful patterns and structural properties within the data, but there is no label or target associated with each data point. Unsupervised learning algorithms serve purposes such as *clustering*, which groups similar data points into distinct clusters, or *association rule learning* which is used to identify interesting relationships or patterns between variables in large datasets, or *dimensionality reduction* where the number of features in a dataset are reduced while preserving crucial information contained in it. There is another variant called **semi-supervised learning** which is an overlap of the former two. It utilizes a limited amount of labeled data and a comparatively larger amount of unlabeled data. In **reinforcement learning** algorithms, a fixed dataset is not processed. Rather, they interact with an environment, establishing a feedback loop between the learning system and its experiences. An agent or learner is trained to accomplish a goal in an unknown complex environment by taking actions and receiving feedback in the form of rewards or penalties.

The different types of machine learning algorithms, their tasks and some examples of specific models are shown in Figure 2.2.

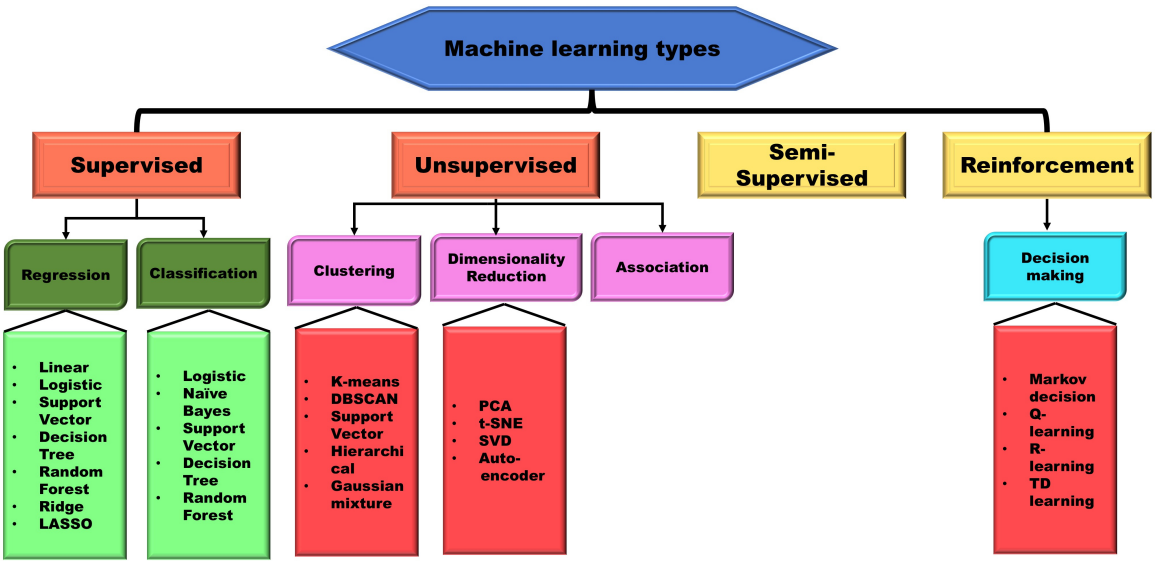

Figure 2.2: *Types of machine learning algorithm.*

In this thesis, the supervised and unsupervised learning schemes have been implemented.

2.2.1 Supervised Learning

Supervised learning schemes have been widely utilized in materials science research in various directions, some examples of which are given below.

Schmidt et al.[2] constructed a dataset of approximately 250,000 cubic perovskites, using all elements up to bismuth while excluding noble gases and lanthanides. After evaluating various machine learning techniques, they found that extremely randomized trees combined with adaptive boosting yielded the best performance, achieving a mean average error of 0.12 eV per atom.Li et al.[3] applied various regression and classification methods to a dataset of approximately 2,150 $A_{1-x}A'_xB_{1-y}B'_yO_3$ perovskites, which are potential cathode materials for high-temperature solid oxide fuel cells. Elemental properties were used as features, and extremely randomized trees emerged as the most effective classifier. Zheng et al.[4] utilized convolutional neural networks and transfer learning to predict the stability of full-Heusler compounds with the formula AB_2C. Oliynyk et al.[5] utilized random forests (RFs) and experimental data to develop a model for predicting the likelihood of forming full-Heusler compounds with a given composition. By using fundamental elemental properties as features, they successfully identified and experimentally confirmed the stability of several new full-Heusler phases. Balachandran et al.[6] analyzed a dataset of 60,000 potential xBiMe'$_y$Me"$_{1-y}$O$_3$–(1–x)PbTiO$_3$ perovskites using various machine learning techniques. Support vector machines (SVMs) were first employed to classify materials as perovskites or non-perovskites, followed by a prediction of the Curie temperature for those identified as perovskites. When a promising candidate was experimentally synthesized, it was added to the training set, and the process was repeated. Out of the ten synthesized compounds, six were confirmed as perovskites. Park et al.[7] used a deep convolutional network that took x-ray diffraction pattern as input and gave output as space group, extinction group, or crystal system. Nouira et al.[8] used a Generative Adversarial Network (GAN) based approach to use binary hydrides to generate novel stable ternary compounds. Zhuo et al.[9] aimed to overcome the challenges posed by different theoretical methods by directly predicting experimental band gaps. Their approach began with classifying materials as either metals or non-metals using support vector machine (SVM) classifiers, followed by band gap prediction using SVM regressors. Weston et al.[10] studied the band gaps of kesterite compounds and developed a logistic regression classifier to predict whether the band gaps were direct or indirect. De Jong et al.[11] used a supervised technique to predict the Voigt–Reuss–Hill averages of bulk and shear modulus based on elemental properties. Furmanchuk et al.[12] used Random Forest to predict bulk modulus, trained on a database ranging from unitary to combinations of 62 elements. Mansouri et al.[13] combined elemental and structural properties as descriptors and employed support vector regressors (SVRs) to screen a chemical

space of approximately 120,000 materials for superhard, incompressible materials. This effort led to the successful synthesis and characterization of two new candidates. Rupp et al.[14] aimed to rapidly predict accurate molecular atomization energies. The machine learning model employed kernel ridge regression (KRR) with Gaussian kernels. It was trained and tested on a dataset of over 7,000 organic molecules containing up to seven atoms. The atomization energies used for training and testing were calculated using density functional theory (DFT).

In this thesis, Random Forest algorithm, which is a conglomeration of several decision trees, and Least Absolute Shrinkage and Selection Operator regression(LASSO) have been used for the purpose of supervised learning.

2.2.1.1 Decision tree and Random Forest

Decision tree[15] is a non-parametric supervised learning technique used in classification and regression. The aim of these models is to establish simple decision rules inferred from the input feature space to predict target variables. A decision tree can be seen as a directional series of nodes, starting at a root node and diverging into sub-nodes called decision nodes that are further split until reaching leaf nodes(c.f Figure 2.3).

When provided with training vectors $x_i \in R^n$, i=1,...,l, and a label vector $y \in R^l$, the feature space is recursively divided to group samples that share the same labels or have similar target values. Let the data with n_m samples at a node m of the tree is represented by Q_m. For each candidate split θ= (j,t_m) with feature j and a threshold t_m, the data Q_m can be partitioned into two subsets $Q_m^{left}(\theta)$ and $Q_m^{right}(\theta)$ where :

$$\begin{aligned} Q_m^{left}(\theta) &= (x,y)|x_j \leq t_m \\ Q_m^{right}(\theta) &= Q_m \backslash Q_m^{left}(\theta) \end{aligned} \tag{2.2.1}$$

A loss(or impurity) function H() is assigned to measure the quality of a split, the choice of which depends on the nature of the problem at hand, for e.g, regression or classification. The goal of splitting is to minimize impurity. The quality of a candidate split is computed as a weighted sum of the impurity of the left and right subsets:

$$G(Q_m,\theta) = \frac{n_m^{\text{left}}}{n_m} H(Q_m^{\text{left}}(\theta)) + \frac{n_m^{\text{right}}}{n_m} H(Q_m^{\text{right}}(\theta)) \tag{2.2.2}$$

This loss function is minimized to find the optimal parameter set

$$\theta^* = argmin_\theta G(Q_m,\theta) \tag{2.2.3}$$

The left and right subsets are recursively split until certain stopping criterion are satisfied : the maximum allowed depth of the tree is reached, the number of samples at a node n_m becomes smaller than a predefined minimum $min_{samples}$ or a node contains only 1 sample (n_m=1).

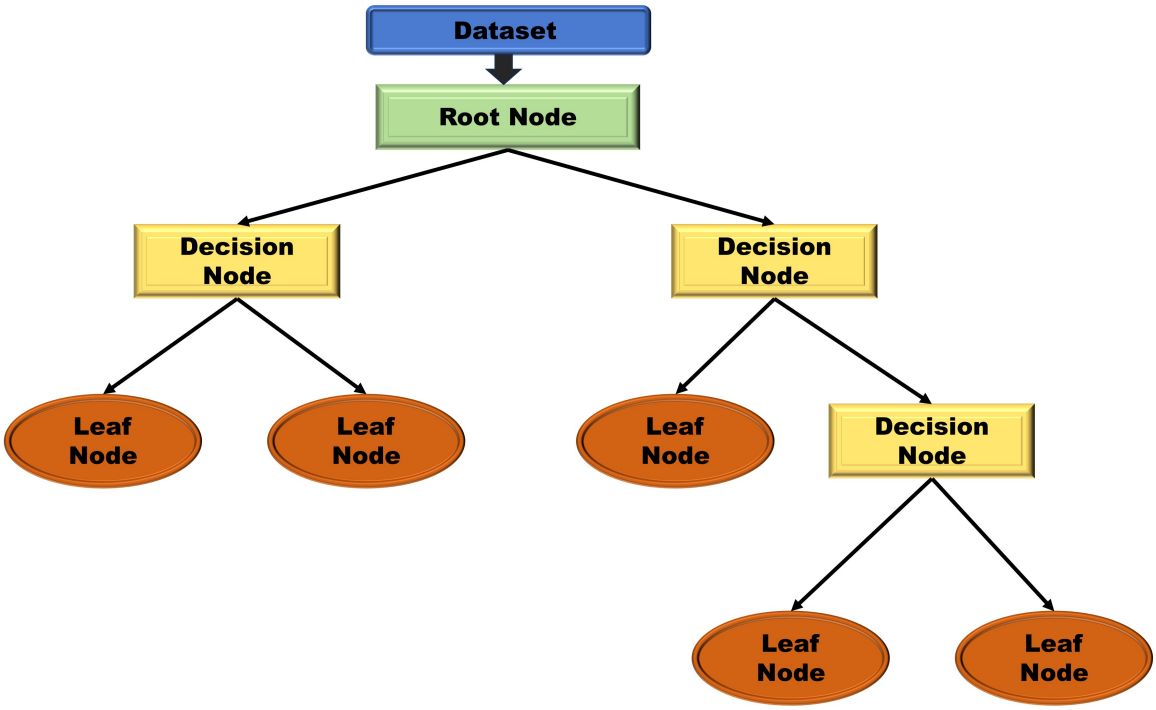

Figure 2.3: *Structure of a Decision Tree.*

Common measures of impurity for classification tasks include the following.

Gini index[16] :

$$H(Q_m) = \sum_k p_{mk}(1 - p_{mk}) \tag{2.2.4}$$

Log Loss[17] or Entropy:

$$H(Q_m) = -\sum_k p_{mk} log(p_{mk}) \tag{2.2.5}$$

where p_{mk} gives the proportion of data in node m that belong to class k, i.e, $p_{mk} = \frac{1}{n_m} \sum_{y \in Q_m} I(y=k)$.

When the task is regression, criteria commonly used are Mean Squared Error or Mean Absolute Error.

Mean Squared Error :

$$\begin{aligned} \bar{y}_m &= \frac{1}{n_m} \sum_{y \in Q_m} y \\ H(Q_m) &= \frac{1}{n_m} \sum_{y \in Q_m} (y - \bar{y}_m)^2 \end{aligned} \tag{2.2.6}$$

Mean Absolute Error:

$$\begin{aligned} median(y)_m &= median_{y \in Q_m}(y) \\ H(Q_m) &= \frac{1}{n_m} \sum_{y \in Q_m} (y - median(y)_m) \end{aligned} \tag{2.2.7}$$

There are a few approaches in implementing the decision tree algorithm, differing in their measure of impurity, data handling, pruning etc. In Random Tree[18], the tree is built by considering a fixed number of random attributes at each node. C4.5[19](also called J48[18] in certain implementations) allows continuous attributes and uses gain ratio as a measure to lower the bias towards features with multiple values. It performs two types of pruning: subtree replacement, where internal nodes are replaced with leaf nodes, and subtree raising, where nodes are moved upward toward the root, replacing other nodes in the process. In the REP Tree[20] implementation, reduced-error pruning is implemented. It removes part of the tree that do not improve accuracy by evaluating performance on a validation set.

Random forest[21] is an ensemble method that combine predictions of several base estimators, viz, decision trees, with randomness introduced in every estimator. This offers a robustness over a single estimator. The ensemble's prediction is obtained by averaging the predictions of the individual estimators(c.f. Figure 2.4). Each tree is built from a bootstrapped sample (sample drawn with replacement) from the training set. Additionally, during the splitting of nodes in a tree, the best split is determined by exhaustively searching the feature values, either across all input features or a random subset of size *max_features*. The purpose of these two sources of randomness is to reduce the variance of the forest estimator. Individual decision trees often have high variance and are prone to overfitting. By introducing randomness, the resulting decision trees exhibit prediction errors that are somewhat independent. Averaging these predictions allows some errors to cancel out. Random forests effectively reduce variance by combining diverse trees, though this may slightly increase bias. In practice, the reduction in variance is usually significant, leading to an overall improved model. Random forests effectively reduce variance by combining diverse trees, though this may slightly increase bias. In practice, the reduction in variance is usually significant, leading to an overall improved model.

The parameters of the Random Forest estimator are:

1. The structure for each decision tree, including features used for each node split and

their respective thresholds based on impurity measures.

2. The final output value for each leaf node (e.g., mean value for regression or majority class for classification).

The main hyper-parameters in a Random Forest estimator are the number of the base estimators(**n_estimators**) and **max_features**. The former indicates the number of trees in the forest and the results stop getting better beyond a critical value. The latter is the size of the random subsets of features used in deciding the split in a node. The lower its value, more the variance is reduced, but the bias increases as well. The other hyper-parameters include:

1. **max_depth**: The maximum allowed depth of each tree.
2. **min_samples_split**: Minimum number of samples required to split an internal node.
3. **min_samples_leaf**: An internal node would be split only if it projects this number of samples to both the left and right branches.
4. **min_impurity_decrease**: A node will be split if the resulting split reduces impurity by an amount greater than or equal to this specified value.
5. **max_leaf_nodes**: Grow trees with this specified number of leaf nodes using a best-first approach, where the best nodes are determined by the relative reduction in impurity.

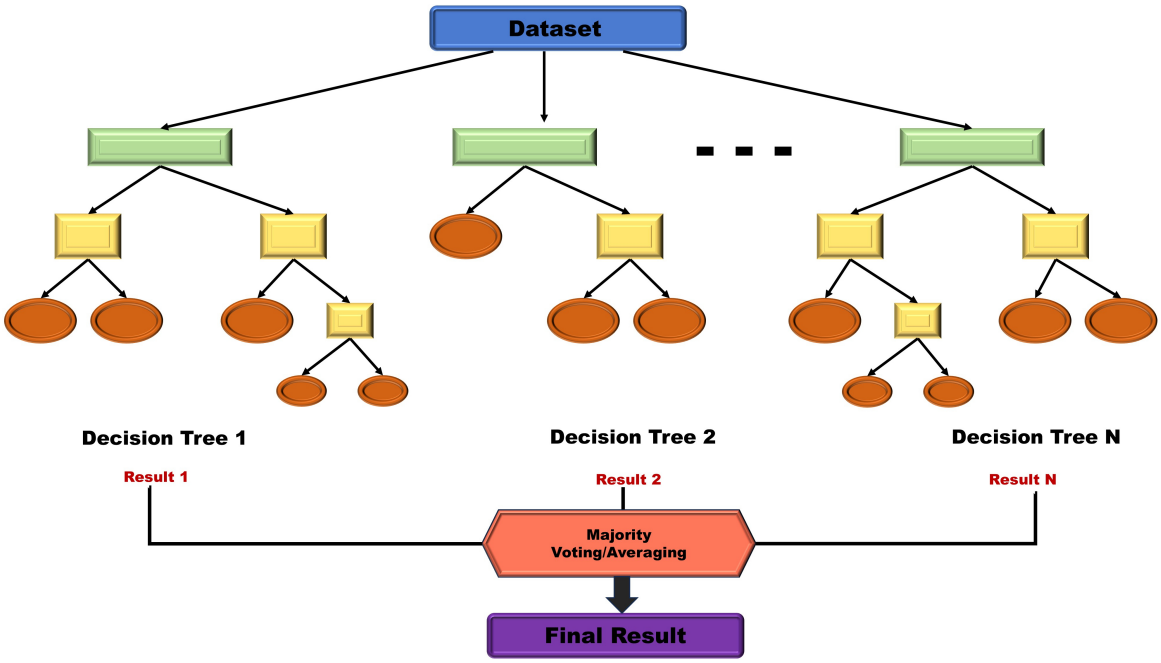

Figure 2.4: *Schematic representation of a Random Forest.*

A combination of setting **max_depth** to no particular limit and **min_samples_split** to '2' grows a fully developed tree. However, the best set of hyper-parameters are to be optimized

by searching the corresponding hyper-parameter space tactfully.

Random forests allow an unique unbiased estimation of their error without cross-validation or a separate test set, called the **out-of-bag(oob)**[22] error estimation. This estimate is calculated internally during training as follows:

Each tree is built using a different bootstrap sample from the original dataset. Approximately one-third of the data is left out of the bootstrap sample and is not used in constructing the k-th tree. These left-out samples are called out-of-bag (OOB) samples. For each tree, the OOB samples are passed through the k-th tree to obtain predictions. In this way, each data point is classified by the subset of trees where it was not included in the training data.

After all trees have been constructed, the final prediction for each data point is determined based on the OOB predictions:

- **For classification**: The predicted class is the one that receives the majority vote from the OOB predictions.
- **For regression** : The predicted value is the average of the OOB predictions.

The OOB error is then computed as:

- **For classification**: The proportion of data points where the predicted class differs from the true class, averaged over all data points.
- **For regression**: The mean squared error (or other chosen error metric) between the predicted and actual values, averaged over all data points.

Random forest can assign 'importance' to the features passed through it. For a given feature, it is calculated as the total decrease in impurity value in each node that splits based on it, weighted by the probability of reaching that node. The probability is approximated by the proportion of samples reaching that node. The mean and standard deviation of these values calculated over all the trees in the ensemble determine the feature's importance.

The original publication by Breiman et.al[21] elaborated two ways by which random forest can replace missing values by imputation during training. In the first approach the following steps are taken:

- **For numerical variables**: The median of all non-missing values of the feature within a class is computed and used to replace the missing values for that feature in that class.
- **For categorical variables**: The most frequent non-missing value of the feature within a class is used as the replacement for all missing values in that feature for that class.

A second more sophisticated, albeit computationally expensive, approach, called proximity-weighted imputation[23], can be used to handle missing values using the concept of proximity between data points. During the training of a random forest, the proximity matrix is calculated, the elements of which are the proximity between two samples i and j. Proximity is defined as the fraction of trees in the forest where both samples land at the same terminal (leaf) node.

$$\text{Proximity(i,j)} = \frac{\text{Number of trees where i and j share the same leaf}}{\text{Total trees}} \tag{2.2.8}$$

Initially, the missing values are replaced roughly with the feature's median(most frequent category) for numerical(categorical) features and a run is done to compute the proximity matrix. A missing numerical feature value for the i-th sample is estimated as the weighted average of the feature values from other samples, where the weights are derived from the proximities:

$$\text{Imputed Value} = \frac{\sum_{\text{j}\in\text{non-missing}} \text{Proximity(i,j)} \times \text{Feature Value(j)}}{\sum_{\text{j}\in\text{non-missing}} \text{Proximity(i,j)}} \tag{2.2.9}$$

For categorical values, the imputed category is the one with highest proximity weighted frequency. This iteration is continued until the imputed values stabilize,i.e, little to no change between iterations.

In the scikit-learn[24] implementation of random forest, as adapted in this thesis, missing data is handled at the decision tree level without data imputation. Here, missing values are handled dynamically during training and prediction using a strategy that evaluates all potential placements of missing values. During training, for a feature with missing value, the algorithm evaluates all possible splits using the non-missing data into two nodes. For each such potential split, the algorithm evaluates the impact of assigning all missing values to the left node or to the right node. The split that minimizes the impurity is chosen. This ensures that the missing values are directed to the child node that leads to the best split. If the impurity reduction is the same when assigning missing values to either node, the algorithm breaks the tie by assigning missing values to the right node. Moreover, the effect of assigning all missing value samples to one child node and the rest to the other node is investigated.

When predicting with a sample that contains missing values, the tree follows the decision path learned during training. Missing values are directed to the child node (left or right) based on the decision made for that feature during training. Similarly, if the impurity criterion was the same for both nodes during training, the missing value is assigned to the right

node by default during prediction.

2.2.1.2 Least Absolute Shrinkage and Selection Operator (LASSO)

The LASSO algorithm applies a shrinkage technique to ordinary linear regression by incorporating L1 regularization, which penalizes the absolute values of the coefficients. This penalty can drive some coefficients to zero, effectively eliminating the corresponding features from the model. The objective of the algorithm is to minimize the following function:

$$\sum_{i=1}^{n}(y_i - \sum_{j} x_{ij}\beta_j)^2 + \lambda \sum_{j=1}^{p} |\beta_j| \tag{2.2.10}$$

where λ decides the strength of regularization and p is the number of features and n is the number of datapoints. The first term is the residual sum of squares in least squares regression. The second term adds L1 regularization. When λ is large, LASSO forces some β_j to become exactly zero, effectively selecting important features while removing others. When λ is set to exactly zero, the problem reduces to a standard linear regression.

In this thesis, LASSO has been implemented through scikit-learn[24].

2.2.1.3 Class-imbalanced learning

Most classification algorithms assume balanced class distributions, but in practice, datasets often exhibit skewed distributions— referred to as imbalanced classification problems. The instances of one type or class are in excess than the other. In these cases,the cost of wrongly classifying a minority class is higher than that of a majority class.

In cost-sensitive learning, rather than simply labeling instances as correctly or incorrectly classified, each class is assigned a specific misclassification cost through a cost matrix. As a result, the objective shifts from maximizing overall accuracy to minimizing the total cost incurred from misclassifications. Considering, for example, a binary classification problem - a 2×2 cost matrix can be defined that quantifies a cost for each element in its confusion matrix. Each element C(i,j) of the cost matrix represents the cost of predicting class i when the true class is j.

	Y_0	Y_1
$\hat{Y}_0$	c_{00}	c_{01}
$\hat{Y}_1$	c_{10}	c_{11}

Here '^' represents predicted class. Correct classifications have no cost, i.e, c_{00}=c_{11}=0. The misclassification error can be achieved by multiplying each element of the confusion matrix

with its corresponding value in the cost matrix.

$$Cost = \frac{TN * c_{00} + FN * c_{01} + FP * c_{10} + TP * c_{11}}{N} = \frac{FN * c_{01} + FP * c_{10}}{N}$$

Here, the minority(majority) class is considered positive(negative), denoted by subscript 1(0).

However, setting the elements of a cost matrix is a non-trivial task. One popular heuristic is to use the imbalance ratio(IR), which is the ratio of the cardinality(number of instances) of the majority and minority class subsets. Thus, the cost matrix of the binary classification problem becomes:

	Y_0	Y_1
$\hat{Y}_0$	0	1
$\hat{Y}_1$	IR	0

Another route to handle the class imbalance problem is by synthetically oversampling the minority class. Synthetic Minority Oversampling Technique(SMOTE) is a technique to generate artificial data to balance an imbalanced dataset with discrete classes. In this, the minority class(class lesser representations in the dataset) is oversampled. In a machine learning dataset, each data point is represented by an n-dimensional feature vector. The SMOTE (Synthetic Minority Over-sampling Technique) method generates synthetic data points for the minority class by considering the difference between a given minority class data point's feature vector and those of its k nearest minority class neighbors in feature space. A new synthetic data point is then created by multiplying this difference by a random number between 0 and 1 and adding the result to the original feature vector. This is shown schematically in Figure 2.5.

In this thesis, SMOTE has been implemented through the imbalanced-learn[25] library.

2.2.2 Unsupervised Learning

Unsupervised learning has found application in materials science research in several instances. Kitaraha and Holm [26] aimed at clustering steel defects by defect type or fracture surface reorientation, using unsupervised deep learning. An unsupervised learning technique, called the non-negative matrix factorization(NMF), has been successfully implemented in generating pertinent XRD spectra out of sets of diffraction patterns[27]. Unsupervised learning has shown exciting results in phase diagram determination. Clustering algorithms have helped to differentiate between spectra and group spectra. In reference [28], the 'distances' among the sampled spectra of Fe-Ga-Pd ternary have been calculated

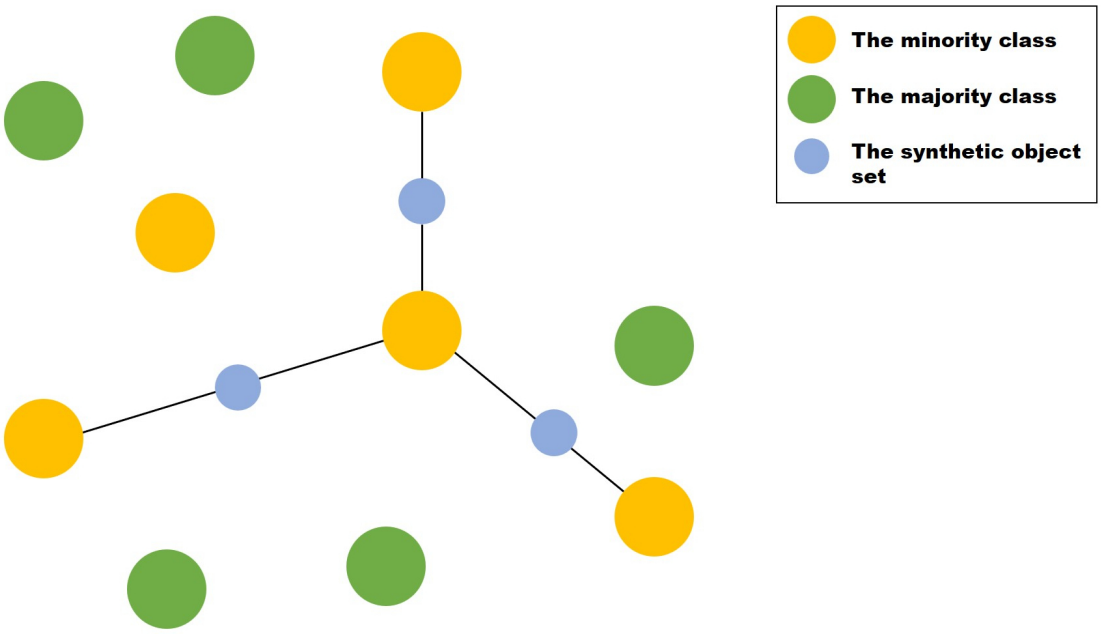

Figure 2.5: *Synthetic data generation using the SMOTE algorithm.*

using a distance matrix(where each entry d_{ij} is the distance in 2θ space between two spectra i and j) and represented in a three-dimensional space using metric multidimensional data scaling (MMDS)[29]. Unsupervised learning has been used in automated micrograph analysis. In [30], the spatial arrangements of the microstructure in α-Ti have been visually represented using the first two or three principle components derived from the analysis of the principal components of the representations of N-point statistics of the same. In the work by Cohn et.al.[31], the construction, use, and evaluation of a high-performance unsupervised machine learning system for classifying images in a microstructural dataset are demonstrated. Feature representations for each micrograph are extracted using a convolutional neural network, which has been pre-trained on a dataset of natural images. Principal component analysis is then applied to extract signal from the feature descriptors, followed by k-means clustering to classify the images without requiring labeled training data. An accuracy of 99.4% ± 0.16% is achieved, and the resulting model can be used to classify new images without retraining. Samudrala et.al [32]have used low-dimensional data extraction techniques like PCA and isomaps on a dataset of Apatite, where each datapoint is characterized by 29 structural descriptors. While associations between similar compounds are found in both the techniques, the nature of the representation has been found to be different since PCA is a linear technique while isomap is a non-linear one. An autoencoder technique has been used for the analysis and design of electromagnetic nanostructures[33]. PCA has again been utilized in dimensionality reduction of the multidimensional parameter space that affect mechanical behavior of nanoporous materials[34]. These outputs are used for further analysis in this study, making them more accessible against computa-

tional limits. In another work,a denoising autoencoder has been used for uniforming the input dimensionality, as it can vary depending on the number of elements in the sampled material[35]. Both conventional clustering algorithms such as K-means, Gaussian mixtures and neural network based algorithms such as self-organizing maps have been used to cluster superconductivity data by Roter et al.[36]. In [37], an unsupervised algorithm used to embed high-dimenisonal data to a low dimensional space,t-SNE, has been applied to a multi-dimensional feature space derived out of bandstructures of several materials. This successfully clustered materials with similar dispersion curves. In the work by Walker et.al.[38], structural changes are identified using unsupervised machine learning methods, with the melting point transition in classical molecular dynamics simulations serving as an example application of the approach. The dimensionality of the feature space across the samples is significantly reduced through principal component analysis. Following this, the samples are partitioned into solid and liquid phases using *k*-means clustering, based on a criterion derived from the geometry of the reduced feature space, enabling the estimation of the melting point transition. In [39], iterative Label Spreading (ILS), an unsupervised machine learning approach, has been applied to classify different types of Al alloys using a curated dataset of 1,154 Al alloys. Through ILS, eight distinct classes of Al alloys have been identified based on a comprehensive feature set under two descriptors. To validate the classification, a decision tree classifier has been employed. Iwasawa et.al.[40] have used a combination of K-means and fuzzy c-means clustering techniques on ARPES data to categorize them. This has enabled them in identifying spatial inhomogenity on electronic structures. Zhang et. al.[41] have used an unsupervised natural language processing(NLP) scheme to extract information about solar cells from textual data. The predicted materials are validated by first-principles calculations to establish the efficacy of the NLP-assisted machine learning model. Kalinin et.al[42] have employed a variational autoencoder based unsupervised learning scheme to derive chemical transformation pathways from Scanning Transmission Electron Microscopy (STEM) data. Zhang et.al.[43] have used unsupervised learning in accelerating the discovery of viable solid electrolytes for Li-batteries. Since, amount of good quality data is scarce, they have implemented a workflow to cluster candidates by their ionic conductivity for all Li-containing compounds in ICSD dataset. The compounds with higher conductivities are further investigated through detailed calculations. Luo et.al.[44] have adopted unsupervised learning to classify experimentally known inorganic crystal structure in terms of local atomic environments, by using a hierarchical clustering algorithm.

In this thesis, an autoencoder, built using artificial neural network, is used for dimensionality reduction and Principle Component Analysis(PCA) to visualize them , and a K-means clustering algorithm for clustering. The details of these techniques are given in the next

sections.

2.2.2.1 Principle Component Analysis(PCA)

PCA is one of the conventional methods of dimensionality reduction and higher-dimensional data visualization. It recognizes a linear subspace that (i) maximizes the variance of the orthogonal projections of the data and (ii) minimizes the mean squared distance between the original data points and their projections. This subspace serves as the optimal linear representation of the dataset.

To determine the linear subspace, the data is first normalized by subtracting the mean from each M-dimensional variable, forming the normalized data matrix Y, where the ith row of Y corresponds to $x_i - \bar{x}$. Next, the covariance matrix $S = Y^T Y$ is computed, and its eigenvectors u_i and corresponding eigenvalues λ_i are determined:

$$Su_i = \lambda_i u_i \tag{2.2.11}$$

The PCA subspace of dimension D is constructed by selecting the D eigenvectors with the highest eigenvalues. These eigenvectors, known as principal components, represent the directions of maximum variance in the data. The corresponding eigenvalues indicate the amount of variance captured along each principal component. The D principal components define a subspace within the original data space, where they serve as an orthogonal basis. By projecting the data vectors onto this basis, a lower-dimensional representation of the data with dimension D is obtained:

$$y_{PCA,i} = y^T u_i \tag{2.2.12}$$

where y=x-$\bar{x}$. The original data can be reconstructed by summing the contributions from each principal component, effectively combining the projected components to approximate the original dataset:

$$x \approx \sum_{i=1}^{D} (y^T u_i) u_i + \sum_{i=1}^{D} (\bar{x}^T u_i) u_i \tag{2.2.13}$$

If the summation in Equation 2.2.13 includes all principal components, the original data x is perfectly reconstructed. However, if the components with the smallest eigenvalues are excluded, the result becomes an approximation of x. This technique is often used to reduce noise in a dataset.

By selecting only the first two or three principal components (setting D to 2 or 3), PCA can

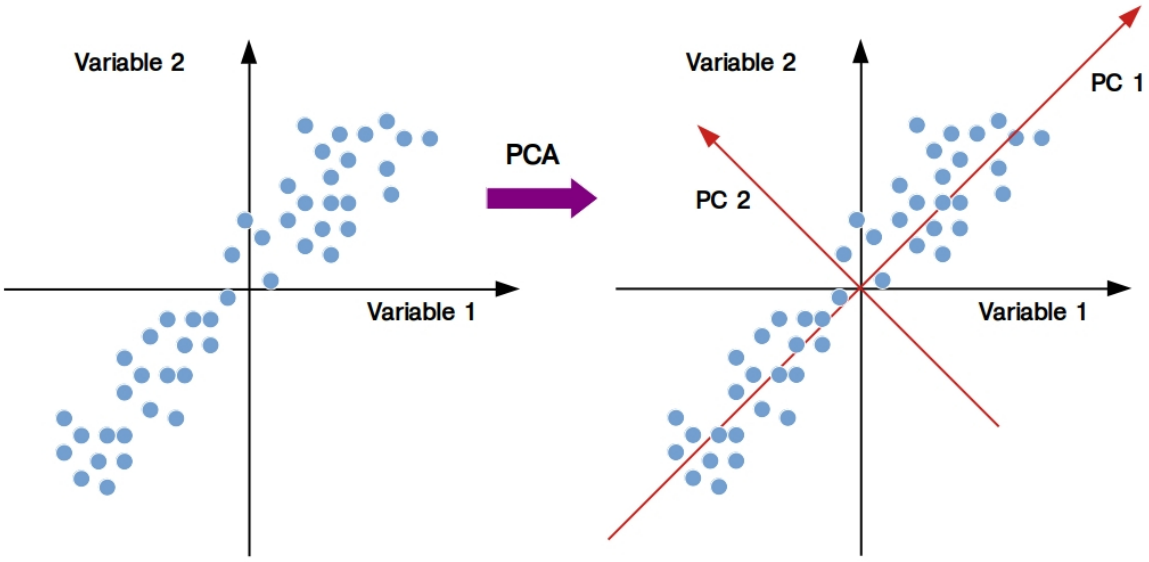

Figure 2.6: *Schematic representation of the first two principal components, PC1 and PC2.*

be used to visualize high-dimensional data in a lower-dimensional space, making patterns and structures easier to interpret. This is shown schematically in Figure 2.6.

In this thesis, PCA has been implemented through scikit-learn[24].

2.2.2.2 Artificial Neural Network

Artificial Neural Network(ANN) is a machine learning model that aims to mimic the complex connectivity of neurons in our brains. ANNs are fundamental to Deep Learning. They are versatile, powerful, and scalable, making them well-suited for handling large-scale and highly complex machine learning tasks. The concept of ANN had been first explored in the 1940s, in the seminal paper by Warren McCulloch and Walter Pitts[45] in which they had proposed a simplified computational model illustrating how biological neurons in animal brains could work together to perform complex computations based on propositional logic. Since then, many different architectures have been invented.

Before proceeding to an artificial neuron, the building block of the artificial neural networks, it would be advantageous to draw its parallel with biological neurons(shown in Figure 2.7(A)) and justify the nomenclature. It consists of a *cell body* that consists of the nucleus and most of the cell's complex components, a single, long extension known as the axon and multiple branching extensions called dendrites. Toward its end, the axon branches into multiple extensions called telodendria, each terminating in tiny structures known as synaptic terminals (or synapses). These synapses connect to the dendrites or cell bodies of other neurons. A Biological neurons generate brief electrical impulses, known as action potentials (APs or signals), which travel along their axons and trigger the release of

chemical signals called neurotransmitters in synapses. If a neuron receives enough of these neurotransmitters within a short time frame, it generates its own electrical impulses. These biological neurons are spread over a billion-plus network, with each neuron interconnected with several thousands of other neurons.

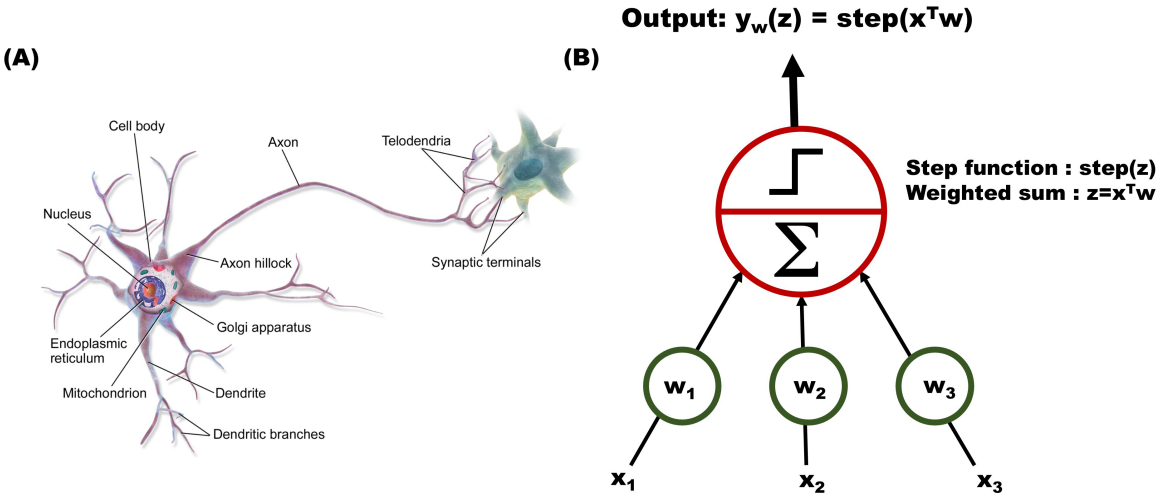

Figure 2.7: *(A) A biological neuron. (B) Architecture of a simple perceptron.*

The concept of an artificial neuron, called the perceptron(shown in Figure 2.7(B)), was introduced by Frank Rosenblatt[46]. In this rudimentary version of the perceptron, it could take several inputs(x_is) with each input associated with a weight(w_is), compute the weighted sum($z = \sum_n w_i x_i = \mathbf{x}^T \mathbf{w}$) and output the result after applying a step function to it : $y_w(z)$=step(z).

The step functions conventionally used are the Heaviside function or the sign function.

$$\text{heaviside}(z) = \begin{cases} 0 & \text{if } z < 0, \\ 1 & \text{if } z \geq 0 \end{cases} \qquad \text{sgn}(z) = \begin{cases} -1 & \text{if } z < 0, \\ 0 & \text{if } z = 0, \\ +1 & \text{if } z > 0 \end{cases} \tag{2.2.14}$$

However, for all practical purposes, a logistic(sigmoid) function is used :

$$\sigma(z) = \frac{1}{1 + exp(-z)} \tag{2.2.15}$$

In addition to sigmoid activation function, there are other activation functions such as(c.f Figure 2.8) :

Hyperbolic tangent(tanh(z))=2σ(2z)-1: While this function bears the same S-shape and are continuous and differentiable as the sigmoid function, the output range is

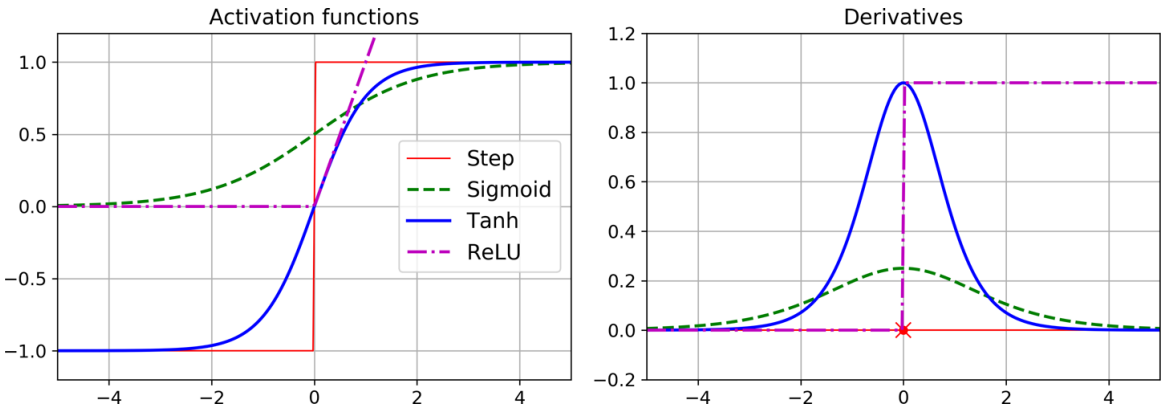

Figure 2.8: *Activation functions and their derivatives, adapted from [47]*

[-1,1]. This aligns the output of each layer about 0 at the beginning of training, helping to accelerate the convergence.

The Rectified Linear Unit function(ReLU(z) = max(0, z)): This function is globally continuous but not differentiable at z=0. In practice, however, this is fast to compute and widely implemented, due to its bypassing of the vanishing/explosive gradient problem as observed in previously mentioned functions.

Softmax: The softmax function is frequently used in the output layer for classification tasks using a neural network model. It transforms the output into a probability distribution by inputting raw scores from its previous layer. The mathematical form for the output of the i-th neuron in the output layer is $\frac{e^{z_i}}{\sum_{j=1}^{K} e^{z_j}}$, where the denominator represents the sum over all the neurons in the layer.

A network of such perceptrons arranged in multiple layers, called the multilayer perceptron (MLP)[48], can be implemented in the handling of complex tasks. In this architecture, a layer of neurons connected to all neurons of its previous layer, constitutes a fully connected layer or a dense layer. The inputs to the network are generally passed through specialized neurons known as input neurons, which simply output the values they receive. Together, these input neurons make up the input layer. Beyond this layer, there are one or more layers called the hidden layers, and a final output layer. Additionally, a bias feature is usually included in every layer (except the output layer) that is fully connected to the next layer. Since the direction of signal flow is from the inputs to the outputs, this architecture is also called the feed-forward neural network.

$$y_{W,b}(\mathbf{X}) = \phi(\mathbf{X}\mathbf{W} + \mathbf{b}) \tag{2.2.16}$$

$\mathbf{X}$ is the input matrix, with each row denoting an instance and each column denoting a

feature. The weight matrix **W** contains all the connection weights (except bias neuron) for every layer. It contains rows corresponding to the number of neurons in the layer and columns as the number of connections from the previous layer. The bias vector **b** enlists the connections between the bias neuron and other artificial neurons, with one bias term each. The function ϕ is the activation function, for e.g., step function in the previous section. An architecture comprising of stack of hidden layers is called a deep neural network(DNN).

For training of a neural network, the weights and biases have to be determined such that the network fairly approximates the target output for all the training instances. This is quantified in terms of a cost function(loss function or objective function):

$$\mathrm{C}(\mathbf{W},\mathbf{b}) = \frac{1}{2n}\sum_{x}\|\mathrm{y(x)\text{-}a}\|^2 \tag{2.2.17}$$

Here n is the number of datapoints used for training, a is the vector of outputs when x is the input and y(x) is the target output vector. The aim for the training is to essentially make the cost C as small as possible by tweaking the weights and biases. This can be achieved by the principle of gradient descent[49]. Gradient descent is an algorithm to minimize a loss function J(θ_1,...,θ_m) by iteratively adjusting the parameters θ in the direction of negative gradient. The change ΔJ of the cost function for change in the parameters θ, represented by the vector $\Delta\theta$ =($\Delta\theta_1$,..,$\Delta\theta_m$), can be written as:

$$\Delta J \approx \nabla J.\Delta\theta, \tag{2.2.18}$$

where ∇ J is the vector of the gradients of function J:

$$\nabla J = (\frac{\partial J}{\partial \theta_1},..,\frac{\partial J}{\partial \theta_m})^T \tag{2.2.19}$$

The Cauchy-Schwarz inequality states :

$$\langle \nabla \mathrm{J}\Delta\theta \rangle \leq \|\nabla \mathrm{J}\|\|\Delta\theta\| \tag{2.2.20}$$

The equality holds when $\Delta\theta$ and ∇J are in the same direction. Therefore, to maximize the magnitude of ∇J.$\Delta\theta$ (and minimize ΔJ), $\Delta\theta$ is set to -$\eta\nabla$J, where η is a small, positive parameter called the learning rate. It can then be guaranteed that J will always decrease,i.e, $\Delta J \leq 0$ since $\Delta J \approx -\eta\|\nabla \mathrm{J}\|^2$ and $\|\nabla \mathrm{J}\|^2 \geq 0$. Thus, by following the gradient in the step lengths as dictated by the parameter η, a minimum can be reached by iterating the rule :

$$\theta \rightarrow \theta' = \theta - \eta\nabla J \tag{2.2.21}$$

By this formulation, the gradient descent update rules for the weights w_k and b_l are:

$$w_k \rightarrow w_k^{'} = w_k - \eta \frac{\partial C}{\partial w_k} \tag{2.2.22}$$

$$b_l \rightarrow b_l^{'} = b_l - \eta \frac{\partial C}{\partial b_l} \tag{2.2.23}$$

For practical purposes where the number of training datapoints are large, the calculation of ∇C entails the calculation of ∇C_x for every training point and averaging them, which can slow down the learning process. Stochastic gradient descent is implemented in handling this issue. A sufficient number p of training points(X_1,...,X_p) are picked randomly, referred to as mini-batch. The average value of the ΔC_{X_j} is used to approximate the average over all the points ,i.e,

$$\frac{\sum_{j=1}^{p} \nabla C_{X_j}}{p} \approx \frac{\sum_x \nabla C_x}{n} = \nabla C \tag{2.2.24}$$

The second sum is calculated over the entire training set. This modifies equations 2.2.22 and 2.2.23 to :

$$w_k \rightarrow w_k^{'} = w_k - \frac{\eta}{p} \sum_j \frac{\partial C_{X_j}}{\partial w_k} \tag{2.2.25}$$

$$b_l \rightarrow b_l^{'} = b_l - \frac{\eta}{p} \sum_j \frac{\partial C_{X_j}}{\partial b_l} \tag{2.2.26}$$

The summations are over all the points in the current mini-batch. Then further batches are considered to train the network until all the training inputs are exhausted. This completes one epoch of training.

The crucial part of the training procedure is the calculation of the gradients. The backpropagation [50] training algorithm is a groundbreaking achievement in this regard. It calculates the gradients of the network's error with respect to every parameter(weights and biases) by two simple passes over the network, one forward and one backward. Every mini-batch is put through the network's input layer and subsequently to the first hidden layer. For every instance, output of every neuron is computed for the present layer and passed on to the next layer, and so on. The forward pass is concluded on reaching the output layer and retaining the intermediate results of each hidden layer. Then, the network's output error is calculated in terms of some loss function and how much each of the output connections contributed to it(using chain rule). The algorithm subsequently determines the proportion of each error contribution that originates from the connections in the layer below, applying the chain

rule as it works backwards until it reaches the input layer. This backward pass effectively calculates the error gradient for all connection weights in the network by propagating the error gradient backward through the network, which is why the algorithm is named as such. Finally, the gradient descent algorithm is called into action to refine the model parameters using the calculated error gradients. The mathematical formulation of the backpropagation algorithm is discussed below.

The weight of the connection between j^{th} neuron in l^{th} layer and k^{th} neuron in $(l-1)^{th}$ layer is represented by $w^l{}_{jk}$. $b^l{}_j$ denotes the bias of the j^{th} neuron of the l^{th} layer and $a^l{}_j$ is the activation of the j^{th} neuron of the l^{th} layer. Using these notations(c.f Figure 2.9 for an example of the notations), the activation $a^l{}_j$ of the j^{th} neuron in the l^{th} layer is connected to the activations in the $(l-1)^{th}$ layer by the following equation:

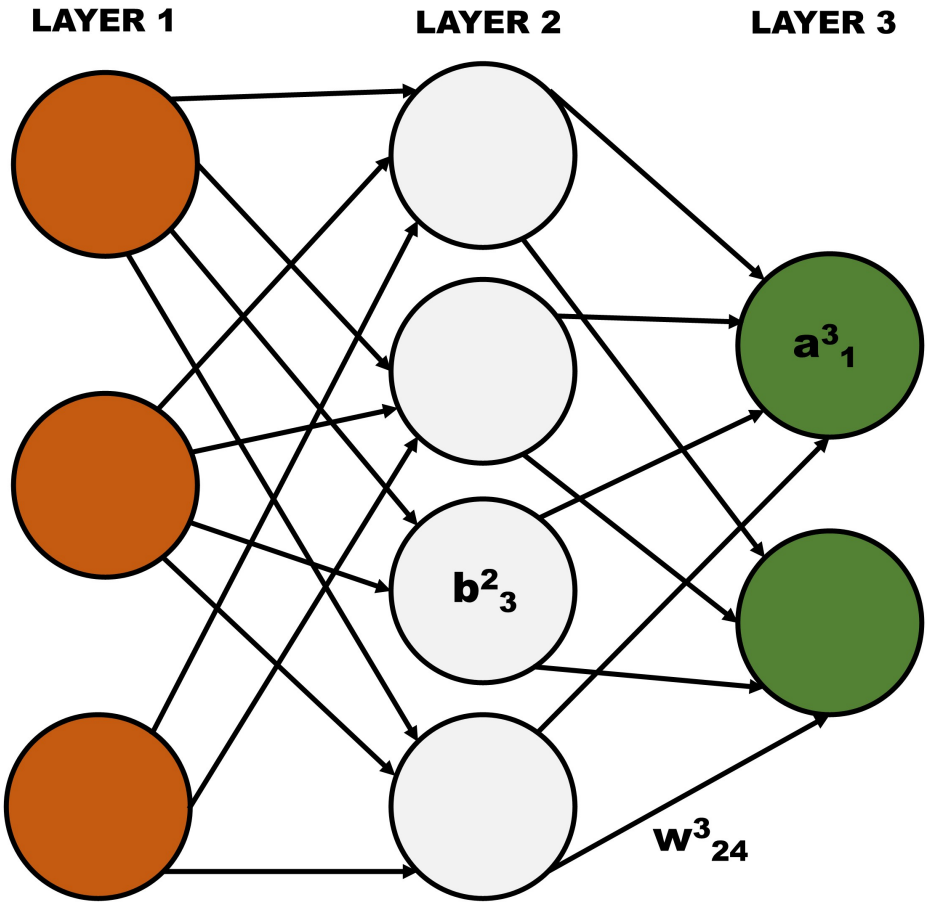

Figure 2.9: *Schematic of a multilayer perceptron and examples of notations used.* b^2_3 *is the bias of the* 3^{rd} *neuron in the* 2^{nd} *layer.* a^3_1 *is the output of the* 1^{st} *neuron of the third layer.* w^3_{24} *is the weight from the* 4^{th} *neuron in the (3-1=)*2^{nd} *layer to the* 2^{nd} *neuron in* 3^{rd} *layer.*

$$a^l_j = \sigma(\sum_k w^l_{jk} a^{l-1}_k + b^l_j) \tag{2.2.27}$$

The summation is over all neurons k in the $(l-1)^{th}$ layer. This equation can be rewritten

using a matrix notation by introducing a weight matrix w^l for layer l, recording weights connecting to the l^{th} layer of the network (value in j^{th} row and l^{th}column is $w^l{}_{jk}$). Similarly a bias vector b^l(elements are $b^l{}_j$) and activation vector a^l(elements are $a^l{}_j$) for every layer l is introduced. The equation 2.2.27 can then be rewritten in a vectorized form as :

$$a^l = \sigma(w^l a^{l-1} + b^l) = \sigma(z^l) \tag{2.2.28}$$

where z^l=($w^l a^{l-1}$+b^l) is the weighted input to layer l.

Backpropagation aims at obtaining the partial derivatives $\frac{\partial C}{\partial w^l_{jk}}$ and $\frac{\partial C}{\partial b^l_j}$. In this derivation, an intermediate term δ^l_j is computed, which is the error in l^{th} layer's j^{th} neuron. This is given by :

$$\delta^l_j = \frac{\partial \mathrm{C}}{\partial \mathrm{z}^l_j} \tag{2.2.29}$$

There are four fundamental equations that guide the backpropagation process.

BP-Equation 1: Equation for error in output layer, δ^L.

$$\delta^L_j = \frac{\partial C}{\partial a^L_j}\sigma'(z^L_j) \tag{2.2.30}$$

[**Derivation:** Using the definition $\delta^L_j = \frac{\partial \mathrm{C}}{\partial z^L_j}$ and applying chain-rule to express it in terms of partial derivatives wrt output activations,

$$\delta^L_j = \sum_k \frac{\partial C}{\partial a^L_k}\frac{\partial a^L_k}{\partial z^L_j}$$

in which the sum is over all neurons k in the output layer L. a^L_k (of the k^{th} neuron) depends only on the input z^l_j for the j^{th} neuron as k=j. Thus other terms in $\partial a^L_k/\partial z^L_j$ vanishes when $k \neq j$. Thus

$$\delta^L_j = \frac{\partial C}{\partial a^L_j}\frac{\partial a^L_j}{\partial z^L_j}$$

Since a^L_j=$\sigma(z^l_j)$,

$$\delta^L_j = \frac{\partial C}{\partial a^L_j}\sigma'(z^L_j)$$

]

BP-Equation 2: Equation for error in the l^{th} layer, δ^l, in terms of error in the $(l+1)^{th}$ layer,δ^{l+1}.

$$\delta^l = ((w^{l+1})^T \delta^{l+1}) \odot \sigma'(z^l) \tag{2.2.31}$$

$(w^{l+1})^T$ is the transpose of the weight matrix for the $(l+1)^{th}$ layer and $\odot$ represents a Hadamard product. Equations 2.2.30 and 2.2.31 together can be used to compute error δ^l for any layer l, starting with 2.2.30 to find δ^L and working backward to find δ^{L-1} and δ^{L-2} and the rest, until traversing the entire network.

[**Derivation:** Using the chain rule:

$$\begin{aligned}\delta_j^l &= \frac{\partial C}{\partial z_j^l} \\ &= \sum_k \frac{\partial C}{\partial z_k^{l+1}} \frac{\partial z_k^{l+1}}{\partial z_j^l} \\ &= \sum_k \frac{\partial z_k^{l+1}}{\partial z_j^l} \delta_k^{l+1}\end{aligned}$$

where the $\frac{\partial C}{\partial z_k^{l+1}} = \delta_k^{l+1}$. Now,

$$z_k^{l+1} = \sum_j w_{kj}^{l+1} a_j^l + b_k^{l+1} = \sum_j w_{kj}^{l+1} \sigma(z_j^l) + b_k^{l+1}$$

Differentiating wrt z_j^l,

$$\frac{\partial z_k^{l+1}}{\partial z_j^l} = w_{kj}^{l+1} \sigma'(z_j^l)$$

Putting it back in the expression connecting δ_j^l and δ_k^{l+1},

$$\delta_j^l = \sum_k w_{kj}^{l+1} \delta_k^{l+1} \sigma'(z_j^l)$$

This is BP-Equation 2 in component form.]

BP-Equation 3: Equation for the rate at which the cost changes with respect to any bias in the network.

$$\frac{\partial C}{\partial b_j^l} = \delta_j^l \tag{2.2.32}$$

This can be easily found since BP-Equation 1 and BP-Equation 2 can readily provide the value of δ_j^l.

[**Derivation:**

$$\frac{\partial C}{\partial b_j^l} = \frac{\partial C}{\partial z_j^l} \frac{\partial z_j^l}{\partial b_j^l} = \delta_j^l \times \frac{\partial (\sum_k w_{jk}^l a_k^{l-1} + b_j^l)}{\partial b_j^l} = \delta_j^l$$

where equation 2.2.29 gives the definition for δ^l_j.]

BP-Equation 4: Equation for the rate at which the cost changes with respect to any weight in the network.

$$\frac{\partial C}{\partial w^l_{jk}} = a^{l-1}_k \delta^l_j \tag{2.2.33}$$

This can be easily found since a^{l-1} and δ^l are already known.

[**Derivation:**

$$\frac{\partial C}{\partial w^l_{jk}} = \frac{\partial C}{\partial z^l_j}\frac{\partial z^l_j}{\partial w^l_{jk}} = \delta^l_j \times \frac{\sum_p w^l_{jp} a^{l-1}_p + b^l_j}{\partial w^l_{jk}}$$

The last expression evaluates to non-zero value when p=k. Thus,

$$\frac{\partial C}{\partial w^l_{jk}} = \delta^l_j a^{l-1}_k$$

]

For practical applications, backpropagation algorithm is used in tandem with a learning algorithm like the stochastic gradient descent. The combined workflow can be laid out as :

- An outer loop is initiated to supply mini-batches of size m sampled from all the training instances.
- For every example x in a mini-batch:
  - ☐ Activation $a^{x,1}$ is initiated for the input layer.
  - ☐ $z^{x,l}$ and $a^{x,l}$ is calculated for l=2,3,..L. This is the feedforward step.
  - ☐ The output error $\delta^{x,L}$ is found using BP-Equation 1.
  - ☐ The error is then backpropagated for each layer l=L, L-1, L-2, i.e, compute $\delta^{x,l}$ from BP-Equation 2.
- Following the gradient descent algorithm, for each layer l=l,L-1,..2, the weights and biases are updated according to $w^l \to w^l - \frac{\eta}{m}\sum_x \delta^{x,l}(a^{x,l-1})^T$ and $b^l \to b^l - \frac{\eta}{m}\sum_x \delta^{x,l}$ (using BP-Equation 3 and BP-Equation 4 in equations 2.2.25 and 2.2.26).
- An outer loop proceeds through the epochs during the training.

A caveat of building a machine learning model is that it can be susceptible to overfitting, replicating the trend in training data closely but fails to generalize to unseen data. Certain

techniques called regularization methods can be employed to reduce the generalization error (or test error), as described below.

L_2-regularization: An extra regularization term is appended to the cost function to drive the model weights close to the origin. This form of regularization penalizes proportionately to the sum of the squares of the weights, that is, $L_2 \propto \sum_w w^2$, where n is the number of weights in the model. The regularized cost function can be written as :

$$C = C_0 + \frac{\lambda}{2n} \sum_w w^2 \tag{2.2.34}$$

where C_0 is the actual unregularized objective function, n is the training set size and λ is the regularization rate. The latter controls the impact of the regularization on the model complexity. When the rate is high, the model weights approach a normal distribution with mean 0. When the rate is low, the distribution is rather flat. The ideal λ is data-dependent and can be found by some systematic tuning. The regularized updation rule of the weights for an MLP (mini-batches of size p and learning rate η) is :

$$w_k \to w'_k = (1 - \frac{\eta\lambda}{n})w - \frac{\eta}{p} \sum_x \frac{\partial C_x}{\partial w} \tag{2.2.35}$$

where the sum is over the instances in the present minibatch.

L_1-regularization: In L_1 regularization, the cost function is modified by the sum of the absolute values of the weights.

$$C = C_0 + \frac{\lambda}{2n} \sum_w |w| \tag{2.2.36}$$

The regularized updation rule of the weights for an MLP (mini-batches of size p and learning rate η) is :

$$w_k \to w'_k = w - \frac{\eta\lambda}{n} \text{sgn(w)} - \frac{\eta}{p} \sum_x \frac{\partial C_x}{\partial w} \tag{2.2.37}$$

where sgn(w) is the sign function.

In L_1 regularization, the weights are reduced by a fixed amount to zero, regardless of their magnitude. In contrast, L_2 regularization decreases weights by an amount proportional to their value (w). This means that for weights with large magnitudes ($|w|$), L_1 regularization reduces them less than L_2 regularization. However, for smaller weights ($|w|$), L_1 regularization reduces them more significantly compared to L_2 regularization. As a result, L_1 regularization tends to concentrate the model's weights on a small number of highly important connections while driving the rest of the weights closer to zero.

An optimal balance must be established between the learning rate(η) and the regularization rate(λ). The reason is that a high η often shifts the weights further from zero, while a high λ takes the weights toward zero. Setting the regularization rate higher than the learning rate can lead to a model that underfits, while the converse can produce a model that overfits.

Dropout: Dropout regularizes by modifying the network itself rather than modifying the cost function. It works by removing a fixed number of neurons from the hidden network (barring input and output layers) for a single gradient step. This prevents co-adaptation in the network where the neurons rely heavily on the outputs of specific other neurons to predict patterns in the training data, rather than utilizing the collective behavior of the entire network. After modification of the weights and biases over a mini-batch on this network structure, the removed neurons are reestablished and another randomized set of neurons are dropped out. By iterating this workflow, a set of model parameters is learned that does not tend to overfit.

2.2.2.2.1 Autoencoder

An autoencoder is a neural network designed to learn by replicating its input on the output. Through unsupervised machine learning, they are trained to identify latent variables within the input data that, while not directly observable, play a crucial role in shaping the data's distribution. Internally, it contains a hidden layer, h, that encodes a representation of the input. This layer is often called the **code** layer, that inherits some useful properties of the input during the training of the autoencoder. The network can be seen as comprising two components: an encoder function, $e = f(x)$, and a decoder that generates a reconstruction, $d = g(e)$. The architecture is shown schematically in Figure 2.10. Autoencoders are intentionally designed to prevent perfect copying. They are typically constrained in ways that allow only approximate replication, focusing on input similar to the training data. By forcing the model to prioritize the aspects of the input to retain, it often captures meaningful properties of the data. This aspect of autoencoders is utilized in dimensionality reduction or feature selection. Autoencoders can be considered as a specific type of feedforward network and are typically trained using the same techniques, such as minibatch gradient descent with gradients computed via backpropagation.

One route to extract crucial features in the code layer h is to limit its dimensionality below $\boldsymbol{x}$, the input dimensionality. Such autoencoders are called **undercomplete**. Training such a network pushes it to extract the predominant patterns of the learning data. The training is basically the minimization of a loss function

$$L(x, g(f(x))), \tag{2.2.38}$$

where L is a loss function,such as the mean squared error, that penalizes g(f(x)) for differing from x. With the decoder being linear and the loss function being the mean squared error,

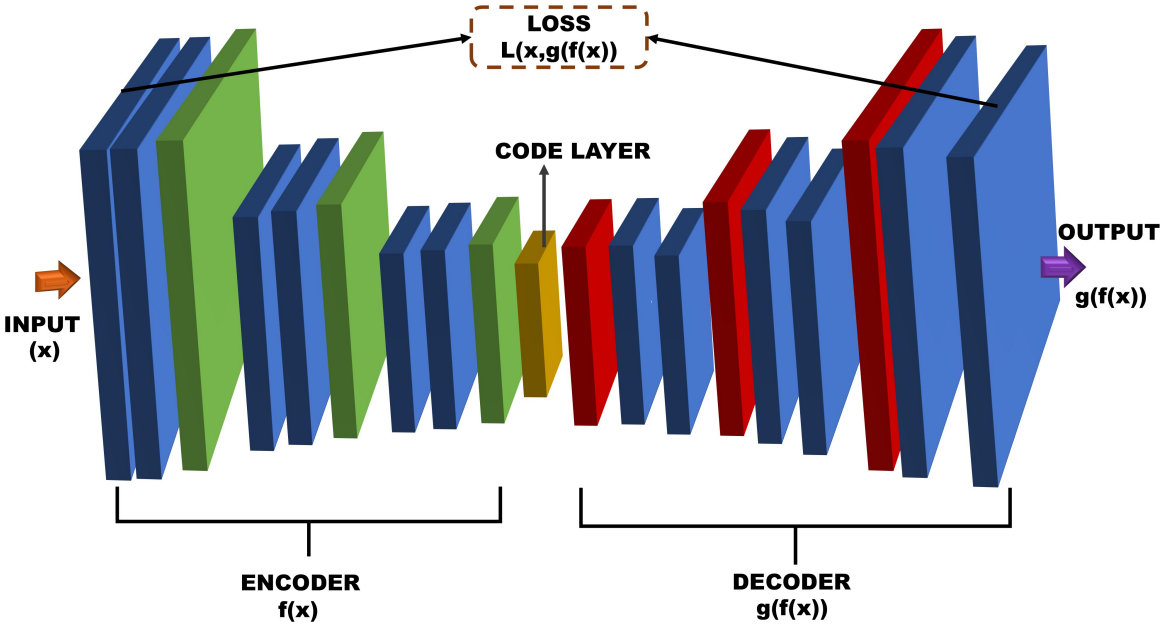

Figure 2.10: *The schematic structure of an autoencoder.*

an undercomplete autoencoder learns to span the same subspace as the PCA. Autoencoders with nonlinear encoder functions f and nonlinear decoder functions g, therefore, have the ability to learn a more powerful nonlinear generalization of PCA. However, an autoencoder trained to perform the copying task may fail to learn anything useful about the dataset if its capacity becomes too large or the code layer has same or greater dimension(overcomplete) than the input. In such cases, even a linear encoder and decoder are capable of simply copying the input to the output, without capturing any meaningful structure or patterns in the data distribution.

Ideally, any autoencoder architecture could be successfully trained by adjusting the code dimension and the capacities of the encoder and decoder according to the complexity of the distribution being modeled. *Regularized autoencoders* make this possible. Unlike constraining model capacity either by shallow encoders and decoders or restricted code sizes, regularized autoencoders define a loss function that enforces additional properties than just that of reproducing input at output. These properties include sparsity in representation, small derivatives in the representation, and robustness with respect to noisy or missing inputs. A regularized autoencoder, even when nonlinear and overcomplete, can still capture meaningful information about the underlying data distribution.

In this thesis, an autoencoder network has been built using the functionalities of Tensorflow [51].

2.2.2.3 K-means clustering

This process iteratively groups data into K clusters, ensuring that the sum of squared distances within each cluster is minimized relative to its centroid. Initially, centroids are randomly placed in the feature space. Then, the distance between each data point and all centroids is computed, and each point is assigned to the cluster of the nearest centroid. The centroids are subsequently updated based on the new cluster assignments. This cycle repeats until the maximum displacement of centroids (O_j, where j denotes centroid indices) between two consecutive iterations falls below a small threshold (ε), i.e., $\max \|O_j^{s+1} - O_j^s\| < \varepsilon$, where s and $s+1$ represent consecutive iterations.

The selection of the number of clusters (K) is critical for achieving meaningful and physically interpretable clustering. To determine the optimal number of clusters (K_{true}), the Knee Method algorithm is employed. This approach involves calculating the sum of squared errors (SSE) for various candidate values of K. Initially, SSE decreases rapidly as K approaches K_{true}, but the rate of decline slows significantly once K_{true} is exceeded. The optimal value of K_{true} is identified by plotting the K-SSE curve and locating the inflection point[52]. Instead of determining this point visually, the kneedle algorithm is applied via KneeLocator[53], which identifies the point of maximum curvature (knee) in the dataset.

In this thesis, K-means clustering has been implemented through scikit-learn[24].

2.3 Ab-initio calculations

A real physical system can be regarded as a system consisting of interacting atoms and molecules, which exist, for instance as isolated species, or as small clusters, or as bulk, in the condensed phase as bulk solids or as surfaces. Regardless of their state, such systems typically consist of heavy, positively charged nuclei and lighter, negatively charged electrons, with their interactions governed by electrostatic Coulomb forces. To accurately describe these systems, a many-body Hamiltonian is required, accounting for interactions among all particles. This Hamiltonian contains terms for the kinetic energy of electrons and nuclei, the potential energy from electron-nucleus interaction, and the potential energy from both electron-electron and nucleus-nucleus interactions. The general form of this many-body Hamiltonian is given by,

$$H = -\sum_{I=1}^{P} \frac{\hbar^2}{2M_I}\nabla_I^2 - \sum_{i=1}^{N} \frac{\hbar^2}{2m_i}\nabla_i^2 + \frac{e^2}{2}\sum_{I=1}^{P}\sum_{J\neq I}^{P} \frac{Z_I Z_J}{|\boldsymbol{R}_I - \boldsymbol{R}_J|} + \frac{e^2}{2}\sum_{i=1}^{N}\sum_{j\neq i}^{N} \frac{1}{|\boldsymbol{r}_i - \boldsymbol{r}_j|} - e^2\sum_{I=1}^{P}\sum_{i=1}^{N} \frac{Z_I}{|\boldsymbol{R}_I - \boldsymbol{r}_i|} \tag{2.3.1}$$

where the ions have Z_I and mass M_I and the electrons have charge e and mass m_i. The first two terms of the Hamiltonian are the kinetic energies of the ions (T_n) and electrons (T_e) respectively. The rest of the terms encapsulate the Coulomb interactions: ion-ion (V_{nn}), electron-electron (V_{ee}) and electron-ion (V_{ne}). The final goal is then to solve the time-independent Schrödinger equation to derive the many-body wave function $\Psi_i(r,R)$.

$$H\Psi_i(\boldsymbol{r},\boldsymbol{R}) = E_i\Psi_i(\boldsymbol{r},\boldsymbol{R}). \tag{2.3.2}$$

Finding an exact analytical solution for Equation (2.3.2) within a fully quantum mechanical framework is challenging, even for a simple system. It happens that barring very simple cases like that of the hydrogen atoms, the many-body nature of the Coulomb interactions and the large numbers of degrees of freedom render the equation non-separable, and an exact solution is not possible. Alternatively, solutions can be attempted via the numerical route. However, it is also practically limited by the presence of a large number of variables (3N) in the wavefunction. D. R. Hartree puts the scenario to perspective in his succinct statement: "The tabulation of a function of one variable requires a page, of two variables a volume, and of three variables a library; but the full specification of a single wave function of neutral Fe is a function of seventy-eight variables. It would be rather crude to restrict to ten the number of values of each variable at which to tabulate this function, but even so, full tabulation of it would require 10^{78} entries, and even if this number could be reduced somewhat from considerations of symmetry, there would still not be enough atoms in the whole solar system to provide the material for printing such a table." Hence, it is evident that to solve this Hamiltonian for real materials, approximations are required at various stages.

The first significant attempt at such an approximation came in 1927, called the *Born-Oppenheimer Approximation(BO)* [54]. This approximation states that since the mass of electrons(m_e) are much lesser than that of the nuclei(M_I), the latter move significantly slower than the electrons, allowing them to be treated as if they are moving in the field of nuclei that appear stationary on the electronic time scale. This approach is known as the adiabatic approximation, which enables the decoupling of electronic and nuclear motion. Consequently, the electronic part of the Hamiltonian can be expressed for a fixed nuclei configuration as follows:

$$H_e = T_e + V_{ee} + V_{ne} + V_{nn}, \tag{2.3.3}$$

The final term in the above expression, V_{nn}, represents a constant resulting from ion-ion interactions, referred to as the Madelung energy, which can be calculated using classical methods. The BO approximation maps the many-body Hamiltonian to a many-electron Hamiltonian. Even with all these simplifications, solving the eigenvalue problem for the

Hamiltonian in Eqn. (2.3.3) is cumbersome considering the electron-electron interactions. When two electrons with the same spin want to exchange their positions, the wave function $\psi(r_i)$ has to change sign under a property called "exchange," originating in the Pauli exclusion principle. Furthermore, every electron interacts with the motion of other electrons-an effect known as "correlation."

To account for these complexities, an independent electron approximation is used. Here, electrons are treated as independent particles moving within the mean field generated by other electrons and the nuclei. Essentially, this maps an interacting electron system onto a non-interacting one that closely mimics the original. This description should be satisfactory in cases where the exchange and correlation effects are not too large.

There are two distinct approaches to the independent electron approximation:

(a) Wave Function-Based Approach: This includes methods such as Hartree[55], Hartree-Fock (HF)[56], and Configuration Interaction (CI) [57].

(b) Density-Based Approach: This is implemented through Kohn-Sham Density Functional Theory (DFT) [58–60].

The primary drawback of wave function-based methods is their high computational cost, which increases exponentially with system size. In contrast, DFT is significantly more computationally efficient, but offers a less detailed description of electron correlation. In this thesis, DFT calculations are performed.

2.3.1 Density Functional Theory

Prior to the development of Hartree's[61] (1928) and Hartree-Fock's[62] (1930) theories, Thomas and Fermi (TF) (1927)[63, 64] introduced a density functional approach for solving many-body problems. They proposed using the electron density of a non-interacting homogeneous electron gas as a fundamental variable. The motivation for this approach is as follows: a system containing$N_e$electrons has a many-body wave function $\Psi(\mathbf{r}_1, \mathbf{r}_2, \ldots, \mathbf{r}_{N_e})$ that depends on $3N_e$variables. In contrast, the corresponding electron density, given by

$$\rho(r) = N \int \Psi^*(r, r_2, \ldots, r_N)\Psi(r_1, r_2, \ldots, r_N)\, dr_2\, dr_3 \ldots dr_N, \tag{2.3.4}$$

depends on only three variables. Here, r_i represents the position vector of the i-th electron. Consequently, working with the full wave function incurs a significant computational cost, whereas using the electron density drastically reduces the complexity due to the lower number of variables.

However, the TF model has several limitations. The expression it provides for kinetic energy is only approximate, and it completely neglects electronic correlation effects. Additionally, it fails to accurately predict atomic bonding. Despite these shortcomings, the TF model laid the groundwork for the development of Density Functional Theory (DFT), which provides a more efficient framework for addressing many-electron problems. Today, DFT remains the most widely used method for electronic structure calculations in condensed matter physics.

2.3.2 Reduced Density Matrices

The following outlines the mathematical formulation underlying the density functional approach. In the ground state, the electron density is defined by

$$\rho(\boldsymbol{r}_1) = N \int \Psi^*(\boldsymbol{r}_1, \boldsymbol{r}_2, ..., \boldsymbol{r}_N)\Psi(\boldsymbol{r}_1, \boldsymbol{r}_2, ..., \boldsymbol{r}_N) d\boldsymbol{r}_2 d\boldsymbol{r}_3 ... d\boldsymbol{r}_N. \tag{2.3.5}$$

where $\Psi(r_1, r_2, ..., r_N)$ is a many-particle wave function. The single-particle electron-ion interaction is written as:

$$\langle V_{ne} \rangle = \langle \Psi | \sum_i v(\mathbf{r}_i) | \Psi \rangle = \int d\mathbf{r}\, v(\mathbf{r})\rho(\mathbf{r}), \tag{2.3.6}$$

where the integration encompasses all space. Similarly, the two-particle electron-electron repulsion can be written as:

$$\langle V_{ee} \rangle = \langle \Psi | \frac{1}{2} \sum_{i,j} \frac{1}{\mathbf{r}_{ij}} | \Psi \rangle = \frac{1}{2} \int d\mathbf{r}_1\, d\mathbf{r}_2\, \frac{\Gamma_2(\mathbf{r}_1, \mathbf{r}_2)}{\mathbf{r}_{12}}, \tag{2.3.7}$$

where $\Gamma_2(\mathbf{r}_1, \mathbf{r}_2)$ is the two-particle density expressing the joint probability of finding an electron in the volume $d\mathbf{r}_1$ at $\mathbf{r}_1$ and another electron in the volume $d\mathbf{r}_2$ at $\mathbf{r}_2$. This can be represented as:

$$\Gamma_2(\mathbf{r}_1, \mathbf{r}_2) = N(N-1) \int \Psi^*(\mathbf{r}_1, \mathbf{r}_2, \ldots, \mathbf{r}_N)\Psi(\mathbf{r}_1, \mathbf{r}_2, \ldots, \mathbf{r}_N)\, d\mathbf{r}_3\, d\mathbf{r}_4 \ldots d\mathbf{r}_N. \tag{2.3.8}$$

The kinetic energy term is:

$$T = -\langle \Psi | \frac{1}{2} \sum_i \nabla_i^2 | \Psi \rangle = -\frac{1}{2} N \int \Psi^*(\mathbf{r}_1, \mathbf{r}_2, \ldots, \mathbf{r}_N) \nabla_1^2 \Psi(\mathbf{r}_1, \mathbf{r}_2, \ldots, \mathbf{r}_N)\, d\mathbf{r}_1\, d\mathbf{r}_2 \ldots d\mathbf{r}_N, \tag{2.3.9}$$

$$= -\frac{1}{2} N \int \left[\nabla_1^2 \Psi^*(\mathbf{r}_1', \mathbf{r}_2, \ldots, \mathbf{r}_N)\Psi(\mathbf{r}_1, \mathbf{r}_2, \ldots, \mathbf{r}_N) \right]_{\mathbf{r}_1 = \mathbf{r}_1'} d\mathbf{r}_1\, d\mathbf{r}_2 \ldots d\mathbf{r}_N, \tag{2.3.10}$$

$$= -\frac{1}{2} \int d\mathbf{r}_1 \left[\nabla_1^2 \gamma(\mathbf{r}_1, \mathbf{r}_1') \right]_{\mathbf{r}_1 = \mathbf{r}_1'}, \tag{2.3.11}$$

where $\gamma(\mathbf{r}_1, \mathbf{r}'_1)$ is the first-order reduced density matrix, defined as:

$$\gamma(\mathbf{r}_1, \mathbf{r}'_1) = N \int \Psi^*(\mathbf{r}'_1, \mathbf{r}_2, \ldots, \mathbf{r}_N)\Psi(\mathbf{r}_1, \mathbf{r}_2, \ldots, \mathbf{r}_N)\, d\mathbf{r}_2\, d\mathbf{r}_3 \ldots d\mathbf{r}_N. \tag{2.3.12}$$

The total energy of the system can be expressed in terms of Reduced Density Matrices (RDMs) using the density matrix formalism:

$$E[\rho, \gamma, \Gamma_2] = T[\gamma(\mathbf{r}_1, \mathbf{r}'_1)] + V_{ne}[\rho(\mathbf{r})] + V_{ee}[\Gamma_2(\mathbf{r}_1, \mathbf{r}_2)], \tag{2.3.13}$$

This formulation enabled the development of a quantum mechanical framework for many-electron systems in reduced space, eliminating the need for the wave function formalism. A key requirement of this approach is to determine the Reduced Density Matrices (RDMs) by minimizing the total energy while adhering to the Pauli exclusion principle. Additionally, it is necessary to verify the existence of an anti-symmetric wave function ψ capable of generating these RDMs. The problem of N representability involves establishing necessary and sufficient conditions for $\gamma(\mathbf{r}_1, \mathbf{r}'_1)$ and $\Gamma_2(\mathbf{r}_1, \mathbf{r}_2)$, which remain incompletely understood. The N-representability condition for the electron density $\rho(\mathbf{r})$ is expressed as :

$$\int \rho(\mathbf{r})\, d\mathbf{r} = N, \quad \rho(\mathbf{r}) \geq 0. \tag{2.3.14}$$

One of the simplest reduced quantities is the single-particle density, which holds significant potential for advancing quantum mechanics within a more streamlined framework.

2.3.3 The Hohenberg-Kohn (HK) Theorems

Density Functional Theory (DFT) is founded on the theorems proposed by Hohenberg and Kohn in 1964[65].

Hohenberg-Kohn Theorem I: A one-to-one correspondence exists between the ground state electron density $\rho(\mathbf{r})$ of a system with N electrons and the external potential $v_{\text{ext}}(\mathbf{r})$ acting on it. This implies that the electron density $\rho(\mathbf{r})$ is uniquely determined for any system of interacting particles under an external potential $v_{\text{ext}}(\mathbf{r})$.

Hohenberg-Kohn Theorem II: There exists a universal functional $E[\rho]$ for the energy, expressed in terms of the electron density $\rho(\mathbf{r})$, which is valid for any external potential. The exact ground state energy of the system, for a given external potential, is obtained as the global minimum of this functional. The electron density that minimizes the functional corresponds to the true ground state density.

Proof of Theorem I

First we consider two external potentials, $v_1(\mathbf{r})$ and $v_2(\mathbf{r})$, which differ only by an additive constant but give the same ground state density $\rho(\mathbf{r})$. Since these potentials are different, they correspond to different Hamiltonians., H_1 and H_2, with corresponding wavefunctions Ψ_1 and Ψ_2. According to the variational principle, no wave function can give an energy lower than that obtained from Ψ_1 for H_1. Thus,

$$E_1 = \langle \Psi_1 | H_1 | \Psi_1 \rangle < \langle \Psi_2 | H_1 | \Psi_2 \rangle.$$

Assuming a non-degenerate ground state and given that both Hamiltonians share the same ground state density, the equation can be rewritten as follows:

$$E_1 < \langle \Psi_2 | H_1 | \Psi_2 \rangle = \langle \Psi_2 | H_2 | \Psi_2 \rangle + \langle \Psi_2 | H_1 - H_2 | \Psi_2 \rangle = E_2 + \int d\mathbf{r}\, \rho(\mathbf{r})[v_1(\mathbf{r}) - v_2(\mathbf{r})].$$

Hence,

$$E_1 < E_2 + \int d\mathbf{r}\, \rho(\mathbf{r})[v_1(\mathbf{r}) - v_2(\mathbf{r})].$$

If we interchange the indices, we get:

$$E_2 < E_1 + \int d\mathbf{r}\, \rho(\mathbf{r})[v_2(\mathbf{r}) - v_1(\mathbf{r})].$$

The addition of these two inequalities gives :

$$E_1 + E_2 < E_2 + E_1,$$

which leads to a contradiction. Therefore, our initial assumption must have been false, that is, a particular $\rho(\mathbf{r})$ corresponds to a unique external potential $v(\mathbf{r})$. As a result, $v(\mathbf{r})$ is decided by $\rho(\mathbf{r})$, which in turn fixes both the Hamiltonian and the wave function. This proves Hohenberg-Kohn's first theorem.

Proof of Theorem II

Since wave function depends on the density, the total energy functional $E_v[\rho]$ for a given external potential $v(\mathbf{r})$ can be expressed as,

$$E_v[\rho] = F[\rho] + \int \rho(\mathbf{r}) v(\mathbf{r})\, d\mathbf{r}, \tag{2.3.15}$$

where,

$$H = T_e + U_{ee} + V_{ne}, \tag{2.3.16}$$

and,

$$F[\rho] = \langle \Psi[\rho] | T_e + U_{ee} | \Psi[\rho] \rangle \tag{2.3.17}$$

where F[ρ] is a universal functional independent of the external potential and with an unknown exact form. The ground state density $\tilde{\rho}$ uniquely defines the ground state energy. Thus,

$$E_v[\tilde{\rho}] = \langle \Psi[\tilde{\rho}]|H|\Psi[\tilde{\rho}]\rangle. \tag{2.3.18}$$

From variational principle, a different density, ρ, would produce higher energy.

$$E_v[\tilde{\rho}] = \langle \Psi[\tilde{\rho}]|H|\Psi[\tilde{\rho}]\rangle < \langle \Psi[\rho]|H|\Psi[\rho]\rangle. \tag{2.3.19}$$

It indicates that by minimizing the total energy functional with respect to the density $\rho(\mathbf{r})$, we should obtain the ground state energy. The density that minimizes the energy is the ground state density. Although the Hohenberg-Kohn theorem is theoretically exact for determining the ground state properties of any system, its main limitation is that we do not know the exact form of the universal functional $F[\rho]$.

2.3.4 Kohn-Sham Formulation

In 1965 Kohn and Sham [59] introduced a formulation that enables the practical application of density functional theory, building on the Hohenberg-Kohn theorem. They mapped the electron density $\rho(\mathbf{r})$ of an interacting N electron system into a system of fictitious non-interacting electrons while maintaining the same electron density as the former. The universal functional $F[\rho]$ for such non-interacting electrons can then be written as,

$$F[\rho(\mathbf{r})] = T_0[\rho(\mathbf{r})] + \frac{e^2}{2}\int\int \frac{\rho(\mathbf{r}_1)\rho(\mathbf{r}_2)}{r_{12}} d\mathbf{r}_1 d\mathbf{r}_2 + E_{\mathrm{XC}}[\rho(\mathbf{r})], \tag{2.3.20}$$

The kinetic energy functional of the interacting electrons is substituted with the kinetic energy of the non-interacting particle system, $T_0[\rho]$. The next term represents the classical electrostatic contribution, often known as the Hartree term. Meanwhile, $E_{XC}[\rho]$, called the exchange-correlation (XC) energy, encompasses all many-body effects, including exchange effects that account for the Pauli exclusion principle and correlation effects that describe electron interactions within the many-body wavefunction. The energy functional can be written as follows:

$$E[\rho] = T_0[\rho(\mathbf{r})] + \int v(\mathbf{r})\rho(\mathbf{r})d\mathbf{r} + \frac{e^2}{2}\int\int \frac{\rho(\mathbf{r}_1)\rho(\mathbf{r}_2)}{r_{12}} d\mathbf{r}_1 d\mathbf{r}_2 + E_{\mathrm{XC}}[\rho(\mathbf{r})]. \tag{2.3.21}$$

$T_0[\rho]$ can be determined by solving the single-particle Schrödinger equation,

$$\left[-\frac{1}{2}\nabla^2 + \lambda(\mathbf{r})\right]\psi_i = \varepsilon_i \psi_i, \tag{2.3.22}$$

A suitable function $\lambda(r)$ leads to the orbitals that give the desired density.

$$\rho(\mathbf{r}) = \sum_i |\psi_i|^2. \tag{2.3.23}$$

The functional is then evaluated as follows:

$$T_0[\rho] = \sum_i \varepsilon_i - \int d\mathbf{r}\lambda(\mathbf{r})\rho(\mathbf{r}). \tag{2.3.24}$$

The energy functional used to determine the equilibrium density then takes the form:,

$$E[\rho] = \sum_i \varepsilon_i - \int d\mathbf{r}\lambda(\mathbf{r})\rho(\mathbf{r}) + \int v(\mathbf{r})\rho(\mathbf{r})d\mathbf{r} + E_{\text{coul}}[\rho] + E_{\text{XC}}[\rho]. \tag{2.3.25}$$

Minimizing we get,

$$\lambda(\mathbf{r}) = v(\mathbf{r}) + \frac{\delta E_{\text{coul}}[\rho]}{\delta\rho(\mathbf{r})} + \frac{\delta E_{\text{XC}}[\rho]}{\delta\rho(\mathbf{r})}, \tag{2.3.26}$$

This demonstrates that choosing $\lambda(r)$ as specified in the above expression results in the correct density derived from the single-particle Schrödinger equation. This leads to a system of N nonlinear integro-differential equations, referred to as the Kohn-Sham (KS) equations. These equations are solved instead of the many-body Schrödinger equation, as follows:

$$\left[-\frac{1}{2}\nabla^2 + v_{\text{eff}}(\mathbf{r};\rho)\right]\psi_i = \varepsilon_i\psi_i, \tag{2.3.27}$$

where the effective potential is given by:

$$v_{\text{eff}}(\mathbf{r}) = v(\mathbf{r}) + \int \frac{\rho(\mathbf{r}')}{|\mathbf{r}-\mathbf{r}'|}d\mathbf{r}' + \frac{\delta E_{\text{XC}}}{\delta\rho(\mathbf{r})} = v(\mathbf{r}) + v_{\text{Hartree}}[\rho(\mathbf{r})] + v_{\text{XC}}[\rho(\mathbf{r})]. \tag{2.3.28}$$

The Kohn-Sham equations are solved iteratively until self-consistency is reached. The procedure can be summarized as follows: Begin with an initial guess ρ_0 to construct the initial Kohn-Sham equation. After solving the eigenvalue problem, a new density is obtained. If the new density differs from the previous one by more than a specified threshold, the next step is to mix the two densities to generate a new one. In the subsequent iteration, the Hamiltonian is determined by this updated density, which then produces the new density for that iteration, and so on. This process is repeated until the densities from two consecutive steps converge to the same solution within an acceptable margin of error. The process is illustrated in Figure 2.11.

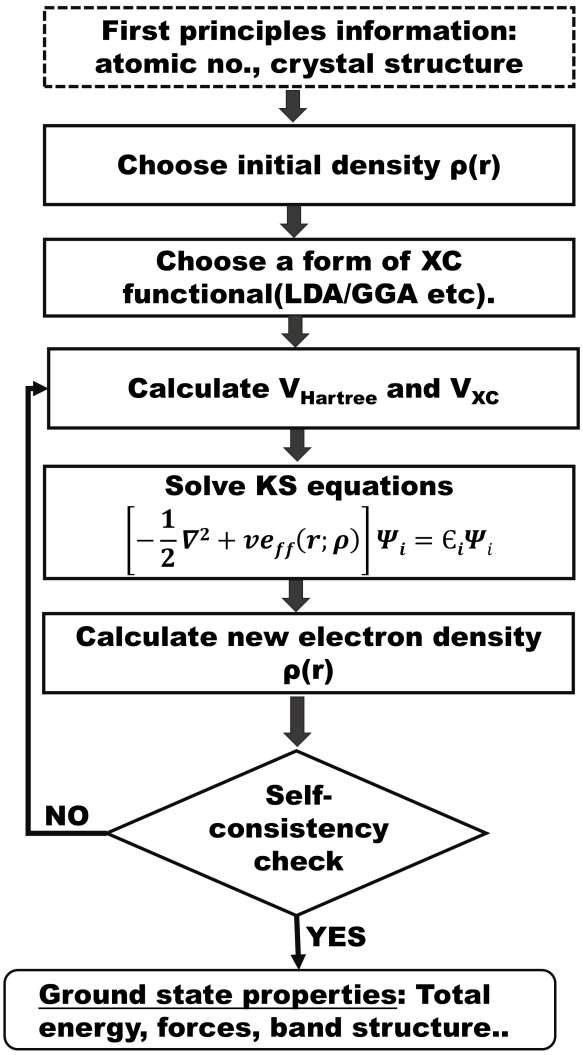

Figure 2.11: *The iterative procedure in Density Functional Theory (DFT) for attaining self-consistency.*

2.3.4.1 Extension to Spin-Polarized Systems

In the case of spin polarization, the electron density is composed of two separate spin densities. It can be expressed as follows:,

$$\rho(\mathbf{r}) = \rho_{\uparrow}(\mathbf{r}) + \rho_{\downarrow}(\mathbf{r}). \tag{2.3.29}$$

Subsequently, the universal energy functional $F[\rho_{\uparrow}, \rho_{\downarrow}]$ incorporates contributions from both spin densities and can be expressed as:

$$F[\rho_{\uparrow}(\mathbf{r}), \rho_{\downarrow}(\mathbf{r})] = T_0[\rho_{\uparrow}, \rho_{\downarrow}] + \frac{e^2}{2}\int\int \frac{\rho(\mathbf{r}_1)\rho(\mathbf{r}_2)}{r_{12}}\, d\mathbf{r}_1\, d\mathbf{r}_2 + E_{\mathrm{XC}}[\rho_{\uparrow}, \rho_{\downarrow}], \tag{2.3.30}$$

where $T_0[\rho_{\uparrow}, \rho_{\downarrow}]$ represents the kinetic energy of the non-interacting spin-polarized elec-

trons, and $E_{\mathrm{XC}}[\rho_\uparrow, \rho_\downarrow]$ is the exchange-correlation energy functional, which now depends on both spin densities.

The total energy functional for the system is then expressed as:

$$E[\rho_\uparrow, \rho_\downarrow] = T_0[\rho_\uparrow, \rho_\downarrow] + \int v(\mathbf{r})\rho(\mathbf{r})\, d\mathbf{r} + \frac{e^2}{2}\int\int \frac{\rho(\mathbf{r}_1)\rho(\mathbf{r}_2)}{r_{12}}\, d\mathbf{r}_1\, d\mathbf{r}_2 + E_{\mathrm{XC}}[\rho_\uparrow, \rho_\downarrow]. \tag{2.3.31}$$

The spin-polarized Kohn-sham equations are:

$$\left[-\frac{1}{2}\nabla^2 + \lambda_\uparrow(\mathbf{r})\right]\psi_{i\uparrow} = \varepsilon_{i\uparrow}\psi_{i\uparrow}, \tag{2.3.32}$$

$$\left[-\frac{1}{2}\nabla^2 + \lambda_\downarrow(\mathbf{r})\right]\psi_{i\downarrow} = \varepsilon_{i\downarrow}\psi_{i\downarrow}. \tag{2.3.33}$$

The spin densities are derived as:

$$\rho_\uparrow(\mathbf{r}) = \sum_i |\psi_{i\uparrow}|^2, \tag{2.3.34}$$

$$\rho_\downarrow(\mathbf{r}) = \sum_i |\psi_{i\downarrow}|^2. \tag{2.3.35}$$

The kinetic energy functional becomes:

$$T_0[\rho_\uparrow, \rho_\downarrow] = \sum_i \varepsilon_{i\uparrow} + \sum_i \varepsilon_{i\downarrow} - \int d\mathbf{r}\left[\lambda_\uparrow(\mathbf{r})\rho_\uparrow(\mathbf{r}) + \lambda_\downarrow(\mathbf{r})\rho_\downarrow(\mathbf{r})\right]. \tag{2.3.36}$$

The energy functional used to determine the equilibrium densities is given by::

$$\begin{aligned} E[\rho_\uparrow, \rho_\downarrow] = &\sum_i \varepsilon_{i\uparrow} + \sum_i \varepsilon_{i\downarrow} - \int d\mathbf{r}\left[\lambda_\uparrow(\mathbf{r})\rho_\uparrow(\mathbf{r}) + \lambda_\downarrow(\mathbf{r})\rho_\downarrow(\mathbf{r})\right] \\ &+ \int v(\mathbf{r})\rho(\mathbf{r})\, d\mathbf{r} + E_{\mathrm{coul}}[\rho] + E_{\mathrm{XC}}[\rho_\uparrow, \rho_\downarrow]. \end{aligned}$$

Minimizing the functional :

$$\lambda_\uparrow(\mathbf{r}) = v(\mathbf{r}) + \frac{\delta E_{\mathrm{coul}}[\rho]}{\delta\rho_\uparrow(\mathbf{r})} + \frac{\delta E_{\mathrm{XC}}[\rho_\uparrow, \rho_\downarrow]}{\delta\rho_\uparrow(\mathbf{r})}, \tag{2.3.37}$$

$$\lambda_\downarrow(\mathbf{r}) = v(\mathbf{r}) + \frac{\delta E_{\mathrm{coul}}[\rho]}{\delta\rho_\downarrow(\mathbf{r})} + \frac{\delta E_{\mathrm{XC}}[\rho_\uparrow, \rho_\downarrow]}{\delta\rho_\downarrow(\mathbf{r})}. \tag{2.3.38}$$

Thus the spin-polarized Kohn-Sham equations are:

$$\left[-\frac{1}{2}\nabla^2 + v_{\text{eff},\uparrow}(\mathbf{r};\rho_\uparrow,\rho_\downarrow)\right]\psi_{i\uparrow} = \varepsilon_{i\uparrow}\psi_{i\uparrow}, \tag{2.3.39}$$

$$\left[-\frac{1}{2}\nabla^2 + v_{\text{eff},\downarrow}(\mathbf{r};\rho_\uparrow,\rho_\downarrow)\right]\psi_{i\downarrow} = \varepsilon_{i\downarrow}\psi_{i\downarrow}. \tag{2.3.40}$$

Here, the effective potentials are in the form:

$$v_{\text{eff},\uparrow}(\mathbf{r}) = v(\mathbf{r}) + \int \frac{\rho(\mathbf{r}')}{|\mathbf{r}-\mathbf{r}'|}\,d\mathbf{r}' + \frac{\delta E_{\text{XC}}}{\delta\rho_\uparrow(\mathbf{r})} = v(\mathbf{r}) + v_{\text{Hartree}}[\rho(\mathbf{r})] + v_{\text{XC},\uparrow}[\rho_\uparrow(\mathbf{r}),\rho_\downarrow(\mathbf{r})], \tag{2.3.41}$$

$$v_{\text{eff},\downarrow}(\mathbf{r}) = v(\mathbf{r}) + \int \frac{\rho(\mathbf{r}')}{|\mathbf{r}-\mathbf{r}'|}\,d\mathbf{r}' + \frac{\delta E_{\text{XC}}}{\delta\rho_\downarrow(\mathbf{r})} = v(\mathbf{r}) + v_{\text{Hartree}}[\rho(\mathbf{r})] + v_{\text{XC},\downarrow}[\rho_\uparrow(\mathbf{r}),\rho_\downarrow(\mathbf{r})]. \tag{2.3.42}$$

The self-consistency procedure for the spin-polarized Kohn-Sham equations follows a similar approach to the non-spin-polarized case, with the key difference being that the spin-up and spin-down densities are handled independently. Initial guesses for $\rho_\uparrow$ and $\rho_\downarrow$ are used to construct the Kohn-Sham equations. These equations are solved iteratively until convergence is reached within a specified tolerance of error.

2.3.5 Exchange-Correlation Functional

Up to this point, Kohn-Sham theory does not rely on any approximations and is, in principle, exact. However, the difficulty lies in the term $E_{XC}[\rho]$, as the exact form of this functional is unknown, necessitating approximations. The Local Density Approximation (LDA) and the Generalized Gradient Approximation (GGA) are commonly used and successful methods for approximating this term.

2.3.5.1 Local Density Approximation (LDA)

This approximation, initially introduced by Kohn and Sham [59], is based on the core principles of Thomas-Fermi-Dirac theory [64, 66]. The central assumption in this approach is that the exchange-correlation energy depends solely on the local electron density $\rho(r)$. The functional form of this approximation can be written as:

$$E_{\text{XC}}^{\text{LDA}} = \int \rho(\mathbf{r})\varepsilon_{\text{XC}}[\rho(\mathbf{r})]\,d\mathbf{r}, \tag{2.3.43}$$

$E_{XC}[\rho(r)]$ represents the exchange-correlation energy density of a homogeneous electron gas with density $\rho(r)$. In the Local Density Approximation (LDA), E_{XC} is determined by

separately adding the contributions from the exchange and correlation parts.

$$\varepsilon_{\mathrm{XC}}^{LDA}[\rho(\mathbf{r})] = \varepsilon_{\mathrm{X}}^{LDA}[\rho(\mathbf{r})] + \varepsilon_{\mathrm{C}}^{LDA}[\rho(\mathbf{r})]. \tag{2.3.44}$$

The exchange part $\varepsilon_X^{\mathrm{LDA}}[\rho]$ is given by the Dirac expression for a uniform electron gas,

$$\varepsilon_X^{\mathrm{LDA}}(\rho) = -\frac{0.458}{r_s} \tag{2.3.45}$$

where r_s is the mean interelectronic distance,

$$\frac{4\pi}{3} r_s^3 = \rho^{-1} \tag{2.3.46}$$

The correlation part is more intricate. E.P. Wigner[67] initially estimated it as:

$$\varepsilon_C^{\mathrm{LDA}} \approx \frac{0.44}{r_s + 7.8} \tag{2.3.47}$$

Later, Ceperley and Alder [68] provided a more precise estimate using quantum Monte Carlo simulations. This is numerically exact and has been parameterized by Perdew and Zunger [69], Vosko, Wilk, and Nusair [70], and John P. Perdew and Yue Wang [71].
In spin-polarized systems, the exchange-correlation (XC) energy density is influenced not only by the electron density ρ but also by the magnetization density ζ, defined as $\zeta = (\rho_\uparrow - \rho_\downarrow)/(\rho_\uparrow + \rho_\downarrow)$. Typically, it is determined by interpolating between the XC energy densities for the fully polarized (ε_{XC}^P) and unpolarized (ε_{XC}^U) cases, using an interpolation function dependent on ζ. Well-established approximations for this interpolation function exist, such as those introduced by Barth and Hedin [72] and Vosko et al. [70].

The Local Density Approximation (LDA) is primarily intended for systems where the electronic charge density varies gradually. However, it surprisingly provides highly accurate results even for inhomogeneous systems, as discussed in the review by R.O. Jones and O. Gunnarsson [73]. Several factors have been proposed to explain this unexpected effectiveness, such as,

- The exchange-correlation (XC) energy is determined solely by the spherical average of the XC hole. The XC energy can be expressed as:

$$E_{XC}[\rho] = -\frac{1}{2} \int \frac{\rho(\mathbf{r})}{R(\mathbf{r})} d\mathbf{r} \tag{2.3.48}$$

where,

$$\frac{1}{R(\mathbf{r})} = \int \frac{\tilde{\rho}_{XC}(\mathbf{r},\mathbf{r}')}{|\mathbf{r}-\mathbf{r}'|}\, d\mathbf{r}' \tag{2.3.49}$$

and $\tilde{\rho}_{XC}$ is the XC-hole, written as the pair correlation function $\tilde{g}(\mathbf{r},\mathbf{r}')$,

$$\tilde{\rho}_{XC}(\mathbf{r},\mathbf{r}') = \rho(\mathbf{r}')[\tilde{g}(\mathbf{r},\ \mathbf{r}') - 1] \tag{2.3.50}$$

- The Local Density Approximation (LDA) adheres to the fundamental sum rule, ensuring that the exchange-correlation (XC) hole adds up to precisely one electron., i.e,

$$\int \tilde{\rho}_{XC}(\mathbf{r},\mathbf{r}')\, d\mathbf{r}' = \int \rho(\mathbf{r})\tilde{g}^{\mathrm{LDA}}(|\mathbf{r}-\mathbf{r}'|,\rho(\mathbf{r}))\, d\mathbf{r}' = -1 \tag{2.3.51}$$

The Local Density Approximation (LDA) performs well in capturing phenomena associated with ion motion, where energy scales are typically around 1 eV. However, it falls short in describing effects that involve much lower energy scales, such as superconductivity, which occurs at energies corresponding to just a few Kelvin.

2.3.5.2 Generalized Gradient Approximation (GGA)

The Generalized Gradient Approximation (GGA) builds upon the Local Density Approximation (LDA) by incorporating both the local electron density $\rho(\mathbf{r})$ and its gradient $\nabla\rho(\mathbf{r})$. By considering spatial variations in the electron density, GGA offers a more precise representation of exchange-correlation effects, leading to improved accuracy in describing real systems.
The energy functional can be expressed as,

$$E_{\mathrm{XC}}^{GGA}[\rho] = \int \varepsilon_{\mathrm{XC}}(\rho(\mathbf{r}),|\nabla\rho(\mathbf{r})|)\rho(\mathbf{r})\, d\mathbf{r} = \int \rho(\mathbf{r})\varepsilon_{\mathrm{XC}}[\rho(\mathbf{r})]F_{\mathrm{XC}}[\rho(\mathbf{r}),\nabla\rho(\mathbf{r})]\, d\mathbf{r} \tag{2.3.52}$$

In the Generalized Gradient Approximation (GGA), the function F_{XC}, known as the enhancement factor, modifies the Local Density Approximation (LDA) expression. Various GGA functionals exist, differing in their choice of enhancement factor. One notable example is the exchange-correlation functional introduced by Perdew and Wang (PW91) in 1991. Later, Perdew, Burke, and Ernzerhof (PBE) developed a simplified version by refining PW91.

GGA improves upon LDA by providing better predictions for properties such as binding energy, total energy, structural parameters, and magnetic behavior in materials. However, it has notable shortcomings, including its inability to capture long-range interactions (following a $1/R^6$ dependence) and a tendency to overestimate electric polarization in polar mate-

rials. Additionally, it struggles with strongly correlated systems, underscoring the necessity for more sophisticated methods to accurately describe electron-electron interactions.

2.3.6 Basis Sets

The selection of a basis set is determined by the specific requirements of a given electronic structure problem. In this thesis, plane wave based method as implemented in Vienna ab initio simulation package (VASP)[74] has been implemented.

2.3.6.1 Plane Wave Basis Method:

In this method, the Kohn-Sham wavefunction is represented as:

$$\psi_{ks}(r) = e^{\mathbf{i.kr}} \sum_{G} C_G(\mathbf{kr}) e^{i\mathbf{G.r}} \tag{2.3.53}$$

where G indicates the reciprocal lattice vector and C_G is the plane wave coefficient on which a normalization condition $\sum_G |C_G(\mathbf{kr})|^2 = 1$ is imposed. Practical implementations require a truncation point which is finite. The cutoff is specified using the plane-wave kinetic energy cutoff, which is defined as:

$$\hbar \frac{|k+G|^2}{2m_e} \leq E_{cut} \tag{2.3.54}$$

Physical quantities are determined only after ensuring convergence with respect to the energy cutoff, ensuring that the results are independent of the chosen cutoff value. The chief advantages of using a plane-wave basis set include:

- The plane-wave basis set does not depend on the positions of atoms or their types.
- Basis set corrections are unnecessary since the forces acting on atoms correspond to the Hellmann-Feynman forces.
- It employs efficient techniques like Fast Fourier Transform (FFT).

A major drawback of this method is the need for a large number of plane waves to precisely describe the wave function near the nucleus, known as the core region. In this area, electrons are strongly bound, causing rapid wave function oscillations due to orthogonality constraints with valence electrons. A common solution is to replace the strong Coulomb potential and core electron effects with an effective potential that influences only the valence electrons, called the pseudopotential, as described in Figure 2.12.

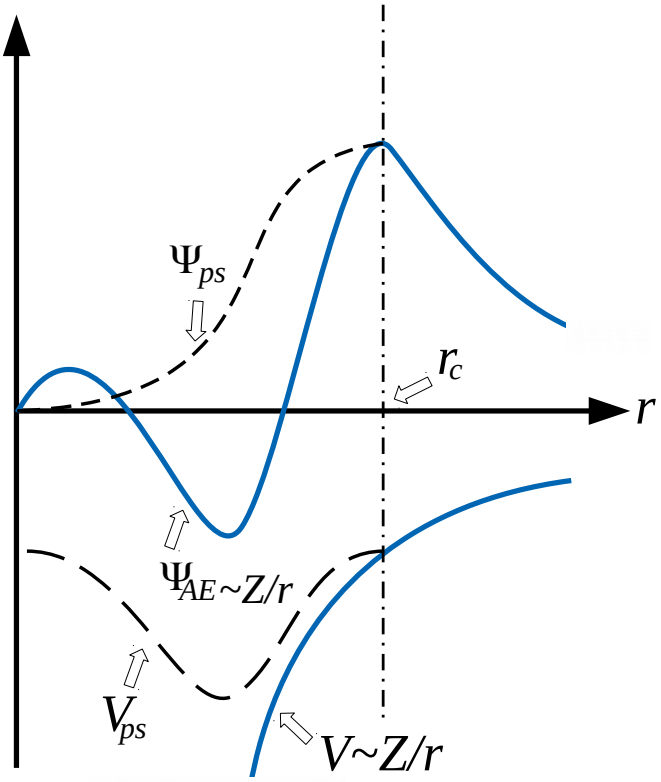

Figure 2.12: *Comparison of all-electron (solid line) and pseudo (dashed line) wavefunctions and potentials. They converge and align beyond the cut-off radius r_c.*

The concept of pseudopotentials can be understood as follows: In the core region, the actual potential is strongly attractive, causing valence electrons to gain kinetic energy due to rapid oscillations, which effectively act as a repulsive potential. Instead of these oscillatory wavefunctions, valence wavefunctions are replaced with smooth, nodeless pseudo wavefunctions within the core region while remaining identical to the actual wavefunction outside it, as illustrated in Figure 2.12. This substitution significantly reduces the number of plane waves needed to represent valence wavefunctions.

Over the past few decades, various methods have been developed to construct more accurate and efficient pseudopotentials (PS). In electronic structure calculations using plane-wave basis sets, three commonly used types of pseudopotentials exist.

- Norm conserving pseudopotential
- Ultrasoft pseudopotential
- Projector augmented wave (PAW) potential

In this thesis, PAW pseudopotentials are utilized for electronic structure calculations, as detailed in the following section.

2.3.6.1.1 The Projector Augmented Wave (PAW) Method

The Projector Augmented Wave (PAW) method, introduced by Blöchl [75], has proven to be computationally efficient, highly transferable, and accurate for electronic structure calculations, enabling density functional theory calculations to be carried out with improved efficiency.

The issue addressed in this method is that the valence wave functions exhibit rapid oscillations near ion cores due to their orthogonality to core states, necessitating many Fourier components for accurate representation. The PAW approach resolves this by applying a linear transformation to convert these oscillatory wave functions into smooth ones, making computations more efficient. In this framework, the all-electron (AE) wave function Ψ_n is obtained from the pseudo wavefunction $\tilde{\Psi}_n$ through a linear transformation:

$$|\Psi_n\rangle = |\tilde{\Psi}_n\rangle + \sum_i (|\phi_i\rangle - |\tilde{\phi}_i\rangle)\langle \tilde{p}_i|\tilde{\Psi}_n\rangle \tag{2.3.55}$$

The index i represents the atomic site at R_i. The all-electron (AE) partial waves ϕ_i are solutions of the radial Schrödinger equation for an isolated atom, while the pseudo (PS) partial waves $\tilde{\phi}_i$ match the AE partial waves outside a core radius r_c. These two wave functions are constructed to have the same value and slope at the boundary r_c.

The projector function p_i, which is localized within the core region, satisfies the orthogonality condition $\langle \tilde{p}_i|\tilde{\phi}_j\rangle = \delta_{ij}$.

The PAW method is commonly used alongside the frozen core approximation, which assumes that core states remain unaffected by their surrounding ionic environment. Additionally, several online repositories provide precomputed atomic PAW data for use in electronic structure calculations.

The PAW method, as implemented in VASP [74, 76], has been used in this thesis.

2.3.7 Ab-initio molecular dynamics

Molecular dynamics (MD) simulations model the time-dependent behavior of systems at the atomic scale. In quantum mechanical molecular dynamics (MD), atomic motion follows Newtonian classical mechanics, while forces are determined using quantum mechanics. A particle that starts at position $\vec{r_0}$ with an initial velocity $\vec{v_0}$ and experiences a force $\vec{F}$ over time t moves to a new position $\vec{r(t)}$ based on the classical physics equation:

$$\vec{r}(t) = \vec{r_0} + \vec{v_0}t + \frac{1}{2}\vec{a}t^2, \quad \vec{a} = \vec{F}/m, \quad \vec{F} = -\frac{dU}{d\vec{r}} \tag{2.3.56}$$

Here, U is the interparticle potential and acceleration is denoted as $\overrightarrow{a}$. the latter is assumed to be constant over the time interval t. However, since acceleration isn't actually constant, this is an approximation that becomes more accurate as the timestep is reduced. Without temperature control, a molecular dynamics simulation functions as a microcanonical ensemble (constant N,V,E). The resulting temperature can be unpredictable and may become very high if the system starts with excessive potential energy due to poor initial geometry. To transition to a canonical ensemble (constant N,V,T), a thermostat algorithm is required to maintain temperature control. Temperature is linked to particle velocities through the equipartition of energy principle.

$$K = \sum_{i=1}^{N} \frac{1}{2} m_i v_i^2 = \frac{3}{2} N k_B T \tag{2.3.57}$$

where K is the total kinetic energy, k_B is the Boltzmann constant and N is the total number of particles. The basic thermostat equation that can be applied at each timestep can be written as :

$$\overrightarrow{v_i}^{scaled} = \sqrt{\frac{T^{desired}}{T}} \overrightarrow{v_i} \tag{2.3.58}$$

However, this crude approach has limitations and a better algorithm, called the Nose-Hoover thermostat, has been implemented in this thesis. This introduces a friction coefficient like term ζ, which accelerates or decelerates particles until desired temperature T is reached. The equation of motion in such a case can be written as:

$$\overrightarrow{v_i}^{scaled} = \frac{\overrightarrow{p_i}}{m_i}, \quad d\overrightarrow{p_i} = (\overrightarrow{F} - \zeta \overrightarrow{p_i})dt, \quad d\zeta = \frac{1}{Q}(\sum_{i=1}^{N} \frac{|\overrightarrow{p_i}|^2}{m_i} - (3N+1)k_B T)dt \tag{2.3.59}$$

where the parameter Q controls the coupling of the heat bath to the system by determining the relaxation of the system's dynamics under the influence of friction.

One possible approach to integrate electronic structure with molecular dynamics to calculate the forces is as follows.

Starting with an initial set of nuclear positions $\overrightarrow{R_1}$,$\overrightarrow{R_2}$....$\overrightarrow{R_N}$, the ground state density $n_0(r)$ and corresponding single particle wavefunctions $\psi_1^{(0)}$,$\psi_2^{(0)}$...$\psi_N^{(0)}$ are found by minimizing the energy functional. Then the forces between nuclei can be expressed in terms of the Hellman-Feynman forces:

$$\overrightarrow{F_I} = -\frac{\partial}{\partial \overrightarrow{R_I}} E[\psi^{(0)}, \overrightarrow{R}] \tag{2.3.60}$$

The calculated forces are subsequently applied in a numerical integration procedure along

with the initial nuclear velocities. A molecular dynamics step is carried out that derives new positions and velocities. The energy functional is again minimized at these new nuclear positions to find a new set of forces, which are subsequently applied for the subsequent MD step. This is repeated until a full trajectory is obtained.

2.4 Force field and classical molecular dynamics

Atomistic simulation allows for the investigation of material behavior at the atomic level through the observation of how atoms interact in a structure. Several phenomena, such as material deformation and defects, require atomic-level precision and a deep understanding of atomic interactions.

The initial step in an atomistic simulation is to build a material structure with a collection of atomic coordinates. In the case of solids, this typically involves creating a crystal lattice and placing atoms at its lattice sites. Then, the simulation needs an energy functional or potential to describe the atomic interactions.

Selecting a potential is one of the greatest challenges. It can be derived from either quantum mechanics or classical dynamics. The quantum method(**see section 2.3.7**) is more accurate as it takes into account the electronic structure of every atom, but it is computationally costly and only feasible for a few atoms. Classical molecular dynamics (MD) is simpler because it substitutes electronic degrees of freedom with an effective potential and forces between nuclei. A rudimentary, empirical potential is the **Lennard-Jones(LJ)** potential that describes the interaction between a pair of neutral atoms or molecules based on their distance. It is especially useful for modeling van der Waals forces and short-range repulsion. The total energy can be written as:

$$E = \sum_i \sum_{j>i} 4\varepsilon \left[\left(\frac{\sigma}{r_{ij}} \right)^{12} - \left(\frac{\sigma}{r_{ij}} \right)^{6} \right] \tag{2.4.1}$$

where ε is the depth of the potential well and σ is the distance at which the potential energy is zero. The **Embedded Atom Method (EAM)** is used for simulating metals and alloys better than LJ-potential. The driving idea is that an atom's energy depends not only on its pairwise interactions but also on the (spherically symmetric) electron density contributed by surrounding atoms. The total energy can be written as :

$$E = \sum_i F_i(\sum_{j \neq i} \rho_j(r_{ij})) + (1/2) \sum_{i<j} \phi_{ij}(r_{ij}) \tag{2.4.2}$$

where F is the embedding energy to place atom i into the electron cloud of neighbors of density ρ,and ϕ is the pair potential interaction. The **Modified Embedded Atom Method (MEAM)** extends EAM by including an explicit three-body term to accommodate directional bonding. The total energy in MEAM is given by:

$$E = \sum_i F_i(\bar{\rho}_i) + (1/2)\sum_{i,j}\phi_{ij}(r_{ij}) \tag{2.4.3}$$

$$\bar{\rho}_i = \sum_{j\neq i}\rho_j(r_{ij}) + 1/2\sum_{j,k\neq i} f_{ij}(r_{ij}) f_{ik}(r_{ik}) g_i(cos\theta_{jik}) \tag{2.4.4}$$

where the functions $\rho_j(r_{ij})$,$\phi_{ij}(r_{ij})$ and F_i are adapted from EAM. The three-body dependence is considered in the local electron density through terms like angular function $g_i(cos\theta_{jik})$ and radial function $f_{ij}(r_{ij})$, where θ_{jik} is the angle between atoms j,i,k centered at i.

Although this approach enables simulations of larger atomic systems, it loses some accuracy because of the lack of detailed electronic structure calculations. Moreover, for several complex classes of materials, feasible potentials are currently unavailable. Thus, compared to the quantum counterpart,albeit being less resource intensive, the classical models lack certain accuracy and adaptability.

Machine learning based methods, in the form of Machine Learning Interatomic Potentials (MLIPs), have recently entered the picture with the aim of solving the aforementioned issues in atomistic simulations. These approaches involve describing the PES as a function of local environment descriptors invariant to rotation,translation, and permutation of homonuclear atoms. Trained over a diverse set of atomic configurations and the corresponding energy, force and stress data obtained from first-principle calculations , MLIPs display remarkable flexibility and accuracy over traditional interatomic potentials, are faster to generate new models, have comparable accuracy to first principle methods and can iteratively reinforce itself. Most importantly, since they use similar platform as utilized in general classical molecular dynamics procedure, they can be employed to simulate large systems and variable temperatures.

In this thesis, a class of MLIP, called the Moment Tensor Potential are generated using the MAML package[77] and atomistic simulations are performed in LAMMPS[78].

2.4.1 Moment Tensor Potential

The Moment Tensor Potential (MTP) is a type of local potential, similar to many other interatomic potentials. To develop this potential, the system's total energy, E^{MTP}, is represented as a sum of individual atomic contributions. Each atom i in a system containing N atoms contributes an energy term, denoted as $V(u_i)$, where u_i represents the local environment of

atom i within a predefined cutoff radius, R_{cut}, as seen in Figure 2.13.

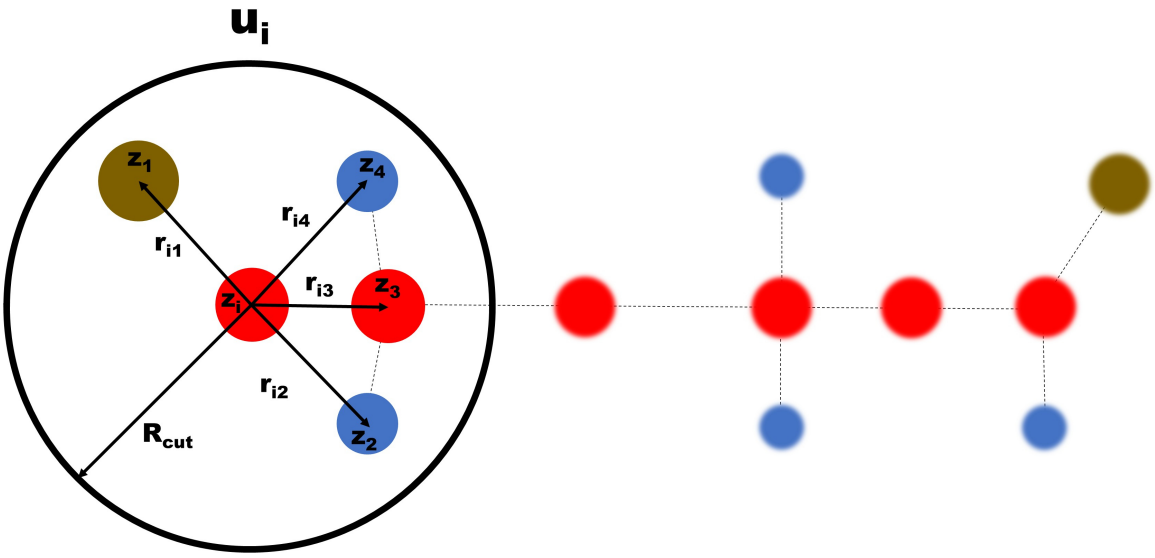

Figure 2.13: *The neighborhood of the ith atom includes only atoms within the cut-off radius R_{cut} that interact with the central atom.*

$$E^{MTP} = \sum_{i=1}^{N} V(u_i) \tag{2.4.5}$$

The neighborhood can be expressed as:

$$u_i = (\{r_{i1}, z_i, z_1\}, ..., \{r_{ij}, z_i, z_j\}, ..., \{r_{iN_{Neigh}}, z_i, z_{N_{Neigh}}\}) \tag{2.4.6}$$

Here, r_{ij} represents the interatomic vectors connecting the central atom to its neighboring atoms. The variables z_i and z_j indicate the types of the central and neighboring atoms, respectively, while N_{neigh} denotes the number of atoms within the defined neighborhood. Each contribution of V to the total energy can be expanded using a set of basis functions, denoted as B_α.

$$V(u_i) = \sum_{n} \eta_\alpha B_\alpha(u_i) \tag{2.4.7}$$

Here, $\eta = \{\eta_\alpha\}$ represents a set of parameters obtained through fitting. The basis functions are constructed from all possible contractions of the moment tensor descriptors, $M_{\mu\nu}$, that result in a scalar quantity [79]. Each of these descriptors is composed of a radial and an angular component, which are defined as follows:

$$M_{\mu\nu}(r_i) = \sum_{j=1}^{N_{Neigh}} f_\mu(|r_{ij}|, z_i, z_j) r_{ij}^{\otimes \nu} \tag{2.4.8}$$

The first component, $f_\mu(|r_{ij}|, z_i, z_j)$, represents the radial part, which depends solely on the distance between atoms i and j as well as their types. This function can be expressed as a combination of radial basis functions, $\phi_\beta(|r_{ij}|)$, each multiplied by a smearing factor to ensure smoothness.

$$f_\mu(|r_{ij}|, z_i, z_j) = \sum_{\beta=1}^{N_Q} c^{(\beta)}_{\mu,z,z_j} \phi_\beta(|r_{ij}|)(R_{cut} - |r_{ij}|)^2 \tag{2.4.9}$$

where the parameters $c = \{c^{(\beta)}_{\mu,z_i,z_j}\}$ represent a set of N_Q radial coefficients that are determined during the training process. The second component encodes the angular characteristics of the local neighborhood n_i. This angular term, represented as $\mathbf{r}_{ij} \bigotimes \cdots \bigotimes \mathbf{r}_{ij}$ (repeated ν times), forms a tensor of rank ν, where $\mathbf{r}_{ij}$ denotes the vector from atom i to atom j. The symbol $\bigotimes$ represents the outer product of these vectors. To construct the basis functions, the *level* of moments is defined as follows:

$$lev(M_{\mu\nu}) = 2 + 4\mu + \nu \tag{2.4.10}$$

The coefficients 2, 4, and 1 mentioned above are fixed, as they have been found to be optimal through various tests [80]. The resulting basis functions are designed to be invariant to rotations, reflections, and atomic permutations. The functional form of the Moment Tensor Potential (MTP) is controlled by two key hyperparameters: N_Q and $\text{lev}_{\max}$. While the number of basis functions and their associated coefficients, η, grows exponentially with $\text{lev}_{\max}$, the number of radial functions, f_μ, increases proportionally to $O(N_Q \,\text{lev}_{\max})$.Therefore, these two hyperparameters should be selected to achieve an optimal balance between accuracy and computational efficiency.

The parameters η and c are optimized by solving a minimization problem.

$$\sum_{k=1}^{K} [w_e(E_k^{AIMD} - E_k^{MTP})^2 + w_f(f_{k,i}^{AIMD} - f_{k,i}^{MTP})^2 + w_s(\sigma_{k,ij}^{AIMD} - \sigma_{k,ij}^{MTP})^2] \to min \tag{2.4.11}$$

Here, K represents the total number of configurations in the training set, while w_e, w_f, and w_s are weighting factors that determine the relative importance of energy, force, and stress in the optimization process. The terms E_k^{AIMD}, $f_{k,i}^{AIMD}$, and $\sigma_{k,ij}^{AIMD}$ correspond to the energies, atomic forces, and stresses obtained from the training set generated using AIMD. Meanwhile, E_k^{MTP}, $f_{k,i}^{MTP}$, and $\sigma_{k,ij}^{MTP}$ are the respective values computed using the trained MTP.

Bibliography

[1] Tom M Mitchell and Tom M Mitchell. Machine learning, volume 1. McGraw-hill New York, 1997.

[2] Jonathan Schmidt, Jingming Shi, Pedro Borlido, Liming Chen, Silvana Botti, and Miguel AL Marques. Predicting the thermodynamic stability of solids combining density functional theory and machine learning. Chemistry of Materials, 29(12):5090–5103, 2017.

[3] Wei Li, Ryan Jacobs, and Dane Morgan. Predicting the thermodynamic stability of perovskite oxides using machine learning models. Computational Materials Science, 150:454–463, 2018.

[4] Xiaolong Zheng, Peng Zheng, and Rui-Zhi Zhang. Machine learning material properties from the periodic table using convolutional neural networks. Chemical science, 9(44):8426–8432, 2018.

[5] Anton O Oliynyk, Erin Antono, Taylor D Sparks, Leila Ghadbeigi, Michael W Gaultois, Bryce Meredig, and Arthur Mar. High-throughput machine-learning-driven synthesis of full-Heusler compounds. Chemistry of Materials, 28(20):7324–7331, 2016.

[6] Prasanna V Balachandran, Benjamin Kowalski, Alp Sehirlioglu, and Turab Lookman. Experimental search for high-temperature ferroelectric perovskites guided by two-step machine learning. Nature communications, 9(1):1668, 2018.

[7] Woon Bae Park, Jiyong Chung, Jaeyoung Jung, Keemin Sohn, Satendra Pal Singh, Myoungho Pyo, Namsoo Shin, and K-S Sohn. Classification of crystal structure using a convolutional neural network. IUCrJ, 4(4):486–494, 2017.

[8] Asma Nouira, Nataliya Sokolovska, and Jean-Claude Crivello. Crystalgan: learning to discover crystallographic structures with generative adversarial networks. arXiv preprint arXiv:1810.11203, 2018.

[9] Ya Zhuo, Aria Mansouri Tehrani, and Jakoah Brgoch. Predicting the band gaps of inorganic solids by machine learning. The journal of physical chemistry letters, 9(7):1668–1673, 2018.

[10] L Weston and C Stampfl. Machine learning the band gap properties of kesterite I 2-II-IV-V 4 quaternary compounds for photovoltaics applications. Physical Review Materials, 2(8):085407, 2018.

[11] Maarten De Jong, Wei Chen, Randy Notestine, Kristin Persson, Gerbrand Ceder, Anubhav Jain, Mark Asta, and Anthony Gamst. A statistical learning framework for materials science: application to elastic moduli of k-nary inorganic polycrystalline compounds. Scientific reports, 6(1):34256, 2016.

[12] Al'ona Furmanchuk, Ankit Agrawal, and Alok Choudhary. Predictive analytics for crystalline materials: bulk modulus. RSC advances, 6(97):95246–95251, 2016.

[13] Aria Mansouri Tehrani, Anton O Oliynyk, Marcus Parry, Zeshan Rizvi, Samantha Couper, Feng Lin, Lowell Miyagi, Taylor D Sparks, and Jakoah Brgoch. Machine learning directed search for ultraincompressible, superhard materials. Journal of the American Chemical Society, 140(31):9844–9853, 2018.

[14] Matthias Rupp, Alexandre Tkatchenko, Klaus-Robert Müller, and O Anatole Von Lilienfeld. Fast and accurate modeling of molecular atomization energies with machine learning. Physical review letters, 108(5):058301, 2012.

[15] J. Ross Quinlan. Learning decision tree classifiers. ACM Computing Surveys (CSUR), 28(1):71–72, 1996.

[16] Ye Yuan, Liji Wu, and Xiangmin Zhang. Gini-impurity index analysis. IEEE Transactions on Information Forensics and Security, 16:3154–3169, 2021.

[17] David G Kleinbaum, K Dietz, M Gail, Mitchel Klein, and Mitchell Klein. Logistic regression. Springer, 2002.

[18] Ian H Witten, Eibe Frank, Leonard E Trigg, Mark A Hall, Geoffrey Holmes, and Sally Jo Cunningham. Weka: Practical machine learning tools and techniques with Java implementations. 1999.

[19] J Ross Quinlan. Improved use of continuous attributes in C4. 5. Journal of artificial intelligence research, 4:77–90, 1996.

[20] Tapio Elomaa and Matti Kaariainen. An analysis of reduced error pruning. Journal of Artificial Intelligence Research, 15:163–187, 2001.

[21] Leo Breiman. Random forests. Machine learning, 45:5–32, 2001.

[22] Robin Genuer, Jean-Michel Poggi, Robin Genuer, and Jean-Michel Poggi. Random forests. Springer, 2020.

[23] Fei Tang and Hemant Ishwaran. Random forest missing data algorithms. Statistical Analysis and Data Mining: The ASA Data Science Journal, 10(6):363–377, 2017.

[24] Fabian Pedregosa, Gaël Varoquaux, Alexandre Gramfort, Vincent Michel, Bertrand

Thirion, Olivier Grisel, Mathieu Blondel, Peter Prettenhofer, Ron Weiss, Vincent Dubourg, et al. Scikit-learn: Machine learning in Python. the Journal of machine Learning research, 12:2825–2830, 2011.

[25] Guillaume Lemaître, Fernando Nogueira, and Christos K. Aridas. Imbalanced-learn: A python toolbox to tackle the curse of imbalanced datasets in machine learning. Journal of Machine Learning Research, 18(17):1–5, 2017.

[26] Andrew R Kitahara and Elizabeth A Holm. Microstructure cluster analysis with transfer learning and unsupervised learning. Integrating Materials and Manufacturing Innovation, 7:148–156, 2018.

[27] C-H Liu, Christopher J Wright, Ran Gu, Sasaank Bandi, Allison Wustrow, Paul K Todd, Daniel O'Nolan, Michelle L Beauvais, James R Neilson, Peter J Chupas, et al. Validation of non-negative matrix factorization for rapid assessment of large sets of atomic pair distribution function data. Applied Crystallography, 54(3):768–775, 2021.

[28] CJ Long, J Hattrick-Simpers, Makoto Murakami, RC Srivastava, Ichiro Takeuchi, Vicky L Karen, and X Li. Rapid structural mapping of ternary metallic alloy systems using the combinatorial approach and cluster analysis. Review of Scientific Instruments, 78(7), 2007.

[29] Chun-houh Chen, Wolfgang Härdle, Antony Unwin, Michael AA Cox, and Trevor F Cox. Multidimensional scaling. Handbook of data visualization, pages 315–347, 2008.

[30] Surya R Kalidindi, Stephen R Niezgoda, and Ayman A Salem. Microstructure informatics using higher-order statistics and efficient data-mining protocols. Jom, 63:34–41, 2011.

[31] Ryan Cohn and Elizabeth Holm. Unsupervised machine learning via transfer learning and k-means clustering to classify materials image data. Integrating Materials and Manufacturing Innovation, 10(2):231–244, 2021.

[32] S Samudrala, K Rajan, and B Ganapathysubramanian. Data dimensionality reduction in materials science. Informatics for Materials Science and Engineering, pages 97–119, 2013.

[33] Yashar Kiarashinejad, Sajjad Abdollahramezani, and Ali Adibi. Deep learning approach based on dimensionality reduction for designing electromagnetic nanostructures. npj Computational Materials, 6(1):12, 2020.

[34] Norbert Huber. A strategy for dimensionality reduction and data analysis applied to

microstructure–property relationships of nanoporous metals. Materials, 14(8):1822, 2021.

[35] Hiroshi Ohno. Uniforming the dimensionality of data with neural networks for materials informatics. Applied Soft Computing, 46:17–25, 2016.

[36] B Roter, N Ninkovic, and SV Dordevic. Clustering superconductors using unsupervised machine learning. Physica C: Superconductivity and its Applications, 598:1354078, 2022.

[37] Matias Nuñez. Exploring materials band structure space with unsupervised machine learning. Computational Materials Science, 158:117–123, 2019.

[38] Nicholas Walker, Ka-Ming Tam, Brian Novak, and M Jarrell. Identifying structural changes with unsupervised machine learning methods. Physical Review E, 98(5):053305, 2018.

[39] Ninad Bhat, Amanda S Barnard, and Nick Birbilis. Unsupervised machine learning discovers classes in aluminium alloys. Royal Society Open Science, 10(2):220360, 2023.

[40] Hideaki Iwasawa, Tetsuro Ueno, Takahiko Masui, and Setsuko Tajima. Unsupervised clustering for identifying spatial inhomogeneity on local electronic structures. npj Quantum Materials, 7(1):24, 2022.

[41] Lei Zhang and Mu He. Unsupervised machine learning for solar cell materials from the literature. Journal of Applied Physics, 131(6), 2022.

[42] Sergei V Kalinin, Ondrej Dyck, Ayana Ghosh, Yongtao Liu, Bobby G Sumpter, and Maxim Ziatdinov. Unsupervised machine learning discovery of structural units and transformation pathways from imaging data. APL Machine Learning, 1(2), 2023.

[43] Xu Zhang, Bin Tang, and Zhen Zhou. Unsupervised machine learning accelerates solid electrolyte discovery. Green Energy & Environment, 6(1):3–4, 2021.

[44] Shulin Luo, Bangyu Xing, Muhammad Faizan, Jiahao Xie, Kun Zhou, Ruoting Zhao, Tianshu Li, Xinjiang Wang, Yuhao Fu, Xin He, et al. Inorganic Crystal Structure Prototype Database Based on Unsupervised Learning of Local Atomic Environments. The Journal of Physical Chemistry A, 126(26):4300–4312, 2022.

[45] Warren S McCulloch and Walter Pitts. A logical calculus of the ideas immanent in nervous activity. The bulletin of mathematical biophysics, 5:115–133, 1943.

[46] Frank Rosenblatt. The perceptron: a probabilistic model for information storage and organization in the brain. Psychological review, 65(6):386, 1958.

[47] Aurélien Géron. Hands-on machine learning with Scikit-Learn, Keras, and TensorFlow: Concepts, to ” O’Reilly Media, Inc.”, 2022.

[48] Eric B Baum. On the capabilities of multilayer perceptrons. Journal of complexity, 4(3):193–215, 1988.

[49] Shun-ichi Amari. Backpropagation and stochastic gradient descent method. Neurocomputing, 5(4-5):185–196, 1993.

[50] David E Rumelhart, Geoffrey E Hinton, and Ronald J Williams. Learning representations by back-propagating errors. nature, 323(6088):533–536, 1986.

[51] Martín Abadi, Ashish Agarwal, Paul Barham, Eugene Brevdo, Zhifeng Chen, Craig Citro, Greg S. Corrado, Andy Davis, Jeffrey Dean, Matthieu Devin, Sanjay Ghemawat, Ian Goodfellow, Andrew Harp, Geoffrey Irving, Michael Isard, Yangqing Jia, Rafal Jozefowicz, Lukasz Kaiser, Manjunath Kudlur, Josh Levenberg, Dandelion Mané, Rajat Monga, Sherry Moore, Derek Murray, Chris Olah, Mike Schuster, Jonathon Shlens, Benoit Steiner, Ilya Sutskever, Kunal Talwar, Paul Tucker, Vincent Vanhoucke, Vijay Vasudevan, Fernanda Viégas, Oriol Vinyals, Pete Warden, Martin Wattenberg, Martin Wicke, Yuan Yu, and Xiaoqiang Zheng. TensorFlow: Large-scale machine learning on heterogeneous systems, 2015. Software available from tensorflow.org.

[52] Dhendra Marutho, Sunarna Hendra Handaka, Ekaprana Wijaya, et al. The determination of cluster number at k-mean using elbow method and purity evaluation on headline news. In 2018 international seminar on application for technology of information and communication, pages 533–538. IEEE, 2018.

[53] Ville Satopaa, Jeannie Albrecht, David Irwin, and Barath Raghavan. Finding a” kneedle” in a haystack: Detecting knee points in system behavior. In 2011 31st international conference on distributed computing systems workshops, pages 166–171. IEEE, 2011.

[54] M. Born and R. Oppenheimer. Zur quantentheorie der molekeln. Annalen der Physik, 389(20):457–484, 1927.

[55] D. R. Hartree. The Wave Mechanics of an Atom with a Non-Coulomb Central Field. Part I. Theory and Methods. Mathematical Proceedings of the Cambridge Philosophical Society, 24(1):89–110, 1928.

[56] C. C. J. Roothaan. New developments in molecular orbital theory. Rev. Mod. Phys., 23:69–89, Apr 1951.

[57] C. David Sherrill. An Introduction to Configuration Interaction Theory. University Science Books, 1995.

[58] P. Hohenberg and W. Kohn. Inhomogeneous electron gas. Phys. Rev., 136:B864–B871, Nov 1964.

[59] W. Kohn and L. J. Sham. Self-consistent equations including exchange and correlation effects. Phys. Rev., 140:A1133–A1138, Nov 1965.

[60] W. Kohn. Nobel lecture: Electronic structure of matter—wave functions and density functionals. Rev. Mod. Phys., 71:1253–1266, Oct 1999.

[61] Douglas Rayne Hartree. The wave mechanics of an atom with a non-coulomb central field. Part II. Some results and discussion. In Mathematical Proceedings of the Cambridge Philosophical Society, volume 24, pages 111–132. Cambridge University Press, 1928.

[62] John C Slater. A simplification of the Hartree-Fock method. Physical review, 81(3):385, 1951.

[63] Llewellyn H Thomas. The calculation of atomic fields. In Mathematical proceedings of the Cambridge philosophical society, volume 23, pages 542–548. Cambridge University Press, 1927.

[64] Enrico Fermi. Un Metodo Statistico per la Determinazione di alcune Proprietà dell'Atomo. Rend. Accad. Naz. Lincei, 6:602–607, 1927.

[65] P Hohenberg and WJPR Kohn. Density functional theory (DFT). Phys. Rev, 136(1964):B864, 1964.

[66] L. H. Thomas. The calculation of atomic fields. Mathematical Proceedings of the Cambridge Philosophical Society, 23(5):542–548, 1927.

[67] Eugene Wigner. On the interaction of electrons in metals. Physical Review, 46(11):1002, 1934.

[68] D. M. Ceperley and B. J. Alder. Ground state of the electron gas by a stochastic method. Phys. Rev. Lett., 45:566–569, Aug 1980.

[69] J. P. Perdew and Alex Zunger. Self-interaction correction to density-functional approximations for many-electron systems. Phys. Rev. B, 23:5048–5079, May 1981.

[70] S. H. Vosko, L. Wilk, and M. Nusair. Accurate spin-dependent electron liquid correlation energies for local spin density calculations: a critical analysis. Canadian Journal of Physics, 59:1200, August 1980.

[71] John P. Perdew and Yue Wang. Accurate and simple analytic representation of the electron-gas correlation energy. Phys. Rev. B, 45:13244–13249, Jun 1992.

[72] U. von Barth and L. Hedin. A local exchange-correlation potential for the spin polarized case. i. Journal of Physics C Solid State Physics, 5(13):1629–1642, July 1972.

[73] R. O. Jones and O. Gunnarsson. The density functional formalism, its applications and prospects. Rev. Mod. Phys., 61:689–746, Jul 1989.

[74] G. Kresse and J. Furthmüller. Efficient iterative schemes for ab initio total-energy calculations using a plane-wave basis set. Phys. Rev. B, 54:11169–11186, Oct 1996.

[75] P. E. Blöchl. Projector augmented-wave method. Phys. Rev. B, 50:17953–17979, Dec 1994.

[76] G. Kresse and J. Hafner. Ab initio molecular dynamics for liquid metals. Phys. Rev. B, 47:558–561, Jan 1993.

[77] Yunxing Zuo, Chi Chen, Xiangguo Li, Zhi Deng, Yiming Chen, Jorg Behler, Gábor Csányi, Alexander V Shapeev, Aidan P Thompson, Mitchell A Wood, et al. Performance and cost assessment of machine learning interatomic potentials. The Journal of Physical Chemistry A, 124(4):731–745, 2020.

[78] Aidan P Thompson, H Metin Aktulga, Richard Berger, Dan S Bolintineanu, W Michael Brown, Paul S Crozier, Pieter J In't Veld, Axel Kohlmeyer, Stan G Moore, Trung Dac Nguyen, et al. LAMMPS-a flexible simulation tool for particle-based materials modeling at the atomic, meso, and continuum scales. Computer Physics Communications, 271:108171, 2022.

[79] Alexander V Shapeev. Moment tensor potentials: A class of systematically improvable interatomic potentials. Multiscale Modeling & Simulation, 14(3):1153–1173, 2016.

[80] Konstantin Gubaev, Evgeny V. Podryabinkin, Gus L.W. Hart, and Alexander V. Shapeev. Accelerating high-throughput searches for new alloys with active learning of interatomic potentials. Computational Materials Science, 156:148–156, 2019.

3

Machine learning classification of binary semiconductor heterostructures

3.1 Introduction and Motivation

Semiconductor heterojunctions are formed by interfacing two different crystalline semiconductors with unequal bandgaps. They have found ubiquitous applications such as light-emitting diodes[1], photovoltaic devices[2], gas sensors[3], etc. When two semiconductor materials with different band gaps are joined, discontinuities arise at the interface between their valence band maxima and conduction band minima. These discontinuities create barriers to electrical transport across the interface. The performance of semiconductor devices critically depends on the band edge discontinuities, also called valence band offsets (VBO) and conduction band offsets (CBO), and the quality of the interface, including its roughness and the absence of defects[4]. The alignment of the bands distinguishes the heterostructures into classes, as introduced in Section 1.1.1.1. In short, in a type-I heterostructure, the band alignment causes the valence and conduction band offsets to have opposite signs. As a result, both the conduction and valence band edges of semiconductor A (the material with the smaller band gap) are positioned within the energy gap of semiconductor B (the material with the larger band gap). In a type-II heterostructure, which includes both type-II staggered and type-II misaligned(sometimes called Type-III) configurations, the conduction and valence band offsets have the same sign. Thus, designing semiconductor heterostructures of a specific type requires careful material selection, which is challenging due to the vast number of possible combinations. Traditional approaches, such as empirical trial-and-

*This chapter is based on publication: Samir Rom[†], **Aishwaryo Ghosh**[†], Anita Halder[†], and Tanusri Saha-Dasgupta, Physical Review Materials 5, 043801 (2021). († These authors contributed equally to this work)

error and first-principles methods, are often costly, time-consuming, and inefficient. On the other hand, machine learning, by leveraging pattern recognition, can significantly reduce the effort required and accelerate the development process. Thus,in this study, we employ a step-by-step approach to predict the type of semiconductor heterostructure by integrating a database-driven materials search with machine learning techniques. Given the vast phase space of potential candidate materials, including elemental, binary, ternary semiconductors, and their alloys, we narrow our focus to heterostructures formed specifically by combining elemental and binary semiconductors.

In an ideal interface, the valence and conduction band offsets are primarily governed by the intrinsic properties of the semiconductors in contact. The band gap difference between the two semiconductors forming the junction establishes the sum of the valence and conduction band offsets. However, determining the relative energy positions of the valence band maximum (VBM) and conduction band minimum (CBM) at the interface, known as "band alignment," is more challenging. Highly accurate methods for calculating band gaps and band alignment include many-body perturbation theory[5], hybrid exchange-correlation functionals[6], time-dependent density functional theory (TDDFT)[7], and quantum Monte Carlo[8] calculations. However, these approaches are computationally expensive compared to conventional density functional theory (DFT) calculations using the local density approximation (LDA) or generalized gradient approximation (GGA) for exchange-correlation. Due to their high computational cost, they are not well-suited for high-throughput calculations. Here, we utilize an existing, digitally accessible electronic-structure database[9] and apply a scissor shift[10] to rigidly adjust conduction bands, ensuring accurate band gap values. Using band-structure information, we compute the branch point energy[11], which serves as a reference for absolute energy levels in band alignment. This approach has been highly successful, as validated against both experimental data and first-principles calculations[11], enabling the rapid screening of a vast number of materials using only electronic-structure data from online databases. To further validate the accuracy of this method in predicting heterostructure types, we compare our results with 31 available experimental data points and perform first-principles calculations on selected heterostructures using hybrid functionals[12].

While our analysis confirms that predicting heterostructure type based on constituent materials is a rational approach, the next step is to develop a machine learning (ML) model using features derived from the band structure of the semiconductors. However, the available dataset of heterostructures with known types is too small for effective ML application. To address this, we employ the Synthetic Minority Oversampling Technique (SMOTE)[13], which not only corrects class imbalance but also expands the dataset to a reasonable size of

78 samples, making it suitable for ML training. Using this expanded dataset, we construct our ML model with the Least Absolute Shrinkage and Selection Operator (LASSO)[14]. Furthermore, extending this approach to nanoscale heterostructures successfully captures some of the available experimental data, demonstrating its broader applicability.

3.2 Heterostructure type prediction using constituent band structures

A complete understanding of the electronic structure of semiconductor heterostructures requires detailed knowledge of the interface, which is often experimentally inaccessible or computationally expensive in high-throughput studies. A more practical approach would be to predict the type of heterostructure solely based on the intrinsic properties of the individual semiconductors: specifically, their band gaps and relative energy alignment. If this approach proves viable, machine learning models can be designed to accurately capture the band-structure properties of individual semiconductors, eliminating the need for complex interface-specific calculations. In order to fix the universal energy level for band alignment without undertaking expensive calculations, in this study the branch point energy(E_{BP}) is used[5, 15, 16], considering negligible interface dipoles. It can be connected to the bulk band structure of a semiconductor as[16]:

$$E_{BP} = \frac{1}{2N_k}\sum_{k}\left(\frac{1}{N_c}\sum_{c_i}^{N_c}\varepsilon_{c_i}(\mathbf{k}) + \frac{1}{2N_v}\sum_{c_i}^{N_v}\varepsilon_{c_v}(\mathbf{k})\right) \tag{3.2.1}$$

Here, N_k represents the number of k-points in the Brillouin zone, while ε_v and ε_c denote the energy eigenvalues of the valence and conduction electrons, respectively. N_c and N_v correspond to the number of conduction and valence bands, respectively. We use bandstructure information from Materials Project[17]. However, the bandstructures obtained are susceptible to the bandgap problem of DFT. To resolve this issue, we resort to a two-pronged approach to calculate a scissor shift, which rigidly shifts the conduction bands to achieve more accurate band gaps. First, given availability, the bandgaps are corrected to experimental values. When such information is not available, the linear bandgap correction, as described in [10], is used. E_{BP} is shifted by half the band-gap correction. The predicted valence band offsets (VBO) and conduction band offsets (CBO) using the proposed scheme show strong agreement with experimentally reported values. The correlation coefficients are 0.98 for VBO and 0.83 for CBO, indicating a high fidelity in the predictions (c.f Figure 3.1). We observe that the valence band offset (VBO) predictions exhibit superior accuracy compared to conduction band offset (CBO) predictions. This is expected, given the inherent

challenges in accurately predicting band gaps.

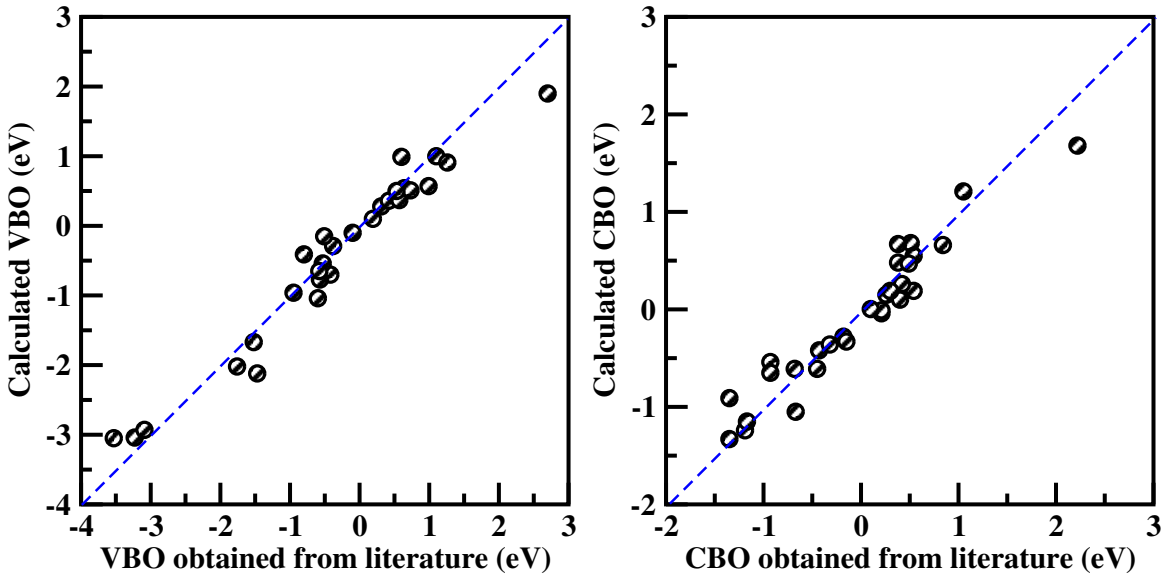

Figure 3.1: *A comparison of valence band offset (VBO) (left) and conduction band offset (CBO) (right) values from the literature with those obtained using corrected DFT band gaps and branch point energy.*

With confidence in our predicted valence band offset (VBO) and conduction band offset (CBO) values derived from the band structures of constituent semiconductors, we proceed to construct a heterostructure heatmap. This heatmap includes all known combinations of elemental and binary semiconductors, categorizing them as either type I or type II heterostructures. Among the 903 possible heterostructures, only 31 have been experimentally realized or studied in detail, with their types known. Our predictions align perfectly with these 31 cases. For the remaining 872 unexplored combinations, our analysis based on band-structure information suggests that approximately 40% (348 cases) are type I, while 60% (524 cases) are type II, highlighted in orange and red, respectively, in Figure 3.2. These findings open new possibilities for designing both types of heterostructures that are yet to be investigated. This exercise further confirms that prediction of the heterostructure type can be made accurately using only the band structure information of the constituent semiconductors. Based on this insight, our machine learning study focuses on developing a predictive model that relies solely on features pertaining to the individual semiconductors.

3.3 Machine Learning

The machine learning workflow in this study follows a systematic approach, as illustrated in Figure 3.3. The key steps include:

- **Dataset Construction:** Collecting known bulk semiconductor heterostructures along

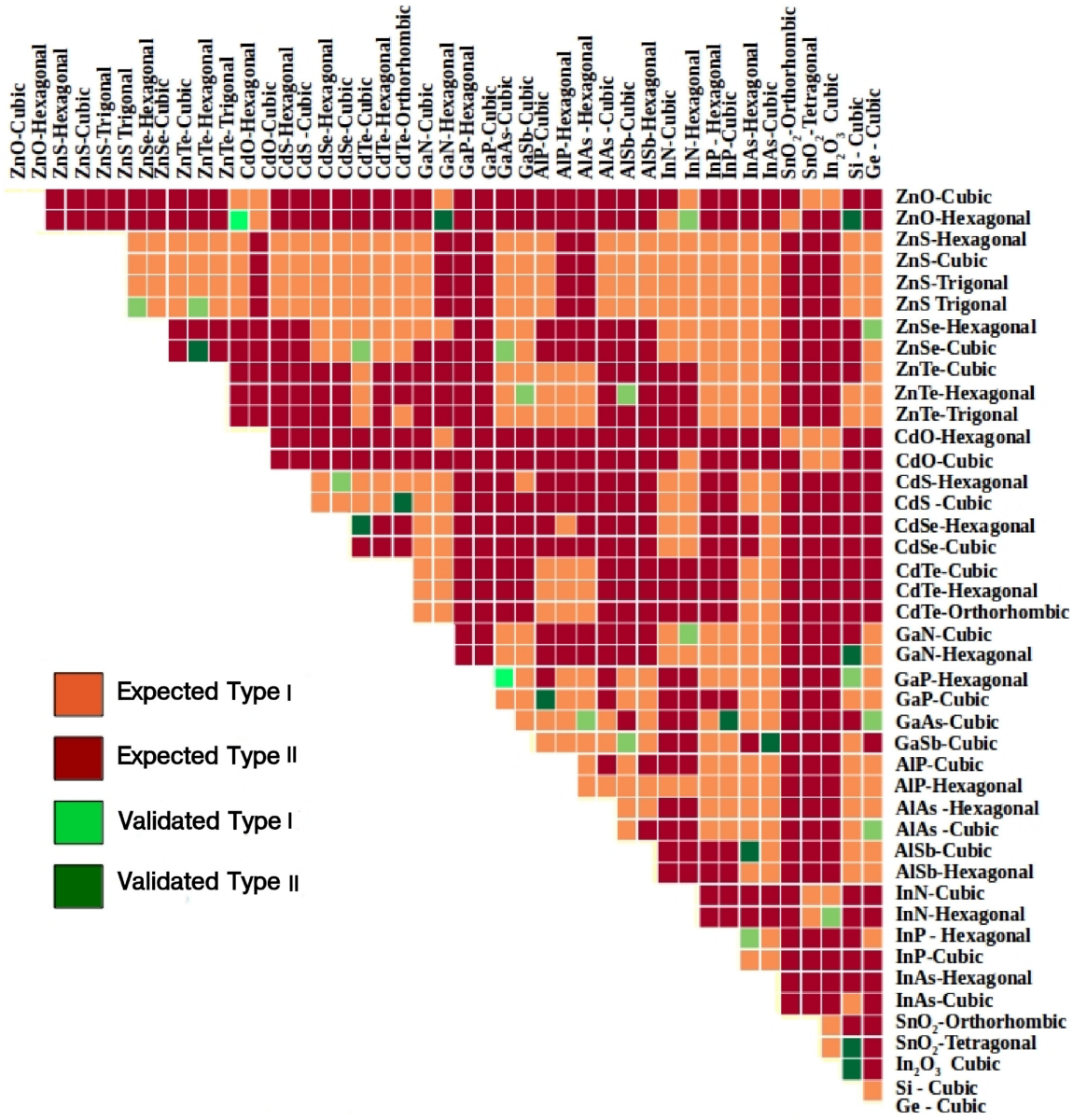

Figure 3.2: *Elemental and binary semiconductor heterostructures classified as type 1 (orange) or type 2 (red) based on the band structure of constituent semiconductors. Heterostructures with experimentally synthesized or theoretically calculated types, validated against the prediction, are shown in light green (type 1) and dark green (type 2).*

with their type classification (Type I or Type II).

- **Dataset Expansion:** Addressing class imbalance by generating synthetic data using a minority oversampling technique.
- **Feature Engineering:** Extracting relevant features from constituent semiconductors.
- **Model Selection:** Evaluating different regression models based on cross-validated error to identify the best performing one.
- **Conversion to Classification:** Transforming the selected regression model into a

binary classification model for distinguishing between Type I and Type II.

- **Heterostructure Type Prediction:** Applying the trained model to predict the type of heterostructures.

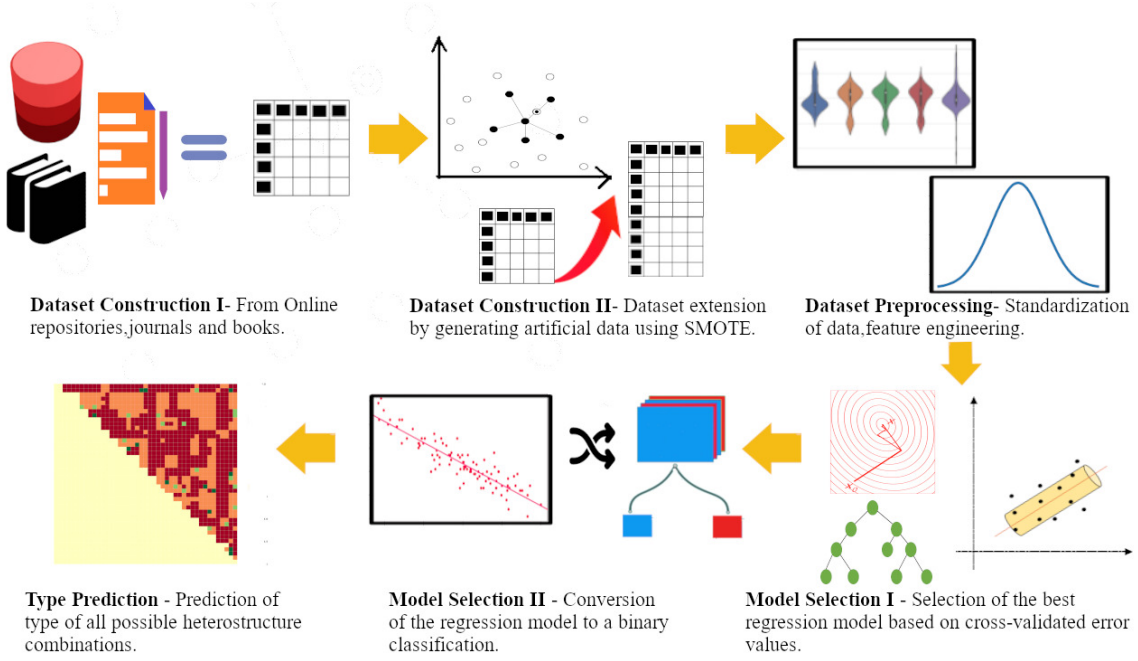

Figure 3.3: *The workflow adapted for the prediction of semiconductor heterostructure type*

3.3.1 Experimental literature on elemental and binary semiconductor heterostructure

An extensive literature review on heterostructures formed by elemental and binary semiconductors, with their types classified, identified a total of 31 known heterostructures: AlP-GaP[18], AlSb-ZnTe[19], GaAs-AlAs[18], GaSb-AlSb[18], Ge-AlAs[20], Ge-GaAs[20], Ge-ZnSe[20], InN-GaN[21], InN-ZnO[22], InP-GaAs[23], InP-InAs[23], Si-GaP[19], ZnSe-GaAs[20], CdS-CdSe[24], CdS-CdTe[24], CdSe-CdTe[24], GaN-Si[25], GaN-ZnO[26], Si-In_2O_3[27], Si-ZnO[28], Si-SnO_2[28], ZnSe-CdTe[29], ZnSe-ZnTe[30], InN-In_2O_3[31], AlN-Si[25], GaN-AlN[16], ZnS-ZnSe[30], ZnS-ZnTe[30], InN-AlN[32], ZnTe-GaSb[19], and AlSb-InAs[33]. AlSb-ZnTe, GaAs-AlAs, GaSb-AlSb, Ge-AlAs, Ge-GaAs, Ge-ZnSe, InN-GaN, InN-ZnO, InP-InAs, Si-GaP, ZnSe-GaAs, CdS-CdSe, ZnSe-CdTe, InN-In_2O_3, AlN-Si, GaN-AlN, ZnS-ZnSe, ZnS-ZnTe, InN-AlN, and ZnTe-GaSb are characterized as type-I heterostructures, the rest being type II.

3.3.2 Synthetic data generation

Our original training dataset, constructed from information found in the literature, consists of only 31 bulk heterostructures, which is too small for machine learning to make meaningful predictions. Additionally, this dataset comprises 20 ($\approx$ 64.5%) type-I heterostructures and 11 ($\approx$ 35.5%) type-II heterostructures, resulting in both a limited dataset size and a significant class imbalance. Thus, using this dataset in this form carries the risk of misclassifying the minority class. To handle this, we employ a minority oversampling technique called SMOTE(see Method section 2.2.1.3 for details). In this study, we use four nearest neighbors, which we found to be the optimal number for our dataset. The quality of the original dataset with 31 data points, as well as the SMOTE-corrected and expanded dataset with 78 data points, is evaluated using a random forest model. The confusion matrix analysis demonstrates a significant improvement in the expanded dataset compared to the original dataset. The false positive and false negative prediction rates for the expanded dataset were reduced to 16%, compared to 42% for the original dataset, as shown in Table 3.1. The enhanced performance of the extended dataset is also reflected in the F1 score, which increased from 0.56 for the original dataset to 0.83 for the expanded dataset.

Table 3.1: *Confusion matrix for the original (expanded) dataset.*

	Type-I predicted	Type-II predicted
Type-I actual	15 (33)	5(7)
Type-II actual	8 (6)	3(32)

3.3.3 Feature Space

Various features have been proposed as predictors for material properties, particularly for band-gap prediction using machine learning. Previous studies have employed different feature spaces and models, achieving varying levels of accuracy. Zhuo et al.[34] used 136 engineered elemental features with a support vector regression (SVR) model trained on 3,896 semiconductors, achieving a root mean square error (RMSE) of 0.45 eV. Lee et al.[35] used 18 features, including elemental properties and low-level DFT results, to train an SVR model on 270 binary and ternary semiconductors, achieving a RMSE of 0.24 eV. Similarly, Weston et al.[36] trained an SVR model on 284 I2-II-IV-VI4 kesterite compounds using 12 elemental features and obtained an RMSE of 0.28 eV.

In the present study, we begin with 12 elemental properties for each of the four elements forming the heterostructure(c.f Table 3.2).

This results in a 48-dimensional feature space, to which the generalized gradient approximation (GGA) band gaps of semiconductor A and B are added, creating a total of 50

Table 3.2: *List of 12 Different Attributes Used in the ML Algorithm*

Sl No	Name of attribute
1	Pauling electronegativity
2	covalent radius
3	atomic number
4	atomic weight
5	melting temperature
6	ionization energy
7	period number
8	number of valence electrons
9	density
10	number of s-electrons
11	number of p-electrons
12	atomic radius

features.

The best features for predicting the valence band offset (VBO) and the conduction band offset (CBO) are analyzed using the violin plots in Figure 3.4. The x-axis represents different features, while the y-axis shows the standardized values and their distributions. Standardized values, derived using the formula $x' = (x - \mu)/\sigma$, where μ is the mean and σ is the standard deviation, allow a direct comparison of characteristics with different scales.

For heterostructures formed by two binary semiconductors, A and B, with elements A1, A2, B1, and B2, we identify the most relevant features by performing linear regression on valence and conduction offsets. Features are ranked by their prediction errors, and the top five features with the lowest errors for both VBO and CBO are highlighted in the figure.

Although the original 50-dimensional feature space performs reasonably well in predicting the magnitude of band offsets using regression techniques, it is inadequate to classify the type of heterostructure. Accurate prediction of heterostructure type requires substantial feature engineering. As an initial approach, we construct differences, means[34], and feature transformations such as exponentiation[37], as previously implemented in similar contexts. However, these do not significantly improve classifier performance. Following the methodology proposed by Weston et al.[36], we expand the feature space by generating polynomial combinations of the original 50 features. Employing third-order polynomial combinations increases the feature count to 23,425, and results in a classification accuracy of 86% that is comparable to accuracy achieved in the indirect-to-direct bandgap classification task reported in[36].

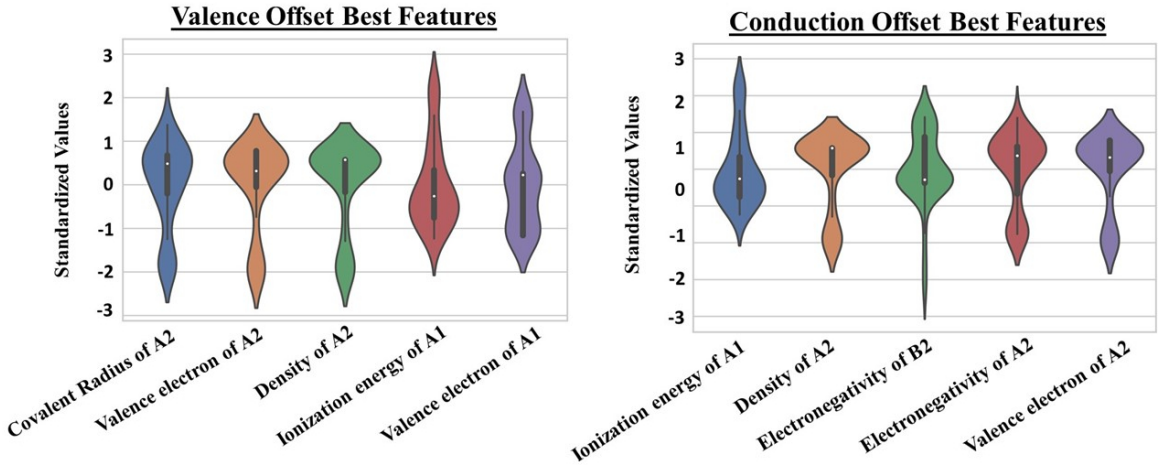

Figure 3.4: *A violin plot illustrating the distributions of the predominant features used for predicting valence band offset (VBO) on the left and conduction band offset (CBO) on the right. The x-axis represents the selected features, while the y-axis shows the standardized values.*

3.3.4 Regression

We use the LASSO algorithm(see Methodology section 2.2.1.2 for details) for the prediction of band offsets in heterostructures. We employ 10-fold cross-validation to evaluate the accuracy of our model. The results indicate a mean absolute error of 0.25 eV for valence band offset (VBO) prediction, while the corresponding error for conduction band offset (CBO) is 0.40 eV. This confirms that predicting the conduction band offset based on the properties of individual semiconductors is more challenging than predicting the valence band offset, as previously observed in Figure 3.1. However, despite this difference in accuracy, the predictions remain reliable enough to effectively distinguish between type I and type II heterostructures. In this context, it is insightful to compare the mean absolute error (MAE) reported in the literature for machine learning models that predict the band gap of single semiconductors. Xie and Grossman[38] reported a band-gap MAE of 0.388 eV. Pilania et al.[39] achieved an MAE of 0.45 eV using multi-fidelity machine learning models for accurate bandgap prediction of solids. Similarly, Gladkikh et al.[40] reported an MAE of 0.5 eV for predicting the band gaps of ABX_3 perovskites based on elemental properties. Compared to these values, our MAE seems to be within an acceptable range.

3.3.5 Classification

Finally, we classify the heterostructure types based on the sign of the predicted offsets. If the predicted valence and conduction band offsets have opposite signs, the classifier predicts a type I heterostructure; if they have the same sign, it predicts type II. Thus, only the signs of the cross-validated predictions matter for classification. Similar classification

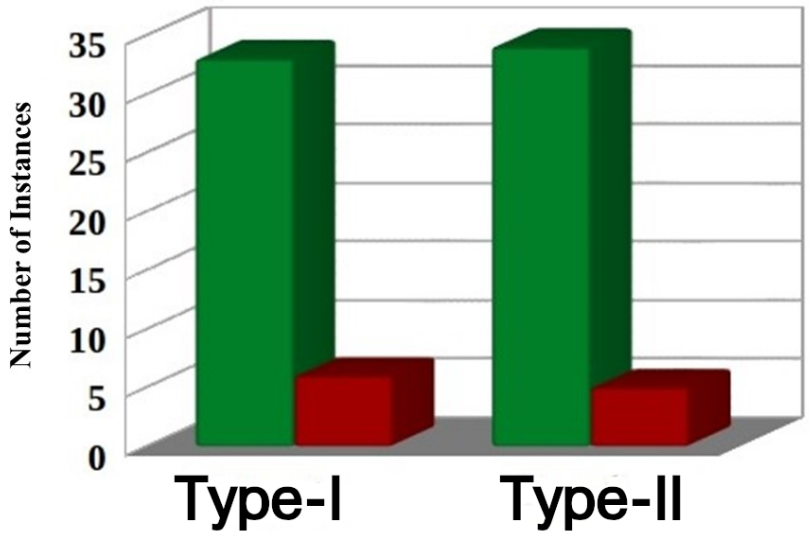

Figure 3.5: *The machine learning classification model for semiconductor heterostructures is validated utilizing an expanded training set of 78 samples. The results of classification are plotted in a bar chart where true positive instances (rightly classified type I) and true negative instances (rightly classified type II) are denoted by green bars. In contrast, misclassified instances are noted with red bars, where false positives are equal to cases incorrectly labeled as type I, and false negatives equal cases mislabeled as type II.*

problems in the literature have been addressed using logistic models. In our case, a logistic model with 10-fold cross-validation correctly predicted 58 instances while misclassifying 20. However, the LASSO model with 10-fold cross-validation showed improved accuracy, correctly predicting 67 out of 78 instances, with 11 misclassified cases(c.f Figure 3.5). Upon analyzing these 11 misclassified cases, we find that five belong to the original dataset, while six are from the synthetic dataset. Only two errors resulted from a sign mismatch in the valence offset, whereas nine were due to sign mismatches in the conduction offset. Notably, in nine of these cases, the misclassification is due to the difficulty in predicting small offset values (approximately 0.2 eV or less).

Using our machine learning model, we predict the types of possible heterostructure combinations, similar to the classification presented in Figure 3.2, but now derived from the machine learning algorithm. Among the 903 possible heterostructures, we observe a perfect match between the machine learning predictions and band alignment-based predictions in 89% of cases. This high level of agreement, as illustrated in Figure 3.6, validates the effectiveness of machine learning as a cost-efficient approach for predicting heterostructure types.

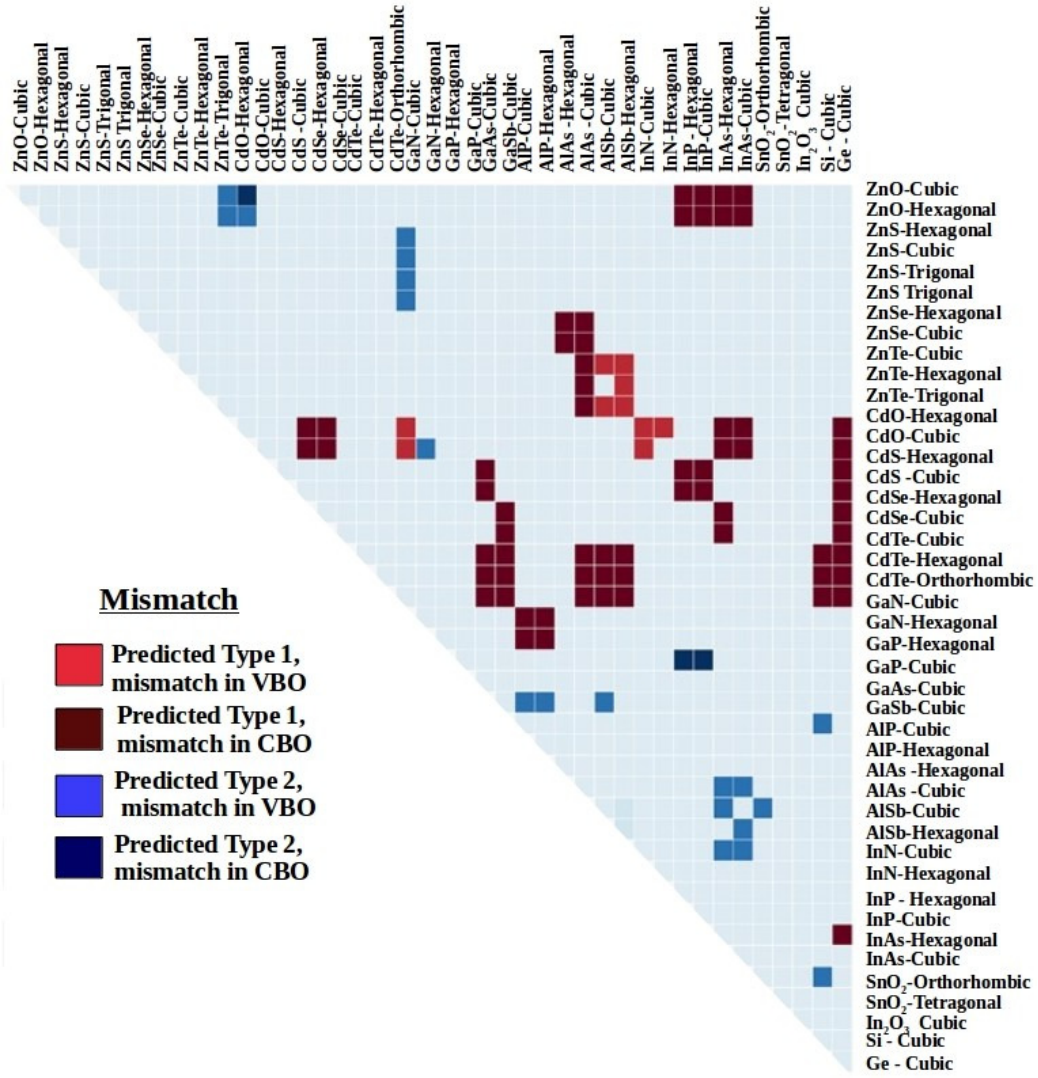

Figure 3.6: *The machine learning (ML)-predicted semiconductor heterostructures. Cases where the ML predictions match the band alignment predictions are shown in cyan. Mismatched cases are categorized into two groups: dark blue/blue for instances where ML predicts type 2 while band alignment predicts type 1, and red/brown for instances where ML predicts type 1 while band alignment predicts type 2.*

3.4 Dependence of heterostructure type on crystal symmetry

We observe that the heterostructure type can depend on the crystal symmetry of the components even for a particular combination of semiconductors. As illustrated in Figure 3.7, three such heterostructure combinations are identified: AlP-GaP, ZnO-GaN, and ZnO-InN.

To validate this hypothesis, first-principles calculations are performed using the Vienna Ab initio Simulation Package (VASP)[41] within the plane-wave basis framework. Due to the significant lattice mismatch between ZnO and InN in both cubic and hexagonal

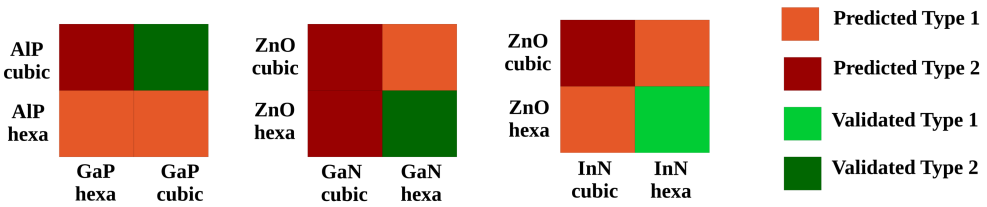

Figure 3.7: *Predicted and known binary semiconductors heterostructure types depending on crystal structure of component semiconductors.*

phases (≈8%), calculations are carried out for heterostructures between cubic-AlP/ZnO and cubic-GaP/GaN, between hexagonal-AlP/ZnO and hexagonal-GaP/GaN, and between cubic-AlP/ZnO and hexagonal-GaP/GaN. To construct the heterostructure models, a five-bilayer (001) surface slab of one semiconductor is stacked on top of a five-bilayer (001) slab of another semiconductor, forming a two-interface system within the computational cell. The slab thickness is selected to preserve bulk atomic properties, ensuring that interfaces are designed to maximize heteropolar bonds. Special attention is given to maintaining bulk-like coordination at interfacial anionic sites. The z-component of atomic coordinates, along with the c-axis lattice constant of the supercells, is allowed to relax to release internal stress. Convergence with respect to cell size is verified by repeating calculations with seven-bilayer (001) surface slabs. The calculations utilize a Monkhorst-Pack k-mesh ranging from 6×6× 2 to 10×10×2, depending on the symmetry (cubic/hexagonal) and heterostructure type (AlP-GaP/ZnO-GaN).

The top panels of Figure 3.8 depict the relaxed AlP/GaP heterostructures, considering both cubic and hexagonal symmetries of the constituent semiconductors. At the interface, only cation-phosphorus bonds are present, with the interfacial four-coordinated P atoms maintaining a bonding environment similar to that found in bulk AlP or GaP. The GGA[42] exchange-correlation functional is used to relax the geometry, while electronic calculations for interface supercells are performed using both the GGA[42] and hybrid HSE06[12] functionals. Interestingly, although the band gap is significantly underestimated in GGA and nearly corrected in HSE06, the heterostructure type remains unchanged regardless of the calculation scheme used.

The bottom panels of Figure 3.8 display the density of states projected onto the AlP and GaP bilayers for cubic-cubic, hexa-hexa, and cubic-hexa relaxed geometries within the GGA-PBE and HSE06 calculation schemes. While the magnitudes of the valence band offset (VBO) and conduction band offset (CBO) vary between the two calculation methods, their signs remain consistent for the cubic-cubic combination. This confirms the experimentally observed type II heterojunction and validates the accuracy of the first-principles calculations. Conversely, for the hexa-hexa combination, the VBO and CBO signs are different

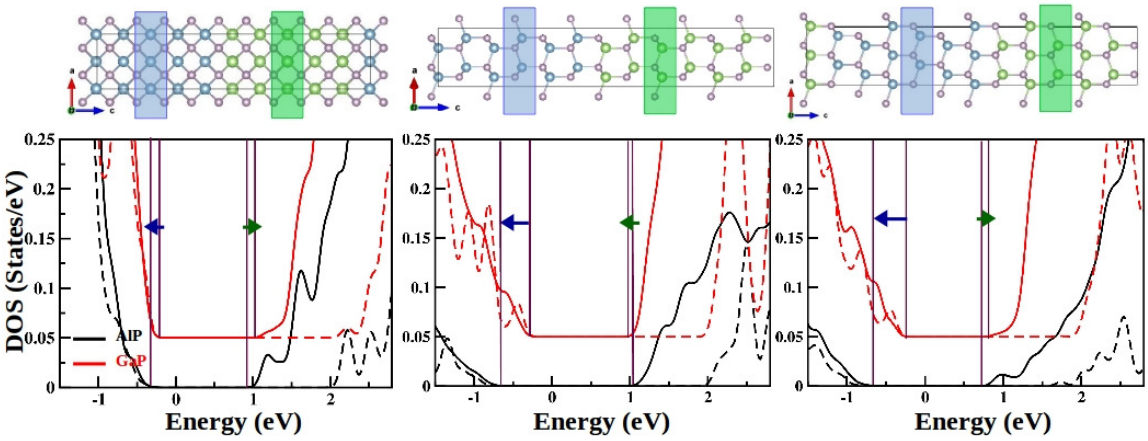

Figure 3.8: *The top panels illustrate the relaxed heterostructure geometries of AlP-GaP in cubic-cubic (left), hexagonal-hexagonal (middle), and cubic-hexagonal (right) crystal structures. In these structures, Al and Ga atoms are depicted as large blue and green spheres, respectively, while P atoms are represented as smaller spheres. The bottom panels present the corresponding density of states (DOS) plots, obtained from two calculation schemes: Generalized Gradient Approximation (GGA) (solid lines) and Hybrid Functional HSE06 (dashed lines). The zero energy level is aligned with the respective Fermi level. The DOS projected onto the AlP and GaP bilayers (highlighted in color in the top panels) is shown in black and red lines, respectively, with an intentional shift for improved visualization. In the GGA calculations, the valence band (VB) and conduction band (CB) edges are indicated by vertical solid lines. Positive and negative offset values are represented by oppositely directed arrows. The offset values in the HSE06 calculations are found to be similar to those in GGA and are omitted for clarity.*

in both GGA-PBE and HSE06 calculations, confirming its type I nature, as predicted by band alignment and machine learning considerations in Figures 3.2 and 3.6. Similarly, the interface between cubic AlP and hexa GaP is identified as type II, again aligning with the predictions.

The results for ZnO-GaN are presented in Figure 3.9, with the top panels displaying the relaxed ZnO/GaN heterostructures in both cubic and hexagonal symmetries of the constituent semiconductors. The bottom panels show the corresponding density of states. Unlike AlP-GaP, which is a common-anion heterostructure, ZnO/GaN does not share a common anion or cation. In principle, two distinct interfaces can form: one where Zn atoms bond to N on one side and O on the other, and another where Ga atoms bond to O on one side and N on the other. For the presented results, Zn bonded to nitrogen interfaces are considered, as they are found to be energetically favorable.

The density of states plots confirm that ZnO-GaN forms a type II heterostructure in both cubic-cubic and hexa-hexa configurations, while the cubic-hexa combination exhibits type I behavior. This aligns perfectly with the predictions.

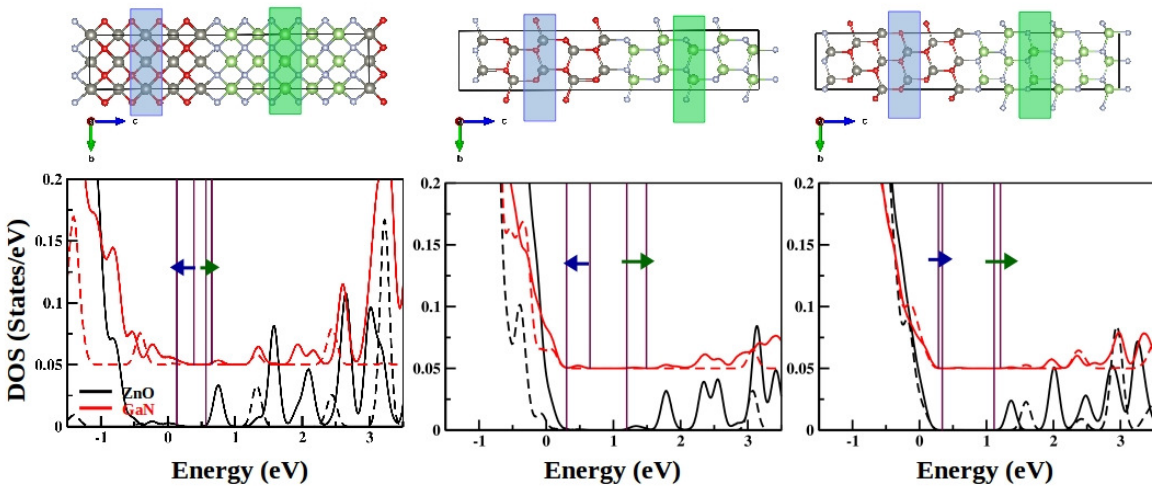

Figure 3.9: *The top panels illustrate the relaxed geometries for cubic-cubic, hexa-hexa, and cubic-hexa configurations of ZnO-GaN, where Zn and Ga atoms are represented as large gray and green spheres, respectively, while O and N atoms appear as smaller spheres. The bottom panels display the density of states (DOS) obtained from two different calculation schemes—Generalized Gradient Approximation (GGA, solid lines) and the hybrid functional HSE06 (dashed lines). The zero-energy reference is set at the respective Fermi level. The DOS projected onto the ZnO and GaN bilayers (shaded regions in the top panels) are shown in black and red, respectively, with a relative shift for better visualization. The valence band (VB) and conduction band (CB) edges from the GGA calculations are indicated by vertical solid lines, with positive and negative offset values marked by oppositely directed arrows. The offset values obtained from the hybrid HSE06 calculations closely resemble those from GGA but are omitted from the figure for clarity.*

It is worth mentioning that to create a smooth interface between cubic and hexagonal systems, the cubic cell is cut along the (111) plane, which exposes a surface with an atomic arrangement resembling hexagonal symmetry. This allows the hexagonal cell to be attached seamlessly. However, the detailed structural parameters reveal key distinctions. In the hexa-hexa configuration, the lattice parameters satisfy a=b≠c, with values of a=b=7.771 Å /6.578 Å and c=38.500 Å/26.400 Å for AlP-GaP and ZnO-GaN, respectively. In contrast for cubic-hexa we get a (6.745 Å/3.274 Å for AlP-GaP/ZnO-GaN) ≠ b (7.788 Å/5.671 Å for AlP-GaP/ZnO- GaN) ≠ c (38.300 Å/31.800 Å for AlP-GaP/ZnO-GaN).

Our study underscores that the heterostructure type can be significantly influenced by the crystal structure of its constituent materials, emphasizing the need for experimental validation.

3.5 Application to nanoscale

We also explore whether our method can be extended to nanoscale heterostructures. Heterostructures composed of two different semiconductor quantum dots (QDs) in a coupled

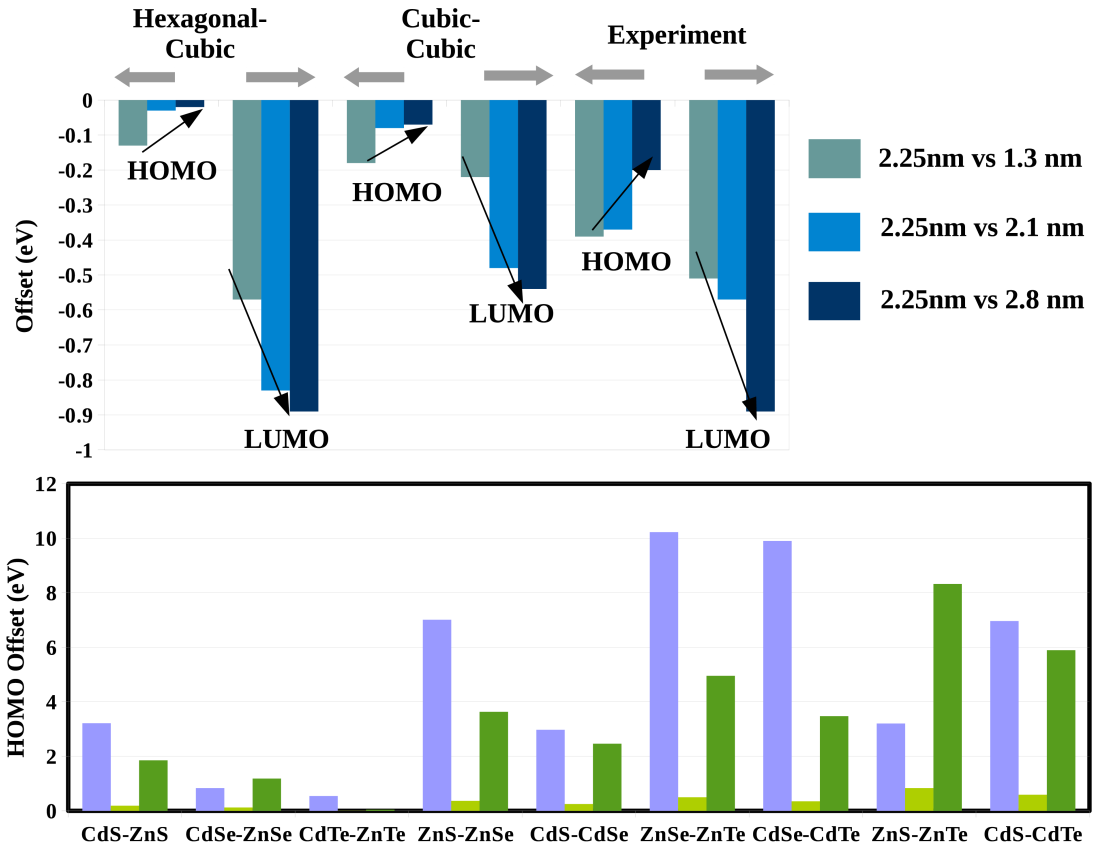

Figure 3.10: *A comparison between predicted and experimentally measured[43] valence (HOMO) and conduction (LUMO) offsets in coupled quantum dots (QDOTs) of 2.5 nm ZnSe and CdS. The results consider varying sizes of CdS QDOTs—1.3 nm, 2.1 nm, and 2.8 nm—marked in different colors for clarity. Predictions account for both cubic and hexagonal crystal symmetries. The bottom panel focuses on the predicted HOMO offset(blue) for common-anion and common-cation II-V $A_{12}B_{12}$ semiconductors. These predictions are compared with computed values from prior studies[44], with the computed offsets scaled by a factor of 10(green).*

quantum dot geometry exhibit band offsets in both the conduction and valence bands. These offsets are primarily dictated by the relative alignment of energy levels between the two QDs. The magnitude of these offsets is strongly influenced by the band gaps of the individual QDs, which, in turn, depend on their sizes.

The available data on nanoscale heterostructures remain extremely limited. A thorough literature search revealed only two relevant prior studies. One experimental study[43] demonstrated that the band offset at the interface of heterostructures could be selectively tuned by adjusting the size of CdS quantum dots (QDs) while keeping ZnSe QDs at a fixed size. This finding highlights the impact of quantum confinement on band alignment.

Additionally, a computational study[44] investigated interfaces between small $A_{12}B_{12}$ nanoclusters composed of 12 cations and 12 anions, where A = Cd/Zn and B = S/Se/Te. These

clusters exhibit a unique structural arrangement, consisting of six-member, four-member, and two-member rings, with 2-bond and 6-bond configurations analyzed in the study. Using energy-resolved first-principles charge density plots, the study computed the offsets in the highest occupied molecular orbital (HOMO) and lowest unoccupied molecular orbital (LUMO), which correspond to the valence band offset (VBO) and conduction band offset (CBO) in bulk materials.

To describe such a situation, we apply the band alignment algorithm, which utilizes bulk band structure information from the Materials Project, corrected by scissor shift and quantum confinement correction. The quantum confinement correction is given by the Brus equation[45]:

$$\Delta E_g = \frac{\hbar^2 \pi^2}{2R^2}\left(\frac{1}{m_e^*} + \frac{1}{m_h^*}\right) \tag{3.5.1}$$

where R gives the nanocrystal radius and m_e^* and $\frac{1}{m_h^*}$ are electron and hole effective masses, respectively, which can be derived from band curvatures at the CBM and VBM, using parabolic fits.

As shown in the top panel of Figure 3.10, even with this approximate approach, the experimental trend of size-dependent conduction band offset (CBO) and valence band offset (VBO) between a 2.25-nm-sized ZnSe quantum dot (QDOT) and CdS QDOTs of sizes 1.3 nm, 2.1 nm, and 2.8 nm is successfully reproduced, provided that the cubic symmetry is chosen for CdS. Experimentally, both ZnSe and CdS QDOTs were observed to exhibit cubic symmetry, aligning well with our predictions.

Predicting the electronic properties of small nanoclusters containing only 24 atoms based on bulk properties presents a significant challenge. A comparison between the energy required to create low-energy excitons, as calculated using Brus's model, and experimental results reveals a marked deviation at radii of approximately 1 nm[46]. Despite this limitation, we conduct a band alignment analysis of AB-coupled quantum dots (QDOTs) for common anion and common cation heterostructures, including CdS-ZnS, CdSe-ZnSe, CdTe-ZnTe, ZnS-ZnSe, CdS-CdSe, ZnSe-ZnTe, CdSe-CdTe, ZnS-ZnTe, and CdS-CdTe, assuming a radius of 0.4 nm and cubic (hexagonal) symmetry for CdTe, ZnS, ZnSe, and ZnTe (CdS and CdSe). While the absolute values of the offsets are found to be off by a factor of 10 compared to first principles calculations on $A_{12}B_{12}$ nanoclusters, the overall trend of valence band offsets (HOMO offsets) is successfully reproduced. Specifically, a decrease in HOMO offset is observed when transitioning from 3p (S) to 4p (Se) to 5p (Te) in common anion systems, while an increase in valence band offset (VBO) is noted between 4d (Cd) and 3d (Zn) in common cation systems. This consistency with expected chemical trends

highlights the applicability of this approximate scheme in capturing essential electronic property variations in nanoscale heterostructures.

To evaluate the applicability of machine learning (ML) in predicting nanoscale heterostructures, we expand our dataset by applying the Synthetic Minority Over-sampling Technique (SMOTE). Initially, the dataset consists of 31 bulk heterostructures and five nanoscale heterostructures, with two of the nanoscale heterostructures classified as type I and three as type II. To enhance the dataset with synthetic data, we incorporate two additional features representing the quantum confinement correction terms for semiconductors A and B. The application of SMOTE results in an expanded dataset of 78 heterostructures, with 57 (approximately 73.08%) belonging to the bulk category and 21 (approximately 26.92%) classified as nanoscale heterostructures. Within this dataset, 38 (approximately 48.71%) are type I heterostructures, while 40 (approximately 51.28%) are type II. The performance of the ML model improves significantly, with the F1 score increasing from 0.58 in the original dataset (36 heterostructures) to 0.83 in the SMOTE-corrected dataset (78 heterostructures), demonstrating the effectiveness of SMOTE in balancing the dataset. With the inclusion of nanoscale heterostructures, the mean absolute error (MAE) values are recorded as 0.29 eV for the CBO and 0.49 eV for the VBO. The ML classification model achieves an overall accuracy of 82% across the 78 instances. The slight decrease in accuracy compared to that of the bulk-only dataset is attributed to the limited availability of nanoscale heterostructure data in the existing literature, which restricted the size and diversity of the training dataset.

3.6 Summary and Discussion

The design of heterostructures of a specific type, achieved by combining two semiconductors with comparable lattice constants but varying band gaps, is a crucial area in the semiconductor industry. This process inherently involves materials engineering, which can follow two main approaches: an experimental route that demands significant costs and efforts in synthesis and characterization or a computational path relying on first-principles calculations. The latter approach requires large simulation cells containing tens to hundreds of atoms and necessitates accurate numerical schemes that go beyond conventional density functional theory (DFT)[47, 48]. In this study, we propose and demonstrate that machine learning can serve as a viable alternative to material selection in semiconductor heterostructure design with a targeted heterostructure type. While machine learning approaches have been previously applied for band-gap prediction of semiconductors, to the best of our knowledge, no prior study has focused on predicting heterostructure types, which presents a greater challenge. By validating our approach on a few synthesized bulk semiconductor heterostructures with known classifications, we extend our predictions to a

large set of 872 bulk semiconductor heterostructures that have either not yet been synthesized or remain uncharacterized in terms of their heterostructure type. These predictions reveal an intriguing insight: the crystal structure of the constituent semiconductors plays a crucial role in determining whether a heterostructure adopts a type I or type II configuration. A key limitation in the selection of semiconductor heterostructure materials is the requirement of lattice matching, as coherent growth requires minimal lattice mismatch to allow epitaxial deposition of one material on another[49]. However, alternative techniques such as heteroepitaxy[50], mechanical-thermal direct bonding[51], and grafting[52] have been explored to enable the formation of lattice-mismatched heterostructures. In particular, successful lattice mismatch heterostructures have been experimentally realized for systems like Ge/Si, Si/GaAs, GaAs/GaN, and Si/GaN, despite lattice mismatches of 4.2%, 4.9%, 77.1%, and 70.2%, respectively. Among the 872 yet-to-be-synthesized heterostructures predicted in this study, 139 cases exhibit a lattice mismatch of less than 2%, while 466 cases show a mismatch within 6%, making their experimental realization highly probable. Furthermore, the promising performance of our machine learning scheme in predicting nanoscale semiconductor heterostructures strengthens the case for its broader applicability.

Bibliography

[1] Ricky W Chuang, Rong-Xun Wu, Li-Wen Lai, and Ching-Ting Lee. ZnO-on-GaN heterojunction light-emitting diode grown by vapor cooling condensation technique. Applied physics letters, 91(23), 2007.

[2] Sanjay K Behura, Chen Wang, Yu Wen, and Vikas Berry. Graphene–semiconductor heterojunction sheds light on emerging photovoltaics. Nature Photonics, 13(5):312–318, 2019.

[3] Karin Potje-Kamloth. Semiconductor junction gas sensors. Chemical reviews, 108(2):367–399, 2008.

[4] John Robertson. High dielectric constant gate oxides for metal oxide Si transistors. Reports on progress in Physics, 69(2):327, 2005.

[5] Yoyo Hinuma, Andreas Grüneis, Georg Kresse, and Fumiyasu Oba. Band alignment of semiconductors from density-functional theory and many-body perturbation theory. Physical Review B, 90(15):155405, 2014.

[6] Jochen Heyd, Juan E Peralta, Gustavo E Scuseria, and Richard L Martin. Energy band gaps and lattice parameters evaluated with the Heyd-Scuseria-Ernzerhof screened hybrid functional. The Journal of chemical physics, 123(17), 2005.

[7] Dahvyd Wing, Jonah B Haber, Roy Noff, Bradford Barker, David A Egger, Ashwin Ramasubramaniam, Steven G Louie, Jeffrey B Neaton, and Leeor Kronik. Comparing time-dependent density functional theory with many-body perturbation theory for semiconductors: Screened range-separated hybrids and the GW plus Bethe-Salpeter approach. Physical Review Materials, 3(6):064603, 2019.

[8] Yubo Yang, Vitaly Gorelov, Carlo Pierleoni, David M Ceperley, and Markus Holzmann. Electronic band gaps from quantum Monte Carlo methods. Physical Review B, 101(8):085115, 2020.

[9] Anubhav Jain, Geoffroy Hautier, Charles J Moore, Shyue Ping Ong, Christopher C Fischer, Tim Mueller, Kristin A Persson, and Gerbrand Ceder. A high-throughput infrastructure for density functional theory calculations. Computational Materials Science, 50(8):2295–2310, 2011.

[10] Wahyu Setyawan, Romain M Gaume, Stephanie Lam, Robert S Feigelson, and Stefano Curtarolo. High-throughput combinatorial database of electronic band structures for inorganic scintillator materials. ACS combinatorial science, 13(4):382–390, 2011.

[11] Ethan P Shapera and André Schleife. Database-driven materials selection for semiconductor heterojunction design. Advanced Theory and Simulations, 1(10):1800075, 2018.

[12] GE Heyd. Scuseria, and M. Ernzerhof. J. Chem. Phys, 118(18):8207, 2003.

[13] Nitesh V Chawla, Kevin W Bowyer, Lawrence O Hall, and W Philip Kegelmeyer. SMOTE: synthetic minority over-sampling technique. Journal of artificial intelligence research, 16:321–357, 2002.

[14] Robert Tibshirani. Regression shrinkage and selection via the lasso. Journal of the Royal Statistical Society. Series B (Methodological), 58(1):267–288, 1996.

[15] Jerry Tersoff. Theory of semiconductor heterojunctions: The role of quantum dipoles. Physical Review B, 30(8):4874, 1984.

[16] André Schleife, Frank Fuchs, Claudia Rödl, Jürgen Furthmüller, and Friedhelm Bechstedt. Branch-point energies and band discontinuities of III-nitrides and III-/II-oxides from quasiparticle band-structure calculations. Applied Physics Letters, 94(1), 2009.

[17] Anubhav Jain, Shyue Ping Ong, Geoffroy Hautier, Wei Chen, William Davidson Richards, Stephen Dacek, Shreyas Cholia, Dan Gunter, David Skinner, Gerbrand Ceder, et al. Commentary: The Materials Project: A materials genome approach to accelerating materials innovation. APL materials, 1(1), 2013.

[18] Amita Wadehra, Jeremy W Nicklas, and John W Wilkins. Band offsets of semiconductor heterostructures: A hybrid density functional study. Applied Physics Letters, 97(9), 2010.

[19] ET Yu, MC Phillips, DH Chow, DA Collins, MW Wang, JO McCaldin, and TC McGill. Interfacial reactions and band offsets in the AlSb/GaSb/ZnTe material system. Physical Review B, 46(20):13379, 1992.

[20] Karim Steiner, Wei Chen, and Alfredo Pasquarello. Band offsets of lattice-matched semiconductor heterojunctions through hybrid functionals and G 0 W 0. Physical Review B, 89(20):205309, 2014.

[21] Basanta Roul, Mahesh Kumar, Mohana K Rajpalke, Thirumaleshwara N Bhat, and SB Krupanidhi. Binary group III-nitride based heterostructures: band offsets and transport properties. Journal of Physics D: Applied Physics, 48(42):423001, 2015.

[22] AL Yang, HP Song, HY Wei, XL Liu, J Wang, XQ Lv, P Jin, SY Yang, QS Zhu, and ZG Wang. Measurement of polar C-plane and nonpolar A-plane InN/ZnO hetero-

junctions band offsets by x-ray photoelectron spectroscopy. Applied Physics Letters, 94(16), 2009.

[23] JR Waldrop, RW Grant, and EA Kraut. GaAs/InP and InAs/InP heterojunction band offsets measured by x-ray photoemission spectroscopy. Journal of Vacuum Science & Technology B: Microelectronics Processing and Phenomena, 7(4):815–819, 1989.

[24] Su-Huai Wei, SB Zhang, and Alex Zunger. First-principles calculation of band offsets, optical bowings, and defects in CdS, CdSe, CdTe, and their alloys. Journal of applied Physics, 87(3):1304–1311, 2000.

[25] Sean W King, Robert J Nemanich, and Robert F Davis. Band alignment at AlN/Si (111) and (001) interfaces. Journal of Applied Physics, 118(4), 2015.

[26] Chen Chen, Mitra Dutta, and Michael A Stroscio. Confined and interface phonon modes in GaN/ZnO heterostructures. Journal of applied physics, 95(5):2540–2546, 2004.

[27] B Höffling, A Schleife, C Rödl, and F Bechstedt. Band discontinuities at Si-TCO interfaces from quasiparticle calculations: Comparison of two alignment approaches. Physical Review B—Condensed Matter and Materials Physics, 85(3):035305, 2012.

[28] B Höffling, A Schleife, F Fuchs, C Rödl, and F Bechstedt. Band lineup between silicon and transparent conducting oxides. Applied Physics Letters, 97(3), 2010.

[29] Andrew M Smith, Aaron M Mohs, and Shuming Nie. Tuning the optical and electronic properties of colloidal nanocrystals by lattice strain. Nature nanotechnology, 4(1):56–63, 2009.

[30] Su-Huai Wei and Alex Zunger. Band offsets and optical bowings of chalcopyrites and Zn-based II-VI alloys. Journal of Applied Physics, 78(6):3846–3856, 1995.

[31] HP Song, AL Yang, HY Wei, Y Guo, B Zhang, GL Zheng, SY Yang, XL Liu, QS Zhu, ZG Wang, et al. Determination of wurtzite InN/cubic In2O3 heterojunction band offset by x-ray photoelectron spectroscopy. Applied Physics Letters, 94(22), 2009.

[32] G Martin, S Strite, A Botchkarev, A Agarwal, A Rockett, H Morkoc, WRL Lambrecht, and B Segall. Valence-band discontinuity between GaN and AlN measured by x-ray photoemission spectroscopy. Applied physics letters, 65(5):610–612, 1994.

[33] Herbert Kroemer. The 6.1 A family (InAs, GaSb, AlSb) and its heterostructures: a selective review. Physica E: Low-dimensional Systems and Nanostructures, 20(3-4):196–203, 2004.

[34] Ya Zhuo, Aria Mansouri Tehrani, and Jakoah Brgoch. Predicting the band gaps of inorganic solids by machine learning. The journal of physical chemistry letters, 9(7):1668–1673, 2018.

[35] Joohwi Lee, Atsuto Seko, Kazuki Shitara, Keita Nakayama, and Isao Tanaka. Prediction model of band gap for inorganic compounds by combination of density functional theory calculations and machine learning techniques. Physical Review B, 93(11):115104, 2016.

[36] L Weston and C Stampfl. Machine learning the band gap properties of kesterite I 2-II-IV-V 4 quaternary compounds for photovoltaics applications. Physical Review Materials, 2(8):085407, 2018.

[37] Narendra Kumar, Padmini Rajagopalan, Praveen Pankajakshan, Arnab Bhattacharyya, Suchismita Sanyal, Janakiraman Balachandran, and Umesh V Waghmare. Machine learning constrained with dimensional analysis and scaling laws: simple, transferable, and interpretable models of materials from small datasets. Chemistry of Materials, 31(2):314–321, 2018.

[38] Tian Xie and Jeffrey C Grossman. Crystal graph convolutional neural networks for an accurate and interpretable prediction of material properties. Physical review letters, 120(14):145301, 2018.

[39] Ghanshyam Pilania, James E Gubernatis, and Turab Lookman. Multi-fidelity machine learning models for accurate bandgap predictions of solids. Computational Materials Science, 129:156–163, 2017.

[40] Vladislav Gladkikh, Dong Yeon Kim, Amir Hajibabaei, Atanu Jana, Chang Woo Myung, and Kwang S Kim. Machine learning for predicting the band gaps of ABX3 perovskites from elemental properties. The Journal of Physical Chemistry C, 124(16):8905–8918, 2020.

[41] Georg Kresse and Jürgen Hafner. Ab initio molecular dynamics for liquid metals. Physical review B, 47(1):558, 1993.

[42] John P Perdew, K Burke, and MJPRL Ernzerhof. Perdew, burke, and ernzerhof reply. Physical Review Letters, 80(4):891, 1998.

[43] Amit Dalui, Arup Chakraborty, Umamahesh Thupakula, Ali Hossain Khan, Sucheta Sengupta, Biswarup Satpati, DD Sarma, Indra Dasgupta, and Somobrata Acharya. Chemical Tailoring of Band Offsets at the Interface of ZnSe–CdS Heterostructures for Delocalized Photoexcited Charge Carriers. The Journal of Physical Chemistry C, 120(19):10118–10128, 2016.

[44] A. Chakraborty, Ph.D. thesis, Calcutta University, 2019.

[45] Louis Brus. Electronic wave functions in semiconductor clusters: experiment and theory. The Journal of Physical Chemistry, 90(12):2555–2560, 1986.

[46] Tadd Kippeny, Laura A Swafford, and Sandra J Rosenthal. Semiconductor nanocrystals: a powerful visual aid for introducing the particle in a box. Journal of Chemical Education, 79(9):1094, 2002.

[47] A Seidl. A. G orling, P. Vogl, JA Majewski, and M. Levy. Phys. Rev. B, 53:3764, 1996.

[48] Lucas K Wagner and David M Ceperley. Discovering correlated fermions using quantum Monte Carlo. Reports on Progress in Physics, 79(9):094501, 2016.

[49] Zh I Alferov, VM Andreyev, VI Korol'Kov, and EL Portnoi. Preparation and Investigation of Epitaxial Layers of AlxGa1-xAs solid Solutions and of Heterojunctions in the AlAs-GaAs system. Kristall und Technik, 4(4):495–503, 1969.

[50] Y Chen and J Washburn. Structural transition in large-lattice-mismatch heteroepitaxy. Physical review letters, 77(19):4046, 1996.

[51] A Black, AR Hawkins, NM Margalit, DI Babic, AL Holmes, Y-L Chang, P Abraham, John E Bowers, and EL Hu. Wafer fusion: materials issues and device results. IEEE Journal of selected topics in quantum electronics, 3(3):943–951, 1997.

[52] Dong Liu, Sang June Cho, Jung-Hun Seo, Kwangeun Kim, Munho Kim, Jian Shi, Xin Yin, Wonsik Choi, Chen Zhang, Jisoo Kim, et al. Lattice-mismatched semiconductor heterostructures. arXiv preprint arXiv:1812.10225, 2018.

4

Understanding the Trend in Core-Shell Preferences for Bimetallic Nanoclusters: A Machine Learning Approach

4.1 Introduction and Motivation

Bimetallic nanoclusters, composed of atoms of two different metallic elements, can generally have three structural patterns(see section 1.1.2.3.2) - core-shell, Janus and mixed(c.f Figure 4.1(A) for schematic representation). Nanoclusters in which one metal core is relatively enriched by the shell of the other form a core–shell structure. In Janus morphology, two types of atoms are segregated to two sides of the cluster, while in mixed alloys the different atoms are randomly distributed. Bimetallic nanoclusters are significant due to their enhanced catalytic[1], biomedical[2–4], magnetic[5], and optical[6] properties compared to their monometallic counterparts. Despite their significant technological relevance, a complete microscopic understanding necessary for the effective design of nanoalloys in core–shell morphology remains elusive. Key factors often cited include cohesive energy, surface energy, atomic radii, and electronegativity. Previously, a database of surface-segregation energy for a single impurity on an FCC lattice using density functional theory (DFT) was established[7]which have been used to explain qualitative trends in the segregation behavior of bulk binary alloys, although segregation energy is expected to vary with temperature and composition. Building on this approach, Wang and Johnson[8] investigated a database of segregation energy (SE) for single-atom binary alloys in small nanopar-

This chapter is based on publication: **Aishwaryo Ghosh**, Soumendu Datta, and Tanusri Saha-Dasgupta, Journal of Physical Chemistry C 126.15 (2022).

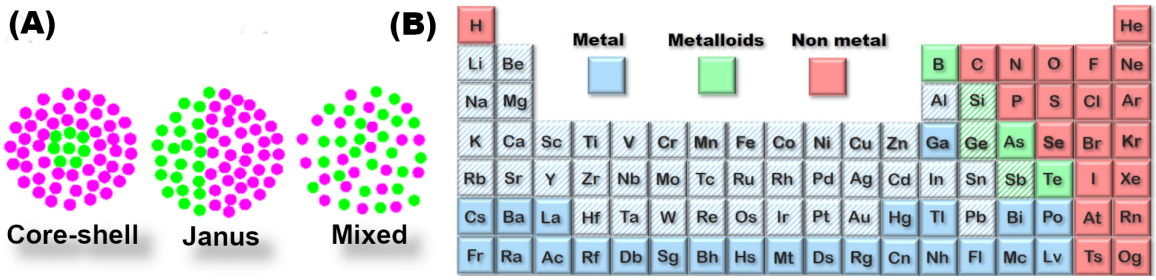

Figure 4.1: *(A) Possible arrangements of A (magenta) and B (green) metals in a binary alloyed nanocluster, featuring core–shell, Janus, and mixed structural patterns. (B) A periodic table highlighting metals, metalloids, and nonmetals, with the metal/metalloid elements considered in this study shown as hashed.*

ticles of late transition metals, emphasizing the roles of cohesive energy and Wigner–Seitz radii. More recently, the segregation behavior of single-atom binary alloys comprising 12 late transition metals has been studied[9] using DFT, highlighting the influence of magnetism, correlation, and strain. A classical simulation study involving Monte Carlo (MC) molecular dynamics (MD) of 47 binary metallic clusters, modeled using embedded atom potentials, has been used to analyze core–shell preferences[10]. Principal component analysis of the MC-MD data identified cohesive energy difference and Wigner–Seitz difference as two primary factors. However, since this study relied on a classical force field, it could not account for the effects of magnetism or spin–orbit interactions[11], which are particularly relevant for heavy metals. Given the backdrop of various theoretical studies, it is crucial to identify which proposed factors play the most significant role in determining core–shell preferences. If multiple factors contribute, what is their relative importance? Does this importance vary depending on the type of metal? Addressing this requires extending the investigation beyond the late transition metal series, unlike most previous studies. With the rise of machine learning (ML) as a powerful tool for pattern recognition, the problem of core–shell preferences in bimetallic nanoclusters can ideally be analyzed within an ML framework[12]. However, a major challenge lies in the limited number of experimentally synthesized binary nanoclusters with well-defined chemical ordering, as well as the small number of core–shell combinations studied theoretically.

Hence, the present study employs DFT calculations to determine segregation energy (SE) for single-atom alloys. DFT calculated SE is a good estimation for single-atom alloys, since a MC-MD study previously demonstrated[10] that finite temperature and composition effects do not significantly alter the general trends observed at $T = 0$ K. Moreover, the same study[10] found that small nanoclusters offer the cleanest systems in terms of core and shell purity, justifying our choice of a 55-atoms system. A diverse set of binary metallic combinations is considered, including alkali, alkaline, basic, transition metal (TM), and p-block metals (cf Figure 4.1(B)), resulting in a dataset of 903 binary combinations. Using

this large dataset, the key attributes influencing core–shell morphology are then analyzed through machine learning-based statistical modeling. A machine learning model is developed to classify core–shell structures into two types: type 1 (where A is in the core and B in the shell, with A having a lower atomic number than B) and type 2 (where B is in the core and A in the shell). The workflow is schematically shown in Figure 4.3. The key findings are:

- Four key factors emerge as primary controlling factors of these structural patterns: cohesive energy difference, atomic radius difference, magnetic nature of the elements, and coordination number difference in their bulk phase.
- Given that the dataset included a comprehensive range of elements—alkali, alkaline, transition metal (TM), basic, and p-block metals—further analysis are carried out to identify the driving factors within specific subsets: alkali/alkaline–alkali/alkaline, TM–TM, and alkali/alkaline–TM combinations. However, the small sample sizes of basic and p-block metals prevent a similar analysis for these groups. Interestingly, the relative importance of the key factors varies across different subsets.
- Additionally, binary combinations that did not exhibit a clear core–shell preference based on DFT-calculated segregation energy (SE) are examined further. In these cases, two alternative structural patterns are identified: mixed alloy clusters and side-segregated Janus structures. The general trend indicates that a small cohesive energy difference between constituents favors a mixed structure, whereas a large cohesive energy difference leads to the formation of a Janus structure rather than a core–shell arrangement.

4.2 Computational Methodology

The Random Forest classification algorithm(see Methodology section 2.2.1.1 for details) is used in this work for performing the classification problem. The class imbalance in the learning set is handled by a synthetic minority oversampling method, SMOTE(see Methodology section 2.2.1.3 for details).

We employ first-principles calculations using the plane-wave basis set combined with projector-augmented-wave (PAW) potentials, as implemented in the Vienna Ab initio Simulation Package (VASP) [13, 14]. The generalized gradient approximation (GGA) is used to describe the exchange-correlation functional. For cluster calculations, a simple cubic supercell with a side length of 25 Å is used, along with periodic boundary conditions. Two neighboring clusters are separated by approximately 15 Å of vacuum space. Reciprocal

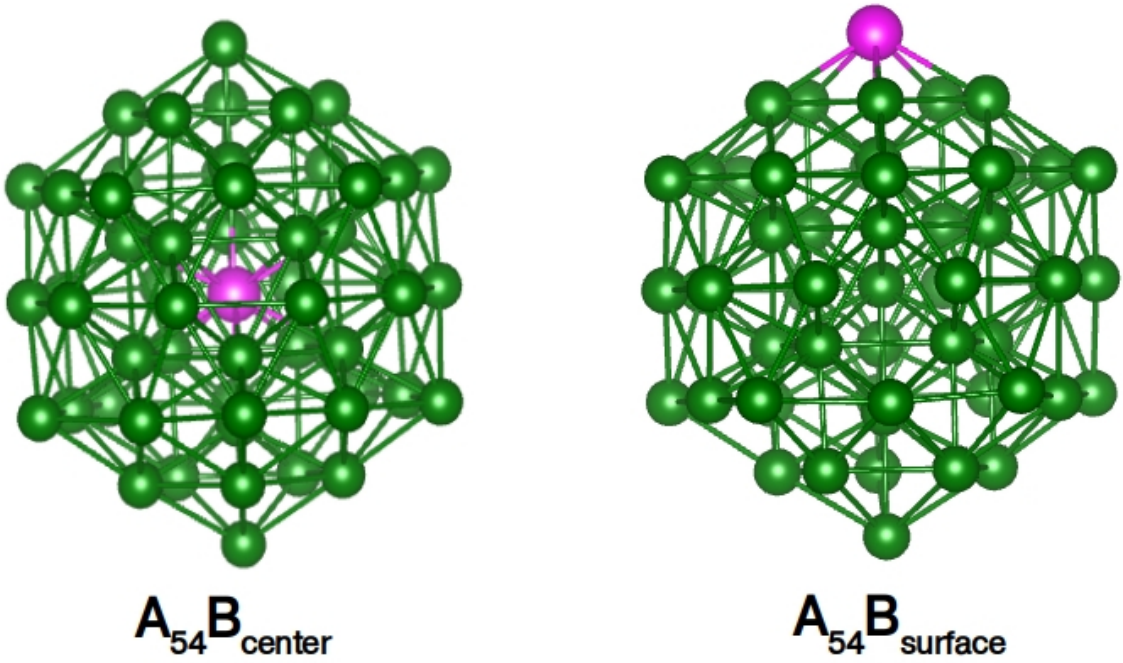

Figure 4.2: *Single impurity structure in a $A_{54}B$ cluster with B at surface and center.*

space integrations take place at the Γ-point. During structural optimization, all atoms undergo relaxation. In each optimized structure, the maximum force component on any atom remains below 0.02 eV/Å.

For the mixed versus Janus relative stability study, a 50:50 composition is chosen to eliminate any composition effects. $A_{28}B_{27}$ composition represents the closest possible 50:50 ratio for a cluster size of 55 atoms in an icosahedral structure. The initial side-segregated Janus configuration is created by filling one-half of the icosahedron with A atoms and the other-half with B atoms. In contrast, the initial mixed alloy structure features a random distribution of the two atomic species. This distribution is achieved by selecting each atom and assigning it as either an A or B type element randomly.

4.3 Results

4.3.1 DFT segregation energy

To analyze the segregation trend between two atomic species at the nanoscale, we consider an icosahedral cluster consisting of 55 A atoms, with substitution by a B atom at either the central site, referred to as $A_{54}B_{center}$, or a surface site, referred to as $A_{54}B_{surface}$(c.f Figure 4.2). It is important to note that the optimized icosahedral structure may not represent the globally optimized structure for the considered single-atom alloy clusters. However, as established in a previous study[9], the segregation trend remains largely unaffected by the

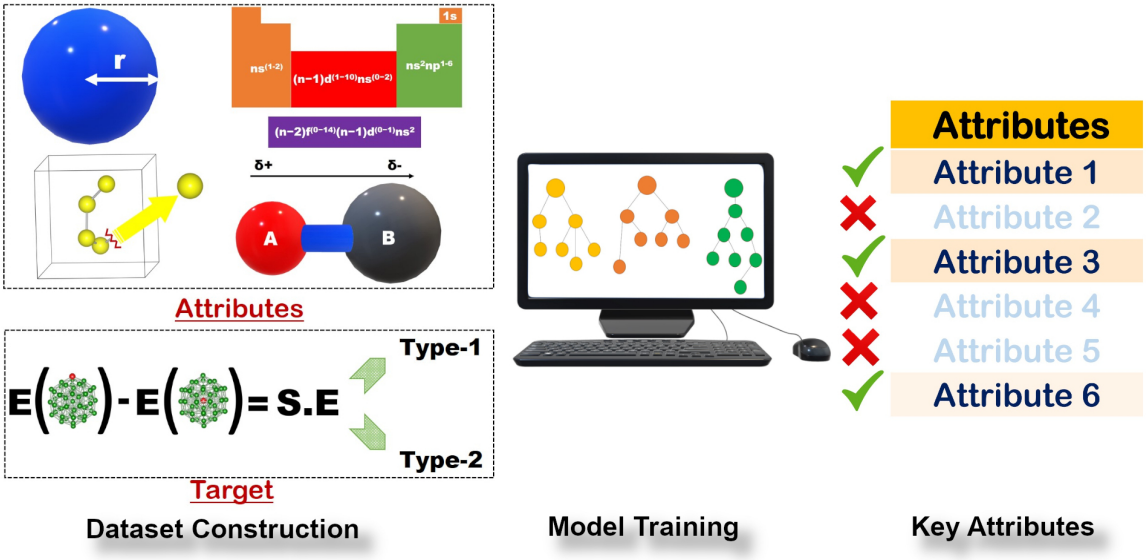

Figure 4.3: *Different steps of the machine learning approach, including dataset construction based on attributes and targets, model training, and key attribute selection.*

symmetry and size of the host cluster despite the confinement effect. In a 55-atom icosahedron, there are 12 six-coordinated surface vertex sites and 30 eight-coordinated surface edge sites. For surface atom substitution, we always select the lower-coordinated vertex site. For a given A–B pair, the segregation energy (SE) is defined as follows

$$\Delta E = E(A_{54}B_{surface}) - E(A_{54}B_{center}) \tag{4.3.1}$$

Following this formulation, a negative/positive value of ΔE supports the segregation of impurity atom B to the surface/center of the cluster. We select 43 elements from the periodic table, including 4 alkali metals (Li, Na, K, and Rb), 4 alkaline earth elements (Be, Mg, Ca, and Sr), 28 transition metals (10 from the 3d series, 10 from the 4d series, and 8 from the 5d series), 4 basic metals (Al, In, Sn, and Pb), and 3 p-block metalloids (Si, Ge, and Sb). We consider all possible A–B combinations among these 43 elements. Out of 903 possible binary combinations, the segregation trend for bimetallic nanoparticles of 169 pairs has been previously reported in the literature(see Appendix A).

For the remaining 734 pairs, we perform SE calculations. Additionally, to verify the composition dependency of the calculated segregation trend in single-atom alloy clusters, we conduct SE calculations considering both cases: A as the host with B as the guest atom, and vice versa. Among the 903 bimetallic A–B pairs analyzed in this study, 641 pairs exhibit a consistent segregation trend of either type 1 or type 2 at both extreme compositions, $A_{54}B$ and B_{54} A(The complete list is available in Appendix B). In the remaining cases, calculations for $A_{54}B$ and $B_{54}A$ yield opposite trends, indicating no clear core–shell preference.

We also examine the influence of spin–orbit coupling by toggling it on and off, finding no significant impact on core–shell preference. A heat map of the 903 combinations, categorized as type 1, type 2, or undecided (no unique segregation trend), is presented in Figure 4.4. In our subsequent ML-based classification analysis, we focus on the 641 combinations that exhibit a unique segregation trend, while the remaining undecided combinations are examined later in the study.

4.3.2 Machine Learning

The key components of ML model construction and the significant findings in each are detailed in the following sections. The different steps of the ML approach has been schematically represented in Figure 4.3.

4.3.2.1 Creation of Synthetic Data

When analyzing the 641 binary nanoalloy data points classified as type 1 or type 2, an imbalance is observed, with 345 classified as type 2 and 296 as type 1. This imbalance may contribute to the misclassification of a minority of cases. In this study, we apply the Synthetic Minority Oversampling Technique (SMOTE)[15](for details see Methodology section 2.2.1.3) to address this issue. By using this method, the dataset expands from 641 to 689, reducing the imbalance from approximately 19% to less than 0.3%.

4.3.2.2 Feature Space

After constructing the dataset, the next step is selecting attributes or features to describe the data points. Previous studies strongly suggest that cohesive energy and atomic radius are the two dominant attributes. Since surface energy[16] follows the same trend as cohesive energy[8], it is not considered an independent feature. Additionally, we include electronegativity, bulk coordination number, s-, p-, and d-electron filling, atomic number, and group number of the constituent elements in the periodic table, resulting in a total of nine features. As an initial approach to feature engineering, we compute the differences and means of these attributes for elements A and B in each binary pair, expanding the feature set to 18. Finally, we incorporate the magnetic nature of elements A and B, defined by nonzero spin multiplicity, bringing the total number of features to 20(c.f Table 4.1).

4.3.2.3 ML Model Performance

The next critical step in ML is selecting an appropriate algorithm that effectively captures patterns in the dataset. To address the classification problem, we test four different tree-based algorithms: J48[17], random tree[18], random forest[19], and REP tree[20]. The

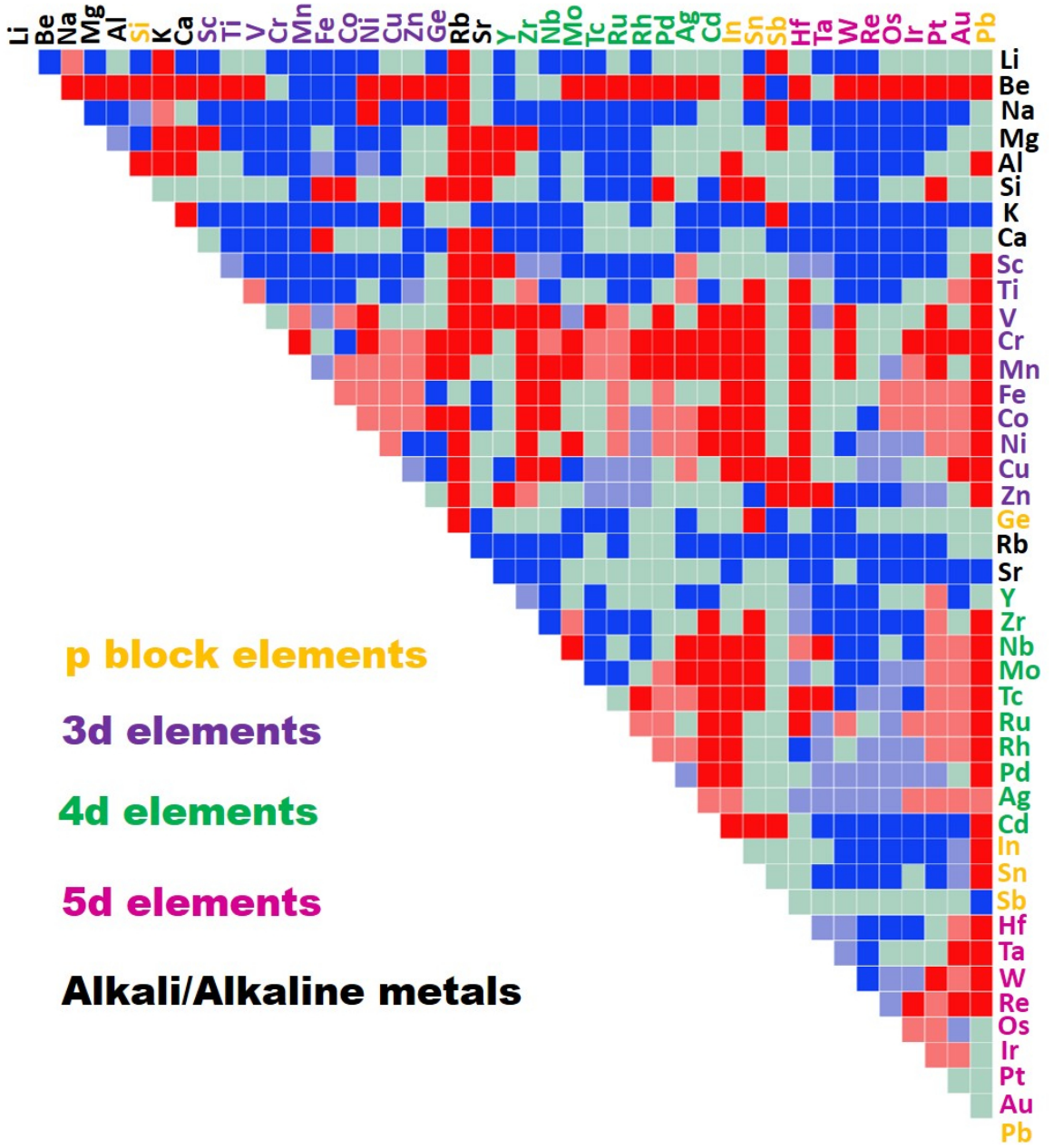

Figure 4.4: *A color-coded matrix represents binary core–shell nanoalloys based on DFT segregation energies. The elements are arranged in increasing atomic number, ensuring that in an A–B binary alloy, the A atom has a lower atomic number than the B atom. Type 1 and Type 2 core–shell combinations are represented in red and blue, respectively. Combinations with a non-unique type are shown in gray. Results from previous literature appear in a light shade, while findings from the present study are highlighted in a bright shade.*

comparison of accuracies are shown in Figure 4.5. As seen, the random forest algorithm demonstrates the best performance. The model's accuracy in classifying binary nanoclusters as type 1 or type 2 is evaluated using 10-fold cross-validation, achieving an accuracy of 89.3%. Performance is further assessed using the F1 score, which is approximately 0.896. The number of trees are set to 200 following a gridsearch.

Table 4.1: *List of 20 Different Attributes Used in the ML Algorithm with Their Description, Notation, and Range*

Sl No	Name of attribute	Notation	Range
1	Atomic radius difference	Δr	-154 pm to 132 pm
2	Atomic radius mean	$< r >$	111.5 pm to 254 pm
3	Cohesive energy difference	ΔE	-8.05 eV to 6.87 eV
4	Cohesive energy mean	$< E >$	0.89 eV to 8.54 eV
5	s electron difference	Δs	-1 to 2
6	s electron mean	$< s >$	0.5 to 2
7	p electron difference	Δp	-6 to 6
8	p electron mean	$< p >$	0 to 4.5
9	d electron difference	Δd	-10 to 10
10	d electron mean	$< d >$	0 to 10
11	Atomic number difference	ΔZ	-79 to -1
12	Atomic number mean	$< Z >$	3.5 to 80.5
13	Coordination number difference	ΔCN	-9 to 9
14	Coordination number mean	$< CN >$	4.5 to 12
15	Column difference	ΔC	-14 to 13
16	Column mean	$< C >$	1 to 14.5
17	Electronegativity difference	$\Delta \chi$	-1.72 to 1.19
18	Electronegativity mean	$< \chi >$	0.82 to 2.45
19	Magnetic nature of A	m_A	Yes/No
20	Magnetic nature of B	m_B	Yes/No

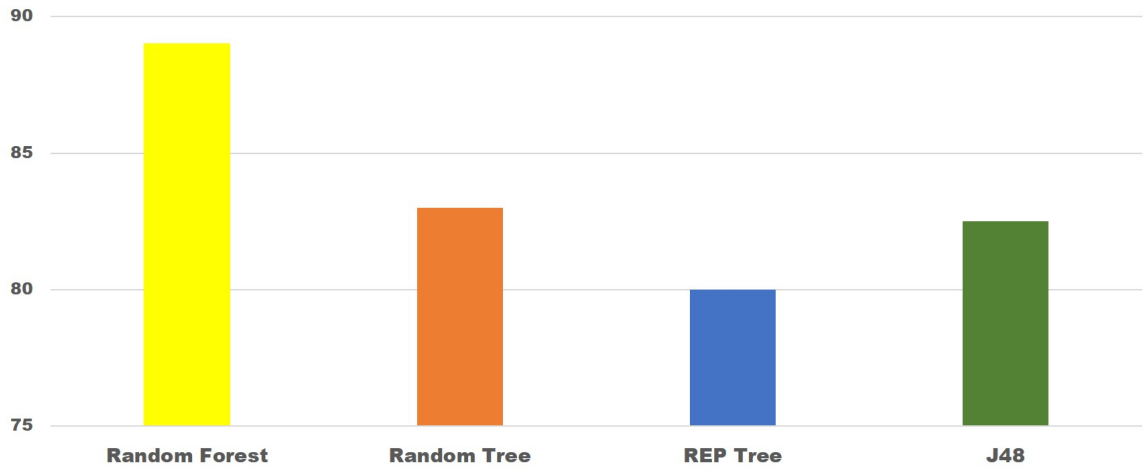

Figure 4.5: *Comparison of accuracies of different algorithms.*

4.3.2.4 Key Attributes

To identify the key attributes among the nine basic features, we analyze the distribution of instances classified as type 1 or type 2 based on the difference in each feature between elements A and B. To incorporate magnetism, we assign values of 1 for ”yes” and 0 for ”no” to m_A and m_B, then compute the difference (Δm) between them. We perform a Gaussian fit

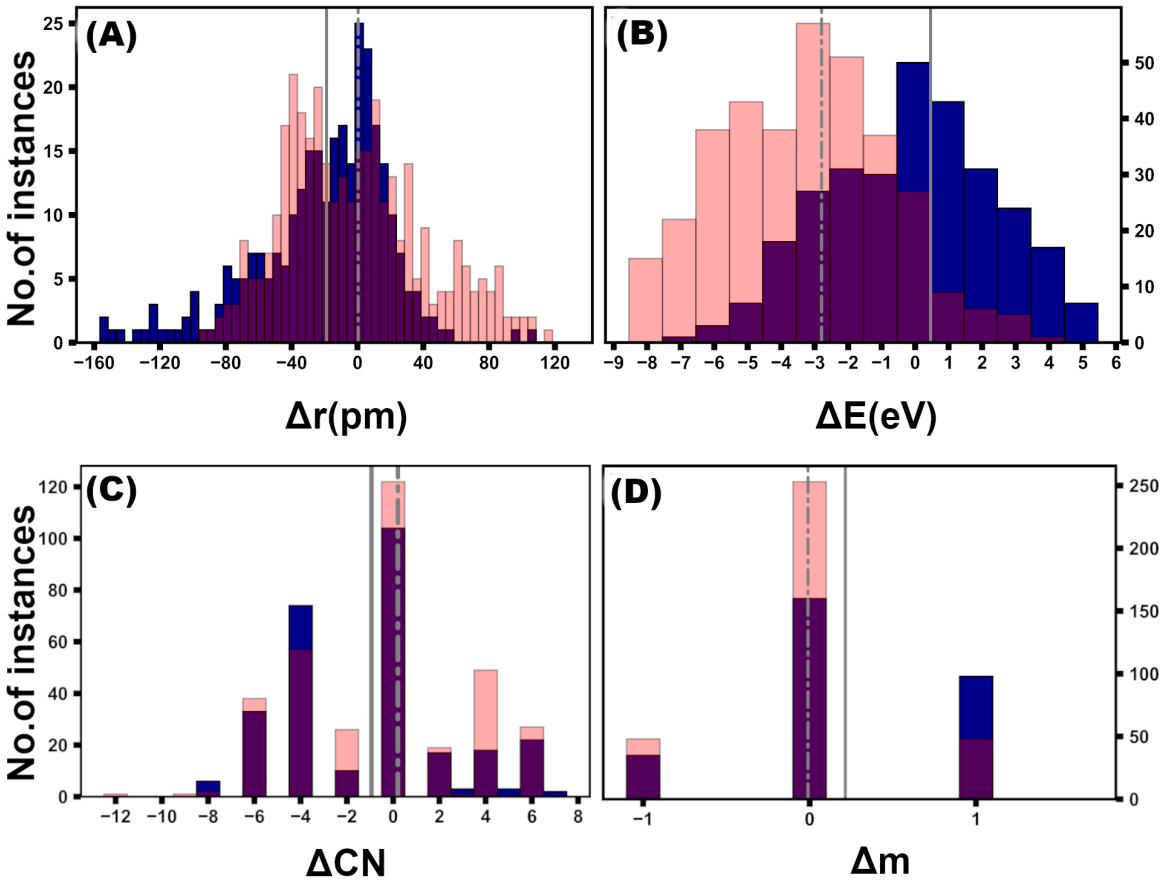

Figure 4.6: *A histogram displays the distribution of key attributes for Type 1 (pink) and Type 2 (blue) classes: (A) Difference in atomic radius (Δr). (B) Difference in cohesive energy (ΔE). (C) Difference in coordination number (ΔCN). (D) Difference in the magnetic nature of A and B (Δm). The overlapping region between the Type 1 and Type 2 distributions is shown in violet. Solid and dashed vertical lines indicate the mean (μ) of the Gaussian distribution fits for Type 1 and Type 2, respectively.*

on the distributions of the nine basic features and the magnetism differences to obtain the mean of the distributions for both the types. A significant difference in the mean (μ) values for types 1 and 2 of a given feature suggests that the feature strongly differentiates between the two types. Notably, the differences in μ values for four features—atomic radius, cohesive energy, coordination number, and magnetism—exhibit the strongest distinction between types 1 and 2, particularly in terms of sign change (see Figure 4.6). This indicates that these features play a primary role in determining the ordering of the core–shell structure. For bimetallic core–shell nanoclusters, the segregation trends based on these four key features are as follows:

- **Atomic Radius**: The element with a smaller atomic radius tends to occupy the more-coordinated core region to minimize strain caused by atomic size mismatch.
- **Cohesive Energy**: The element with higher cohesive energy prefers the core to

enhance bonding strength.

- **Coordination Number**: The element with a higher bulk coordination number is more likely to occupy the highly coordinated core region.
- **Magnetism**: Magnetic elements tend to segregate at the lower-coordinated surface region.

The overall structural ordering results from the interplay of these features.

We further examine the relative importance of the four key features by evaluating ML performance on the complete dataset of 689 instances, using only a single-feature difference as an attribute. Among these, the best performance is achieved with the cohesive energy difference, yielding a 10-fold cross-validation accuracy of 75.3%, followed by atomic radius (67.5%), magnetism (64.9%), and coordination number (56.2%). Given the diverse range of metals in our dataset, we repeat this analysis for specific subsets: (i) combinations of only transition metals (TMs), (ii) only alkali/alkaline earth metals, and (iii) mixed combinations of alkali/alkaline earth metals with TMs. The results, presented in Figure 4.8A–C, highlight the relative importance of these attributes.

- **Alkali/Alkaline Earth Metal Combinations**: The significance of atomic radius and coordination number increases, while cohesive energy and magnetism become less relevant. Since alkali/alkaline metals are diamagnetic, magnetism is not a key factor in determining whether an element prefers the surface or core. However, atomic radius varies significantly within this group (e.g., 182 pm for Li versus 290 pm for Rb), making it a stronger distinguishing feature.
- **TM–TM Combinations**: A similar trend is observed, as TMs are all magnetic. Because both elements in a TM–TM pair are magnetic, magnetism does not strongly differentiate between them.
- **Alkali/Alkaline–TM Combinations**: Magnetism and atomic radius become the dominant attributes, while coordination number and cohesive energy play a lesser role. This is expected because, in such combinations, one element is magnetic and the other is nonmagnetic, making magnetism a strong differentiating factor. Additionally, atomic radius exhibits large variations due to the combination of elements from different periodic table families.

4.3.3 Undecided Cases: Janus versus Mixed Structures

Finally, we evaluate the A-B combinations where $A_{54}B$ and $B_{54}A$ calculations result in two different signs of SE. In a large number of cases (262), no specific segregation trend

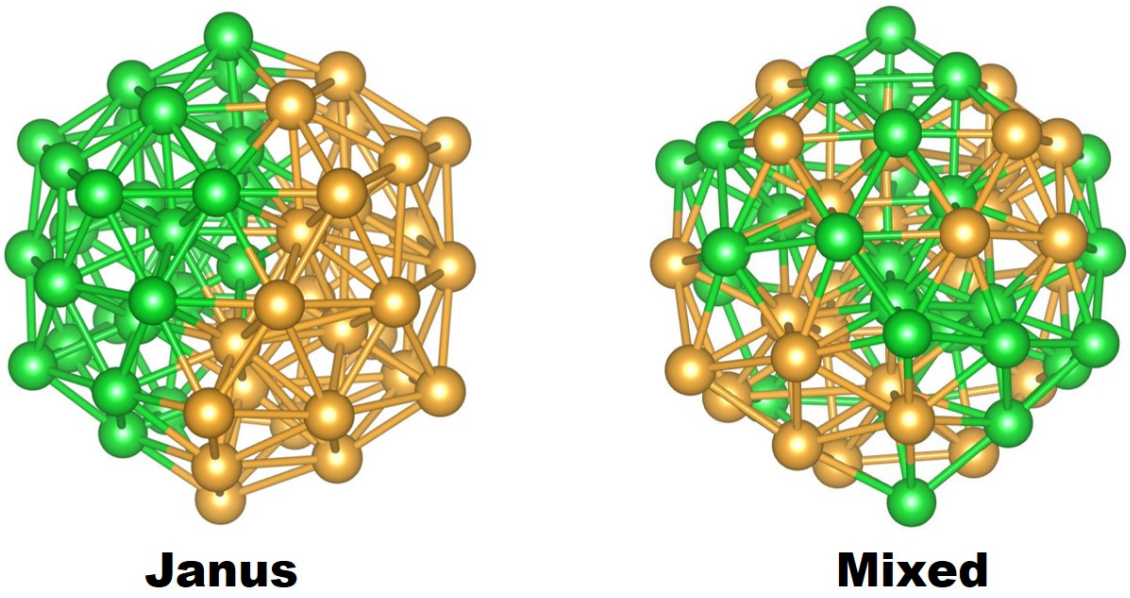

Figure 4.7: *Janus and mixed structures considered in this work.*

is observed, suggesting that the core-shell structure may not be favored by these A-B combinations. Figure 4.8D illustrates the relative contributions of different A-B combinations within this category, with the largest contribution coming from the p-block elements. Figure 4.8E illustrates the elemental contributions. Besides the core-shell structure, possible alternative structures[21] include the mixed or Janus patterns . To determine the most favorable configuration, we compute the DFT total energies for the undecided cases, considering the optimized Janus and mixed structures. For this analysis, we use $A_{28}B_{27}$ clusters with an approximately 50:50 composition of A and B, facilitating the construction of a Janus-like structure with 55 atoms(c.f Figure 4.7). Machine learning (ML) is performed using the

Table 4.2: *The mean of the Gaussian distribution of the four features for janus, and mixed structures.*

Mean of the Gaussian fit(μ) of the distribution	Janus	Mixed
$\mu_{\Delta E}$	-3.28 eV	0.025 eV
$\mu_{\Delta CN}$	-0.73	1.45
$\mu_{\Delta r}$	-13.15 pm	7.96 pm
$\mu_{\Delta m}$	-0.11	0.45

DFT total energy difference as the target, with instances sharing the same set of attributes as in the core–shell study. Following this, the distribution of four key features,differences in atomic radius, cohesive energy, coordination number, and magnetism,is analyzed for Janus versus mixed structures. The mean of the Gaussian distribution for these features shows $\mu_{\Delta E}$ to be 0.02 eV for mixed structures and -3.28 eV for Janus structures, compared to 0.45 eV for type 1 and -2.50 eV for type 2. This indicates that very small and very large

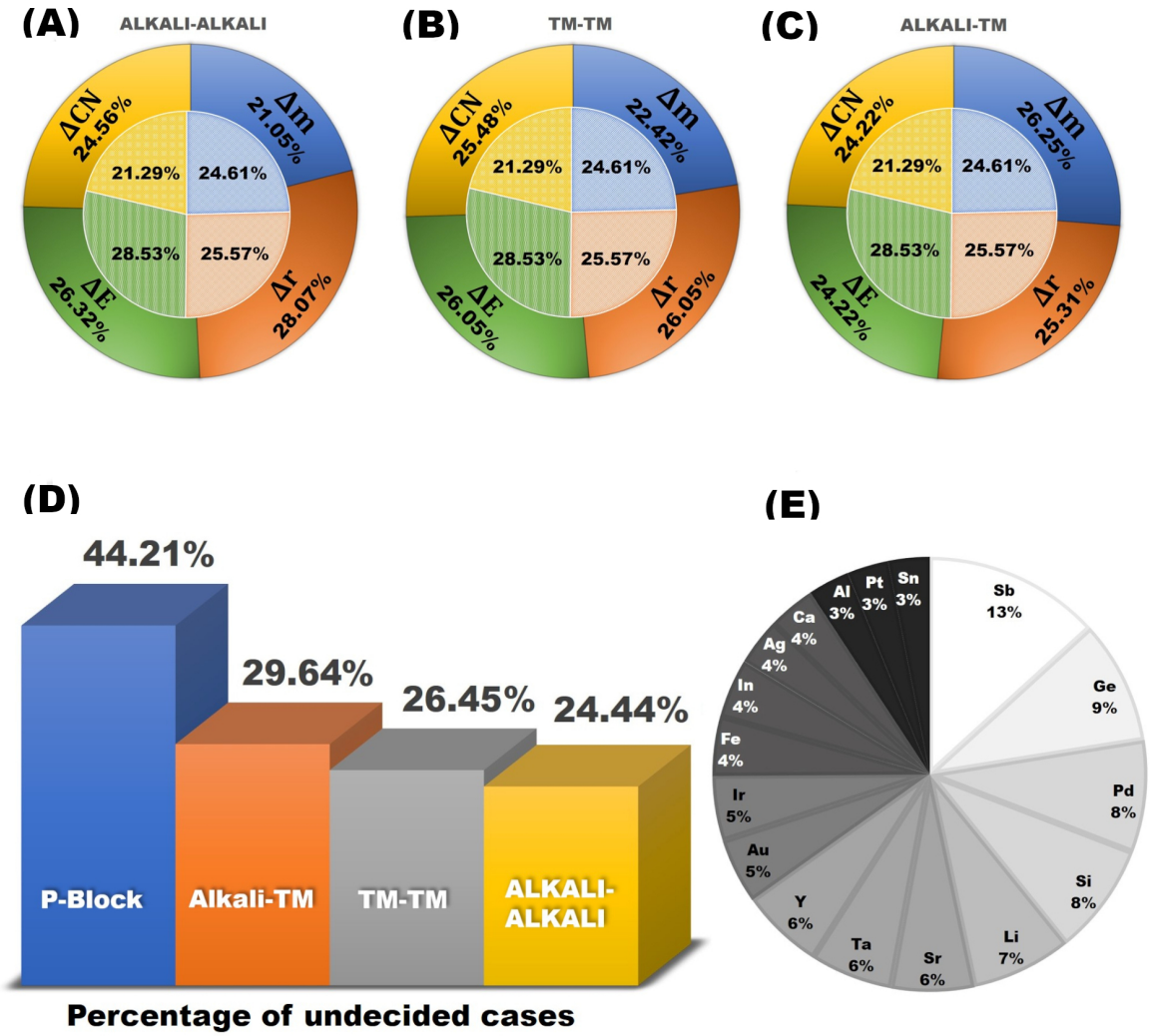

Figure 4.8: *The relative performance of four key attributes and the distribution of undecided cases with no unique core–shell preference are analyzed: (A) Relative performances of differences in atomic radius, cohesive energy, coordination number, and magnetic nature in alkali/alkaline–alkali/alkaline binary combinations, compared to the performance in the full dataset, represented as a concentric shell. (B) Performance analysis for transition metal (TM)–TM combinations. (C) Performance analysis for alkali/alkaline–TM combinations. (D) Percentage distribution of dominant A–B pair contributions in cases where no unique core–shell preference is observed. (E) Percentage of elemental contributions in cases without a unique core–shell preference, with only contributions greater than 3% shown.*

differences in the cohesive energy of A and B favor mixed and Janus patterns, respectively, over the core-shell pattern. Additionally, for mixed structures, the difference in coordination number is significant, with $\mu_{\Delta CN} = 1.50$. The mean of the four features are tabulated in Table 4.2.

4.4 Summary and Discussion

The stability of nanoscale alloys carries significant technological relevance, from catalytic processes[22] to biomedical applications[2]. One key structural motif among binary alloy nanoparticles is the core–shell configuration. A central question is whether such a structure is energetically preferred and, if so, which element tends to occupy the core and which the surface. Despite the importance of this issue, existing studies remain limited;typically based on a small number of synthesized nanoalloys[21] or select DFT-based investigations[8, 9]. Recent efforts using molecular dynamics and Monte Carlo simulations across 45 bimetallic nanoclusters—followed by principal component analysis—have attempted to shed light on the governing trends. However, establishing a generalized understanding requires a far broader data set and a more robust pattern-recognition approach. In this study, we analyze a comprehensive dataset of 903 bimetallic nanoclusters composed of elements ranging from alkali and alkaline earth metals to 3d, 4d, 5d transition metals and p-block elements. Using DFT calculations, we compute the segregation energy of single-atom alloy structures. This yields a subset of 641 binary pairs with a clear core–shell preference. We then apply machine learning techniques—supported by feature engineering and synthetic minority oversampling—to uncover the key factors that influence this preference. Our analysis reveals that differences in cohesive energy, atomic radius, coordination number, and magnetism are the most critical parameters. The relative influence of these factors varies across elemental groups. For the remaining pairs that do not show a clear core–shell segregation, we observe a tendency toward mixed or Janus-type structures, typically associated with very small or very large cohesive energy differences, respectively. Altogether, our machine learning–driven, large-scale computational approach offers valuable insights for the rational design of bimetallic nanoalloys with tailored mixing patterns.

Bibliography

[1] Manoj B Gawande, Anandarup Goswami, Tewodros Asefa, Huizhang Guo, Ankush V Biradar, Dong-Liang Peng, Radek Zboril, and Rajender S Varma. Core–shell nanoparticles: synthesis and applications in catalysis and electrocatalysis. Chemical Society Reviews, 44(21):7540–7590, 2015.

[2] Rajib Ghosh Chaudhuri and Santanu Paria. Core/shell nanoparticles: classes, properties, synthesis mechanisms, characterization, and applications. Chemical reviews, 112(4):2373–2433, 2012.

[3] AM Molenbroek, S Haukka, and BS Clausen. Alloying in Cu/Pd nanoparticle catalysts. The Journal of Physical Chemistry B, 102(52):10680–10689, 1998.

[4] Karrina McNamara, Syed AM Tofail, Nanasaheb D Thorat, Joanna Bauer, and John JE Mulvihill. Biomedical applications of nanoalloys. Nanoalloys, pages 381–432, 2020.

[5] S Tamil Selvan, Pranab K Patra, Chung Yen Ang, and Jackie Y Ying. Synthesis of silica-coated semiconductor and magnetic quantum dots and their use in the imaging of live cells. Angewandte chemie, 119(14):2500–2504, 2007.

[6] Jaehoon Lim, Byeong Guk Jeong, Myeongjin Park, Jai Kyeong Kim, Jeffrey M Pietryga, Young-Shin Park, Victor I Klimov, Changhee Lee, Doh C Lee, and Wan Ki Bae. Influence of shell thickness on the performance of light-emitting devices based on CdSe/Zn_{1-X}CdXS core/shell heterostructured quantum dots. Advanced Materials, 26(47):8034–8040, 2014.

[7] AV Ruban, Hans Lomholt Skriver, and Jens Kehlet Nørskov. Surface segregation energies in transition-metal alloys. Physical review B, 59(24):15990, 1999.

[8] Lin-Lin Wang and Duane D Johnson. Predicted trends of core- shell preferences for 132 late transition-metal binary-alloy nanoparticles. Journal of the American Chemical Society, 131(39):14023–14029, 2009.

[9] Qiang Yin, Fang Ma, Yan Zhou, Zhi-Jun Sui, Xing-Gui Zhou, De Chen, and Yi-An Zhu. Size-dependent segregation preference in single-atom alloys of late transition metals: effects of magnetism, electron correlation, and geometrical strain. The Journal of Physical Chemistry C, 123(30):18417–18424, 2019.

[10] Namsoon Eom, Maria E Messing, Jonas Johansson, and Knut Deppert. General trends in core–shell preferences for bimetallic nanoparticles. ACS nano, 15(5):8883–8895, 2021.

[11] Stephan Furthmeier, Florian Dirnberger, Martin Gmitra, Andreas Bayer, Moritz Forsch, Joachim Hubmann, Christian Schüller, Elisabeth Reiger, Jaroslav Fabian, Tobias Korn, et al. Enhanced spin–orbit coupling in core/shell nanowires. Nature communications, 7(1):12413, 2016.

[12] Yuying Jia, Xuan Hou, Zhongwei Wang, and Xiangang Hu. Machine learning boosts the design and discovery of nanomaterials. ACS Sustainable Chemistry & Engineering, 9(18):6130–6147, 2021.

[13] G. Kresse and J. Hafner. Ab initio molecular dynamics for liquid metals. Physical Review B, 47(1):558–561, 1993.

[14] G. Kresse and J. Furthmüller. Efficient iterative schemes for ab initio total-energy calculations using a plane-wave basis set. Physical Review B, 54(16):11169–11186, 1996.

[15] Nitesh V Chawla, Kevin W Bowyer, Lawrence O Hall, and W Philip Kegelmeyer. SMOTE: synthetic minority over-sampling technique. Journal of artificial intelligence research, 16:321–357, 2002.

[16] FR de Boer, R Boom, WCM Mattens, AR Miedema, and AK Niessen. Cohesion and structure, Cohesion in metals, vol. 1, 1988.

[17] J Ross Quinlan. C4. 5: programs for machine learning. Elsevier, 2014.

[18] Ali Mirza Mahmood, Naganjaneyulu Satuluri, Mrithyumjaya Rao Kuppa, et al. An Overview of recent and traditional decision tree classifiers in machine learning. International Journal of Research and Reviews in Ad Hoc Networks, 1(1):2011, 2011.

[19] Leo Breiman. Random forests. Machine learning, 45:5–32, 2001.

[20] W Nor Haizan W Mohamed, Mohd Najib Mohd Salleh, and Abdul Halim Omar. A comparative study of reduced error pruning method in decision tree algorithms. In 2012 IEEE International conference on control system, computing and engineering, pages 392–397. IEEE, 2012.

[21] Riccardo Ferrando, Julius Jellinek, and Roy L Johnston. Nanoalloys: from theory to applications of alloy clusters and nanoparticles. Chemical reviews, 108(3):845–910, 2008.

[22] James Dean, Michael G Taylor, and Giannis Mpourmpakis. Unfolding adsorption on metal nanoparticles: Connecting stability with catalysis. Science advances, 5(9):eaax5101, 2019.

5

First principles insights into the relative stability, electronic and catalytic properties of core-shell, Janus and mixed structural patterns for bimetallic Pd-X nanoalloys (X = Co, Ni, Cu, Rh, Ag, Ir, Pt, Au)

5.1 Introduction and Motivation

Multi-elemental nanoalloys serve as promising functional materials due to their enhanced practical applications in various fields, including catalysis[1], optics[2], sensing[3], advanced biomedicine[4], and magnetic storage[5]. These applications are primarily driven by the synergistic effects of size, composition, and chemical ordering-dependent properties[6]. As discussed in Chapter 4, depending on the arrangement of the two atomic species, bimetallic nanoparticles generally adopt one of three structural patterns: core-shell, Janus, or mixed. The ordering is primarily determined by several key factors that characterize the two constituent metallic species. These factors include atomic size mismatch, differences in bulk cohesive and surface energies, coordination differences in their bulk crystal structures, bulk miscibility, and magnetism[7–9]. We have seen that (a) atoms with lower radius

This chapter is based on publication: Soumendu Datta, **Aishwaryo Ghosh** and Tanusri Saha-Dasgupta, Phys. Chem. Chem. Phys.,2023, 25, 4667.

prefer the core, (b) elements with higher cohesive region segregate to core (c) element with higher bulk coordination number occupy the core (d) magnetic elements reside in the shell. The final ordering depends on a cumulative effect of these factors. We also find that the relative importance of such factors for core-shell segregation depends on the metal type of the constituents, which has been investigated for alkali/alkaline-alkali/alkaline, TM-TM, and alkali/ alkaline-TM combinations. In the case of alkali-alkaline and TM-TM combinations, atomic radius and coordination number are found to be more important, while in TM-alkali/alkaline combinations, magnetism and atomic radius are found to be crucial. Our analysis further suggests that when the difference in cohesive energy between the constituent elements is either very small or very large, the core–shell structure becomes unfavorable. Instead, mixed structures are stabilized in the case of small cohesive energy differences, while Janus structures are favored when the cohesive energy difference is large.

The calculations of segregation energies, used to determine the ordering in the previous chapter, have been done considering single atom alloys made out of 55-atoms icosahedral cluster. The effect of the concentration of the components and cluster size have not been explored. Hence in this chapter, we attempt at monitoring how these factors affect the cluster stability by (a) considering two composition limits, where the concentration of atoms of one kind of element is more than the other and vice versa and, (b) considering two cluster sizes of 147 atoms and 55 atoms. We also identify key microscopic properties that vary in sync with changes in the relative stability of the three structural patterns at the two composition limits. However, a machine-learning approach in this scenario would require a large number of high-throughput calculations(pertaining to different structural patterns as well as compositions) for generating an ample-sized training set to aid in pattern recognition. So, we rather rely on detailed calculations restricting only to Pd-based binary nanoalloys, and try to connect the consequent observations with our previous results, wherever applicable. The choice is made based on the rationale that these nanoalloys are explored as an alternative to Pt-based electro-catalysts since they are scarce and expensive. Pd-based alloys are particularly favored due to their similar electronic structure, comparable performance, better methanol tolerance, greater resistance to CO poisoning, and, most importantly, the lower cost of Pd compared to Pt[10]. We consider alloys with 3d,4d and 5d metals which are reported to augment catalytic properties in fuel cells[11–13]. Particularly, we focus on eight Pd-based bimetallic nanoalloys, namely three bimetallic Pd-3d nanoalloys - Pd-Co, Pd-Ni and Pd-Cu; two bimetallic Pd-4d nanoalloys - Pd-Rh and Pd-Ag; and three bimetallic Pd-5d nanoalloys - Pd-Ir, Pd-Pt and Pd-Au. Notably, the eight alloying elements include magnetic elements (Co and Ni), catalytic elements (Rh, Ir, and Pt), and plasmonic elements (Cu, Ag, and Au). We also consider the two composition limits in each case: Pd-poor/-rich, where Pd concentration is less/more than the concentration of the other d-block element in

the nanoalloy.

To prepare the three structural configurations with a fixed total number of atoms and identical composition, we start with a 147-atom icosahedral structure of a pristine Pd_{147} cluster. From this, we construct three initial structural patterns for each bimetallic Pd-X nanoalloy, considering two compositions: $Pd_{55}X_{92}$ (Pd-poor) and $Pd_{92}X_{55}$ (Pd-rich), where "X" represents one of the remaining eight elements. Although the physical properties of nanosystems are size and shape dependent[14, 15], we choose an atomic shell-structured icosahedron due to its high stability in noble metal nanoparticles[16, 17]. Additionally, the icosahedral geometry facilitates the construction of core-shell, Janus, and mixed structural patterns while maintaining the same composition. Based on the optimized structures, we examine the relative stability of the three structural patterns for each bimetallic nanoalloy of either composition. We then analyze their structural and electronic properties using first-principles density functional theory (DFT) calculations, observing variations across the bimetallic Pd-X nanoalloy series. Our Crystal Orbital Hamiltonian Population(COHP)[18] analysis indicates that relative stability is primarily influenced by changes in atom-atom covalency between structural patterns for each Pd-X nanoalloy of fixed composition. Additionally, the three patterns are distinctly characterized by an orbital hybridization index. Finally, we evaluate catalytic activity trends using the d-band model[19] for each structural configuration of the bimetallic nanoalloy. This indicates that the catalytic activity of most studied bimetallic Pd-X nanoalloys falls between that of a pristine Pt_{147} and Pd_{147} cluster, regardless of composition, except for the Pd-poor Pd-Ag nanoalloy. The overall analysis of relative stability and catalytic properties suggests that the bimetallic Pd-Ni nanoalloy is the most promising candidate for designing a non-Pt catalyst. Specifically, the Janus and mixed structures are preferable for the Pd-poor composition, while the core-shell structure, with Pd atoms on the surface, is favored for the Pd-rich composition. Finally, we confirm the predicted catalytic activity trend for the three structures of the bimetallic Pd-Ni nanoalloy relative to the pristine Pd_{147} cluster through a rigorous analysis of the adsorption reaction with a CO molecule on their surface.

5.2 Computational Methodology

For calculations related to interconvertibility among the three structural motifs of bimetallic nanoclusters, icosahedrons with 147 atoms are used. This choice is justified since the icosahedron-shaped concentric cell structure has previously been predicted as the ground-state geometry for larger pristine Pd nanoclusters[20]. An initial core-shell structural pattern for a bimetallic $X_{55}Pd_{92}$ nanoalloy is easily constructed from the pristine Pd_{147} cluster by replacing its 55 core atoms with X elemental atoms. Similarly, the initial Janus-patterned

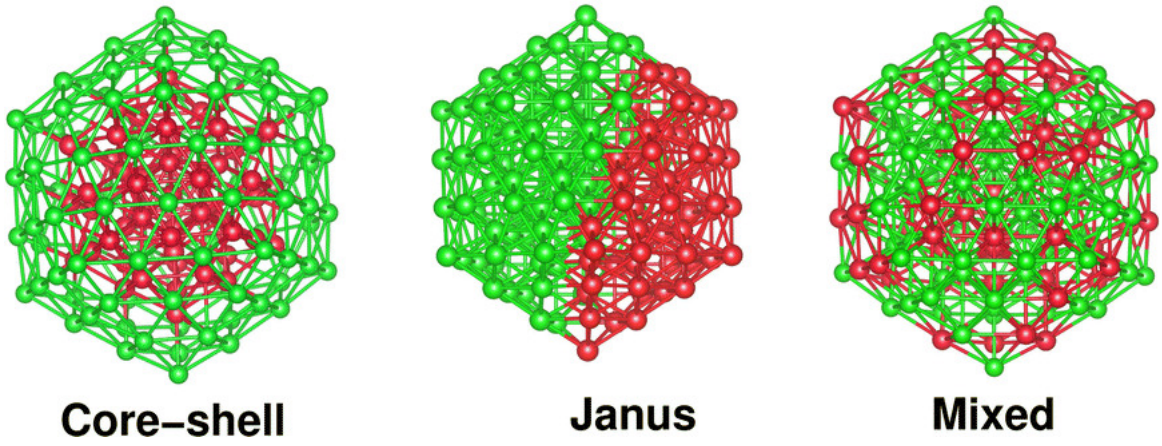

Figure 5.1: *The initial structural patterns of core-shell, Janus, and mixed configurations in a bimetallic $Pd_{92}X_{55}$ nanocluster in an icosahedral arrangement with 147 atoms. Green spheres represent Pd atoms, while red spheres correspond to atoms of the X element.*

structure for a bimetallic $X_{55}Pd_{92}$ nanoalloy is created by substituting a hemispherical fraction of Pd_{55} on one side with 55 X atoms, positioning the $X_{55}$and Pd_{92} fractions side by side. Finally, the initial mixed-pattern structure for a bimetallic $X_{55}Pd_{92}$ nanoalloy is formed by randomly distributing the 55 X atoms among the 92 Pd atoms throughout the entire structure.

Figure 5.1 illustrates the initial structural patterns for the core-shell, Janus, and mixed bimetallic nanoalloys with an $X_{55}Pd_{92}$ composition. Similarly, the initial structural patterns for the core-shell, Janus, and mixed structures of a bimetallic $Pd_{55}X_{92}$ nanoalloy are obtained by interchanging X and Pd atoms in the $X_{55}Pd_{92}$ nanoalloy. For the cluster calculations, a simple cubic supercell with each side measuring 28 Å is used, incorporating periodic boundary conditions. Two neighboring clusters remain separated by approximately 12 Å of vacuum. The large cell size effectively minimizes interactions between cluster images.

This study employs Density Functional Theory (DFT) within the pseudo-potential plane wave framework using the Vienna Ab Initio Simulation Package (VASP)[21, 22]. It applies the Projected Augmented Wave (PAW) pseudopotential alongside the Generalized Gradient Approximation (GGA) for the exchange-correlation energy functional, as formulated by Perdew, Burke, and Ernzerhof (PBE). All structures are optimized until all force components fall below the threshold value of 0.001 eV/Å. Due to the presence of heavy 4d and 5d atoms, non-collinear DFT calculations incorporating spin-orbit interactions are performed for all calculations. In addition, 55-atom bimetallic Ni-Pd clusters are considered to examine the effect of the cluster size.

Table 5.1: *Atomic radius (r), bulk cohesive energy (E_c), surface energy (S) and electronegativity (χ) of the constituent elements[23]*

Element	r (Å)	E_c (eV per atom)	S (J m^{-2})	χ (Pauli scale)
Co	1.52	4.39	2.55	1.88
Ni	1.49	4.44	2.38	1.91
Cu	1.45	3.49	1.79	1.90
Rh	1.73	5.75	2.70	2.28
Pd	1.69	3.89	2.05	2.20
Ag	1.65	2.95	1.25	1.93
Ir	1.80	6.94	3.00	2.20
Pt	1.77	5.84	2.475	2.28
Au	1.74	3.81	1.50	2.54

5.3 Results

The key properties of the constituent elements that influence the formation of binary nanoalloys include atomic radius, bulk cohesive energy, surface energy, and electronegativity. Table 5.1 presents the values of these properties for each element. The cohesive and surface energies of Cu, Ag, and Au are lower compared to Pd, while the other elements exhibit higher values for these properties. Ir has the largest atomic radius, whereas Cu has the smallest. Au is the most electronegative element, while Co is the least. Ir also has the highest cohesive and surface energy, whereas Ag has the lowest. The following analysis examines the optimized structures, relative stability trends, and electronic and catalytic properties of the three structural patterns for each bimetallic nanoalloy.

5.3.1 Optimized Structures

After structural optimization, the overall icosahedral pattern remains intact across all three structural configurations for each bimetallic Pd-X nanoalloy. However, the effective cluster sizes vary along the Pd-X series. The cluster size is determined by the average distance between the cluster center and the outermost surface atoms. The cluster size for an optimized pristine Pd_{147} cluster is 0.703 nm. The initial structures of the three patterns for each binary Pd-X cluster originate from the optimized structure of the Pd_{147} cluster. The estimated cluster sizes for the three morphologies of each binary Pd-X nanocluster, across both composition limits, fall within a range of 0.65-0.73 nm, as shown in Table 5.2.

Figure 5.2 presents the plot of our estimated cluster sizes for the three morphologies of each binary nanocluster across both composition limits. The overall trend remains nearly consistent for both compositions. As expected, the Pd-Ni and Pd-Co clusters in their Pd-poor composition exhibit smaller sizes due to their smaller atomic radii. The cluster size then

Binary Pd-X Cluster	Coreshell (nm)	Janus (nm)	Mixed (nm)
Size for binary $Pd_{55}X_{92}$ cluster			
Pd-Co	0.673	0.662	0.657
Pd-Ni	0.676	0.654	0.657
Pd-Cu	0.683	0.667	0.669
Pd-Rh	0.691	0.689	0.689
Pd-Ag	0.723	0.727	0.725
Pd-Ir	0.687	0.692	0.691
Pd-Pt	0.699	0.706	0.703
Pd-Au	0.721	0.732	0.726
Size for binary $Pd_{92}X_{55}$ cluster			
Pd-Co	0.666	0.674	0.676
Pd-Ni	0.666	0.673	0.676
Pd-Cu	0.673	0.682	0.682
Pd-Rh	0.693	0.694	0.696
Pd-Ag	0.717	0.717	0.717
Pd-Ir	0.687	0.694	0.697
Pd-Pt	0.707	0.702	0.703
Pd-Au	0.723	0.722	0.718

Table 5.2: *Our estimated cluster sizes for the optimized structures of the three patterns in each binary Pd-X cluster, across both composition limits.*

increases with the atomic number of the X element, peaking for binary Pd-Ag clusters. This could be attributed to weaker atom-atom interactions resulting from the filled 4d valence orbital of Ag. Notably, the variation in cluster size aligns qualitatively with the trends in orbital hybridization, as discussed in Section 5.3.3.

In a bimetallic Pd-X nanoalloy, three types of nearest-neighbor (NN) bonds exist: Pd-Pd, Pd-X, and X-X. The number of each type of NN bond remains approximately consistent across different X elements within a fixed composition. The plot in Figure 5.3 illustrates the overall percentage of X-X, Pd-X, and Pd-Pd NN bonds relative to the total NN bonds for each structural pattern in a 147-atom icosahedral structure, across both composition limits.

Each structural pattern is characterized by the dominance or deficiency of a particular NN bond type. In $Pd_{55}X_{92}$ (Pd-poor) nanoalloys:

1. The optimized core-shell structure has the highest number of Pd-X NN bonds and the fewest X-X NN bonds.
2. The optimized Janus structure contains the most X-X NN bonds and the least Pd-X NN bonds.
3. The optimized mixed structure features the highest number of Pd-X NN bonds and the fewest Pd-Pd NN bonds.

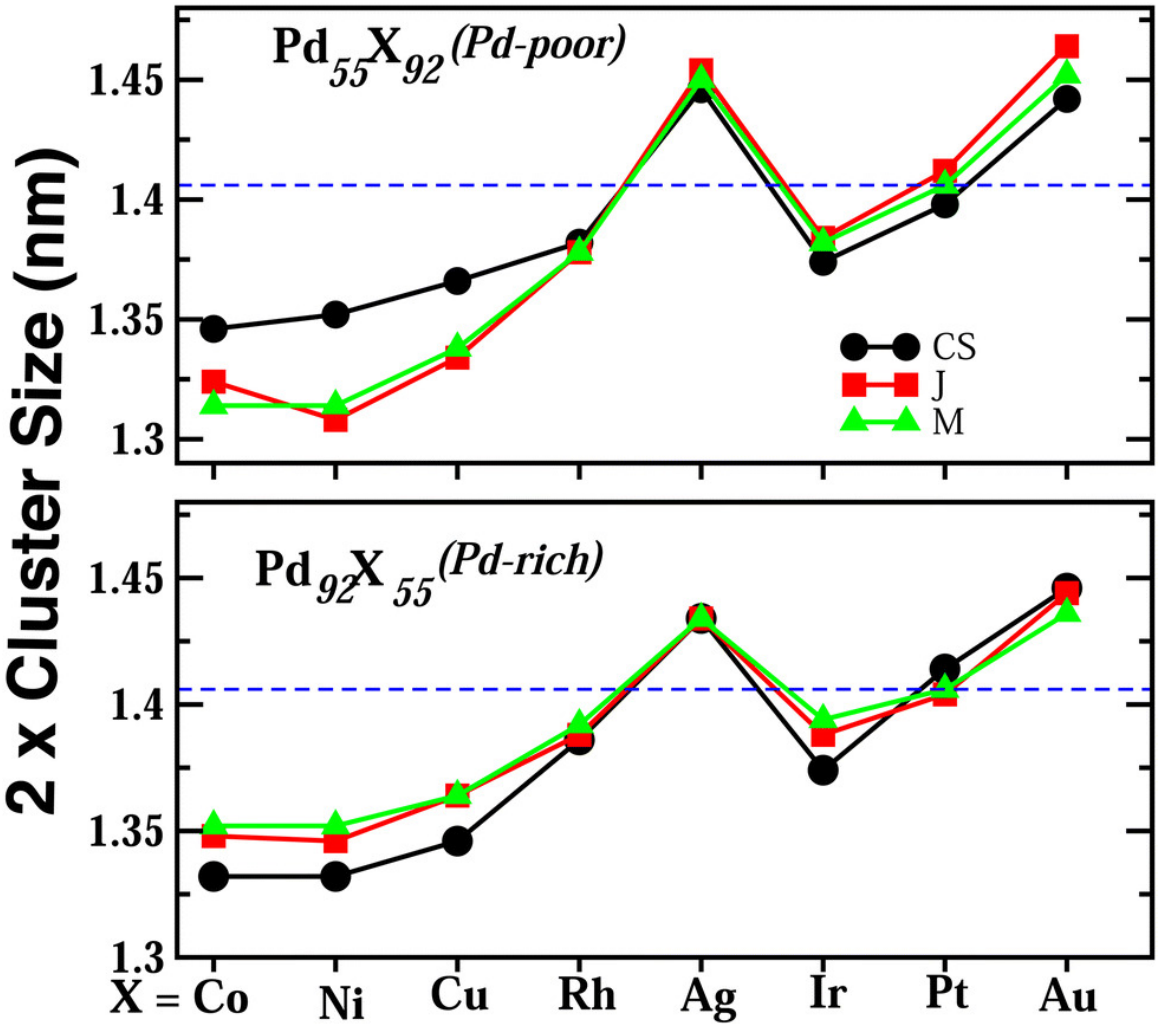

Figure 5.2: *The plot illustrates the estimated cluster sizes of the optimized structures for the three morphologies of each Pd-X nanoalloy across both compositions. Black circles represent the core-shell (CS) morphology, red squares denote the Janus (J) structure, and green triangles indicate the mixed (M) configuration. A horizontal dashed line marks the estimated size of the pristine Pd_{147} cluster, serving as a reference for comparison.*

For $Pd_{92}X_{55}$ (Pd-rich) nanoalloys:

1. The optimized core-shell structure has the most Pd-X NN bonds and the fewest Pd-Pd NN bonds.
2. The optimized Janus structure contains the highest number of Pd-Pd NN bonds and the least Pd-X NN bonds.
3. The optimized mixed structure involves the greatest number of Pd-X NN bonds and the lowest number of X-X NN bonds.

The nearest-neighbor (NN) bond length in a bimetallic $Pd_{55}X_{92}$ or $Pd_{92}X_{55}$ nanoalloy varies across the three structural patterns. Figure 5.4 illustrates the variation in the average Pd–Pd NN bond length for each optimized structure, comparing it to the pristine Pd_{147} nanocluster.

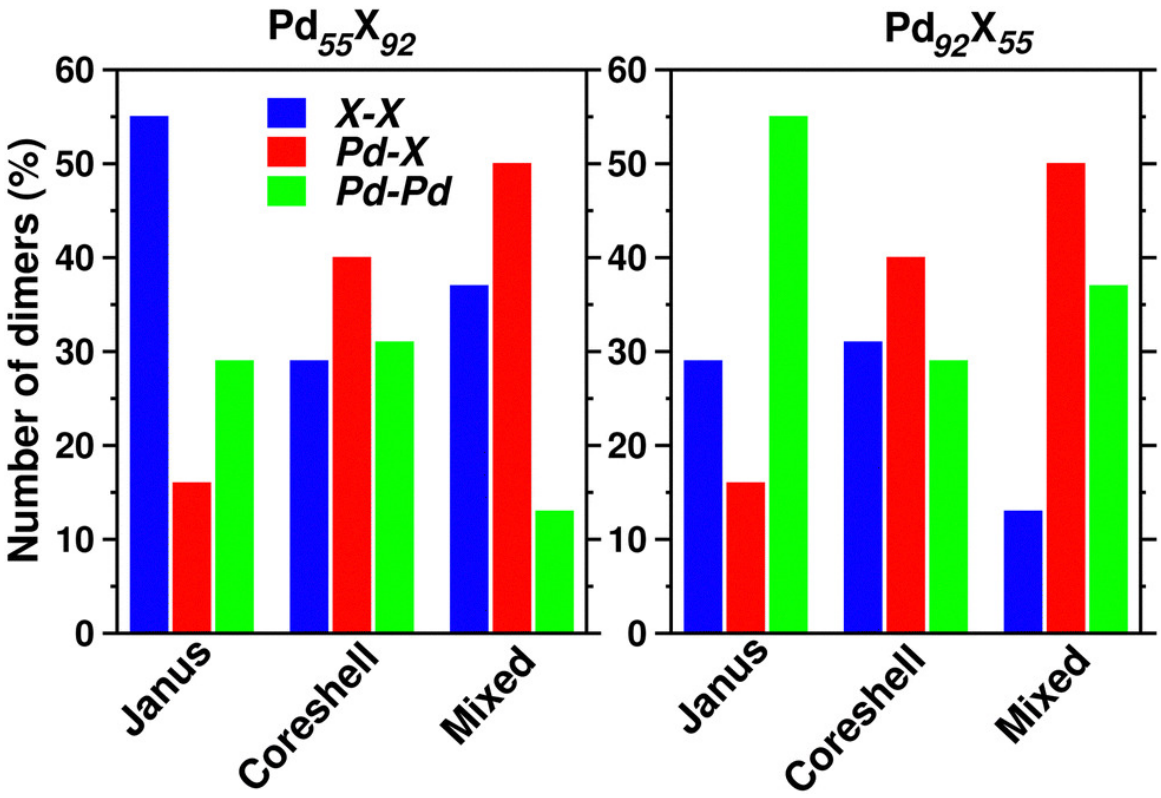

Figure 5.3: *The overall percentage of X–X, Pd–X, and Pd–Pd nearest-neighbor dimers in the optimized Janus, core–shell, and mixed structures for each bimetallic $Pd_{55}X_{92}$ and $Pd_{92}X_{55}$ cluster.*

The Janus structures, particularly in the Pd-rich composition, show minimal deviation from the pristine Pd_{147} cluster's Pd–Pd NN bond length. However, the core–shell and mixed structures exhibit significant changes in bond length across different Pd–X alloys and compositions. For Pd alloys with 3d elements, the Pd-poor mixed structure shows a reduction in Pd–Pd NN bond length, with the most pronounced decrease occurring in the $Pd_{55}Ni_{92}$ nanoalloy. In the Pd-rich composition, both the core–shell and mixed structures display shorter Pd–Pd NN bonds, with a more noticeable reduction in the core–shell structure. In contrast, alloying Pd with plasmonic elements such as Ag and Au leads to an increase in Pd–Pd NN bond length in both composition limits, with the most substantial increase observed in the core–shell structure of the $Au_{55}Pd_{92}$ nanoalloy. However, the core–shell configuration of the $Au_{55}Pd_{92}$ alloy, where Au forms the core, is not a stable structure, as will be further discussed.

5.3.2 Relative stability trend

To assess the relative stability of the three structural configurations in a binary Pd–X nanoalloy with a fixed composition, we calculate the total energy difference (ΔE) between the optimized Janus/mixed structures and the optimized core–shell structure. This is given by

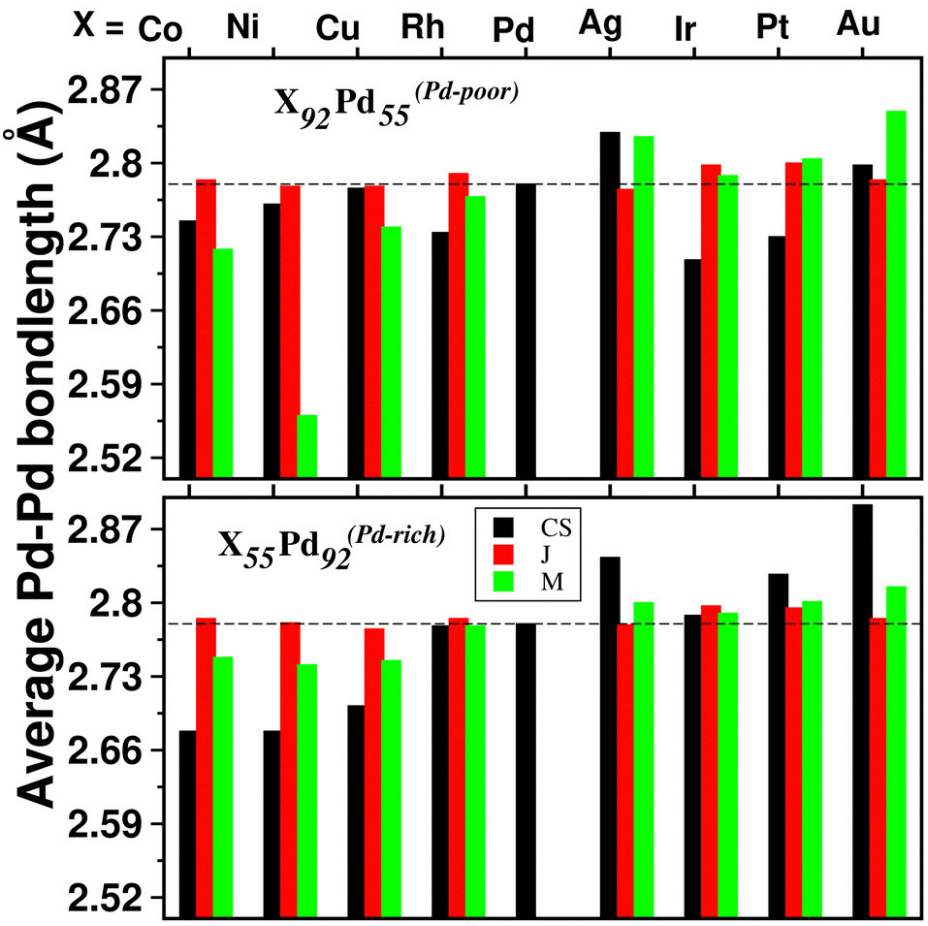

Figure 5.4: *A bar plot illustrating the average Pd–Pd nearest-neighbor (NN) bond lengths for the optimized Janus (J), core–shell (CS), and mixed (M) structures in each bimetallic $Pd_{55}X_{92}$ (top panel) and $Pd_{92}X_{55}$ (bottom panel) nanoalloy. The horizontal dashed line represents the Pd–Pd NN bond length in the pristine Pd_{147} cluster, providing a reference for comparison.*

$\Delta E = E_{Janus/mixed} - E_{core-shell}$, where E represents the DFT-calculated total energy of the optimized structure. A positive ΔE indicates that the core–shell structure with the chosen atomic ordering is more stable, whereas a negative ΔE suggests that the core–shell structure is less stable than the corresponding Janus or mixed configuration. If ΔE is positive for both Janus and mixed structures, the core–shell arrangement is the most stable. Conversely, if ΔE is negative for both, the core–shell configuration is the least stable. Figure 5.5 presents a plot of the calculated ΔE values for both compositions of each bimetallic Pd–X nanoalloy.

The relative stability of Pd-rich binary Pd–Co, Pd–Ni, Pd–Cu, and Pd–Pt nanoalloys follows a consistent order of preference among the three structural patterns: core–shell (Pd-shell) is the most stable, followed by mixed, and then Janus. Similarly, Pd-rich Pd–Rh and Pd–Ir nanoalloys exhibit a stability order of core–shell (Pd-shell) being the most stable, followed by Janus and then mixed. In contrast, Pd-rich Pd–Ag and Pd–Au nanoalloys show an inverse trend, where Janus is the most stable, followed by mixed, and core–shell

(Pd-shell) is the least stable. When the composition is inverted, the relative stability order among the three optimized structural patterns shifts. For Pd-poor bimetallic Pd–Co, Pd–Ni, Pd–Rh, and Pd–Ir nanoalloys, Janus is the most stable, followed by mixed, and core–shell (Pd-core) is the least stable. In Pd-poor Pd–Cu and Pd–Pt nanoalloys, mixed structures are the most stable, followed by Janus and then core–shell (Pd-core). Meanwhile, for Pd-poor Pd–Ag and Pd–Au nanoalloys, core–shell (Pd-core) is the most stable, followed by mixed, with Janus being the least stable. To further understand the relative stability among the three structural patterns for each binary Pd–X nanocluster with a fixed composition, formation energies[24, 25] have also been calculated. For a nanoalloy Pd_mX_n, where m+n=147, it is defined as :

$$E_{form} = E(Pd_mX_n) - \frac{m}{147}E(Pd_{147}) - \frac{n}{147}E(X_{147}) \tag{5.3.1}$$

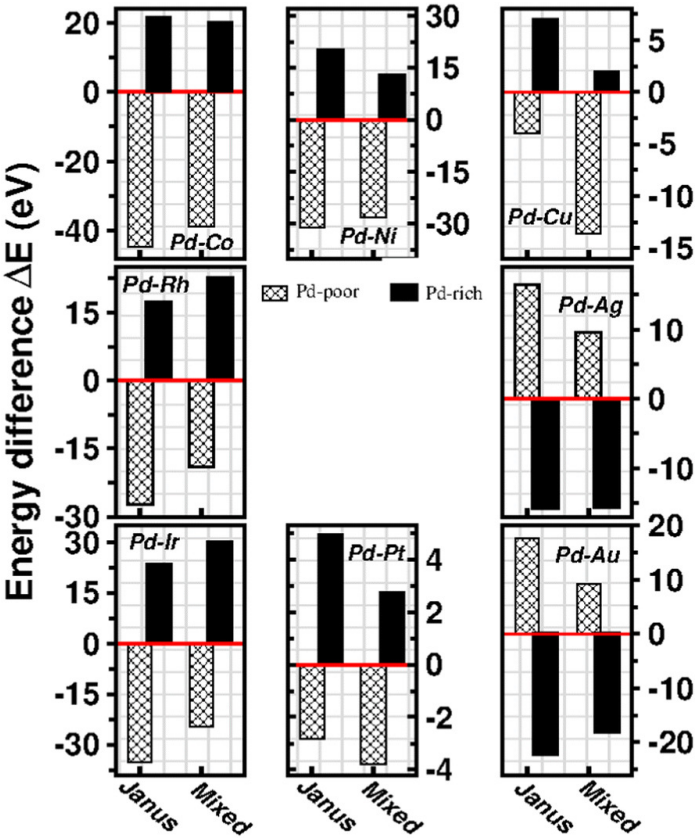

Figure 5.5: *The total energy difference for the optimized Janus and mixed structures relative to the optimized core–shell configuration for each $Pd_{55}X_{92}$ and $Pd_{92}X_{55}$ nanoalloy. Patterned bars represent $Pd_{55}X_{92}$ clusters, while filled bars correspond to $Pd_{92}X_{55}$ clusters. The energy of the optimized core–shell structure is set as the reference at zero, indicated by the horizontal red line. The plot is divided into three sections: the top panel represents binary Pd-3d clusters, the middle panel corresponds to Pd-4d clusters, and the bottom panel shows Pd-5d clusters.*

where total energy of the binary Pd_mX_n nanoalloy is denoted as $E(Pd_mX_n)$, and the total

energies of the pure elemental clusters as $E(Pd_{147})$ and $E(X_{147})$. A negative E_{form} value indicates that the alloy formation is thermodynamically favorable, whereas a positive E_{form} suggests a tendency toward phase segregation rather than alloying. Our calculated formation energy (E_{form}) for each bimetallic Pd-X nanoalloy is presented in Figure 5.6 for both Pd-poor and Pd-rich compositions. Notably, the most stable structure among the three structural patterns, as determined from the energy difference analysis, corresponds to the most negative formation energy. For instance, in the Pd-poor Pd-X nanoalloys, where Pd

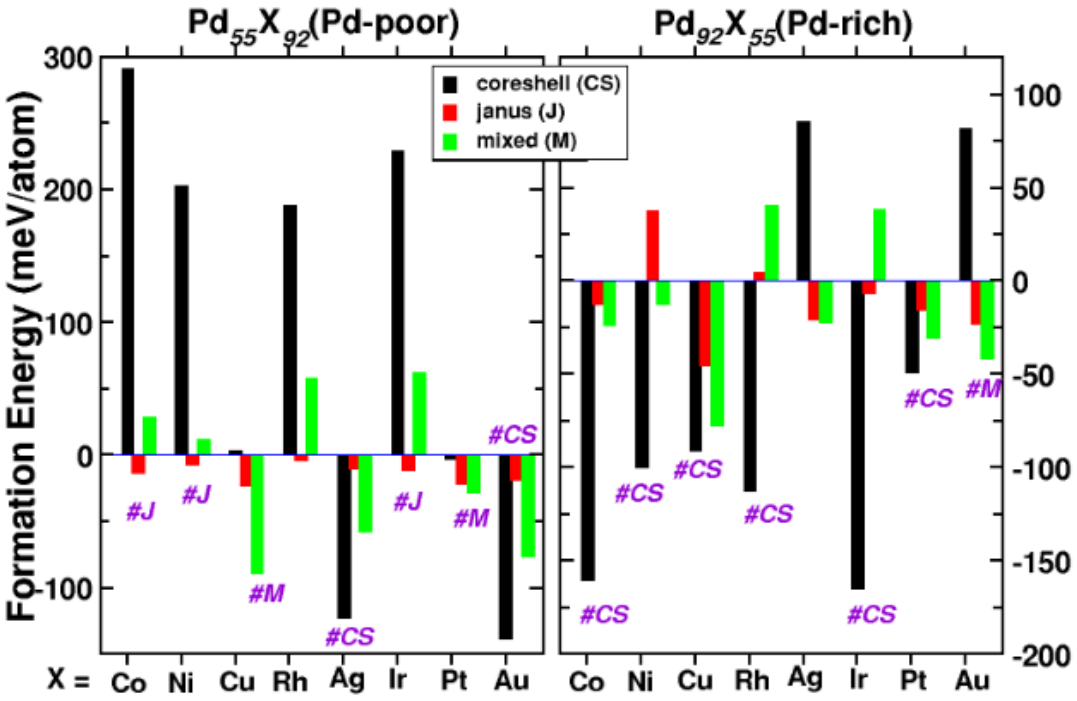

Figure 5.6: *Plot of the calculated formation energy for the optimized structures of three patterns for each bimetallic Pd-X nanocluster in both Pd-poor (left) and Pd-rich (right) compositions. The most stable pattern, determined based on energy differences, is marked with a "#" symbol for each bimetallic Pd-X cluster.*

atoms are at the core, the core-shell structures of Pd-Co, Pd-Ni, Pd-Rh, and Pd-Ir exhibit large positive formation energies, indicating their energetic instability. In contrast, Pd-Ag and Pd-Au nanoalloys in the same Pd-poor configuration have significantly negative formation energies, suggesting that their core-shell structures are favorable. This preference arises because Ag and Au atoms at the surface have lower surface energy than Pd, making surface segregation of Ag or Au energetically favorable. Similarly, in the Pd-rich composition, where Pd atoms are at the surface, the core-shell pattern becomes favorable for Pd-Co, Pd-Ni, Pd-Rh, and Pd-Ir, which were previously unfavorable in the Pd-poor composition. Conversely, for Pd-Ag and Pd-Au nanoalloys, the core-shell pattern becomes less favorable when Pd is at the surface.

Examining the mixed structural pattern, Figure 5.6 further shows that this configuration remains energetically unfavorable for Pd-Rh and Pd-Ir nanoalloys in both composition limits. This may be attributed to the large cohesive energy difference between the two constituent elements. Finally, regarding the Janus pattern, it generally exhibits some degree of formability in both composition limits for most Pd-X nanoalloys. The only exception is the Pd-rich Pd-Ni nanoalloy, which has a positive formation energy, indicating its unfavorable nature.

5.3.2.1 Understanding from atomic and elemental properties

5.3.2.1.1 In terms of surface energy

To understand the trend in relative stability, we first examine the variation in surface energies among the three structural configurations for each bimetallic nanoalloy. Surface energy represents the excess energy of the nanoparticle's surface relative to its bulk. We define the surface energy per atom[26] for a bimetallic A_mB_n nanoalloy as:

$$E_{sur}(A_mB_n) = \frac{E(A_mB_n) - me_A - ne_B}{N_s} \tag{5.3.2}$$

where $E(A_mB_n)$ is the total energy of the binary A_mB_n nanoalloy, e_A and e_B are the bulk cohesive energies per atom of elements A and B, respectively, and N_s represents the total number of surface atoms in the optimized structure.

In terms of the effect of surface energy on relative stability, a higher surface energy generally indicates lower stability, while a lower surface energy suggests greater stability. Figure 5.7 presents the calculated surface energy for the three structural configurations of each bimetallic Pd–X nanoalloy. The structure with the highest stability generally corresponds to the lowest surface energy for most bimetallic nanoalloys, regardless of composition. Additionally, as shown in Figure 5.7, the surface energy magnitude for bimetallic Pd–Ag and Pd–Au nanoalloys—especially in their Pd-poor compositions—is significantly lower compared to other bimetallic nanoalloys. This aligns with the well-established tendency of Ag and Au atoms to segregate at the surface in Ag- or Au-containing bimetallic nanoalloys[27].

5.3.2.1.2 In terms of the key elemental features

We attempt at better understanding the significance of the key factors, as discussed in Chapter 4, in determining the stability of bimetallic Pd–X nanoalloys. We have observed there that magnetism is not crucial in case of TM-TM combinations, and coordination number differences are same for all the Pd-X combinations considered. Hence an interplay of the atomic radius difference between the constituent elements (Δr = r(X) - r(Pd)) and the differ-

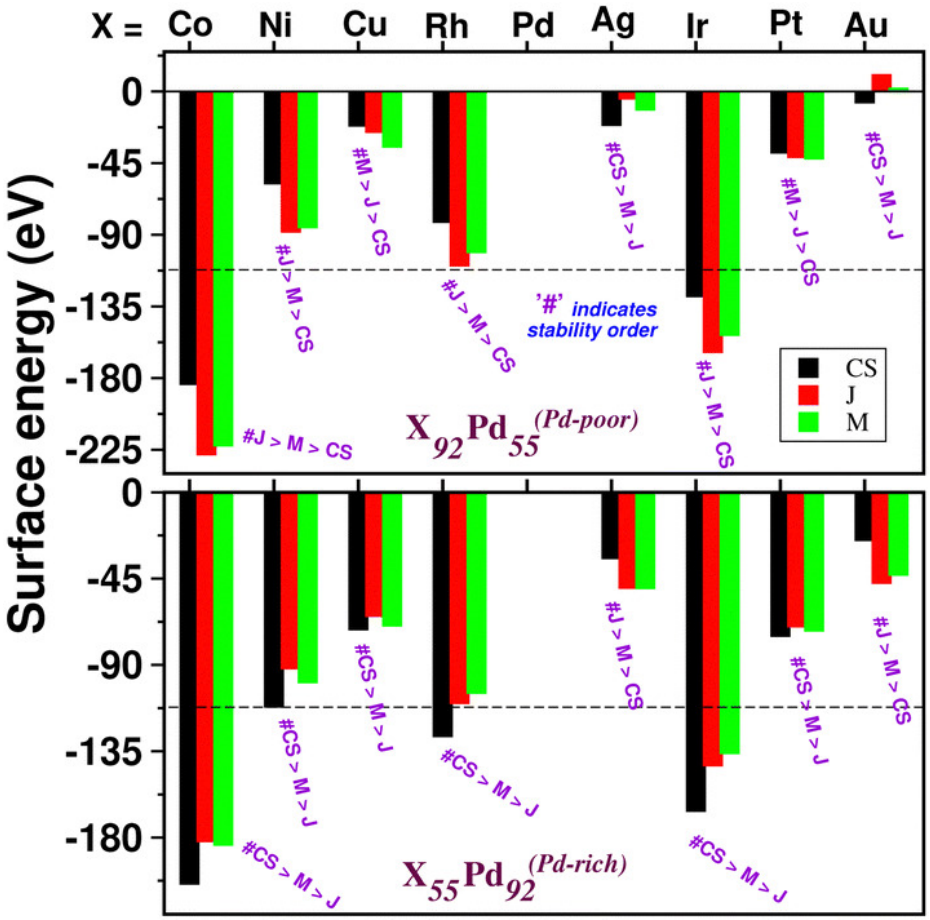

Figure 5.7: *The bar plot presents the surface energy for the three structural configurations of each bimetallic Pd–X nanoalloy, considering both Pd-poor (top panel) and Pd-rich (bottom panel) compositions. Since the number of surface atoms remains consistent across all systems, we report the total surface energy. The horizontal dashed line indicates the surface energy of the pristine Pd_{147} cluster. Additionally, for each bimetallic nanoalloy, the order of energetic stability is denoted using a "#" symbol.*

ence in their bulk cohesive energies (ΔE_c = E_c(X) - E_c(Pd)) determines the structural phase stability. Figure 5.8 presents two color-coded plots: Figure 5.8(a) illustrates the most stable structure for each bimetallic nanoalloy in either composition. Each box (except for the central one) corresponds to a binary Pd–X nanoalloy, with its lower-left triangle representing the stable structure for the Pd-poor composition and the upper-right triangle indicating the stable structure for the Pd-rich composition. Figure 5.8(b) displays the respective values of Δr and ΔE_c for each (X, Pd) pair,normalized. It presents how atomic radius difference (Δr) and bulk cohesive energy difference (ΔE_c) influence the stability of Pd–X nanoalloys. Each box corresponds to a specific Pd–X pair, with the lower-left triangle representing ΔE_c and the upper-right triangle representing Δr. Below we connect the segregation trends according to Δr and ΔE_c,as uncovered in the previous chapter, with the current results.

The 3d-Pd pairs exhibit large negative Δr, which plays a crucial role in determining stability.

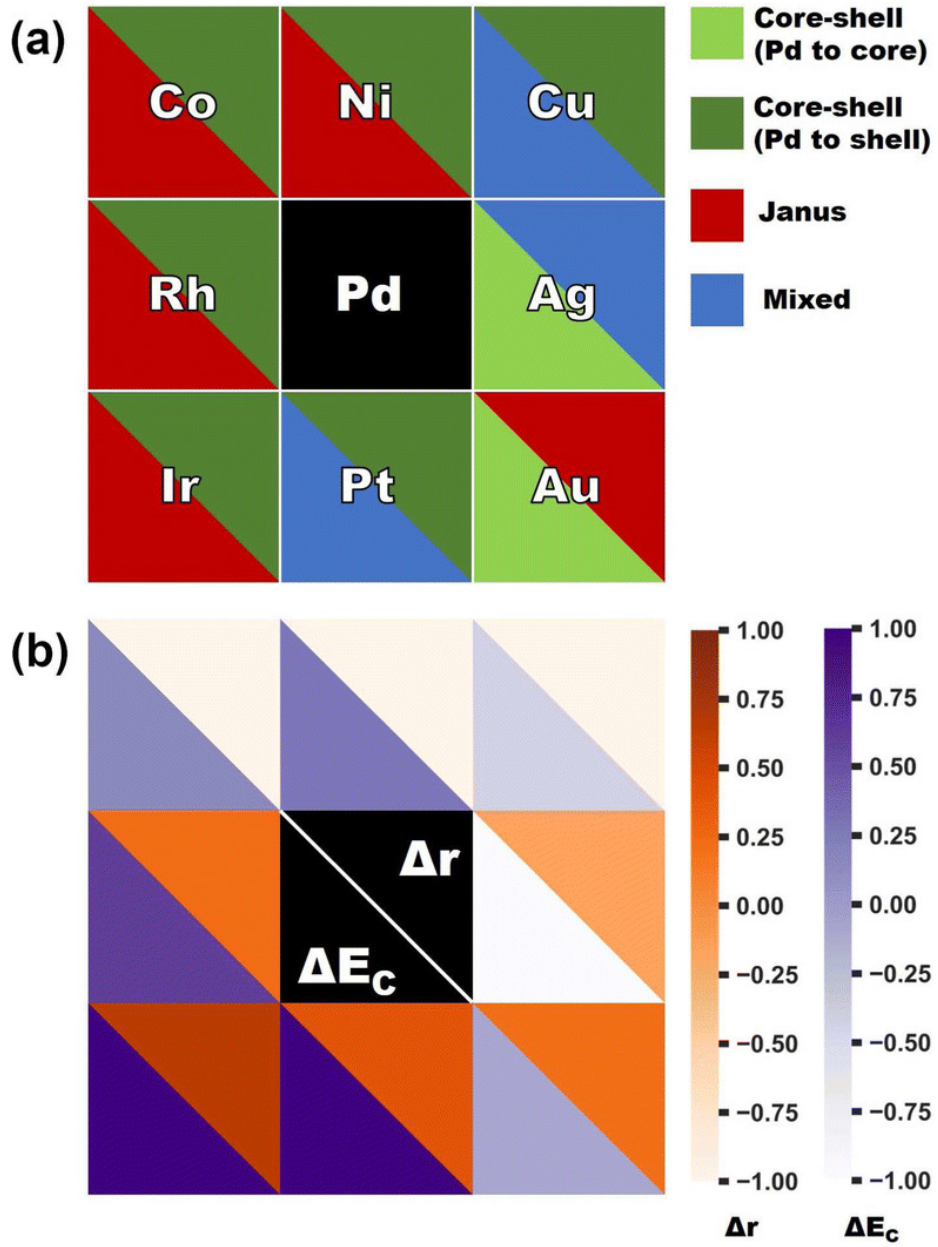

Figure 5.8: *The color-coded plots of (a) the most stable structure for each Pd–X nanoalloy, where each box corresponds to a specific binary alloy. The lower triangle of each box represents the stable structure for the Pd-poor composition ($Pd_{55}X_{92}$), while the upper triangle represents the stable structure for the Pd-rich composition ($Pd_{92}X_{55}$). Only the "X" element is labeled in each box for clarity. (b) two key atomic factors that influence structural stability: the difference in atomic radii and the difference in bulk cohesive energy.*

For Pd-rich compositions, this leads to a preference for the core–shell structure with larger Pd atoms forming the shell. In contrast, for Pd-poor compositions, the icosahedral structure prevents Pd from forming the shell, making ΔE_c the dominant factor in stability. When ΔE_c is large, the Janus structure becomes more stable in Pd–Co and Pd–Ni nanoalloys, while a smaller ΔE_c favors a mixed structure in Pd–Cu. For Pd–Rh, Pd–Ir, and Pd–Pt pairs, both Δr and ΔE_c are positive, leading to competition between the two factors. In Pd–Ir

and Pd–Rh nanoalloys, ΔE_c dominates, stabilizing the core–shell structure with Pd(lower cohesive energy) on the surface for Pd-rich compositions and the Janus structure for Pd-poor compositions. For Pd-rich Pd–Pt, ΔE_c favors the core–shell structure with Pd to shell owing to its lower cohesive energy, but in Pd-poor compositions, competition between the two effects results in a stable mixed structure. For Pd–Ag and Pd–Au nanoalloys, surface segregation effects become significant. Due to their lower surface energy, Ag and Au atoms preferentially migrate to the surface, influencing the stability of these alloys. In these cases, the term ”surface segregation” refers to the tendency of the element with lower surface energy to dominate the outer layer of the nanoalloy.

5.3.2.2 Understanding from electronic properties

The relative stability of different structural patterns in bimetallic Pd–X nanoalloys can also be qualitatively understood by analyzing the relative bond strengths and the distribution of three types of nearest-neighbor (NN) dimers. Experimental dimer binding energy measurements suggest that the bond strength varies significantly among different elements. The ordering of dimer binding energies is as follows: Ir_2 (3.50 eV)[28] > Co_2 (3.44 eV)[29] > Pt_2 (3.14 eV)[30] > Rh_2 (2.77 eV)[31] > Au_2 (2.29 eV)[32] > Cu_2 (2.08 eV)[33] > Ni_2 (2.06 eV)[34] > Ag_2 (1.66 eV)[35] > Pd_2 (1.03 eV)[36].

This ranking indicates that Ir–Ir dimers exhibit the strongest bonding, whereas Pd–Pd dimers have the weakest. Thus, the order of the relative bond strengths in a bimetallic Pd-X nanoalloy with three kinds of bonds can be expected to be X-X > Pd-X> Pd-Pd. The number of the three types of NN dimers depends on both the structural pattern and composition. Figure 5.3 shows that the order of the number of X–X NN dimers (N_{X-X}), Pd–X NN dimers (N_{Pd-X}), and Pd–Pd NN dimers (N_{Pd-Pd}) in the three structures of a bimetallic Pd–X nanoalloy varies depending on the specific structural pattern and composition.

For Pd-poor alloys:

- $N^{J}_{X-X} > N^{M}_{X-X} > N^{C-S}_{X-X}$
- $N^{M}_{X-PD} > N^{C-S}_{Pd-X} > N^{J}_{Pd-X}$
- $N^{C-S}_{Pd-Pd} > N^{J}_{Pd-Pd}$ ¿ N^{M}_{Pd-Pd}

For Pd-rich alloys:

- $N^{C-S}_{X-X} > N^{J}_{X-X} > N^{M}_{X-X}$
- $N^{M}_{X-PD} > N^{C-S}_{Pd-X} > N^{J}_{Pd-X}$
- $N^{J}_{Pd-Pd} > N^{M}_{Pd-Pd} > N^{C-S}_{Pd-Pd}$

The relative bond strength and the distribution of various types of dimers in a binary nanoalloy provide a qualitative understanding of the trends observed in the calculated relative stability of different structural patterns. For instance, in the case of the bimetallic Pd–Co nanoalloy, the bond strength hierarchy follows the order Co–Co > Pd–Co > Pd–Pd. For the Pd-poor Pd–Co nanoalloy, the dominance of the strongest Co–Co nearest-neighbor (NN) bonds follows the order $N_J^{Co–Co} > N_M^{Co–Co} > N_{CS}^{Co–Co}$. Interestingly, the relative stability exhibits the same trend, where the Janus structure (J) is more stable than the Mixed (M), which in turn is more stable than the Core–Shell (C–S) configuration. On the other hand, in the Pd-rich Pd–Co nanoalloy, the total number of Pd–Co and Co–Co NN bonds follows the trend $N^{CS}_{Co–Co+Pd–Co} > N^{M}_{Co–Co+Pd–Co} > N^{J}_{Co–Co+Pd–Co}$. Once again, the trend in relative stability aligns with this order, with the Core–Shell structure being the most stable, followed by the Mixed and Janus structures. This pattern is observed consistently across all bimetallic nanoalloys, regardless of composition. The similarity in the trends between relative stability and the prevalence of specific NN dimers raises an intriguing question: does the relative stability of these structural patterns have a direct correlation with NN bond strength?

To examine how atom–atom covalency changes among the three structural patterns when alloying a Pd nanocluster with different elements, we analyze the Integrated Crystal Orbital Hamilton Population (ICOHP)[18] for each bimetallic nanoalloy. The COHP represents the hopping-weighted density of states between adjacent atoms, where a negative value signifies bonding interactions. The ICOHP, obtained by integrating the COHP up to the highest occupied molecular orbital (HOMO), quantifies the covalent bond strength. For each bimetallic Pd–X nanoalloy, including the pristine Pd_{147} cluster, we compute the ICOHP averaged over all nearest-neighbor (NN) interactions. The resulting ICOHP values for the optimized structures of the three structural patterns are presented in Figure 5.9 as a function of electron energy for each bimetallic nanoalloy in both compositions.

The ICOHP plots are obtained by averaging the values over both spin channels for every nanoalloy. It is evident from these plots that the structure with the highest stability is generally associated with enhanced covalency, indicated by a more positive ICOHP value throughout the bonding region. To systematically compare the ICOHP values at the Fermi energy among the three structures for each bimetallic nanoalloy, we calculate the difference in ICOHP between the optimized Janus/mixed structure and the optimized core–shell structure for the same system, defined as ΔICOHP = ICOHP(Janus/mixed) – ICOHP(core–shell). A positive ΔICOHP suggests that the optimized core–shell structure, with the chosen atomic ordering, possesses enhanced covalency. Conversely, a negative ΔICOHP indicates that the core–shell structure exhibits lower covalency than the optimized

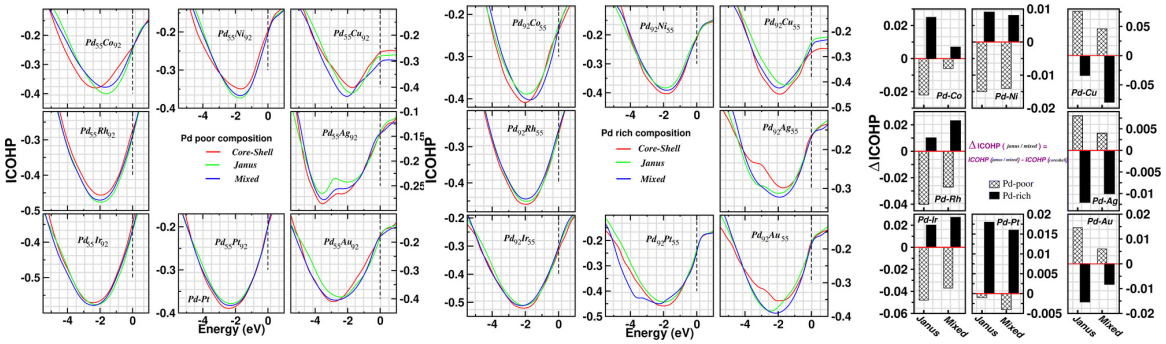

Figure 5.9: *The ICOHP plots display the bonding characteristics for the optimized core–shell, Janus, and mixed structures of each bimetallic $Pd_{55}X_{92}$ cluster (left box) and $Pd_{92}X_{55}$ cluster (middle box). In these plots, the Fermi energy of each binary nanocluster is fixed at zero energy, indicated by a vertical dashed line. The right box presents the difference in ICOHP values (ΔICOHP) at the Fermi energy for the optimized Janus and mixed structures relative to the core–shell structure. Here, the ICOHP of the optimized core–shell configuration is set to zero, represented by the horizontal red line passing through zero. This panel is divided into three sections: the left, middle, and right panels correspond to the binary Pd-3d, Pd-4d, and Pd-5d clusters, respectively.*

Janus/mixed structure. It is important to note that the formulation and interpretation of ΔICOHP closely resemble those of ΔE as defined in Section 5.3.2. Figure 5.9 also presents the calculated ΔICOHP values for all Pd-poor (patterned bars) and Pd-rich (filled bars) nanoalloys. Interestingly, the variation in ΔICOHP follows a similar trend to that observed in the ΔE plot in Figure 5.5. This clear one-to-one correspondence between relative stability and atom–atom covalency change suggests that the stability of these structures is fundamentally governed by covalency. The more stable a structure is, the higher its atom–atom covalency, whereas the least stable structure exhibits the lowest covalency.

5.3.3 Microscopic characterization of the three morphologies

To characterize the three structural patterns of a bimetallic nanoalloy, the radial distribution function (RDF) is a well-known and widely used quantity. The RDF for a bimetallic nanostructure is defined as the number of atoms $N_{A,B}(r)$ of species A or B located within a shell at a distance between r and $r+\Delta r$ from the center of the nanocluster[37],i,e, $\rho_{A,B}(r) = \frac{N_{A,B}(r)}{4\pi r^2 \Delta r}$. In the case of core–shell and Janus clusters, the radial distribution function (ρ_A) and (ρ_B) exhibits distinct bimodal distributions. On the other hand, bimetallic alloyed nanoparticles show a more uniform mixing of the two atomic species, leading to RDF plots with narrower peak distributions[38]. The ordering of the two elemental species in a core–shell structure can be further understood by analyzing the segregation energy[39]. Similarly, a mixed structure is typically characterized by an increase in mixing energy and a greater number of hetero-atomic bonds[40]. Thus RDF and mixing energy do not always distinctly dif-

ferentiate between core–shell and Janus configurations. This suggests the need for a more precise microscopic descriptor. In this regard, the "Orbital Hybridization Index" emerges as a promising tool, offering a clearer distinction among the three structural patterns. Since the constituent atomic species possess nearly filled valence orbitals, these systems are expected to exhibit significant orbital hybridization. To quantify this effect, we calculate the orbital hybridization index[40–42] , which provides a measure of the extent of orbital mixing between atoms in the nanoalloy. The orbital hybridization index is determined using the expression:

$$h_{kl} = \sum_{I=1}^{147} \sum_{i=1}^{\text{occ}} w_{i,k}^{(I)} w_{i,l}^{(I)} \tag{5.3.3}$$

where k and l represent the orbital indices (s, p, and d), and $w_{i,k}^{(I)}$ and $w_{i,l}^{(I)}$ denote the projections of the i-th Kohn–Sham orbital onto the respective spherical harmonics centered at atom I, integrated over a sphere of specified radius. The summation implicitly accounts for spin contributions. Figure 5.10 presents the total hybridization index $(h_{sd} + h_{pd} + h_{sp})$

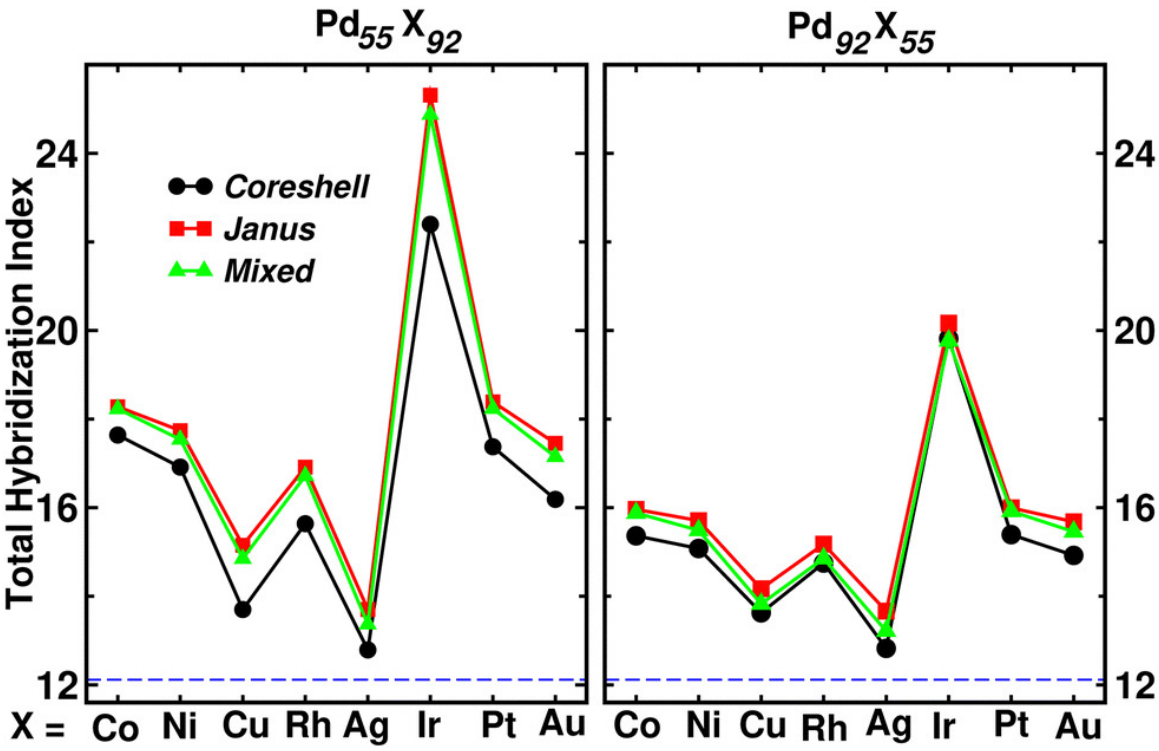

Figure 5.10: *The plot of the total orbital hybridization index illustrates the variations in orbital interactions among the optimized core–shell (black curve), Janus (red curve), and Mixed (green curve) structures for each $Pd_{55}X_{92}$ (left) and $Pd_{92}X_{55}$ (right) cluster. The horizontal dashed line represents the hybridization index for the pristine Pd_{147} cluster, serving as a reference.*

for each $Pd_{55}X_{92}$ (left) and $Pd_{92}X_{55}$ (right) cluster. The dashed line represents the total hybridization index of the pristine Pd_{147} cluster, allowing for a direct comparison with

bimetallic nanoalloys. The results indicate that the total hybridization index for all three structural patterns in each bimetallic nanoalloy surpasses that of the pristine Pd_{147} cluster. This increase stems from the higher number of itinerant electrons present in the bimetallic systems. Among the nanoalloys, Pd–Ir exhibits the most significant enhancement in total hybridization. This effect arises due to the presence of Ir, which contributes additional itinerant valence d-electrons, leading to stronger p–d and s–d hybridizations, thereby amplifying the overall hybridization index. Conversely, the Pd–Ag nanoalloy exhibits the smallest increase in orbital hybridization due to the reduced itinerancy of Ag's valence d-electrons. The variation of the total hybridization index in Figure 5.10 closely aligns with the trend observed in cluster size in Figure 5.2. Specifically, lower hybridization correlates with larger cluster sizes and vice versa. An intriguing observation from the hybridization index plot within a fixed composition is that the optimized Janus structure generally exhibits the highest total hybridization among the three structural patterns. In contrast, the optimized core–shell structure consistently shows the lowest total hybridization index, while the optimized mixed structure falls in between.

5.3.4 Catalytic properties

5.3.4.1 Trend from d-band model

The catalytic activity of a given catalyst depends on the activation barrier of the rate-determining step or the adsorption ability of an intermediate involved in that step[43, 44]. In catalytic processes over transition metals, the adsorption energies of different molecules tend to follow a predictable scaling relationship, as do the transition state energies and overall reaction energies[45–48]. This forms the foundation of the d-band model. Instead of calculating the energy of intermediates and transition states for each catalyst, the well-established d-band center model, proposed by Hammer and Nørskov[19], provides a straightforward way to relate catalytic activity to adsorption energy and, consequently, to the electronic structure of a transition metal catalyst's surface. The position of the d-band center relative to the Fermi energy serves as a first-order descriptor of a catalyst's ability to bind adsorbates. According to this model, the strength of the adsorbate's binding to the catalyst surface effectively indicates the rate of catalytic activity. For an efficient catalytic process, this bond strength should be balanced—not too strong nor too weak. If the bond is too strong, the desorption barrier becomes too high, making it difficult for the product to leave the surface after the reaction. Conversely, if the bond is too weak, the adsorption barrier is high, limiting the overall reaction kinetics. Thus, an upward shift of the occupied d-band center toward the Fermi energy corresponds to a stronger adsorption strength, whereas a downward shift results in weaker adsorption. For our binary nanoalloys, we

calculate the position of the occupied d-band center using the expression:

$$d_{\text{center}} = \frac{\int_0^{E_{\text{HOMO}}} \rho E \, dE}{\int_0^{E_{\text{HOMO}}} \rho \, dE} \tag{5.3.4}$$

where ρ is the d-density of states (DOS), E represents the d-level energy, and ρdE gives the number of d-states within the energy interval E and $E + dE$. Our calculated position for the occupied d-band center of the three structures for each bimetallic nanoalloy, relative to the respective E_{HOMO} (set at zero), is plotted in Figure 5.11. The d-band center position is averaged over both spin channels. To provide a comparative reference, the corresponding values for the pristine Pd_{147} and Pt_{147} clusters are marked with horizontal dashed lines. For further insight, the d-orbital projected density of states (d-PDOS) for the three structures of each bimetallic nanoalloy is also displayed in the right panel of Figure 5.11. The occupied d-states for the structure showing the maximum up-shifting of the d-band center are highlighted with a shaded region.

The plot of the occupied d-band center position in Figure 5.11 shows a clear up-shifting for both compositions of the bimetallic Pd–Ni nanoalloys ($Pd_{55}Ni_{92}$ and $Pd_{92}Ni_{55}$) compared to the pristine Pd_{147} cluster. This shift suggests that Pd–Ni nanoalloys will have a stronger interaction with adsorbates, which is a key factor in catalytic performance. A similar up-shifting is observed for the mixed structure of the Pd-rich Pd–Cu nanoalloy ($Pd_{92}Cu_{55}$). For the remaining studied bimetallic nanoalloys, the occupied d-band center positions lie between those of the pristine Pd_{147} and Pt_{147} clusters. This suggests that their catalytic activity is likely to be intermediate between the catalytic performances of these two monometallic clusters. Additionally, it also reveals that the differences in occupied d-band center positions among the three structural patterns are minimal for both Pd–Ni and Pd–Pt nanoalloys, regardless of composition. This implies that the catalytic activity of these systems is not significantly influenced by changes in structural patterns. However, in practical applications, catalytic activity is primarily determined by the availability of active surface sites.

The effect of the structural patterns in catalytic performance, based on our d-band model based analysis, can be seen as the following.

- **Pd-poor configuration:** The core–shell structure is predicted to exhibit stronger interactions with adsorbate molecules in Pd–Cu, Pd–Rh, and Pd–Ir nanoalloys. The Janus structure is expected to enhance adsorbate binding in Pd–Co, Pd–Ni, and Pd–Pt nanoalloys. Meanwhile, the mixed structure appears to favor stronger adsorbate interactions in Pd–Ag and Pd–Au nanoalloys. The structure with the most up-shifting of the occupied d-band center follows the predicted order: Ni (Janus) > Cu (Core–Shell) > Co (Janus) > Rh (Core–Shell) > Pt (Janus) > Au (Mixed) > Ir (Core–Shell) >

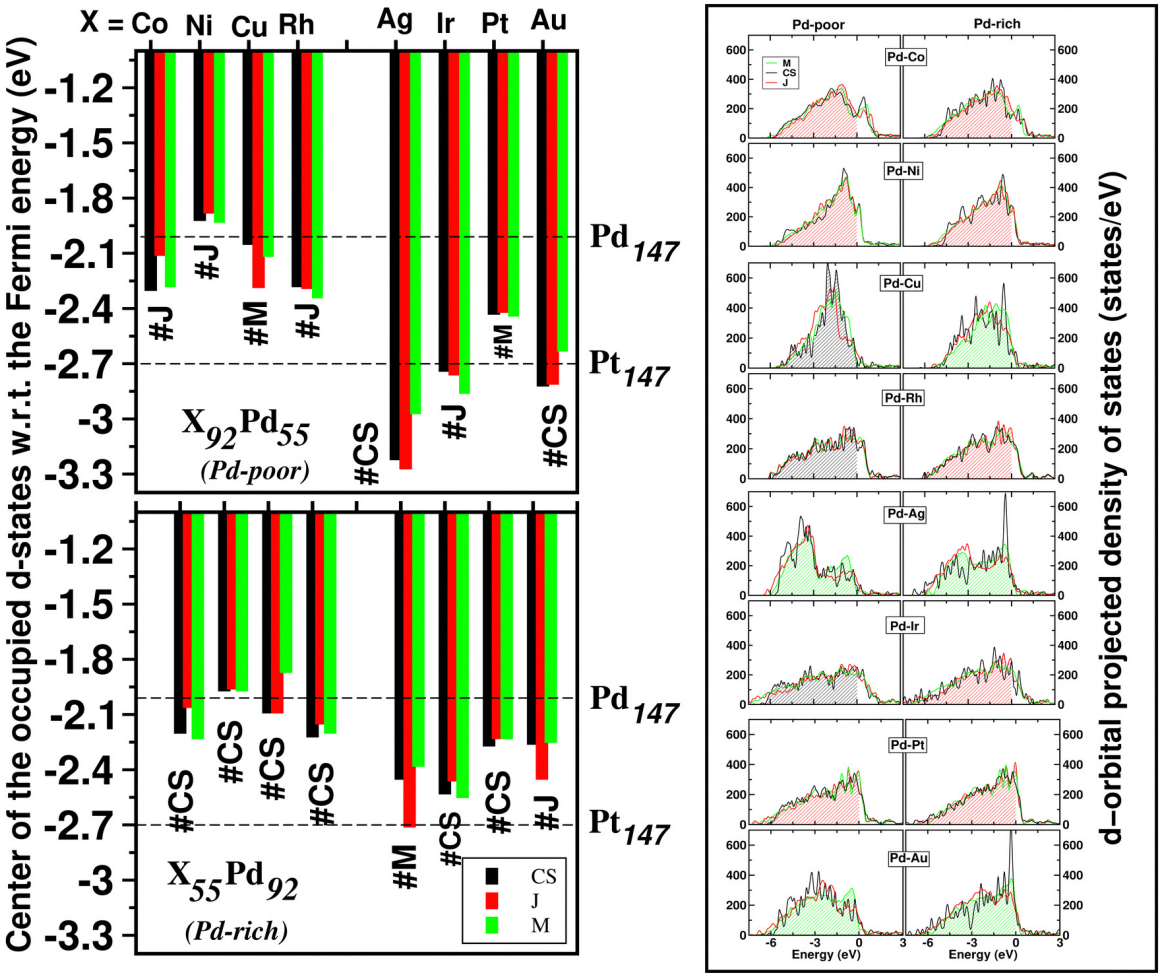

Figure 5.11: *The left panel shows the position of the center of gravity of the occupied d-band relative to the energy of the highest occupied level. The dashed horizontal lines mark the corresponding values for the pristine icosahedral Pt_{147} and Pd_{147} clusters. The right panel displays the d-PDOS for the three structures of each bimetallic nanoalloy. The shaded region highlights the occupied d-states for the structure that exhibits the greatest up-shifting of the occupied d-band center.*

Ag (Mixed).

- **Pd-rich configuration:** Janus structures exhibit escalated reaction with adsorbate molecules in case of alloying with Ni, Co, Rh, Pt, and Ir, while for mixed structures in cases of alloying with Cu, Au, and Ag. The structure with the most up-shifting of the occupied d-band center follows the predicted order: Cu (Mixed) > Ni (Janus) > Co (Janus) > Rh (Janus) > Pt (Janus) > Au (Mixed) > Ag (Mixed) > Ir (Janus).

Figure 5.11 also marks the energetically most stable structure for each bimetallic nanoalloy of either composition with the # symbol. Interestingly, in most cases, the structure exhibiting the highest catalytic activity does not correspond to the most energetically stable configuration. This aligns with the fundamental understanding that non-equilibrium systems tend to show enhanced catalytic activity[49]. The Janus structure appears more frequently

as the catalytically most active configuration, likely due to the presence of a highly strained interface between the two atomic species[50, 51]. According to our analysis of the occupied d-band center position, the bimetallic Pd–Ni nanoalloy exhibits the most significant up-shifting of the occupied d-center towards the Fermi level in both compositions.

5.3.4.2 Catalytic activity in CO molecule adsorption

To directly compare the catalytic activity relative to the pristine Pd_{147} cluster, we conduct a rigorous analysis of CO molecule adsorption on each structure of the bimetallic Pd–Ni nanoalloy for both compositions. To simplify our analysis, we focus on the adsorption of a carbon monoxide (CO) molecule at the atop position on a least-coordinated vertex site. For the pristine Pd_{147} cluster and the three structures of the Pd-rich bimetallic Pd–Ni cluster ($Pd_{92}Ni_{55}$), the CO molecule is adsorbed on a surface Pd site. In contrast, for the three structures of the Pd-poor cluster, CO adsorption occurs on a surface Ni site at the vertex position. The optimized CO-adsorbed structures are depicted in Figure 5.12. This choice of adsorption site is supported by previous studies, which have also found that CO adsorption at the atop position on a Pd surface is energetically favorable[52].

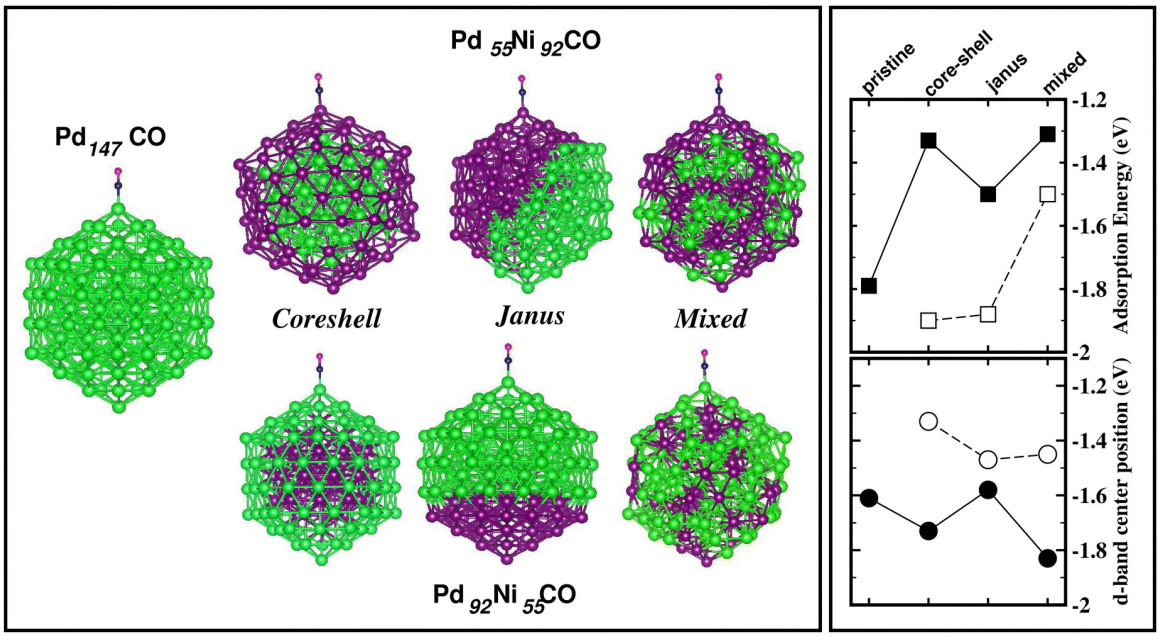

Figure 5.12: *The left panel presents the optimized configurations for CO adsorption on a surface Pd atom at the atop position for both the pristine Pd_{147} cluster and the three structural patterns of the $Pd_{92}Ni_{55}$ cluster. In the right panels, the top plot illustrates our calculated adsorption energy for these four systems, while the bottom plot displays the position of the d-band center with respect to the Fermi energy at the corresponding adsorption site. The filled symbols represent data for the pristine Pd_{147} cluster and the Pd-rich Pd–Ni nanoalloy, whereas empty symbols indicate those for the Pd-poor Pd–Ni nanoalloy.*

The adsorption energy for the CO-adsorbed systems is calculated using the formula E_{abs}

= E(Ni_mPd_nCO) - E(Ni_mPd_n) - E(CO). To interpret the observed trends in this, we also analyze the position of the occupied d-band center at the adsorption site. The calculated adsorption energy and corresponding d-band center positions are illustrated in Figure 5.12. Our calculated adsorption energy for the pristine Pd_{147} cluster ($E_{abs}(Pd_{147})$ = 1.79 eV) aligns well with previously reported values, such as the adsorption energy of a CO molecule on a Pt(111) surface (E_{abs}(Pt(111)/CO) = 1.64 eV)[53, 54] or on a Pt_{55} nanocluster($E_{abs}(Pt_{55}CO)$=2.04-2.37 eV) obtained via DFT-PBE calculations[52]. From Figure 5.12, it is evident that the Pd-poor Pd–Ni nanoalloy exhibits a higher adsorption energy compared to the Pd-rich Pd–Ni nanoalloy. This is primarily due to the stronger bond between the CO molecule and a surface Ni atom compared to a surface Pd atom. Additionally, the right panel illustrates the position of the occupied d-band center relative to the Fermi energy at the adsorption site. Notably, the occupied d-band center is up-shifted more for each structure of the Pd-poor Pd–Ni nanoalloy compared to that of the Pd-rich Pd–Ni nanoalloy. This trend aligns with the observed enhancement in adsorption energy for the Pd-poor bimetallic Pd–Ni nanoalloy.

5.3.5 Size effects

The calculated results discussed so far have been based on a cluster size of 147 atoms. To explore potential cluster size effects, a similar analysis is conducted on a 55-atom icosahedral geometry, specifically for the bimetallic Pd–Ni nanoalloy. This represents the second closed-shell structure, with 13 atoms in the core and 42 atoms on the surface. The analysis is done for the three structural patterns for two compositions: $Pd_{13}Ni_{42}$(Pd-poor) and $Pd_{42}Ni_{13}$ (Pd-rich).

The results, plotted in Figure 5.13, reveal that the relative stability order differs between compositions. For the $Pd_{13}Ni_{42}$ (Pd-poor) cluster, the stability follows the trend Janus > Mixed > Core–Shell. Conversely, for the $Pd_{42}Ni_{13}$ (Pd-rich) cluster, the order is Core–Shell > Mixed> Janus. These trends are consistent with the variation in surface energy, reinforcing the observed stability hierarchy. Additionally, the analysis of orbital hybridization in the 55-atom Pd–Ni nanocluster shows a clear pattern: the Janus structure exhibits the highest total hybridization, while the Core–Shell structure has the least. The position of the occupied d-band center relative to the Fermi level follows the same trend in catalytic activity among the three structural patterns of the 55-atom Pd–Ni nanoalloy as observed in the 147-atom Pd–Ni clusters, regardless of composition. This consistency across different cluster sizes suggests that cluster size does not significantly impact the overall trends in stability, orbital hybridization, or catalytic activity for the Pd–X bimetallic nanoalloys.

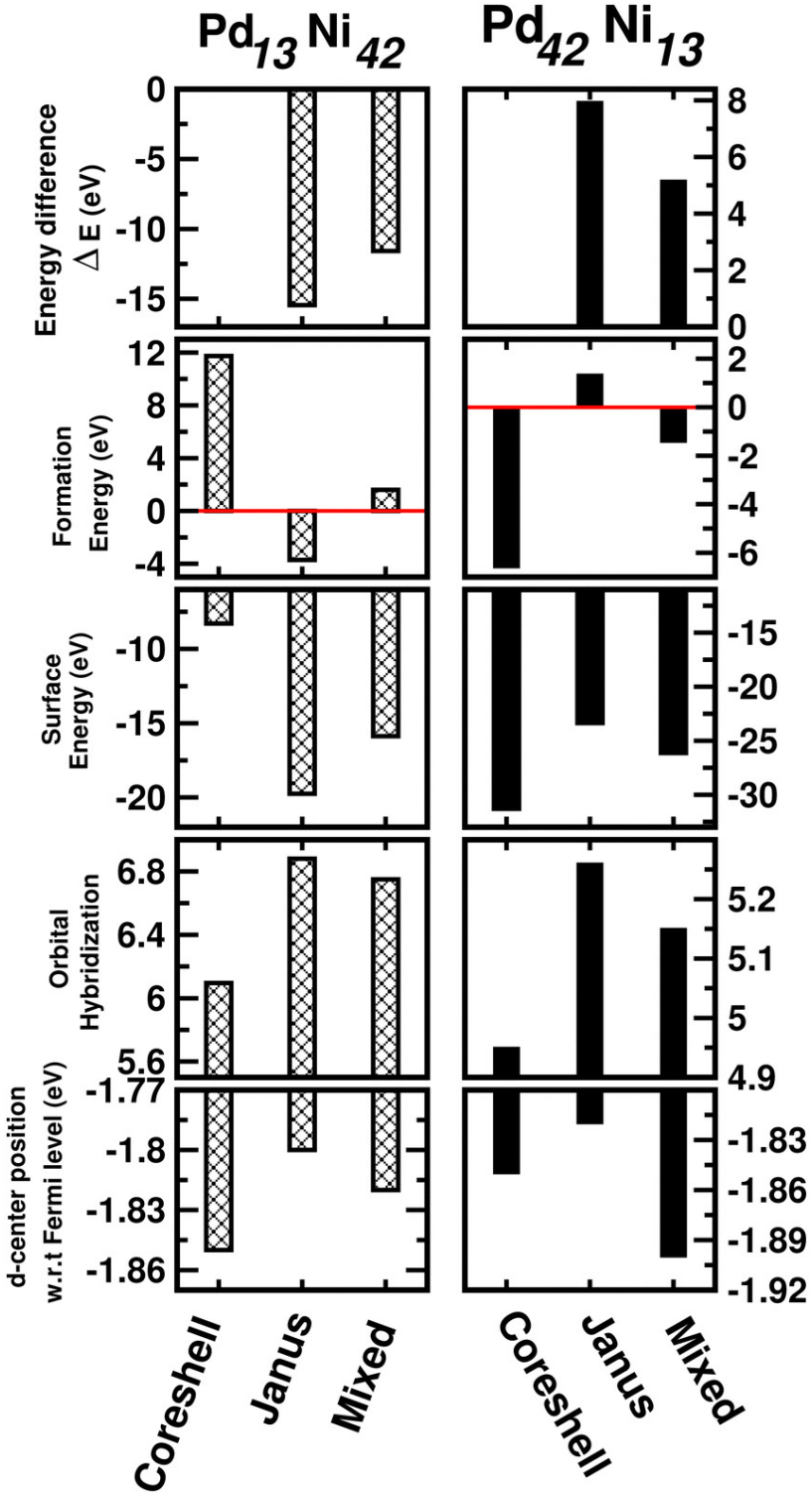

Figure 5.13: *Plot of total energy difference, formation energy, surface energy, orbital hybridization and position of the d-band center for the optimized core–shell, Janus and Mixed structures of the 55-atom sized bimetallic Pd–Ni cluster in both compositions.*

5.4 Summary and Discussions

This study builds on the previous work by investigating the effects of composition and size on nanocluster stability. We consider two composition limits(where the concentration of one component in the bimetallic cluster is greater than the other and vice versa) and two cluster sizes of 147 and 55 atoms. Based on DFT calculations, the structural stability, electronic properties and catalytic performance of eight bimetallic Pd–X nanoalloys (X = Co, Ni, Cu, Rh, Ag, Ir, Pt, Au) are explored. The Pd-X systems are chosen for exploration because they can be probable alternatives to Pt-based electrocatalysts, which are scarce and expensive. The relative stability of these structures is influenced by several factors. For Pd-3d pairs, the primary governing factor is the atomic-radius difference between Pd and X. In the case of Pd–Rh, Pd–Ir, and Pd–Pt pairs, stability is determined by a competition between atomic-radius difference and bulk cohesive energy. For Pd–Ag and Pd–Au pairs, surface energy differences play a dominant role. Using Integrated Crystal Orbital Hamiltonian Population (ICOHP) analysis, it is found that higher atom–atom covalency corresponds to greater structural stability, while the least stable structures exhibit weaker covalent bonding. The three structural patterns (Core–Shell, Janus, and Mixed) exhibit distinct orbital hybridization trends. The Janus structure shows the highest orbital hybridization, the Mixed structure has an intermediate level, and the Core–Shell structure has the least hybridization. The catalytic activity of these Pd–X nanoalloys is predicted by analyzing the shifting of the occupied d-band center position. Most Pd–X nanoalloys exhibit catalytic activity intermediate to that of pristine Pt and Pd clusters. However, in many cases, the catalytically most active structure differs from the energetically most stable structure, reinforcing the idea that non-equilibrium structures often exhibit higher catalytic efficiency. Among the studied nanoalloys, Pd–Ni shows the most significant up-shifting of the occupied d-band center, indicating a stronger interaction with adsorbate molecules. A CO adsorption study on Pd–Ni clusters confirms that the trend in adsorption energy aligns with the d-band center shifting, further validating the catalytic potential of Pd–Ni alloys. To investigate cluster size effects, the analysis is repeated for a 55-atom Pd–Ni cluster, showing that size does not significantly alter the observed trends in stability, hybridization, or catalytic activity.

Bibliography

[1] Manoj B Gawande, Anandarup Goswami, Tewodros Asefa, Huizhang Guo, Ankush V Biradar, Dong-Liang Peng, Radek Zboril, and Rajender S Varma. Core–shell nanoparticles: synthesis and applications in catalysis and electrocatalysis. Chemical Society Reviews, 44(21):7540–7590, 2015.

[2] Jaehoon Lim, Byeong Guk Jeong, Myeongjin Park, Jai Kyeong Kim, Jeffrey M Pietryga, Young-Shin Park, Victor I Klimov, Changhee Lee, Doh C Lee, and Wan Ki Bae. Influence of shell thickness on the performance of light-emitting devices based on CdSe/$Zn_{1-X}Cd_XS$ core/shell heterostructured quantum dots. Advanced Materials, 26(47):8034–8040, 2014.

[3] John Rick, Meng-Che Tsai, and Bing Joe Hwang. Biosensors incorporating bimetallic nanoparticles. Nanomaterials, 6(1):5, 2015.

[4] Karrina McNamara, Syed AM Tofail, Nanasaheb D Thorat, Joanna Bauer, and John JE Mulvihill. Biomedical applications of nanoalloys. Nanoalloys, pages 381–432, 2020.

[5] Sibin Duan and Rongming Wang. Bimetallic nanostructures with magnetic and noble metals and their physicochemical applications. Progress in Natural Science: Materials International, 23(2):113–126, 2013.

[6] Indranath Chakraborty and Thalappil Pradeep. Atomically precise clusters of noble metals: emerging link between atoms and nanoparticles. Chemical reviews, 117(12):8208–8271, 2017.

[7] Riccardo Ferrando, Julius Jellinek, and Roy L Johnston. Nanoalloys: from theory to applications of alloy clusters and nanoparticles. Chemical reviews, 108(3):845–910, 2008.

[8] Lin-Lin Wang and Duane D Johnson. Predicted trends of core- shell preferences for 132 late transition-metal binary-alloy nanoparticles. Journal of the American Chemical Society, 131(39):14023–14029, 2009.

[9] Aishwaryo Ghosh, Soumendu Datta, and Tanusri Saha-Dasgupta. Understanding the trend in core–shell preferences for bimetallic nanoclusters: A machine learning approach. The Journal of Physical Chemistry C, 126(15):6847–6853, 2022.

[10] Tianlei Wang, Arunabhiram Chutia, Dan JL Brett, Paul R Shearing, Guanjie He, Guoliang Chai, and Ivan P Parkin. Palladium alloys used as electrocatalysts for the oxygen reduction reaction. Energy & Environmental Science, 14(5):2639–2669, 2021.

[11] Robert Raja, Vladimir B Golovko, John M Thomas, Angel Berenguer-Murcia, Wuzong Zhou, Songhai Xie, and Brian FG Johnson. Highly efficient catalysts for the hydrogenation of nitro-substituted aromatics. Chemical communications, (15):2026–2028, 2005.

[12] Sue V Myers, Anatoly I Frenkel, and Richard M Crooks. X-ray absorption study of PdCu bimetallic alloy nanoparticles containing an average of 64 atoms. Chemistry of materials, 21(20):4824–4829, 2009.

[13] Neetha A Khan, Alexander Uhl, S Shaikhutdinov, and H-J Freund. Alumina supported model Pd–Ag catalysts: A combined STM, XPS, TPD and IRAS study. Surface science, 600(9):1849–1853, 2006.

[14] Soumendu Datta, Mukul Kabir, and Tanusri Saha-Dasgupta. Effects of shape and composition on the properties of CdS nanocrystals. Physical Review B—Condensed Matter and Materials Physics, 86(11):115307, 2012.

[15] Soumendu Datta, Mukul Kabir, Tanusri Saha-Dasgupta, and DD Sarma. First-principles study of structural stability and electronic structure of CdS nanoclusters. The Journal of Physical Chemistry C, 112(22):8206–8214, 2008.

[16] T Teranishi and M Miyake. Size control of palladium nanoparticles and their crystal structures. Chemistry of materials, 10(2):594–600, 1998.

[17] Alexis Front and Christine Mottet. Trends of chemical ordering in Pt-based nanoalloys. Theoretical Chemistry Accounts, 141(1):2, 2022.

[18] Stefan Maintz, Volker L Deringer, Andrei L Tchougréeff, and Richard Dronskowski. LOBSTER: A tool to extract chemical bonding from plane-wave based DFT, 2016.

[19] Jens K Nørskov, Frank Abild-Pedersen, Felix Studt, and Thomas Bligaard. Density functional theory in surface chemistry and catalysis. Proceedings of the National Academy of Sciences, 108(3):937–943, 2011.

[20] Siyu Zhou, Chenxiao Wang, and Younan Xia. Polyol synthesis of Pd icosahedral nanocrystals: Insights into the growth mechanism and size control. Chemistry of Materials, 34(11):5065–5073, 2022.

[21] G. Kresse and J. Hafner. Ab initio molecular dynamics for liquid metals. Physical Review B, 47(1):558–561, 1993.

[22] G. Kresse and J. Furthmüller. Efficient iterative schemes for ab initio total-energy calculations using a plane-wave basis set. Physical Review B, 54(16):11169–11186, 1996.

[23] David R Lide. CRC handbook of chemistry and physics, volume 85. CRC press, 2004.

[24] Marcel HF Sluiter, C Colinet, and Alain Pasturel. Ab initio calculation of the phase stability in Au-Pd and Ag-Pt alloys. Physical Review B—Condensed Matter and Materials Physics, 73(17):174204, 2006.

[25] LG Wang and Alex Zunger. Structure, structural phase transitions, mechanical properties, defects, etc.-Why are the 3d-5d compounds CuAu and NiPt stable, whereas the 3d-4d compounds CuAg and NiPd are not . Physical Review-Section B-Condensed Matter, 67(9):92103–92103, 2003.

[26] Zahra Valizadeh and Mohsen Abbaspour. Surface energy, relative stability, and structural properties of Au-Pt, Au-Rh, Au-Cu, and Au-Pd nanoclusters created in inert-gas condensation process using MD simulation. Journal of Physics and Chemistry of Solids, 144:109480, 2020.

[27] J Magnus Rahm and Paul Erhart. Understanding chemical ordering in bimetallic nanoparticles from atomic-scale simulations: The competition between bulk, surface, and strain. The Journal of Physical Chemistry C, 122(49):28439–28445, 2018.

[28] ZJ Wu, B Han, ZW Dai, and PC Jin. Electronic properties of rhenium, osmium and iridium dimers by density functional methods. Chemical physics letters, 403(4-6):367–371, 2005.

[29] Arthur Kant and Bernard Strauss. Dissociation energies of diatomic molecules of the transition elements. II. Titanium, chromium, manganese, and cobalt. The Journal of Chemical Physics, 41(12):3806–3808, 1964.

[30] Alexander Grushow and Kent M Ervin. Ligand and metal binding energies in platinum carbonyl cluster anions: Collision-induced dissociation of Pt_m^- and $Pt_m(CO)_{n^-}$. The Journal of chemical physics, 106(23):9580–9593, 1997.

[31] Chang-Hong Chien, Estela Blaisten-Barojas, and Mark R Pederson. Many-body potential and structure for rhodium clusters. The Journal of Chemical Physics, 112(5):2301–2307, 2000.

[32] Gregory A Bishea and Michael D Morse. Spectroscopic studies of jet-cooled AgAu and Au_2. The Journal of chemical physics, 95(8):5646–5659, 1991.

[33] Eric A Rohlfing and James J Valentini. UV laser excited fluorescence spectroscopy of the jet-cooled copper dimer. The Journal of chemical physics, 84(12):6560–6566, 1986.

[34] E Curotto, Alexander Matro, David L Freeman, and JD Doll. A semi-empirical potential for simulations of transition metal clusters: minima and isomers of Ni_n (n= 2–13) and their hydrides. The Journal of chemical physics, 108(2):729–742, 1998.

[35] René Fournier. Theoretical study of the structure of silver clusters. The Journal of chemical physics, 115(5):2165–2177, 2001.

[36] Joe Ho, Kent M Ervin, Mark L Polak, Mary K Gilles, and WC Lineberger. A study of the electronic structures of Pd^{-2} and Pd^2 by photoelectron spectroscopy. The Journal of chemical physics, 95(7):4845–4853, 1991.

[37] F Baletto, C Mottet, and R Ferrando. Growth simulations of silver shells on copper and palladium nanoclusters. Physical Review B, 66(15):155420, 2002.

[38] Georg Daniel Förster, Magali Benoit, and Julien Lam. Alloy, Janus and core–shell nanoparticles: numerical modeling of their nucleation and growth in physical synthesis. Physical Chemistry Chemical Physics, 21(41):22774–22781, 2019.

[39] Lin-Lin Wang and Duane D Johnson. Predicted trends of core- shell preferences for 132 late transition-metal binary-alloy nanoparticles. Journal of the American Chemical Society, 131(39):14023–14029, 2009.

[40] Soumendu Datta and Tanusri Saha-Dasgupta. Structural, electronic and magnetic properties of transition metal binary alloy clusters with isoelectronic components: case study with Mn_mTc_n, Ti_mZr_n and Mn_mRe_n. Journal of Physics: Condensed Matter, 25(22):225302, 2013.

[41] Hannu Häkkinen, Michael Moseler, and Uzi Landman. Bonding in Cu, Ag, and Au clusters: relativistic effects, trends, and surprises. Physical review letters, 89(3):033401, 2002.

[42] CM Chang and MY Chou. Alternative low-symmetry structure for 13-atom metal clusters. Physical review letters, 93(13):133401, 2004.

[43] Carsten Stegelmann, Anders Andreasen, and Charles T Campbell. Degree of rate control: how much the energies of intermediates and transition states control rates. Journal of the American Chemical Society, 131(23):8077–8082, 2009.

[44] Robert Pestman, Wei Chen, and Emiel Hensen. Insight into the rate-determining step and active sites in the Fischer–Tropsch reaction over cobalt catalysts. ACS Catalysis, 9(5):4189–4195, 2019.

[45] Angelos Michaelides, Z-P Liu, CJ Zhang, Ali Alavi, David A King, and Peijun Hu. Identification of general linear relationships between activation energies and enthalpy

changes for dissociation reactions at surfaces. Journal of the American Chemical Society, 125(13):3704–3705, 2003.

[46] Jens K Nørskov, Thomas Bligaard, Ashildur Logadottir, S Bahn, Lars B Hansen, Mikkel Bollinger, H Bengaard, Bjørk Hammer, Z Sljivancanin, Manos Mavrikakis, et al. Universality in heterogeneous catalysis. Journal of catalysis, 209(2):275–278, 2002.

[47] Thomas Bligaard, Jens Kehlet Nørskov, Søren Dahl, J Matthiesen, Claus H Christensen, and JJJoC Sehested. The Brønsted–evans–polanyi relation and the volcano curve in heterogeneous catalysis. Journal of catalysis, 224(1):206–217, 2004.

[48] Eva M Fernández, Poul G Moses, Anja Toftelund, Heine A Hansen, José I Martínez, Frank Abild-Pedersen, Jesper Kleis, Berit Hinnemann, Jan Rossmeisl, Thomas Bligaard, et al. Scaling relationships for adsorption energies on transition metal oxide, sulfide, and nitride surfaces. Angewandte Chemie International Edition, 47(25):4683–4686, 2008.

[49] Rui Chen, Simona Neri, and Leonard J Prins. Enhanced catalytic activity under non-equilibrium conditions. Nature Nanotechnology, 15(10):868–874, 2020.

[50] Taekyung Kim, Jongsik Park, Yongju Hong, Aram Oh, Hyunsuck Baik, and Kwangyeol Lee. Janus to Core–Shell to Janus: Facile Cation Movement in $Cu_{2-x}S/Ag_2S$ Hexagonal Nanoplates Induced by Surface Strain Control. ACS nano, 13(10):11834–11842, 2019.

[51] H-Y He, Z He, and Q Shen. Novel assembly of Janus RGO/1 T-SeMoS nanosheets structures showing high-efficient electrocatalytic activity for hydrogen evolution. Colloid and Interface Science Communications, 45:100509, 2021.

[52] Diego Guedes-Sobrinho, Rafael LH Freire, Anderson S Chaves, and Juarez LF Da Silva. Ab initio Investigation of the Role of CO Adsorption on the Physical Properties of 55-atom PtCo Nanoalloys. The Journal of Physical Chemistry C, 121(49):27721–27732, 2017.

[53] Laurids Schimka, Judith Harl, Alessandro Stroppa, Andreas Grüneis, Martijn Marsman, Florian Mittendorfer, and Georg Kresse. Accurate surface and adsorption energies from many-body perturbation theory. Nature materials, 9(9):741–744, 2010.

[54] Yun Wang, Stefano de Gironcoli, Noel S Hush, and Jeffrey R Reimers. Successful a priori modeling of CO adsorption on Pt (111) using periodic hybrid density functional theory. Journal of the American Chemical Society, 129(34):10402–10407, 2007.

6

Machine-learning prediction of the formation of atomic gold wires by mechanically controlled break junctions

6.1 Introduction and Motivation

The thinnest metallic wire possible consists of one-dimensional array of metal atoms connected between two metal leads. Due to relativistic effects[1–3], the formation of such atomic chains is commonly observed in break-junction experiments involving late 5d metals like Ir, Pt, and Au, particularly at cryogenic temperatures[4–7]. These atomic chains, as ideal one-dimensional systems, serve as a valuable platform for studying quantum mechanical transport[8–12], atomistic magnetism[13–18], and many-body phases driven by strong Coulomb interactions, such as the Tomonaga–Luttinger liquid[19–21]. Notably, these chains exhibit remarkable mechanical stability, lasting up to an hour, and can sustain extremely high current densities, reaching approximately 2.1×10^{15} A/m^2 at cryogenic temperatures[22, 23].

In mechanically controlled break-junction(MCBJ) experiments, thousands of junctions are typically created and their conductance measured, resulting in a vast number of distinct conductance traces. A crucial step toward utilizing atomic chains for desired functionalities is understanding and controlling external factors that influence chain formation. The electric field and stretching rate in the break-junction setup have been shown to affect both the mechanical stability and transport properties of these chains[24–27]. The electric field

*This chapter is based on publication: **Aishwaryo Ghosh**†, Biswajit Pabi†, Atindra Nath Pal and Tanusri Saha-Dasgupta, Nanoscale 15,17045-17054(2023). († These authors contributed equally to this work)

is supplied by applying a bias voltage across the atomic junction to make conductance measurements, while the stretching rate defines the speed at which a wire sample is effectively pulled apart to form a chain. However, the combined effect of these factors has not been thoroughly investigated with the goal of optimizing atomic chain formation. Standard histogram analysis often falls short in identifying the specific characteristics of conductance traces influenced by the nanoscale structure of the metal electrode before the rupture of the metal point contact.

An effective approach to address this challenge is the use of machine learning, which leverages computational power to identify patterns within system features and their outcomes. Machine learning has gained popularity as an efficient optimization tool, particularly when dealing with large datasets. Given the extensive data generated in break-junction experiments, machine learning is well-suited for optimizing atomic wire formation. Recent studies have already demonstrated the use of machine learning in predicting single-molecule conductance[28–34]. Deep learning methods have also been used to identify molecular junction characteristics in scanning tunneling microscope-based break junctions[35–38]. In this study, we apply a combination of supervised and unsupervised machine learning, along with molecular dynamics (MD) simulations, to investigate the formation of long atomic chains of gold on the experimental dataset generated in MCBJ experiments conducted by the group of Professor Atindra Nath Pal. The details of the experiment can be found at [39].

6.2 Methodology

To predict the optimal conditions for chain formation, a supervised machine learning algorithm is employed(for details, see section 2.2.1.1). The random forest algorithm, implemented in the Scikit-learn[40] package, is used with the number of trees in the forest set to 500(determined through a grid search method) with no limit on tree depths. The model's fidelity is evaluated using 10-fold cross-validation, with the correlation coefficient serving as the assessment metric. For feature extraction, an unsupervised learning approach based on a stacked auto-encoder is adopted (details in section 2.2.2.2.1). A clustering algorithm is applied to differentiate various types of traces based on extracted features, with the elbow method used to determine the optimal number of clusters(details in section 2.2.2.3). Finally, principal component analysis is performed to project the multidimensional feature space into a lower-dimensional data representation for facilitating visualization, while preserving essential information(details in section 2.2.2.1).

The experimental setup is modeled using density functional theory-based ab initio molec-

ular dynamics calculations within the framework of the plane wave pseudo-potential approach, as implemented in the Vienna Ab Initio Simulation Package (VASP)[41, 42].

6.3 Results and Discussions

6.3.1 Description of dataset

The conductance of a gold atomic junction is measured at 77K by gradually and consistently increasing the interelectrode separation. The mechanism breaks the sample gold wire from its weak spot, which is then relaxed again to reestablish the contact(schematically represented in Figure 6.1(A)). This process is repeated multiple times, with each cycle forming a new junction distinct from the previous one. The conductance vs displacement data recorded during a complete cycle constitutes a conductance trace. Conductance traces at varying breaking speeds and bias voltages are recorded for two independent samples, resulting in two distinct data sets (Set-1 and Set-2). For Set-1, the stretching rate varies between 0.5 nm/s to 12.5 nm/s. At each rate, conductance measurements are taken across bias voltages ranging from 25 mV to 200 mV in 25 mV steps, yielding 72 unique combinations. For each combination, 1000 consecutive conductance traces are collected. Based on insights from Set-1, Set-2 focuses on lower stretching rates between 1 nm/s and 5 nm/s (in 1 nm/s steps) and bias voltages from 10 mV to 425 mV, resulting in 90 different combinations—again with 1000 traces per combination. Thus, in totality, there are 72000(90000) traces in Set1(Set2). A few representative traces are shown in Figure 6.1(B), where a flat conductance plateau at $1.0G_0$ (G_0, quantum of conductance) demonstrates the formation of a single atomic junction at its narrowest constriction[43–45].

6.3.2 Optimal conditions for long chain formation

The first step in setting up a supervised machine learning model is to create a training dataset consisting of instances or data points and descriptors or attributes that describe each data point. The attributes chosen for this study are bias voltage and stretching rate, the two most important external parameters in the MCBJ experiment. As discussed earlier, in total, 72 different combinations of bias voltages and stretching rates are used for Set-1, while 90 combinations are used for Set-2. The development of a machine learning model also requires defining a target. In line with the goal of the present study, the probability percentage of forming an atomic chain within a length range and at a given combination of bias and breaking speed is set as the corresponding target. We consider several ranges of chain lengths: 0–2 $\AA$, 2–4 $\AA$, 4–6 $\AA$, 6–8 $\AA$, and 8–10 $\AA$. The atomic radius of gold is 1.46 $\AA$, and experimentally, the distance between gold atoms in a dimer is found to be 2.5 ± 0.2 $\AA$[46].

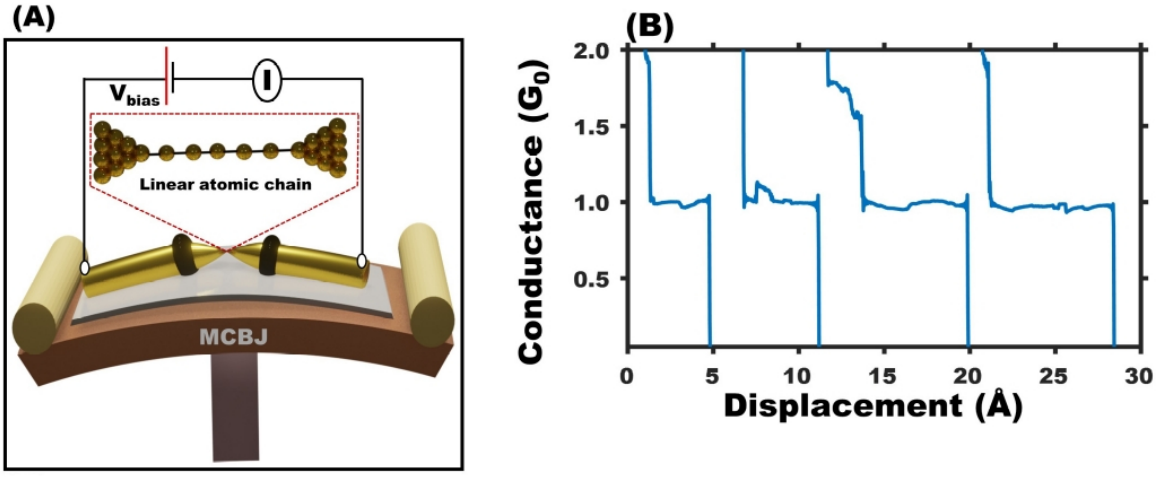

Figure 6.1: *(A) The schematic layout of the three-point bending configuration of the MCBJ setup illustrating a linear atomic chain at the narrowest cross-section of the junctions. (B) Representative conductance displacement breaking traces of the gold atomic junction, with traces shifted horizontally for better visualization.*

Thus, a distance of more than 4 $\AA$ between the electrodes corresponds to a chain of three or more atoms. For a particular bias voltage and stretching rate, the probability percentage of forming a chain within a specific length range is calculated by determining the percentage of traces recorded at that voltage and stretching rate that correspond to the given length range. Among various supervised regression machine learning models, we choose the random forest model, which has been successfully applied to different applications[47–49]. The correlation coefficient is found to be 0.94, with a mean absolute error of approximately 3%. The model is then used to predict the probabilities of forming chains of lengths between 4 $\AA$ and 10 $\AA$ at intermediate bias voltages and stretching rates that were not directly sampled during experimentation. The probabilities of chain formation as a function of bias voltage and stretching rate, derived from machine learning analysis on Set-1(Set-2), are shown in contour plots in Figure 6.2 (inset of Figure 6.2). Chains of lengths between 4 and 10 $\AA$ for Set-1 are consistently formed around a bias voltage of 25–75 mV and a stretching rate of 2–4 nm/s, with probabilities significantly higher (0.8 and above) than in other conditions. A similar trend is observed for Set-2, which focuses on the low-speed regions (approximately 1–5 nm/s). The highest probabilities are found around a bias voltage of approximately 50 mV and a stretching rate of approximately 3 nm/s. These results indicate that the optimal conditions for forming longer atomic chains lie in the low bias voltage and low stretching rate regime. The ML-predicted values for optimized settings can be explained by the combined effects of current-induced embrittlement[50] and the stretching rate-dependent breaking mechanism of atomic contacts[51]. The influence of bias voltage or current operates in two ways. First, the current-induced force, resulting from electron scattering, weakens the bonds in the chain, reducing its tensile strength. Second, a large

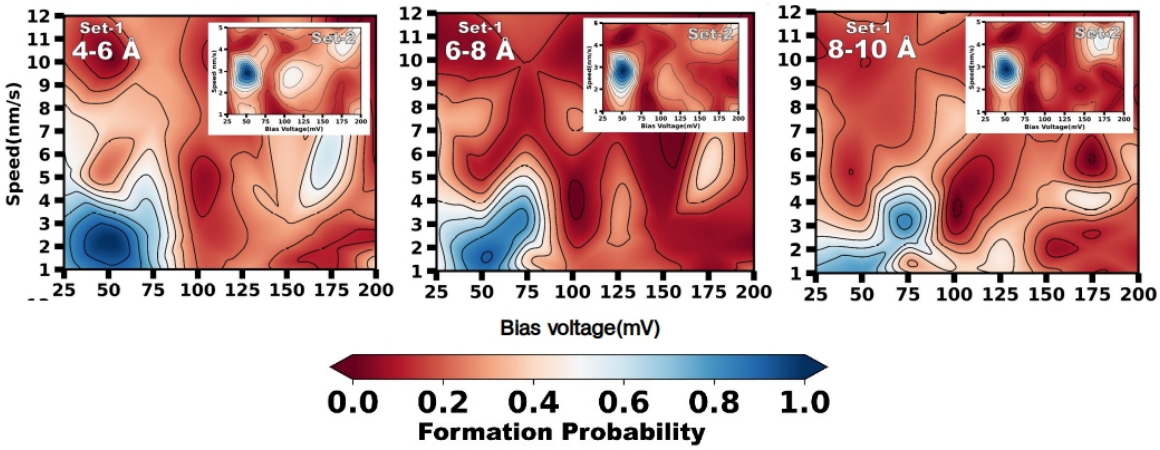

Figure 6.2: *Chain formation probabilities for three different ranges of chain length are analyzed as a function of bias voltage and stretching rate for Set-1, with the corresponding results for Set-2 shown in the inset.*

current increases the effective temperature of the chain through local ionic heating, even in the ballistic transport regime, as suggested by Todorov[52]. As a result, the probability of thermally activated fracture increases with rising current[50], necessitating a delicate balance. Similarly, the optimal stretching rates of 2–4 nm/s fall within an intermediate range that allows for sufficient structural relaxation near the contacts during mechanical elongation, facilitating the formation of longer chains. At higher stretching speeds, this relaxation may not occur, as the junction may break before reaching a stable configuration due to excessive mechanical loading. On the other hand, if the stretching rate is too slow or comparable to atomic diffusion velocity[51], the mechanical elongation completely relaxes through atomic rearrangements near the contacts, rather than pulling atoms from the atomic reservoir.

It is important to note that the diameter of the starting Au wire ($\approx$ 100 μm) and the size or shape of the notch (around 30–40 μm) do not significantly affect chain formation, as these dimensions are in the bulk limit, whereas the study focuses on the atomic limit. Temperature is also expected to play a crucial role in the chain formation process. However, our specific interest lies in optimizing the chain formation phenomena at a given temperature. While the obtained optimal conditions may vary at different temperatures, the fundamental mechanism uncovered in our study should remain unchanged. Additionally, the intrinsic mechanical vibrations of the experimental setup also influence the lifetime of atomic contacts, although quantifying this effect is difficult.

6.3.3 Trace features

After establishing the optimal bias and speed settings for long chain formation, we next examine whether specific characteristics in the conductance–displacement traces correspond to particular electrode configurations that lead to such long chains. To answer this, individual traces must be analyzed, as they contain detailed information about atomic chain formation that is not immediately evident. Each trace represents a unique formation and breaking sequence of an atomic junction. The most crucial aspect is the shape and length of the conductance plateaus near the conductance value of $1G_0$, which provide insights into atomic arrangements just before breaking. The main challenge is extracting relevant chain formation information from a large and highly varied dataset of traces. Since there is no prior knowledge of possible atomic junction variations formed during the experiment, an unsupervised machine learning approach is the most suitable method. In this context, deep learning methods[53], which have recently gained prominence in solving scientific and engineering problems[54], are applied in an unsupervised scheme. These methods have been widely used in various fields, including natural language processing[55], speech recognition[56], and image recognition[57], to analyze and extract information from raw data[58]. Unlike supervised machine learning, (unsupervised) deep learning can uncover complex, non-linear relationships between input and output without the need for explicit feature construction. For the next step, focusing on Set-2, we apply an unsupervised deep learning algorithm similar to that of Huang et al[59] to analyze the inherent characteristics of experimental conductance traces and classify them accordingly. The first step of this analysis involves pre-processing the experimental data to ensure that each conductance trace has the same dimensionality. This is achieved by selecting the same number of equispaced data points M from each trace within the conductance range of $0.7G_0$ to $1.4G_0$, the region that primarily encodes information about atomic chain formation before breaking. A value of M = 100 is found to provide sufficient accuracy without adding computational overhead. Consequently, traces with fewer than M data points in the specified range are discarded, reducing the original dataset from approximately 90,000 to around 22,000. This results in a modified dataset of the form $G_n(m)$; $n \in 1,2,\ldots N$; $m \in 1,2,\ldots M$, where n represents the trace index, N is the total number of traces in the dataset and m denotes the points in each trace. These data are then used in a stacked auto-encoder for feature extraction. The working principle of an autoencoder can be found in Section 2.2.2.2. Certain algorithm-specific hyperparameters are associated with the training of the stacked autoencoder model. These include the size of the code layer or feature space, the number of layers in both the encoder and decoder, and the number of nodes in each layer. The detailed network architecture is provided in Table 6.1. The Adam optimizer is used in the model. Additionally,

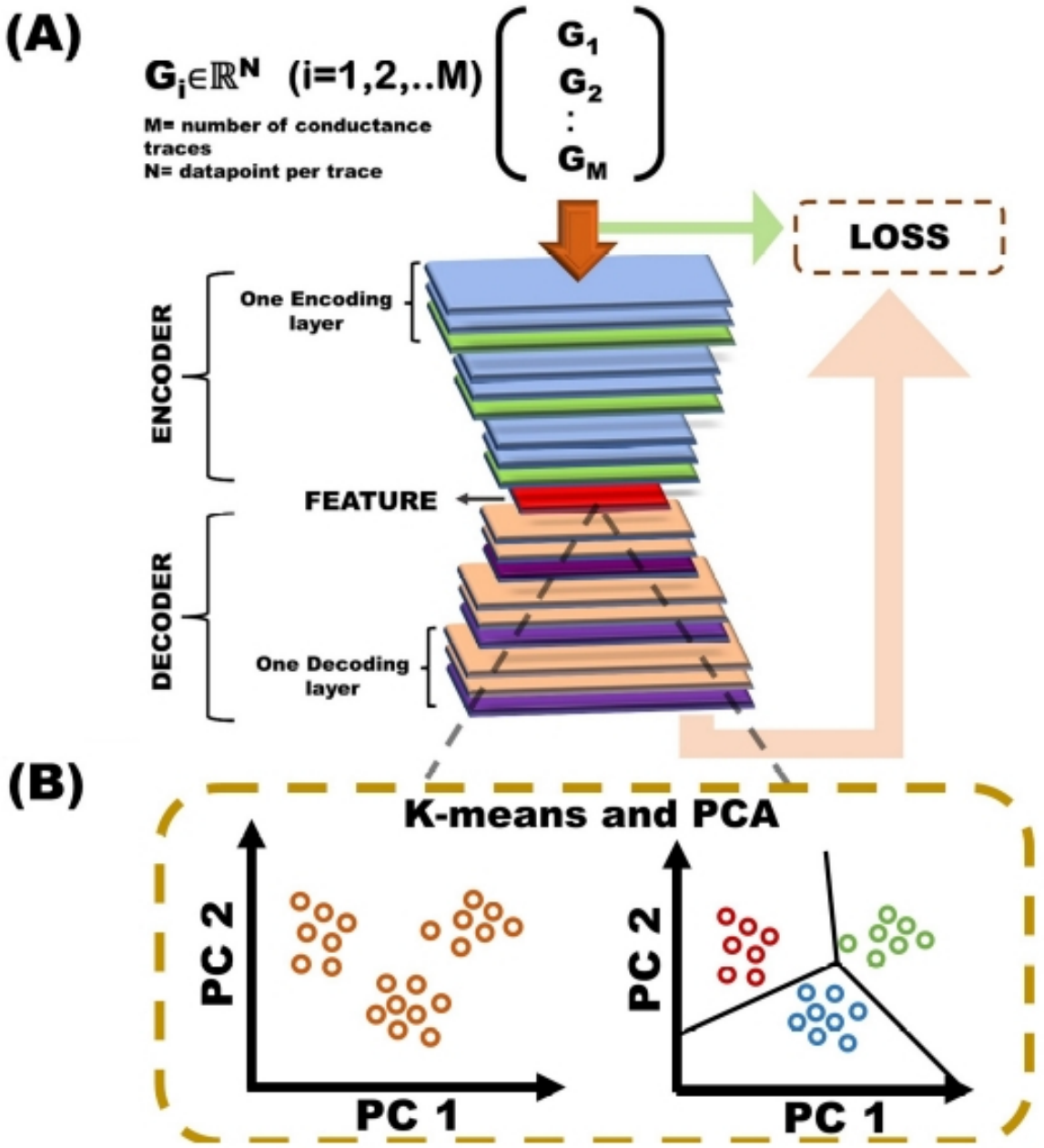

Figure 6.3: *(A) Schematic illustration of the autoencoder algorithm used to extract latent features from experimental data traces. (B) Schematic representation of the K-means clustering combined with Principal Component Analysis (PCA) for grouping and visualizing the extracted features in a reduced-dimensional space.*

two key parameters required for neural network training, the learning rate and batch size, are set to 1e-5 and 100, respectively. The model is trained for 400 epochs, beyond which the loss function saturates. Next, a K-means clustering algorithm(see section 2.2.2.3) is used to group the data based on the similarity of the extracted features. Since clustering is performed based on the multidimensional feature space, a reduced representation of this space is needed for ease of interpretation while maintaining maximum data variance. This is achieved using the Principal Component Analysis (PCA) algorithm(see section 2.2.2.1).

	Layer Name	No of Nodes	Activation function
Encoder	Input Layer	100	None
	Hidden Layer 1	75	Sigmoid
	Hidden Layer 2	50	Sigmoid
Feature	Feature Layer	25	Sigmoid
Decoder	Hidden Layer 1	50	Sigmoid
	Hidden Layer 2	75	Sigmoid
	Output Layer	100	None

Table 6.1: *The network architecture of the stacked auto-encoder model*

The clustered data are projected onto the first two principal components. The combination of feature extraction (Figure 6.3(A)) and the clustering exercise (Figure 6.3(B)) results in three distinct cluster classes with 5614, 7032, and 9225 instances, which are labeled Type0, Type1, and Type2, respectively. The clustered and PC-projected traces are shown in Figure 6.4(A). To probe the distinctive characteristics of these three types, a few representative conductance displacement traces for each case are shown in Figure 6.4(B). The traces are shifted horizontally for better visualization. One immediate observation is that the plateaus of Type1 are flat at $1.0G_0$, in contrast to the slanted plateaus of Type0 and Type2. To gain a clearer picture from a large number of statistically independent configurations, 2D conductance displacement histograms and 1D conductance histograms are presented in the left and right panels for each distinguished type in Figure 6.4(C). The histograms of Type0 reveal two peaks around $1.0G_0$, with the conductance plateaus extending over a broad range. In contrast, Type1 exhibits a sharp and highly intense peak centered around $1.0G_0$ with a symmetric distribution. Meanwhile, Type2 plateaus show an asymmetric distribution of weight around the sharp, high-intensity peak. A comparison of the 1D histograms of the three types is presented in Figure 6.5, clearly demonstrating the characteristic differences among them.

It has been explored that the electrical conductance of an atomic contact is closely linked to its structural configuration[60]. A monomeric contact exhibits conductance values ranging from $1.2G_0$ to $0.76G_0$, with an average of $0.97G_0$. In contrast, a dimeric contact has a narrower conductance range of $0.99G_0$ to $0.85G_0$, averaging at $0.92G_0$[61]. This suggests that monomeric contacts exhibit a broader range of conductance values compared to dimers. The reason is straightforward: in a monomeric contact, the central atom's neighboring atoms can adopt multiple degenerate structures, leading to greater variability. In contrast, a dimeric contact is constrained by the specific arrangement of its two atoms. Additionally, monomers can be positioned either closer to or farther from the rest of the contact, further

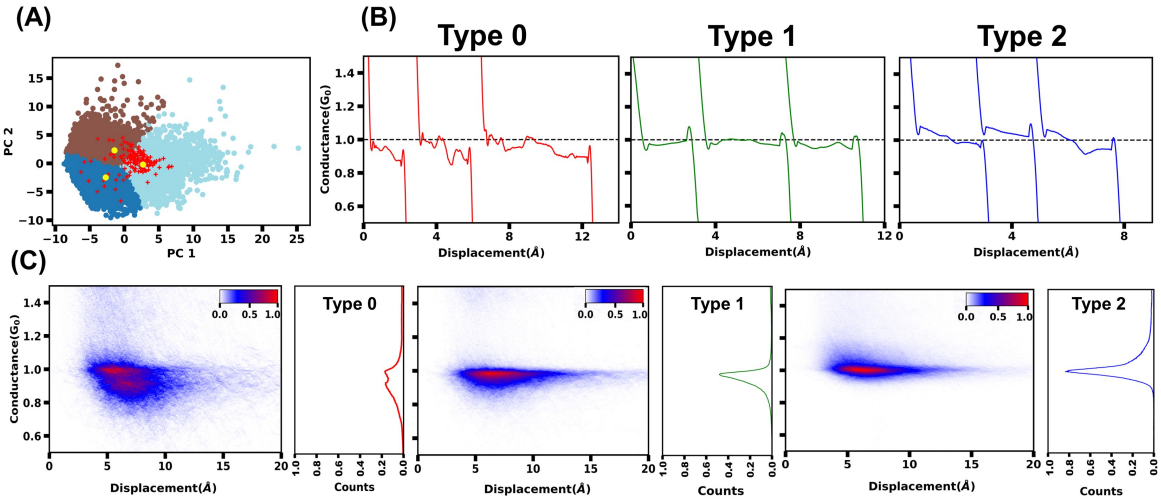

Figure 6.4: *(A) The cluster classes of experimental traces projected onto the first two principal components (PC1 and PC2) of the feature space. The yellow points indicate the cluster centers. The dark blue, brown, and cyan circles correspond to Type0, Type1, and Type2, respectively. The traces recorded at 50 mV and 3 nm/s are represented by red symbols. (B) Three distinct classes of conductance displacement traces—Type0 (red), Type1 (green), and Type2 (blue). (C) Conductance displacement histogram (left panel) and conductance histogram (right panel) corresponding to the three different classes.*

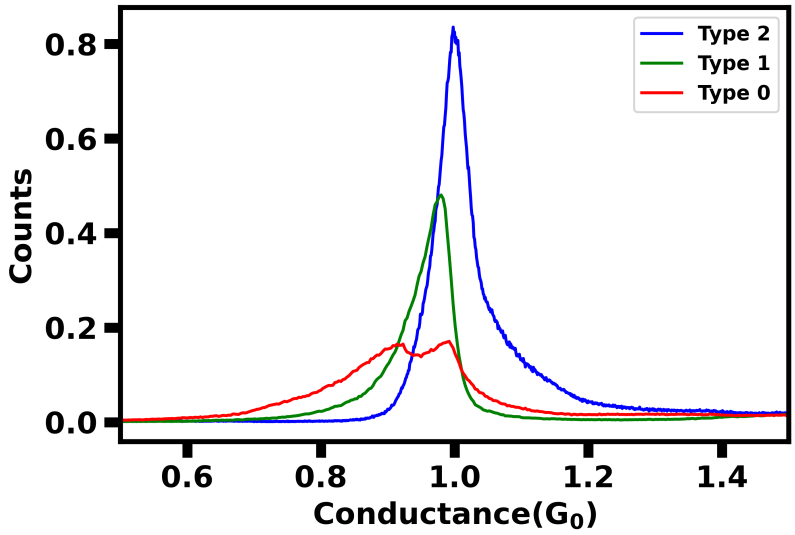

Figure 6.5: *A comparison of the 1D histograms of three types demonstrating the characteristics difference among them.*

contributing to their wider conductance distribution[61]. Therefore, the two peaks observed in the histogram of Type0 likely result from the formation of stable monomeric and dimeric contacts during stretching. In contrast, a closer look at the 2D and 1D histograms of Type2 reveals that its initial conductance value exceeds $1.0G_0$ but decreases to $1.0G_0$ or even lower as stretching progresses. This behavior differs from that of Type1, where the plateaus begin at or below $1.0G_0$ and remain relatively unchanged during stretching. The characteristics of Type1 and Type2 can be understood by linking the experimentally measured transmission

channel contributions of gold atomic contacts to their conductance, as reported in previous studies[60, 62–64]. According to these studies, atomic contacts dominated by a single channel at the initial stage exhibit conductance values ranging from $0.3G_0$ to $0.9G_0$, which aligns with our observations for Type1 contacts. In cases where two channels are initially involved but reduce to one upon stretching, the conductance can reach up to $1.2G_0$, similar to our Type2 contacts. Additionally, theoretical simulations suggest that these two channels arise from contributions of two atoms at the narrowest junction, displaced relative to each other[60]. Therefore, the initial geometric configuration of the atomic junctions plays a crucial role in defining the distinct conductance traces observed in Type1 and Type2.

6.4 Molecular understanding: ab initio MD simulations

After classifying the traces, we analyze which category is most associated with the formation of long atomic chains. As shown in Figure 6.4(A), $\approx 75\%$ of these traces belong to Type2. This suggests that the unique structural characteristics of Type2 junctions play a crucial role in promoting long-chain formation. As previously discussed, Type2 junctions likely exhibit an initial double-contact-like structure that gradually transitions into a single-channel configuration. This structural evolution helps sustain the chain for longer lengths before eventual breaking. To support our findings, we utilize ab-initio molecular dynamics simulations[65, 66]. The objective is to investigate the microscopic influence of the initial atomic arrangement on chain formation. For this, we model the experimental setup using density functional theory-based ab-initio electronic structure calculations within the plane-wave pseudo-potential framework, as implemented in the Vienna ab-initio Simulation Package (VASP)[41, 42]. In our simulations, a gold slab is used for constructing initial atomic junction structures. These structures include single-atom and two-atom configurations to replicate single-contact and double-contact-like atomic junctions and their evolution under mechanical stretching. The system is separated by a 15 $\AA$ vacuum and maintained at a fixed temperature using an NVT canonical ensemble with a Nosé–Hoover thermostat[67–69]. The stretching process is simulated by symmetrically increasing the separation between the gold electrodes in incremental steps. The effective stretching speed is ≈ 1 m/s, and the elongation continues until the atomic contacts rupture. It is important to note that due to the computational expense of ab initio molecular dynamics (AIMD) simulations, the stretching speed is artificially increased to observe the growth process within a feasible timeframe. This adjustment is justified, as the primary objective of the AIMD simulation is to gain microscopic insights into the influence of initial atomic arrangements rather than to precisely replicate experimental conditions. Similar approaches have been employed in lierature[70].

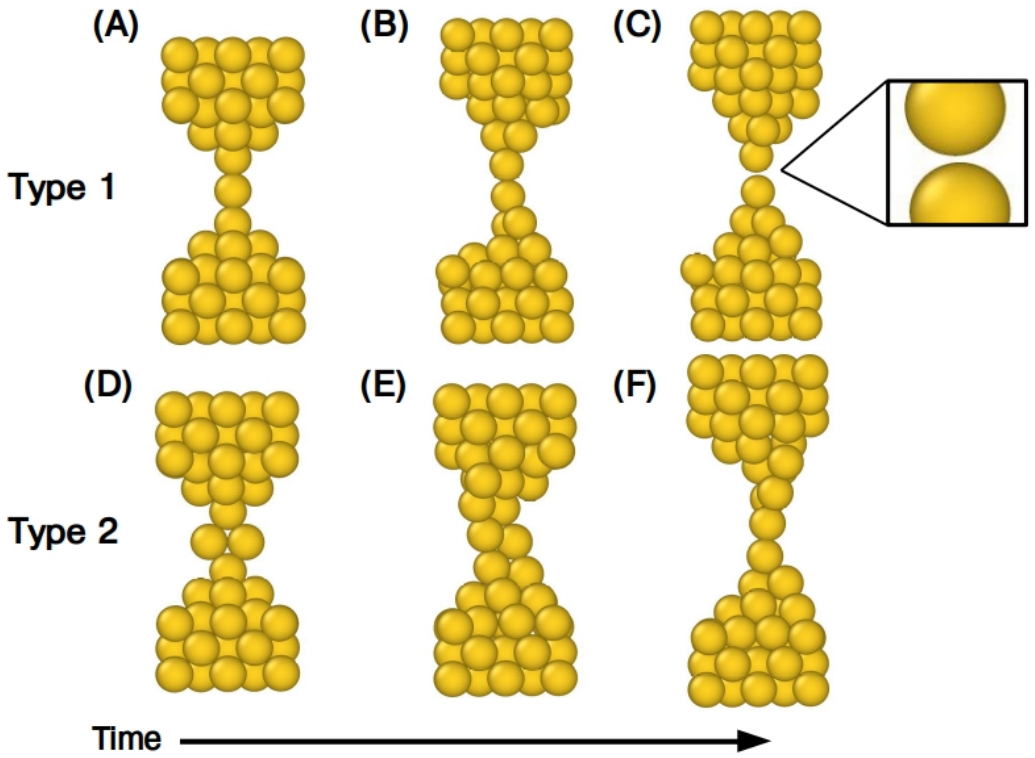

Figure 6.6: *MD simulation capturing the time evolution of atomic chains, starting from two distinct initial configurations. The top row (A–C) represents the evolution from a single atomic contact, corresponding to our Type1 traces. The bottom row (D–F) illustrates the evolution from a double atomic contact, associated with Type2 traces.*

Figures 6.6(A)–(C) illustrate the evolution of an atomic junction with a single atomic contact, corresponding to Type1 traces. Initially, as shown in Figure 6.6(A), the junction exhibits a single conductance channel. Upon stretching, this configuration transitions into a dimer of gold atoms (Figure 6.6(B)), which ultimately separates upon further elongation (Figure 6.6(C) and the zoomed-in view). This observation aligns with a previous study[60], which reported that the final conductance plateau of a contact with a single-atom cross-section is formed by a dimer of gold atoms. Figures 6.6(D)–(F) illustrate the evolution of an atomic junction with a double atomic contact, corresponding to Type2 traces. Unlike Type1, where a single conductance channel forms before breaking, the initial junction in Type2 (Figure 6.6(D)) develops two parallel conductance channels upon pulling (Figure 6.6(E)). With further elongation, these two channels merge into a single atomic chain (Figure 6.6(F)), which sustains the structure for a longer duration before rupture. This microscopic difference in initial configurations explains why Type2 traces exhibit longer chain lengths compared to Type1. Notably, in the case of a dual atomic junction, the transition from two parallel channels to a coalesced single atomic junction is driven by the starting geometry, which ultimately determines the chain length.

6.5 Summary and Conclusion

One of the key challenges in break-junction experiments aimed at forming atomic wires is achieving stable monoatomic chains of sufficient length. In this study, we address this issue through an integrated approach combining unsupervised and supervised machine learning models, trained on experimentally obtained conductance traces. Using two independent datasets, each comprising 72,000 and 90,000 conductance–displacement traces from single-atom junctions, we first determine the optimal conditions of bias voltage and stretching rate for the formation of chains longer than 4 Å. The optimal conditions are found to be low bias and low stretching rate limit. We then employ a deep learning model to classify individual breaking traces, allowing us to identify specific trace features that correlate with long-chain formation. We find three kinds of traces, and it is seen that a specific type, emerging from a double-contact like initial structure, gives the majority of long chains . We perform ab initio molecular dynamics simulations, which provide microscopic insights into the mechanisms underlying atomic wire formation and corroborates our finding. This understanding offers valuable guidance for future MCBJ experiment design and optimization.

Bibliography

[1] Hannu Häkkinen, Michael Moseler, and Uzi Landman. Bonding in Cu, Ag, and Au clusters: relativistic effects, trends, and surprises. Physical review letters, 89(3):033401, 2002.

[2] M Reyes Calvo, Carlos Sabater, Wynand Dednam, Enrico B Lombardi, Maria J Caturla, and Carlos Untiedt. Influence of relativistic effects on the contact formation of transition metals. Physical Review Letters, 120(7):076802, 2018.

[3] RHM Smit, Carlos Untiedt, AI Yanson, and JM Van Ruitenbeek. Common origin for surface reconstruction and the formation of chains of metal atoms. Physical Review Letters, 87(26):266102, 2001.

[4] AI Yanson, G Rubio Bollinger, HE Van den Brom, N Agrait, and JM Van Ruitenbeek. Formation and manipulation of a metallic wire of single gold atoms. Nature, 395(6704):783–785, 1998.

[5] Hideaki Ohnishi, Yukihito Kondo, and Kunio Takayanagi. Quantized conductance through individual rows of suspended gold atoms. Nature, 395(6704):780–783, 1998.

[6] Yoshizo Takai, Tadahiro Kawasaki, Yoshihide Kimura, Takashi Ikuta, and Ryuichi Shimizu. Dynamic observation of an atom-sized gold wire by phase electron microscopy. Physical Review Letters, 87(10):106105, 2001.

[7] Tokushi Kizuka and Kosuke Monna. Atomic configuration, conductance, and tensile force of platinum wires of single-atom width. Physical review B, 80(20):205406, 2009.

[8] P Segovia, D Purdie, M Hengsberger, and Y Baer. Observation of spin and charge collective modes in one-dimensional metallic chains. Nature, 402(6761):504–507, 1999.

[9] RHM Smit, Carlos Untiedt, Gabino Rubio-Bollinger, RC Segers, and JM Van Ruitenbeek. Observation of a parity oscillation in the conductance of atomic wires. Physical review letters, 91(7):076805, 2003.

[10] JR Ahn, HW Yeom, HS Yoon, and I-W Lyo. Metal-insulator transition in Au atomic chains on Si with two proximal bands. Physical review letters, 91(19):196403, 2003.

[11] Stefan Fölsch, Per Hyldgaard, R Koch, and KH Ploog. Quantum confinement in monatomic Cu chains on Cu (111). Physical review letters, 92(5):056803, 2004.

[12] Nicolás Agraıt, Alfredo Levy Yeyati, and Jan M Van Ruitenbeek. Quantum properties of atomic-sized conductors. Physics Reports, 377(2-3):81–279, 2003.

[13] Cyrus F Hirjibehedin, Christopher P Lutz, and Andreas J Heinrich. Spin coupling in engineered atomic structures. Science, 312(5776):1021–1024, 2006.

[14] R Toskovic, R Van Den Berg, A Spinelli, IS Eliens, B Van Den Toorn, B Bryant, J-S Caux, and AF Otte. Atomic spin-chain realization of a model for quantum criticality. Nature Physics, 12(7):656–660, 2016.

[15] Binbin Chen, Haoran Xu, Chao Ma, Stefan Mattauch, Da Lan, Feng Jin, Zhuang Guo, Siyuan Wan, Pingfan Chen, Guanyin Gao, et al. All-oxide–based synthetic antiferromagnets exhibiting layer-resolved magnetization reversal. Science, 357(6347):191–194, 2017.

[16] Sudipto Chakrabarti, Ayelet Vilan, Gai Deutch, Annabelle Oz, Oded Hod, Juan E Peralta, and Oren Tal. Magnetic control over the fundamental structure of atomic wires. Nature communications, 13(1):4113, 2022.

[17] Manohar Kumar, Oren Tal, Roel HM Smit, Alexander Smogunov, Erio Tosatti, and Jan M van Ruitenbeek. Shot noise and magnetism of Pt atomic chains: Accumulation of points at the boundary. Physical Review B, 88(24):245431, 2013.

[18] Atindra Nath Pal, Dongzhe Li, Soumyajit Sarkar, Sudipto Chakrabarti, Ayelet Vilan, Leeor Kronik, Alexander Smogunov, and Oren Tal. Nonmagnetic single-molecule spin-filter based on quantum interference. Nature communications, 10(1):5565, 2019.

[19] Marc Bockrath, David H Cobden, Jia Lu, Andrew G Rinzler, Richard E Smalley, Leon Balents, and Paul L McEuen. Luttinger-liquid behaviour in carbon nanotubes. Nature, 397(6720):598–601, 1999.

[20] Latha Venkataraman, Yeon Suk Hong, and Philip Kim. Electron transport in a multichannel one-dimensional conductor: molybdenum selenide nanowires. Physical review letters, 96(7):076601, 2006.

[21] Zhen Yao, Henk W Ch Postma, Leon Balents, and Cees Dekker. Carbon nanotube intramolecular junctions. Nature, 402(6759):273–276, 1999.

[22] SK Nielsen, Mads Brandbyge, K Hansen, Kurt Stokbro, JM Van Ruitenbeek, and Flemming Besenbacher. Current-voltage curves of atomic-sized transition metal contacts: an explanation of why Au is ohmic and Pt is not. Physical review letters, 89(6):066804, 2002.

[23] Carlos Untiedt, G Rubio Bollinger, S Vieira, and N Agraït. Quantum interference in atomic-sized point contacts. Physical Review B, 62(15):9962, 2000.

[24] Makusu Tsutsui, Kohei Shoji, Masateru Taniguchi, and Tomoji Kawai. Formation and self-breaking mechanism of stable atom-sized junctions. Nano Letters, 8(1):345–349, 2008.

[25] RHM Smit, Carlos Untiedt, and JM Van Ruitenbeek. The high-bias stability of monatomic chains. Nanotechnology, 15(7):S472, 2004.

[26] Jianwei Zhao, Kei Murakoshi, Xing Yin, Manabu Kiguchi, Yan Guo, Nan Wang, Shuai Liang, and Hongmei Liu. Dynamic characterization of the postbreaking behavior of a nanowire. The Journal of Physical Chemistry C, 112(50):20088–20094, 2008.

[27] SK Nielsen, Yves Noat, Mads Brandbyge, RHM Smit, K Hansen, LY Chen, AI Yanson, Flemming Besenbacher, and JM Van Ruitenbeek. Conductance of single-atom platinum contacts: Voltage dependence of the conductance histogram. Physical Review B, 67(24):245411, 2003.

[28] Damien Cabosart, Maria El Abbassi, Davide Stefani, Riccardo Frisenda, Michel Calame, Herre S. J. van der Zant, and Mickael L. Perrin. A reference-free clustering method for the analysis of molecular break-junction measurements. Applied Physics Letters, 114(14):143102, 2019.

[29] Nicholas A. Lanzillo and Curt M. Breneman. Predicting single-molecule conductance through machine learning. Journal of Applied Physics, 120(13):134902, 2016.

[30] Nathan D. Bamberger, Jeffrey A. Ivie, Keshaba N. Parida, Dominic V. McGrath, and Oliver L. A. Monti. Unsupervised Segmentation-Based Machine Learning as an Advanced Analysis Tool for Single Molecule Break Junction Data. The Journal of Physical Chemistry C, 124(33):18302–18315, 2020.

[31] Masateru Taniguchi, Takahito Ohshiro, Yuki Komoto, Takayuki Takaai, Takeshi Yoshida, and Takashi Washio. High-Precision Single-Molecule Identification Based on Single-Molecule Information within a Noisy Matrix. The Journal of Physical Chemistry C, 123(25):15867–15873, 2019.

[32] András Magyarkuti, Nóra Balogh, Zoltán Balogh, Latha Venkataraman, and András Halbritter. Unsupervised feature recognition in single-molecule break junction data. Nanoscale, 12:8355–8363, 2020.

[33] Dongying Lin, Zhihao Zhao, Haoyang Pan, Shi Li, Yongfeng Wang, Dong Wang, Ste-

fano Sanvito, and Shimin Hou. Using Weakly Supervised Deep Learning to Classify and Segment Single-Molecule Break-Junction Conductance Traces. ChemPhysChem, 22(20):2107–2114, 2021.

[34] Nathan D. Bamberger, Jeffrey A. Ivie, Keshaba N. Parida, Dominic V. McGrath, and Oliver L. A. Monti. Unsupervised Segmentation-Based Machine Learning as an Advanced Analysis Tool for Single Molecule Break Junction Data. The Journal of Physical Chemistry C, 124(33):18302–18315, 2020.

[35] Tianren Fu, Kathleen Frommer, Colin Nuckolls, and Latha Venkataraman. Single-Molecule Junction Formation in Break-Junction Measurements. The Journal of Physical Chemistry Letters, 12(44):10802–10807, 2021. PMID: 34723548.

[36] Tianren Fu, Yaping Zang, Qi Zou, Colin Nuckolls, and Latha Venkataraman. Using Deep Learning to Identify Molecular Junction Characteristics. Nano Letters, 20(5):3320–3325, 2020. PMID: 32242671.

[37] Dongying Lin, Zhihao Zhao, Haoyang Pan, Shi Li, Yongfeng Wang, Dong Wang, Stefano Sanvito, and Shimin Hou. Using Weakly Supervised Deep Learning to Classify and Segment Single-Molecule Break-Junction Conductance Traces. ChemPhysChem, 22(20):2107–2114, 2021.

[38] Anton Vladyka and Tim Albrecht. Unsupervised classification of single-molecule data with autoencoders and transfer learning. Machine Learning: Science and Technology, 1(3):035013, aug 2020.

[39] Biswajit Pabi and Atindra Nath Pal. An experimental set-up to probe the quantum transport through a single atomic/molecular junction at room temperature. Pramana, 97(1):8, 2022.

[40] F. Pedregosa, G. Varoquaux, A. Gramfort, V. Michel, B. Thirion, O. Grisel, M. Blondel, P. Prettenhofer, R. Weiss, V. Dubourg, J. Vanderplas, A. Passos, D. Cournapeau, M. Brucher, M. Perrot, and E. Duchesnay. Scikit-learn: Machine Learning in Python. Journal of Machine Learning Research, 12:2825–2830, 2011.

[41] Jürgen Hafner and Georg Kresse. The vienna ab-initio simulation program VASP: An efficient and versatile tool for studying the structural, dynamic, and electronic properties of materials. Properties of Complex Inorganic Solids, 140:69–82, 1997.

[42] G. Kresse and J. Furthmüller. Efficiency of ab-initio total energy calculations for metals and semiconductors using a plane-wave basis set. Computational Materials Science, 6(1):15–50, 1996.

[43] Nicolás Agraït, Alfredo Levy Yeyati, and Jan M. van Ruitenbeek. Quantum properties of atomic-sized conductors. Physics Reports, 377(2):81–279, 2003.

[44] Elke Scheer, Nicolás Agraït, Juan Carlos Cuevas, Alfredo Levy Yeyati, Bas Ludoph, Alvaro Martín-Rodero, Gabino Rubio Bollinger, Jan M. van Ruitenbeek, and Cristián Urbina. The signature of chemical valence in the electrical conduction through a single-atom contact. Nature, 394(6689):154–157, Jul 1998.

[45] Biswajit Pabi, Debayan Mondal, Priya Mahadevan, and Atindra Nath Pal. Probing metal-molecule contact at the atomic scale via conductance jumps. Phys. Rev. B, 104:L121407, Sep 2021.

[46] C. Untiedt, A. I. Yanson, R. Grande, G. Rubio-Bollinger, N. Agraït, S. Vieira, and J.M. van Ruitenbeek. Calibration of the length of a chain of single gold atoms. Phys. Rev. B, 66:085418, Aug 2002.

[47] Anita Halder, Samir Rom, Aishwaryo Ghosh, and Tanusri Saha-Dasgupta. Prediction of the Properties of the Rare-Earth Magnets $Ce_2Fe_{17-x}Co_xCN$: A Combined Machine-Learning and Ab Initio Study. Phys. Rev. Appl., 14:034024, Sep 2020.

[48] Anita Halder, Aishwaryo Ghosh, and Tanusri Saha Dasgupta. Machine-learning-assisted prediction of magnetic double perovskites. Phys. Rev. Mater., 3:084418, Aug 2019.

[49] Anton O. Oliynyk, Erin Antono, Taylor D. Sparks, Leila Ghadbeigi, Michael W. Gaultois, Bryce Meredig, and Arthur Mar. High-Throughput Machine-Learning-Driven Synthesis of Full-Heusler Compounds. Chemistry of Materials, 28(20):7324–7331, 2016.

[50] T. N. Todorov, J. Hoekstra, and A. P. Sutton. Current-Induced Embrittlement of Atomic Wires. Phys. Rev. Lett., 86:3606–3609, Apr 2001.

[51] Makusu Tsutsui, Kohei Shoji, Masateru Taniguchi, and Tomoji Kawai. Formation and Self-Breaking Mechanism of Stable Atom-Sized Junctions. Nano Letters, 8(1):345–349, Jan 2008.

[52] TN Todorov. Local heating in ballistic atomic-scale contacts. Philosophical Magazine B, 77(4):965–973, 1998.

[53] Ian Goodfellow, Yoshua Bengio, and Aaron Courville. Deep learning. MIT press, 2016.

[54] E. Samaniego, C. Anitescu, S. Goswami, V.M. Nguyen-Thanh, H. Guo, K. Hamdia, X. Zhuang, and T. Rabczuk. An energy approach to the solution of partial differential

equations in computational mechanics via machine learning: Concepts, implementation and applications. Computer Methods in Applied Mechanics and Engineering, 362:112790, 2020.

[55] Ronan Collobert, Jason Weston, Léon Bottou, Michael Karlen, Koray Kavukcuoglu, and Pavel Kuksa. Natural language processing (almost) from scratch. Journal of machine learning research, 12:2493–2537, 2011.

[56] M. Benzeghiba, R. De Mori, O. Deroo, S. Dupont, T. Erbes, D. Jouvet, L. Fissore, P. Laface, A. Mertins, C. Ris, R. Rose, V. Tyagi, and C. Wellekens. Automatic speech recognition and speech variability: A review. Speech Communication, 49(10):763–786, 2007.

[57] Myeongsuk Pak and Sanghoon Kim. A review of deep learning in image recognition. In 2017 4th International Conference on Computer Applications and Information Processing Technology (CAIPT), pages 1–3, 2017.

[58] Yann LeCun, Yoshua Bengio, and Geoffrey Hinton. Deep learning. nature, 521(7553):436–444, 2015.

[59] Feifei Huang, Ruihao Li, Gan Wang, Jueting Zheng, Yongxiang Tang, Junyang Liu, Yang Yang, Yuan Yao, Jia Shi, and Wenjing Hong. Automatic classification of single-molecule charge transport data with an unsupervised machine-learning algorithm. Phys. Chem. Chem. Phys., 22:1674–1681, 2020.

[60] M. Dreher, F. Pauly, J. Heurich, J. C. Cuevas, E. Scheer, and P. Nielaba. Structure and conductance histogram of atomic-sized Au contacts. Phys. Rev. B, 72:075435, Aug 2005.

[61] Carlos Sabater, María José Caturla, Juan José Palacios, and Carlos Untiedt. Understanding the structure of the first atomic contact in gold. Nanoscale research letters, 8:1–6, 2013.

[62] D Averin and A Bardas. AC Josephson effect in a single quantum channel. Physical review letters, 75(9):1831, 1995.

[63] JC Cuevas, A Martín-Rodero, and A Levy Yeyati. Hamiltonian approach to the transport properties of superconducting quantum point contacts. Physical Review B, 54(10):7366, 1996.

[64] Elke Scheer, Wolfgang Belzig, Yehuda Naveh, Michel H Devoret, Daniel Esteve, and Cristián Urbina. Proximity effect and multiple Andreev reflections in gold atomic contacts. Physical Review Letters, 86(2):284, 2001.

[65] Daan Frenkel, Berend Smit, and Mark A Ratner. Understanding molecular simulation: from algorithms to applications, volume 2. Academic press San Diego, 1996.

[66] G. Kresse and J. Hafner. Ab initio molecular dynamics for liquid metals. Phys. Rev. B, 47:558–561, Jan 1993.

[67] Shuichi Nosé. A unified formulation of the constant temperature molecular dynamics methods. jcp, 81(1):511–519, July 1984.

[68] Nosé Shuichi. Constant Temperature Molecular Dynamics Methods. Progress of Theoretical Physics Supplement, 103:1–46, 01 1991.

[69] William G. Hoover. Canonical dynamics: Equilibrium phase-space distributions. Phys. Rev. A, 31:1695–1697, Mar 1985.

[70] M. Dreher, F. Pauly, J. Heurich, J. C. Cuevas, E. Scheer, and P. Nielaba. Structure and conductance histogram of atomic-sized Au contacts. Phys. Rev. B, 72:075435, Aug 2005.

7

Ab-initio trained machine learning potential for MAX compound Ti_2AlC: construction, validation, and study of non linear elasticity

7.1 Introduction and Motivation

The MAX phase compounds, initially discovered in powder form by Nowotny and colleagues in the 1970s and 1980s[1, 2], and later synthesized in phase-pure bulk form by Barsoum and coworkers in 1996[3], have generated significant interest in the materials science community due to their exceptional properties[4–7]. These layered materials belong to a growing family of ternary carbides and/or nitrides with the general formula $M_{n+1}AX_n$, where n = 1, 2, or 3. Here, M represents an early transition metal, A is an A-group element, and X denotes carbon and/or nitrogen(cf Figure 7.1). The unit cell of MAX phases consist of M_6X octahedra, where X atoms occupy the octahedral sites between M atoms, similar to MX binary compounds. These octahedral layers alternate with layers of A elements, which are larger in size compared to M or X atoms(cf Figure 7.1). The separation of A layers depends on the n value, determining the number of octahedral layers in the structure. MAX compounds exhibit a unique combination of properties, bridging the gap between metals and ceramics. They are excellent electrical conductors, with resistivity values ranging from 0.2 to 0.7 $\mu\Omega$m at room temperature[4, 7], while also demonstrating high elastic

This chapter is based on publication: **Aishwaryo Ghosh**, Amitava Moitra and Tanusri Saha-Dasgupta, J. Phys. Mater. 8 025001 (2025).

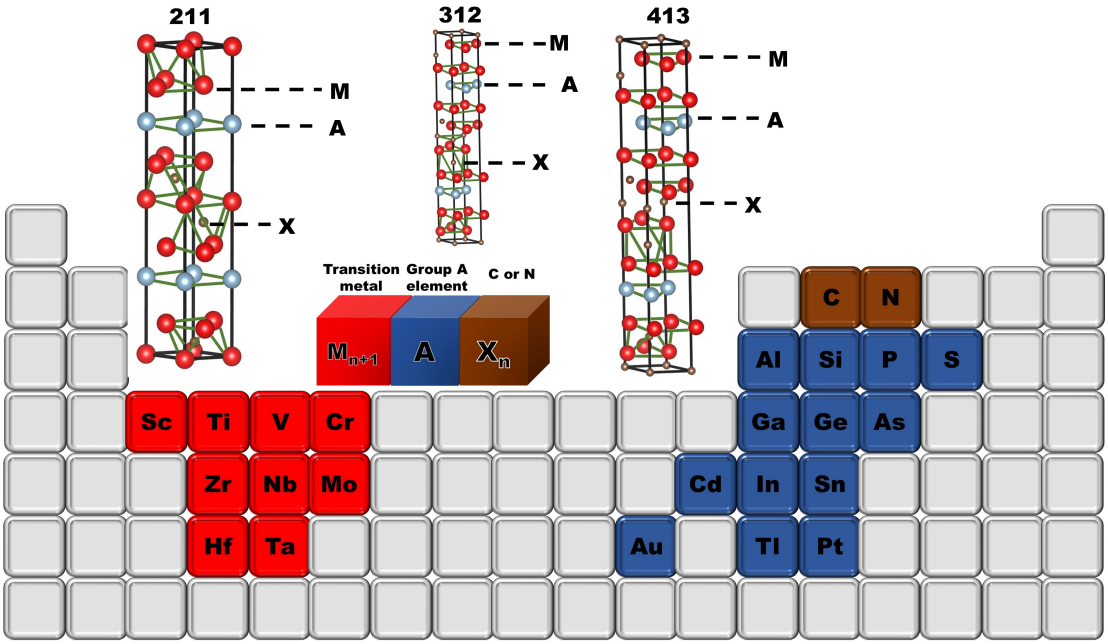

Figure 7.1: *The elements present in reported MAX phases, with their crystal structures varying across the 211, 312, and 413 phases.*

rigidity[8, 9]. Despite their stiffness, unlike conventional binary MX compounds, MAX phases are highly machinable[10]-even with a manual hacksaw. These remarkable characteristics have positioned MAX compounds as a highly discussed material with promising applications across various fields. Extensive research has been conducted to investigate the unique physical, chemical, and mechanical properties of MAX compounds[11–18]. Theoretical studies on MAX phase properties predominantly rely on first-principles density functional theory (DFT) calculations[11, 12, 16–20], which examine electronic structure, bonding, and related phenomena such as magnetism. In contrast, fewer theoretical studies have focused on the mechanical properties of these compounds. Notably, one of the most intriguing aspects of MAX phases is their nonlinear hysteretic elastic behavior which is an uncommon trait for materials with high elastic stiffness. This nonlinear response is observed as reversible hysteresis loops in the stress–strain behavior during loading and unloading cycles, with the shape and size of these loops being strongly dependent on the grain size of the sample.

MAX compounds exhibit a layered geometry similar to that of graphite or mica. The deformation mechanisms of layered crystalline solids have traditionally been explained using basal dislocations[21–24]. More recently, Kushima et al.[25] introduced the concept of ripplocations to describe near-surface deformations in van der Waals solids. Barsoum and colleagues[26, 27]further expanded this idea, proposing that layered crystalline solids fail through the nucleation and propagation of ripplocations rather than basal dislocations. While experimental evidence for ripplocations in MAX compounds has been confirmed via

transmission electron microscopy (TEM) observations on Ti_3SiC_2, the theoretical calculations supporting this concept were primarily conducted on graphite[28].

First-principles DFT simulations in this context are limited by their poor scaling behavior ($O(n_e{}^3)$ or higher), restricting studies to relatively small systems of a few hundred atoms and short timescales of a few hundred picoseconds. To complement this, large-scale atomistic simulations offer a viable approach for investigating deformation behavior and dislocation mobility under varying temperature and strain conditions, as demonstrated for graphite in Refs[29, 30]. However, molecular dynamics (MD) simulations require reliable interaction potentials, which pose a challenge in multicomponent MAX phases due to the presence of multiple bonding types. Unlike graphite and other layered materials where layers are bound by van der Waals forces, MAX phases exhibit a unique combination of bonding types: strong, directional covalent M–X bonds, relatively weaker M–A bonds, and metallic M–M bonding. The M–A bonds are too strong to be disrupted by shear or mechanical forces, which is why MXene, the two-dimensional derivative of MAX, is synthesized through selective chemical etching of the A layers rather than mechanical exfoliation[31].

To the best of our knowledge, only a few recent efforts have been made to develop force fields for MAX compounds. A modified embedded atom method (MEAM) interatomic potential[32] was created for Ti_2AlC[33], where second-nearest-neighbor MEAM parameters were derived using Ti (HCP), Al (FCC), C (Diamond), TiAl (BCC-B2), TiC (FCC-B1), and AlC (FCC-B1) as reference structures, fitted to target properties. Additionally, a bond-order potential[34, 35] has been developed for Ti_3AlC_2 and Ti_3SiC_2 MAX phases[36], based on structural, elastic, and defect properties across unary, binary, and ternary systems. However, since these are fitting models, their applicability to diverse physical properties remains uncertain. Ideally, force fields would be derived directly from first-principles calculations for greater reliability.

In recent years, machine learning (ML) techniques have revolutionized computational studies, addressing several challenges in atomistic simulations. ML-based methods, particularly ML interatomic potentials (MLIPs), have emerged as powerful tools for accurately modeling potential energy surfaces based on local environment descriptors that remain invariant to rotation, translation, and permutation of homonuclear atoms. These potentials have proven highly effective in studying the mechanical and structural properties of various materials. Trained on extensive datasets of atomic configurations with corresponding energy, force, and stress information from first-principles calculations, MLIPs offer remarkable accuracy and adaptability compared to traditional interatomic potentials[37, 38]. They not only accelerate the development of new models, but also achieve accuracy comparable to first-principles methods while iteratively improving their predictions. MLIPs have

been successfully applied to elemental crystalline[39, 40] and amorphous[39, 40] solids, as well as nanoparticles[41–44]. Moreover, their applicability has extended to binary and multinary[45–48] systems. Recently, deep-graph-neural-network-based universal foundational models are being explored to develop MLIPs that can be applied across diverse systems, covering nearly all elements in the periodic table[49].

In this study, we employ an approach to develop a machine-learned interatomic potential trained on first-principles data for MAX compounds. Using Ti_2AlC—a well-studied MAX phase—as a test case, we evaluate the effectiveness of the developed potential by comparing key structural properties such as lattice parameters, elastic constants, bulk and Young's modulus, Poisson's ratio, formation energy, and stacking fault behavior. The results demonstrate that the machine-learned potential accurately represents both the mechanical properties and energetics of Ti_2AlC. Building on this, we further explore the nonlinear hysteresis behavior in stress–strain properties, revealing that the developed potential effectively captures the material's nonlinear elasticity and identifies ripplocations as the underlying micromechanism. Additionally, we investigate the impact of defects, particularly Al vacancies, on elastic properties.

7.2 Method

To develop machine-learned interatomic potential for the three-component MAX compound with diverse chemical bonding characteristics, we utilize the moment tensor potential (MTP) approach[50], implemented using the MAML package[51]. We also explored other available machine-learned potential frameworks, such as the Spectral Neighbor Analysis Potential (SNAP)[52] and Gaussian Approximation Potentials (GAP)[53]. However, MTP demonstrated the best performance for our study. A comparative analysis of these potentials in terms of MAE and RMSE of force and energy in our specific case is provided in the Table 7.1.

Model	Force		Energy	
	MAE (eV/Å)	RMSE (eV/Å)	MAE (meV/atom)	RMSE (meV/atom)
SNAP	0.04	0.07	0.8	1.1
GAP	0.092	0.16	1.8	2.5
MTP	0.02	0.04	0.6	0.8

Table 7.1: *Comparison of the performance of different machine learning algorithms in predicting force and energy on the test set.*

The workflow of the algorithm is represented in Figure 7.2. The MTP parameters are optimized using a training set composed of various configurations of Ti_2AlC. These con-

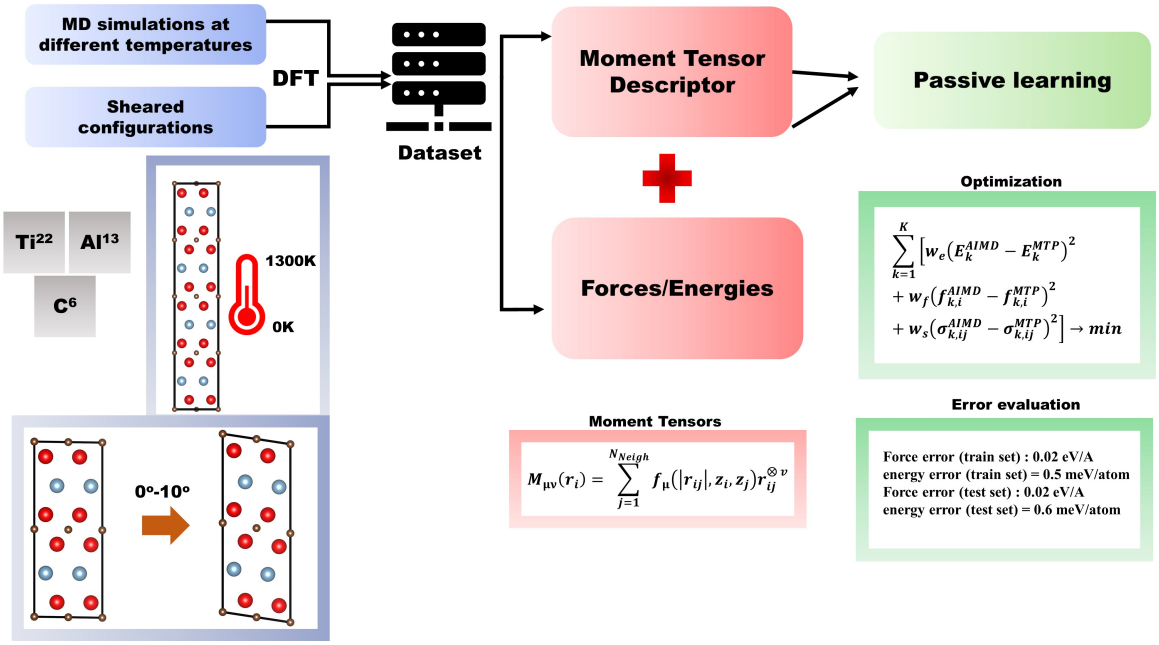

Figure 7.2: *Workflow of generating the MLIP based on MTP algorithm*

figurations include snapshots extracted from ab initio molecular dynamics (AIMD) simulation trajectories of both unstrained and strained systems. The AIMD simulations are conducted within a plane-wave framework using the Vienna Ab-initio Simulation Package (VASP)[54, 55], with the Perdew–Burke–Ernzerhof (PBE)[56] generalized gradient approximation chosen for the exchange-correlation potential. A plane-wave energy cutoff of 600 eV is applied, and the convergence threshold for the forces is set to 0.001 eV/Å. MD simulations are carried out over a 200 fs timespan with a 1 fs time step under temperature conditions ranging from 50 K to 1300 K. Since our focus remains on the deformation properties of the solid phase, we intentionally avoid configurations exceeding the melting temperature of Ti_2AlC (1898 K)[57]. A $2 \times 2 \times 2$ supercell and an $8 \times 8 \times 2$ k-point grid are employed. The Nose thermostat[58] is used to regulate the simulation temperature. Furthermore, structures subjected to shear parallel to the ab plane up to 10 degrees are included. In total, approximately 1900 different configurations are incorporated into the training set.

The mathematical formulation of the MTP can be found in Section 2.4.1. In brief, the total energy of the system can be seen as a collection of individual atomic contributions. Each contribution can be expanded in terms of basis functions B_α which in turn are contractions of the so-called moment tensor descriptors $M_{\mu\nu}$. These descriptors have a radial part and an angular part. The former can be expanded in terms of a set of N_Q radial basis functions, while the latter is a tensor of rank ν. For constructing the basis functions, the level of moments(=$2+4\mu+\nu$) is constructed and all functions lower than a preset maximum value,lev_{max}, are considered. The hyperparameters N_Q and lev_{max} are chosen using a

cross-validated grid-search method. The grid search space consists of a 3×3 parameter grid with $N_Q = [4, 6, 8]$ and $\text{lev}_{\text{max}} = [14, 16, 18]$. Model evaluation is conducted using a 10-fold cross-validation scheme, where the training dataset is divided into 10 equal subsets (folds). The model is trained on 9 folds while the remaining fold is used for validation, with this process repeated 10 times to ensure each fold serves as the validation set once. The final performance of each hyperparameter combination is determined by averaging the results across these iterations. Scoring is based on absolute errors in force evaluation, as force precision is crucial for our application. During the creation of the n-fold cross-validation, special care is taken to ensure that each fold maintains a similar distribution of different configurations (such as temperature snapshots and strained structures) as the full dataset. The final hyperparameter selection is based on achieving an acceptable score while avoiding unnecessary model complexity, as further increases in complexity yield only marginal improvements. A comparison of different hyperparameter combinations (see table 7.2) indicates that the variation in mean absolute error (MAE) is mild, with the optimal choice being $N_Q = 8$ and $\text{lev}_{\text{max}} = 16$.

Hyperparameters		
N_Q	lev_{max}	Force MAE (eV/Å)
6	14	0.030
6	16	0.032
6	18	0.034
8	14	0.035
8	16	0.025
8	18	0.024

Table 7.2: *Hyperparameter settings and corresponding Force MAE values.*

For lev_{max} = 16, four radial functions f_μ are considered, and 92 basis functions are formed by contracting one or more allowed moments $\text{M}_\mu\nu$. For N_Q = 8 and the four radial functions, 32 radial coefficients are required for each combination of atomic types z_i and z_j. In the Ti-Al-C system, there are 9 such combinations. Consequently, MTPs are fitted with 288 radial coefficients (32 × 9) and 92 moment coefficients (η).

7.3 Results

7.3.1 Performance of the MLIP

During potential training, the mean absolute errors in force and energy per atom for the test set, which comprises 10% of the total dataset, are 0.02 eV/Å and 0.6 meV/atom, respectively. These values fall within the acceptable range, aligning with literature values

(0.03–0.15 eV/Å for force and 0.22–2.73 meV/atom for energy) reported for monoatomic[59, 60], binary[61, 62], and multinary[63, 64] compounds. The root mean squared errors for force and energy are 0.04 eV/Å and 0.8 meV/atom, respectively. Plots comparing the true (DFT) and MLIP-predicted forces and energies are provided in Figure 7.3 (A,B) and the histograms depicting the error distributions for forces and energies are included in Figure 7.3(C,D).

However, validating the reliability of the generated potentials requires assessing various physical properties. This helps establish the accuracy of the force fields in enabling atomistic simulations. To achieve this, we compute formation energy, lattice constants, elastic parameters, and stacking fault energies using the machine-learned force fields at T = 0 K.

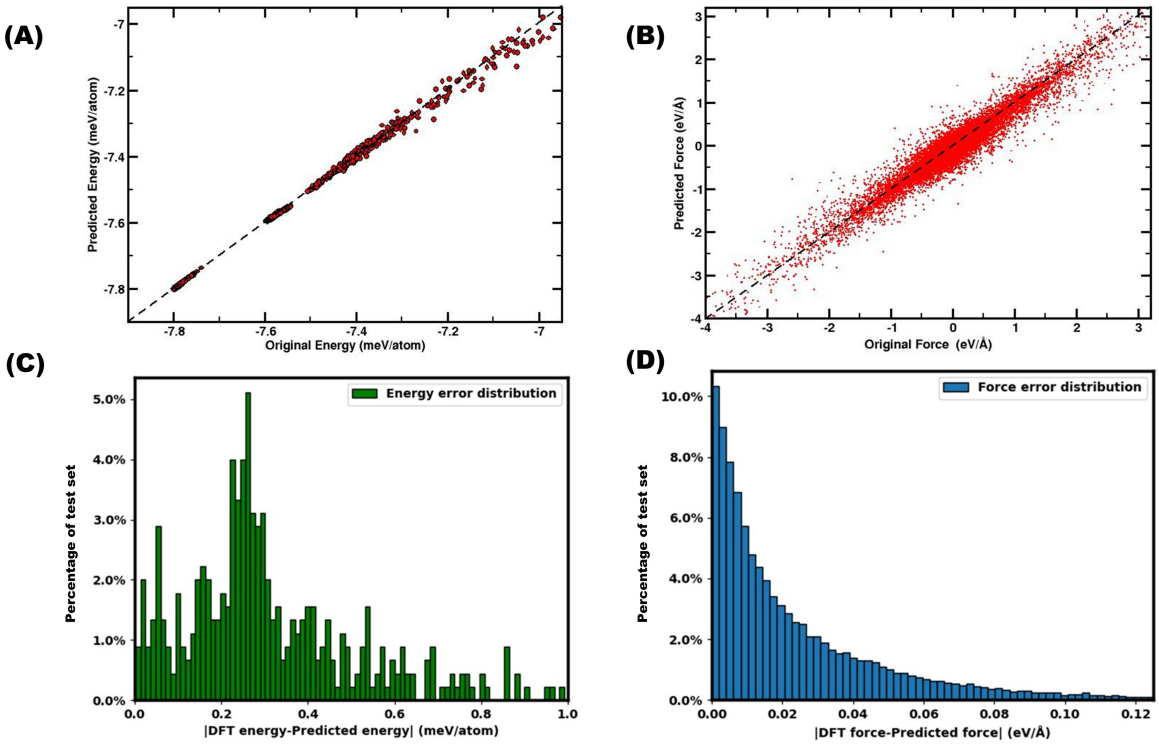

Figure 7.3: *Original (DFT) vs MTP interatomic potential predicted (A) energy and (B) forces. Histogram of error between DFT calculated and ML predicted (C) energy and (D)forces.*

Formation energy (ΔH_F) represents the energy required to form a compound from its constituent elements. It is determined using the total energy of the system containing N_{tot} atoms (E_{tot}) and the total energy of its individual elemental components ($E_{tot}(x)$):

$$\Delta H_F = \frac{E_{tot} - \sum_x E_{tot}(x)}{N_{tot}} \tag{7.3.1}$$

For force field calculations, separate models are constructed for the elemental components, considering the FCC phase for Al, HCP for Ti, and graphite for C. The formation energy

computed using DFT and the present force field differs by 0.03–0.05 eV/atom. The corresponding lattice parameters, obtained by optimizing the cell parameters with the force field, closely match experimental values, with an almost exact match for the a lattice parameter and a maximum deviation of 1% for the c lattice parameter.

The generalized Hooke's relation, expressed in Voigt notation, is given by $\sigma_i = C_{ij}\varepsilon_j$, where ε and σ represent the strain and stress vectors, each with six elements, and C_{ij} are 6×6 matrices. The elastic constants are determined using the explicit deformation method[65], which involves applying deformations in various directions within the elastic limit. By setting all strain tensor elements to zero except for one, all C_{ij} elements can be computed, acting as proportionality factors between the stress component σ_i and the strain component ε_j. The elastic constants derived from the force field satisfy the mechanical stability criteria for the hexagonal system, $C_{44} > 0$, $C_{11} > |C_{12}|$, $(C_{12} + 2C_{12})C_{33} > 2C_{13}^2$. Additionally, mechanical parameters such as Young's modulus (Y), bulk modulus (B), shear modulus (G), and Poisson's ratio (η) are calculated using the Voigt–Reuss–Hill approximation[66] and validated against literature values. Table 7.3 tabulates the comparison. The force field values exhibit deviations of only a few percent from literature values, which is particularly encouraging, as none of these properties were included in the fitting procedure.

Table 7.3: *Calculated values of formation energy (ΔH_F), lattice constants (a, c), elastic constants (C_{11}, C_{12}, C_{44}), Young's (Y), bulk (B), shear modulus (G), Poisson's ratio (η), computed using the MTP force field. The literature values are shown for comparison.*

Material property	Calculated Value	Literature
ΔH_F(eV/atom)	-0.78	(-0.83) - (-0.81)[32, 67]
a(Å)	3.06	3.06-3.07[68, 69]
c(Å)	13.61	13.62-13.74[12, 68, 69]
C_{11}(GPa)	310	297 -309[70–73]
C_{12}(GPa)	70.5	56.9 - 72[70–73]
C_{44}(GPa)	96.3	105 - 112[70–73]
Y(GPa)	240.2	217.2 - 293.3[70–73]
B(GPa)	163.8	136 - 186[70–73]
G(GPa)	95.7	110.6-118.8[72]
η	0.24	0.185-0.19[72]

Since the objective is to use the machine-learned force field to study deformation properties, the stacking fault properties of Ti_2AlC are further examined. Given its layered structure, a slip in the basal plane that disrupts the stacking order coincides with the formation of a stacking fault. During slip along the $[0\bar{1}10]$ direction, the system transitions through a high-symmetry configuration where atoms in the upper block align with the 'voids' of the lower block. This process gives rise to the generalized stacking fault energy (GSFE) curve, which exhibits a local minimum known as the stable stacking fault energy (SSFE)[74].

The energy barrier preceding this minimum is referred to as the unstable stacking fault energy (USFE)[75]. Two possible slip planes exist: one at the Ti-Al interface and another at the Ti-C interface, as illustrated in Figure 7.4(A). Previous studies on V_2AlC[76] indicate that M-Al slip is energetically favorable than M-X slip. Based on this, the GSFE curve is computed from both DFT simulations and machine-learned force fields, defining the total energy difference between fault-free and faulted systems per unit area of the glide plane. A supercell of size 20 × 10 × 5, resulting in a simulation box of 61.2 Å × 53.3

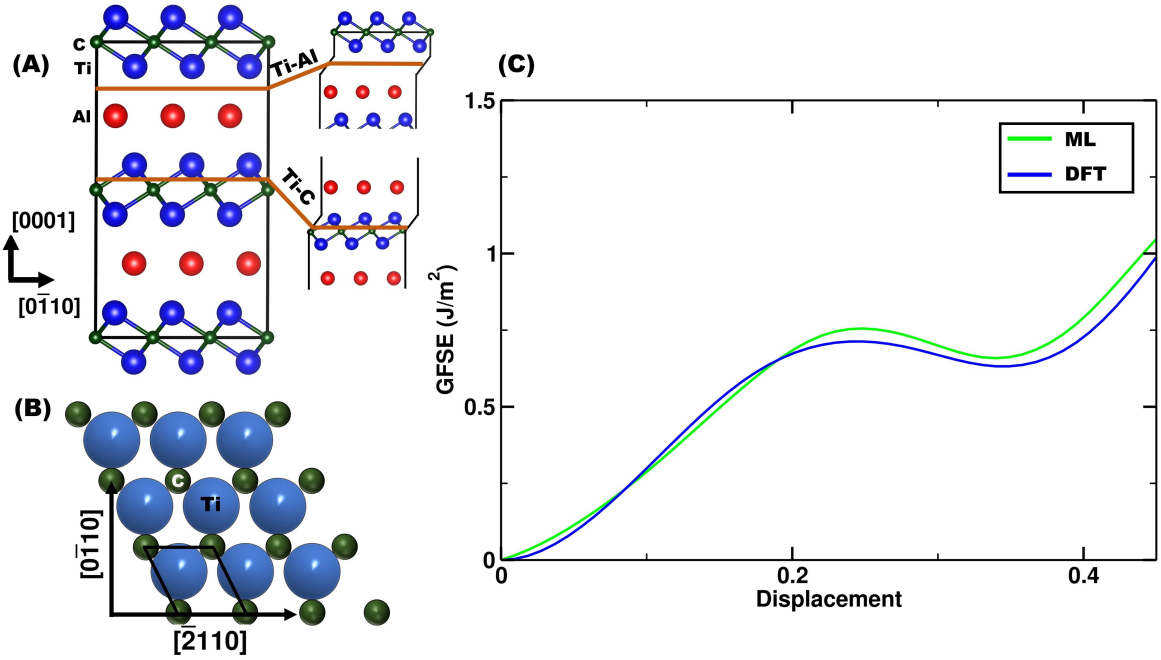

Figure 7.4: *(A) The possible slip planes in Ti_2AlC include Ti-Al and Ti-C. (B) The top view of the structure is shown in the [0$\bar{1}$10]-[$\bar{2}$110] plane, with the hexagonal unit cell outlined in black. (C) The generalized stacking fault energy (GSFE) for slip along the [0$\bar{1}$10] direction is computed using both DFT and the machine-learned force field. Displacements are expressed in units of lattice spacing.*

Å × 68.5 Å and containing 16,000 atoms, is used to calculate the GSFE from the ML potential. Due to computational constraints, a smaller supercell of size 2 × 2 × 2 is used for DFT calculations. This analysis is performed systematically for displacements along a fine displacement grid of 20 points in the [0$\bar{1}$10] direction along the Γ line in the basal planes (0001) (cf Figure 7.4(B)). This provides a cut in the stacking fault energy surface, known as the Γ surface, as defined by Vitek[74]. The GSFE curves, computed from both the ML force field and DFT, are shown in Figure 7.4(C). Specifically, the SSFE and USFE values calculated using DFT (ML force field) are 0.656 J/m^2 (0.631 J/m^2) and 0.758 J/m^2 (0.712 J/m^2), respectively. This indicates that the ML force field successfully captures the qualitative behavior, although it slightly underestimates the SSFE and USFE. Nonetheless, the level of agreement is impressive, considering that stacking fault structures were not explicitly included in the training set.

7.3.2 Stress–strain behavior: nonlinear elasticity

One of the distinctive features of the mechanical properties of MAX compounds is their nonlinear elasticity. While both linear and nonlinear elastic materials return to an unloaded state after deformation, the relationship between stress and strain in the nonlinear case deviates from the linear behavior described by Hooke's law. A key characteristic of this nonlinear response is the presence of hysteresis in the stress–strain curve.

Despite their stiffness, MAX phase compounds exhibit fully reversible, strain rate-independent hysteretic stress–strain loops under cyclic loading[77]. For instance, cyclic compressive stress–strain curves for Ti_3SiC_2 with two different grain sizes reveal grain size-dependent hysteretic loops[78]. Similar hysteretic behavior has also been observed in Ti_3AlC_2[79], Ti_3GeC_2[80], and the compound under present study, Ti_2AlC[81]. This phenomenon was initially understood in terms of kink band formation originating from basal deformations[82]. However, recent studies[26, 27, 83] have revised this perspective, attributing the observed nonlinearity to bulk ripplocations, similar to those found in other layered materials undergoing two-dimensional confined deformations[84]. This explanation is supported by evidence of c-axis strain at multiple length scales, including TEM images[85], and the significant influence of confining pressure on the compressive strength of both polycrystals and single crystals[86–88]. Although experimental observations strongly suggest that ripplocations act as a micro-mechanism of deformation, direct atomic-scale simulation evidence for this process in MAX compounds has remained elusive, primarily due to the lack of suitable computational approaches.

With the confidence gained in our ML-constructed force field, based on the computed structural, energetic, and mechanical properties, we now explore the stress–strain properties of Ti_2AlC under cyclic loading and unloading. To atomistically simulate the stress–strain behavior, a $20 \times 10 \times 5$ supercell undergoes incremental uniaxial compressive strain along the $[0\bar{1}10]$ direction of the basal plane at a strain rate of 10^9 s^{-1}. The maximum stress is ensured to stay below the yield point, after which tensile uniaxial strain is applied to return the structure close to its original state. At the beginning of loading, the same supercell is equilibrated using the Nosé–Hoover barostat and thermostat. Periodic boundary conditions are applied in the basal plane, while out-of-plane directions are treated as free surfaces. During each step of deformation at a fixed strain rate, the NPT method monitors temperature fluctuations and adjusts the box size along the perpendicular directions to achieve negligible tensile stress. The simulation temperature is set at 100 K. The corresponding stress–strain response, shown in Figure 7.5(A), depicts different loading conditions with varying maximum stress values. The yield stress, computed using the MLIP potential, is marked with a dotted horizontal line. In all cases, nonlinear elastic behavior is evident

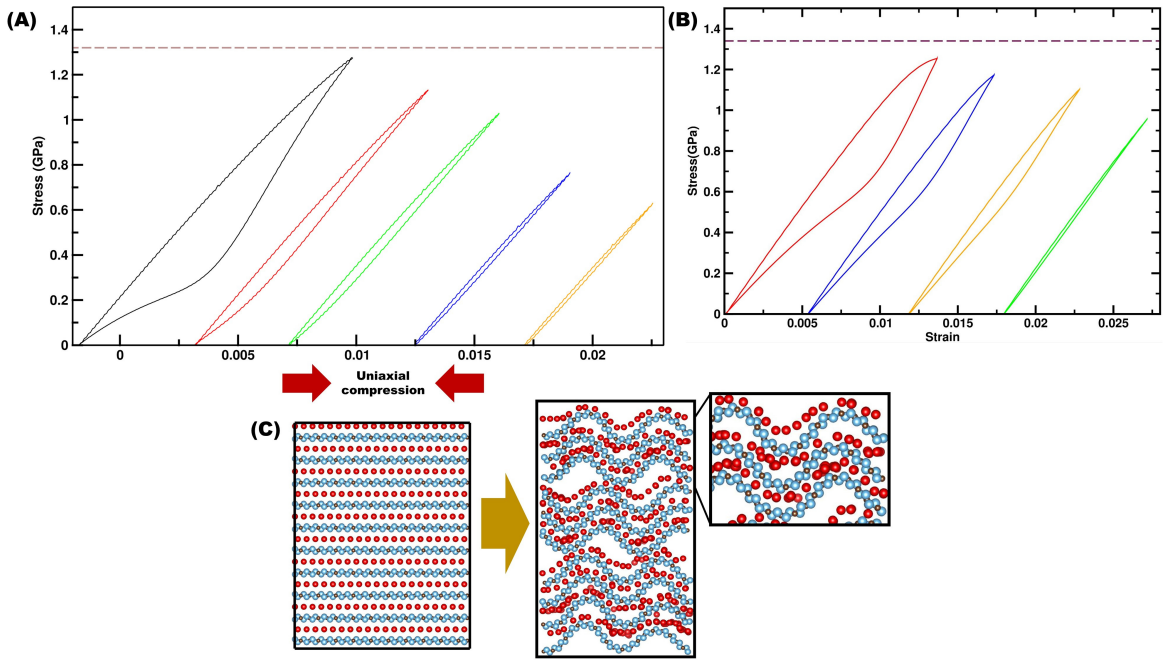

Figure 7.5: *Molecular dynamics (MD) simulation results using the moment tensor potential (MTP) for the stress–strain behavior of Ti_2AlC under uniaxial strain during cyclic loading and unloading at different maximum stress values. To facilitate visualization, the plots for different maximum stress values are shifted horizontally relative to each other. Plots are shown for the (A) 20 × 20 × 5 simulation cell and (B) 15 × 15 × 5 simulation cell. The dotted horizontal line represents the yield point. (C) Atomic structures of bulk ripplocations formed during the MD simulation of Ti_2AlC under uniaxial compression. Zoomed-in views are provided for enhanced visualization of the ripplocations.*

through the presence of a hysteresis loop. However, the width of the hysteresis loop depends on the maximum stress value. When the maximum stress approaches the yield point, the hysteresis loop develops a bulge, which gradually disappears as the maximum strain moves further from the yield point. The qualitative nature of the hysteresis loop aligns well with experimental data[77, 79, 89, 90]. To verify system size dependency, we repeat the calculations on a 15 × 15 × 5 simulation cell (45.9 Å × 79.9 Å × 68.5 Å) containing 18,000 atoms. The qualitative trend remains intact, as shown in Figure 7.5(B).

As mentioned earlier, the origin of nonlinear elastic behavior has been a topic of ongoing discussion, with evolving interpretations over time. Initially, it was attributed to the formation and annihilation of incipient kink bands, which arise due to the attraction between oppositely signed basal dislocation walls[6, 82, 91, 92]. Later, following the work of Kushima et al.[25], which introduced the concept of ripplocations in describing near-surface defects in van der Waals compounds like MoS_2, Barsoum and Tucker[27] argued that ripplocations are not confined to van der Waals solids or surface defects but also exist in layered solids such as MAX compounds. Our atomistic simulations of Ti_2AlC under uniaxial compression provide direct support for this idea. Figure 7.5(C), shown for 20%

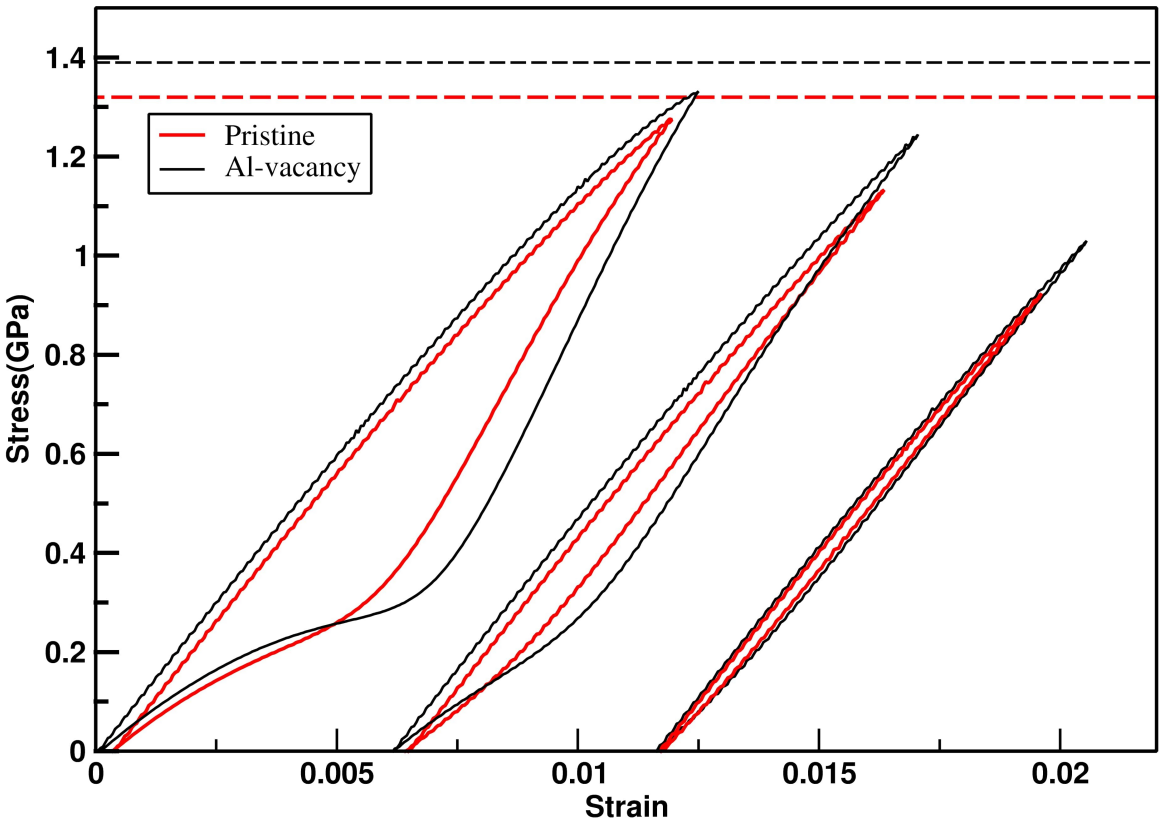

Figure 7.6: *The stress–strain behavior of pristine Ti_2AlC(red lines) is compared with that of Ti_2AlC containing 40% Al vacancies(black lines). To enhance visualization, the plots are horizontally shifted. Horizontal lines indicate the respective yield stresses.*

strain, reveals the nucleation of discrete localized ripplocations, which results from energy reduction associated with buckling.

7.3.3 Effect of defects

MAX phases exhibit a remarkable ability to accommodate structural vacancies[93–95]. In these materials, the formation energy of M-site vacancies (5–8 eV) is significantly higher than that of A- and X-site vacancies (approximately 2 eV)[96–98]. As a result, vacancies predominantly form at the A and X sites. Motivated by this, we examine the effect of Al vacancies on nonlinear elasticity. DFT calculations indicate that Ti_2AlC can accommodate up to 50% Al vacancies[99]. The compositional analysis of $Ti_3Al_{1-X}C2$ further reveals local Al vacancy concentrations of up to 50%[100], consistent with DFT predictions. Based on this, we consider a defected structure with 40% Al vacancies to investigate their impact. It is important to clarify that the vacancies considered in our model are not thermally activated but rather formed during the synthesis protocol. This explains the constant percentage of vacancies maintained throughout our MD simulations. Previous studies on MoS_2[101] and graphite[102] have investigated the interaction between extended defects, such as ripploca-

tions, and point defects like vacancies. These studies concluded that vacancies tend to form near ripplocations, and ripplocations spontaneously migrate toward vacancies. However, the effect of this interaction on nonlinear elasticity has not been explored. Specifically, how vacancies influence the shape and width of hysteresis in stress–strain curves remains an open question. Given that vacancies form near ripplocations, in addition to being randomly distributed throughout the system, we also consider extended defect lines—one on each side of the ripplocation—to examine their impact. The results, presented in Figure 7.6, compare the stress–strain curves under cyclic loading for a 40% Al vacancy-bearing system and a vacancy-free system. First, the vacancy-bearing system exhibits an increase in yield strength. Second, for the same maximum stress-to-yield stress ratio, the hysteresis loop in the vacancy-bearing system shows more pronounced bulging compared to the pristine system, leading to a significant increase in hysteresis width. To understand the

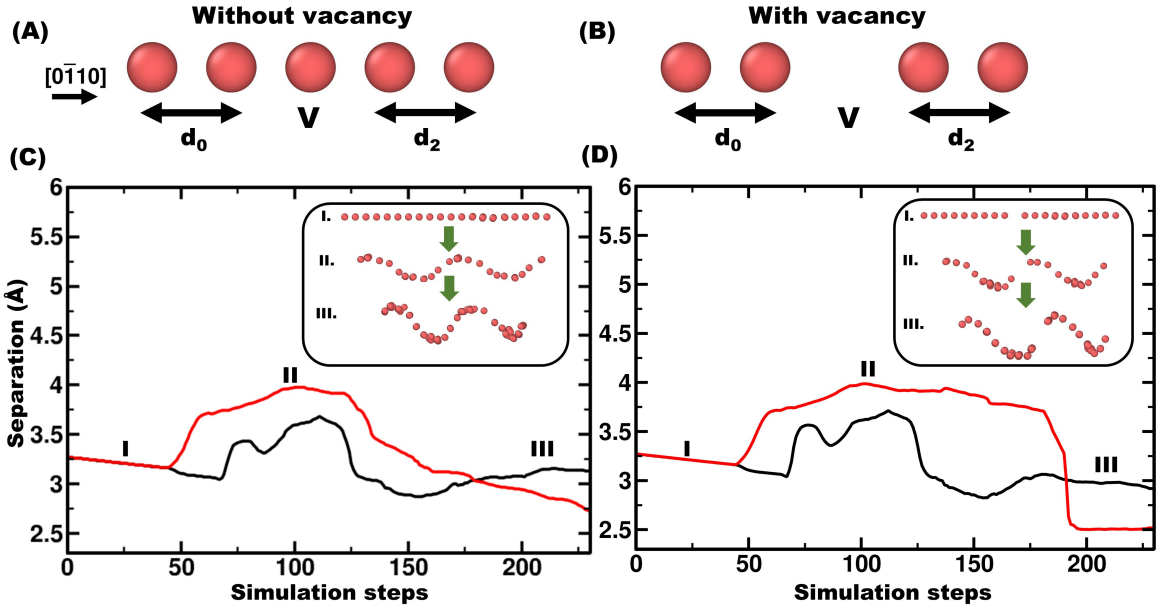

Figure 7.7: *Interatomic distances within the atomic chains in an Al layer are viewed along the [$\bar{2}$110] direction for both (A) vacancy-free and (B) vacancy-bearing systems. d_0 (d_2) represents the separation between two consecutive lines of Al atoms to the left (right) of the line of Al atoms or vacancies, denoted as V. The evolution of d_0 (red lines) and d_2 (black lines) during compression is shown for the (C) vacancy-free and (D) vacancy-bearing structures. The insets illustrate the atomic configurations of the Al layer at points I, II, and III during the simulation steps.*

differences in stress–strain properties between vacancy-free and vacancy-bearing systems, we examine the atomic configurations at a specific Al layer where the line defect (vacancy) is introduced. We track the evolution of two interatomic separations, d_0 and d_2, between consecutive lines of Al atoms on each side of the defect, particularly near the formation of ripplocations, as a function of simulation steps during loading. The same analysis is conducted for the vacancy-free system, focusing on the corresponding Al atom line (see

Figures 7.7(A) and 7.7(B)).

Both d_0 and d_2 exhibit sudden jumps upon ripplocation nucleation. However, while these jumps are similar for the vacancy-free system due to the symmetric nature of the ripplocation (as seen in the Figure 7.7(C) inset), the vacancy-bearing system displays a highly asymmetric response(as seen in the Figure 7.7(D). The evolution of d_2 remains comparable to the vacancy-free case, whereas d_0 shows distinct behavior, featuring a well-defined plateau after the initial jump, leading to strong anisotropy between them. As a result, the ripplocation bends asymmetrically toward the vacancy, forming a pleat-like morphology. Such a pleat-like structure is believed to facilitate self-folding of ripplocations[25], further amplifying the nonlinearity in the system.

7.4 Summary and Discussion

Using the MTP protocol of the ML algorithm, we generate the force field for the multi-component layered MAX compound, Ti_2AlC, which has recently gained attention among materials scientists. We employ a passive learning scheme, as previously implemented in the literature for layered materials[103, 104], while an active learning scheme remains an alternative avenue. The versatility of the developed machine-learned force field is established through a faithful description of energetics via formation energy, structural properties via lattice parameters, and elastic properties, including dislocation behavior. Having established confidence in the MTP, we apply the force field in the MD study to investigate the stress–strain properties of Ti_2AlC. The calculated stress–strain curve under uniaxial strain applied in the basal plane shows strong nonlinearity with hysteresis, in marked deviation from Hooke's law. Interestingly, the width of the hysteresis strongly depends on the value of maximum applied stress, defining a critical stress for nonlinear behavior. The microscopic origin of this nonlinear deformation behavior is driven by the formation of bulk atomic-scale ripples, known as ripplocations. The elastic energy stored in ripplocation boundaries and surrounding areas accounts for the loops in the stress–strain curve[105]. Our simulations, incorporating Al vacancies demonstrates that vacancies further enhance nonlinearity, thereby increasing the critical stress. As shown in our study, Al vacancies influence the elastic properties in multiple ways, increasing the yield stress as well as widening the stress–strain loop. Our findings can contribute to the defect engineering of MAX compounds to achieve controlled nonlinearity, with potential applications in aerospace, rubber industries, and biomechanics.

Bibliography

[1] Von Hans Nowotny. Strukturchemie einiger verbindungen der übergangsmetalle mit den elementen C, Si, Ge, Sn. Progress in Solid State Chemistry, 5:27–70, 1971.

[2] Hans Nowotny, Peter Rogl, and Julius C Schuster. Structural chemistry of complex carbides and related compounds. Journal of Solid State Chemistry, 44(1):126–133, 1982.

[3] Michel W Barsoum and Tamer El-Raghy. Synthesis and characterization of a remarkable ceramic: Ti_3SiC_2. Journal of the American Ceramic Society, 79(7):1953–1956, 1996.

[4] Michel W Barsoum. MAX phases: properties of machinable ternary carbides and nitrides. John Wiley & Sons, 2013.

[5] Effect of temperature, strain rate and grain size on the mechanical response of Ti_3SiC_2 in tension.

[6] MW Barsoum, T Zhen, SR Kalidindi, M Radovic, and A Murugaiah. Fully reversible, dislocation-based compressive deformation of Ti_3SiC_2 to 1 GPa. Nature Materials, 2(2):107–111, 2003.

[7] Michel W Barsoum. Physical properties of the MAX phases. Encyclopedia of Materials: Science and Technology, pages 1–11, 2006.

[8] ZM Sun. Progress in research and development on MAX phases: a family of layered ternary compounds. International Materials Reviews, 56(3):143–166, 2011.

[9] Miladin Radovic and Michel W Barsoum. MAX phases: bridging the gap between metals and ceramics. American Ceramics Society Bulletin, 92(3):20–27, 2013.

[10] XH Wang and YC Zhou. Layered machinable and electrically conductive Ti_2AlC and Ti_3AlC_2 ceramics: a review. Journal of Materials Science & Technology, 26(5):385–416, 2010.

[11] Gilles Hug and Evelyne Fries. Full-potential electronic structure of Ti_2AlC and Ti_2AlN. Physical Review B, 65(11):113104, 2002.

[12] G Hug, M Jaouen, and MW Barsoum. X-ray absorption spectroscopy, EELS, and full-potential augmented plane wave study of the electronic structure of Ti_2AlC, Ti_2AlN, Nb_2AlC, and $(Ti_{0.5}Nb_{0.5})_2AlC$. Physical Review B, 71(2):024105, 2005.

[13] H-I Yoo, MW Barsoum, and T El-Raghy. Ti_3SiC_2 has negligible thermopower. Nature, 407(6804):581–582, 2000.

[14] S Li, Rajeev Ahuja, MW Barsoum, Puru Jena, and Börje Johansson. Optical properties of Ti_3SiC_2 and Ti_4AlN_3. Applied Physics Letters, 92(22), 2008.

[15] Michel W Barsoum. MAX phases: properties of machinable ternary carbides and nitrides. John Wiley & Sons, 2013.

[16] Zhimei Sun and Yanchun Zhou. Ab initio calculation of titanium silicon carbide. Physical Review B, 60(3):1441, 1999.

[17] Denis Music, Zhimei Sun, and Jochen M Schneider. Electronic structure of Sc_2AC (A= Al, Ga, In, Tl). Solid state communications, 133(6):381–383, 2005.

[18] Martin Dahlqvist, Björn Alling, IA Abrikosov, and Johanna Rosén. Magnetic nanoscale laminates with tunable exchange coupling from first principles. Physical Review B, 84(22):220403, 2011.

[19] VJ Keast, S Harris, and DK Smith. Prediction of the stability of the $M_{n+1}AX_n$ phases from first principles. Physical Review B, 80(21):214113, 2009.

[20] J-P Palmquist, Sa Li, PO Å Persson, Jens Emmerlich, Ola Wilhelmsson, Hans Högberg, MI Katsnelson, Börje Johansson, Rajeev Ahuja, Olle Eriksson, et al. $M_{n+1}AX_n$ phases in the Ti-Si-C system studied by thin-film synthesis and ab initio calculations. Physical Review B, 70(16):165401, 2004.

[21] L Farber. Transmission electron microscopy study of a low-angle boundary in plastically deformed Ti_3SiC_2. Philosophical magazine letters, 79(4):163–170, 1999.

[22] BT Kelly. Physics of Graphite (Applied Science. New Jersey, 1981.

[23] IA Bell, CJL Wilson, AC McLaren, and MA Etheridge. Kinks in mica: role of dislocations and (001) cleavage. Tectonophysics, 127(1-2):49–65, 1986.

[24] Annemarie Meike. In situ deformation of micas; a high-voltage electron-microscope study. American Mineralogist, 74(7-8):780–796, 1989.

[25] Akihiro Kushima, Xiaofeng Qian, Peng Zhao, Sulin Zhang, and Ju Li. Ripplocations in van der Waals layers. Nano letters, 15(2):1302–1308, 2015.

[26] Jacob Gruber, Andrew C Lang, Justin Griggs, Mitra L Taheri, Garritt J Tucker, and Michel W Barsoum. Evidence for bulk ripplocations in layered solids. Scientific reports, 6(1):33451, 2016.

[27] MW Barsoum and GJ Tucker. Deformation of layered solids: Ripplocations not basal dislocations. Scripta Materialia, 139:166–172, 2017.

[28] Jacob Gruber, Andrew C Lang, Justin Griggs, Mitra L Taheri, Garritt J Tucker, and Michel W Barsoum. Evidence for bulk ripplocations in layered solids. Scientific reports, 6(1):33451, 2016.

[29] D Freiberg, MW Barsoum, and GJ Tucker. Nucleation of ripplocations through atomistic modeling of surface nanoindentation in graphite. Physical Review Materials, 2(5):053602, 2018.

[30] Hussein O Badr and Michel W Barsoum. On ripplocations and the deformation of graphite. Carbon, 201:599–615, 2023.

[31] Michael Naguib, Murat Kurtoglu, Volker Presser, Jun Lu, Junjie Niu, Min Heon, Lars Hultman, Yury Gogotsi, and Michel W Barsoum. Two-dimensional nanocrystals produced by exfoliation of Ti_3AlC_2. In MXenes, pages 15–29. Jenny Stanford Publishing, 2011.

[32] Michael I Baskes. Modified embedded-atom potentials for cubic materials and impurities. Physical review B, 46(5):2727, 1992.

[33] Pei Liu, Jingpei Xie, Aiqin Wang, Douqin Ma, and Zhiping Mao. An interatomic potential for accurately describing the atomic-scale deformation behaviors of Ti_2AlC crystal. Computational Materials Science, 182:109757, 2020.

[34] DG Pettifor and II Oleinik. Analytic bond-order potential for open and close-packed phases. Physical Review B, 65(17):172103, 2002.

[35] DG Pettifor and II Oleinik. Analytic bond-order potentials beyond Tersoff-Brenner. I. Theory. Physical review B, 59(13):8487, 1999.

[36] Gabriel Plummer and Garritt J Tucker. Bond-order potentials for the Ti_3AlC_2 and Ti_3SiC_2 MAX phases. Physical Review B, 100(21):214114, 2019.

[37] Volker L Deringer, Miguel A Caro, and Gábor Csányi. Machine learning interatomic potentials as emerging tools for materials science. Advanced Materials, 31(46):1902765, 2019.

[38] Oliver T Unke, Stefan Chmiela, Huziel E Sauceda, Michael Gastegger, Igor Poltavsky, Kristof T Schutt, Alexandre Tkatchenko, and Klaus-Robert Muller. Machine learning force fields. Chemical Reviews, 121(16):10142–10186, 2021.

[39] Venkatesh Botu and Rampi Ramprasad. Learning scheme to predict atomic forces and accelerate materials simulations. Physical Review B, 92(9):094306, 2015.

[40] Evgeny V Podryabinkin, Evgeny V Tikhonov, Alexander V Shapeev, and Artem R Oganov. Accelerating crystal structure prediction by machine-learning interatomic potentials with active learning. Physical Review B, 99(6):064114, 2019.

[41] Marco Fronzi, Roger D Amos, Rika Kobayashi, Naoki Matsumura, Kenta Watanabe, and Rafael K Morizawa. Evaluation of machine learning interatomic potentials for the properties of gold nanoparticles. Nanomaterials, 12(21):3891, 2022.

[42] Jan Kloppenburg, Livia B Pártay, Hannes Jónsson, and Miguel A Caro. A general-purpose machine learning Pt interatomic potential for an accurate description of bulk, surfaces, and nanoparticles. The Journal of chemical physics, 158(13), 2023.

[43] Ning Wang and Shiping Huang. Molecular dynamics study on magnesium hydride nanoclusters with machine-learning interatomic potential. Physical Review B, 102(9):094111, 2020.

[44] Kaiwei Wan, Jianxin He, and Xinghua Shi. Construction of high accuracy machine learning interatomic potential for surface/interface of nanomaterials—a review. Advanced Materials, page 2305758.

[45] Jesper Byggmästar, Kai Nordlund, and Flyura Djurabekova. Modeling refractory high-entropy alloys with efficient machine-learned interatomic potentials: Defects and segregation. Physical Review B, 104(10):104101, 2021.

[46] Xiang-Guo Li, Chi Chen, Hui Zheng, Yunxing Zuo, and Shyue Ping Ong. Complex strengthening mechanisms in the NbMoTaW multi-principal element alloy. npj Computational Materials, 6(1):70, 2020.

[47] Linus C Erhard, Jochen Rohrer, Karsten Albe, and Volker L Deringer. Modelling atomic and nanoscale structure in the silicon–oxygen system through active machine learning. Nature Communications, 15(1):1927, 2024.

[48] Niklas Leimeroth, Jochen Rohrer, and Karsten Albe. Structure–property relations of silicon oxycarbides studied using a machine learning interatomic potential. Journal of the American Ceramic Society, page , 2024.

[49] Bruno Focassio, Luis Paulo M. Freitas, and Gabriel R Schleder. Performance assessment of universal machine learning interatomic potentials: Challenges and directions for materials' surfaces. ACS Applied Materials & Interfaces, page , 2024.

[50] Alexander V Shapeev. Moment tensor potentials: A class of systematically improv-

able interatomic potentials. Multiscale Modeling & Simulation, 14(3):1153–1173, 2016.

[51] Yunxing Zuo, Chi Chen, Xiangguo Li, Zhi Deng, Yiming Chen, Jorg Behler, Gábor Csányi, Alexander V Shapeev, Aidan P Thompson, Mitchell A Wood, et al. Performance and cost assessment of machine learning interatomic potentials. The Journal of Physical Chemistry A, 124(4):731–745, 2020.

[52] Aidan P Thompson, Laura P Swiler, Christian R Trott, Stephen M Foiles, and Garritt J Tucker. Spectral neighbor analysis method for automated generation of quantum-accurate interatomic potentials. Journal of Computational Physics, 285:316–330, 2015.

[53] Albert P Bartók, Mike C Payne, Risi Kondor, and Gábor Csányi. Gaussian approximation potentials: The accuracy of quantum mechanics, without the electrons. Physical review letters, 104(13):136403, 2010.

[54] Jürgen Hafner and Georg Kresse. The vienna ab-initio simulation program VASP: An efficient and versatile tool for studying the structural, dynamic, and electronic properties of materials. Properties of Complex Inorganic Solids, 140:69–82, 1997.

[55] G. Kresse and J. Furthmüller. Efficiency of ab-initio total energy calculations for metals and semiconductors using a plane-wave basis set. Computational Materials Science, 6(1):15–50, 1996.

[56] John P Perdew, Kieron Burke, and Matthias Ernzerhof. Generalized gradient approximation made simple. Physical review letters, 77(18):3865, 1996.

[57] Shinobu Hashimoto, Noriko Nishina, Kiyoshi Hirao, You Zhou, Hideki Hyuga, Sawao Honda, and Yuji Iwamoto. Formation mechanism of Ti_2AlC under the self-propagating high-temperature synthesis (SHS) mode. Materials Research Bulletin, 47(5):1164–1168, 2012.

[58] Shuichi Nosé. A unified formulation of the constant temperature molecular dynamics methods. The Journal of chemical physics, 81(1):511–519, 1984.

[59] J Chapman, R Batra, and R Ramprasad. Machine learning models for the prediction of energy, forces, and stresses for Platinum. Computational Materials Science, 174:109483, 2020.

[60] Venkatesh Botu and Rampi Ramprasad. Adaptive machine learning framework to accelerate ab initio molecular dynamics. International journal of quantum chemistry, 115(16):1074–1083, 2015.

[61] Wenwen Li and Yasunobu Ando. Construction of accurate machine learning force fields for copper and silicon dioxide. arXiv preprint arXiv:1807.02042, 2018.

[62] April M Cooper, Johannes Kästner, Alexander Urban, and Nongnuch Artrith. Efficient training of ANN potentials by including atomic forces via Taylor expansion and application to water and a transition-metal oxide. npj Computational Materials, 6(1):54, 2020.

[63] Tran Doan Huan, Rohit Batra, James Chapman, Sridevi Krishnan, Lihua Chen, and Rampi Ramprasad. A universal strategy for the creation of machine learning-based atomistic force fields. NPJ Computational Materials, 3(1):37, 2017.

[64] Cheol Woo Park, Mordechai Kornbluth, Jonathan Vandermause, Chris Wolverton, Boris Kozinsky, and Jonathan P Mailoa. Accurate and scalable multi-element graph neural network force field and molecular dynamics with direct force architecture. arXiv preprint arXiv:2007.14444, 2020.

[65] Germain Clavier, Nicolas Desbiens, Emeric Bourasseau, Véronique Lachet, Nadège Brusselle-Dupend, and Bernard Rousseau. Computation of elastic constants of solids using molecular simulation: comparison of constant volume and constant pressure ensemble methods. Molecular Simulation, 43(17):1413–1422, 2017.

[66] Chi-Sing Man and Mojia Huang. A simple explicit formula for the Voigt-Reuss-Hill average of elastic polycrystals with arbitrary crystal and texture symmetries. Journal of Elasticity, 105:29–48, 2011.

[67] YL Du, ZM Sun, and H Hashimoto. First-principles study on phase stability and compression behavior of Ti_2SC and Ti_2AlC. Physica B: Condensed Matter, 405(2):720–723, 2010.

[68] Thierry Cabioc'h, Per Eklund, Vincent Mauchamp, and Michel Jaouen. Structural investigation of substoichiometry and solid solution effects in $Ti_2Al(C_x, N_{1-x})y$ compounds. Journal of the European Ceramic Society, 32(8):1803–1811, 2012.

[69] Mohammad Khazaei, Masao Arai, Taizo Sasaki, Mehdi Estili, and Yoshio Sakka. Trends in electronic structures and structural properties of MAX phases: a first-principles study on M_2AlC (M= Sc, Ti, Cr, Zr, Nb, Mo, Hf, or Ta), M_2AlN, and hypothetical M_2AlB phases. Journal of Physics: Condensed Matter, 26(50):505503, 2014.

[70] Sitaram Aryal, Ridwan Sakidja, Michel W Barsoum, and Wai-Yim Ching. A genomic approach to the stability, elastic, and electronic properties of the MAX phases. physica status solidi (b), 251(8):1480–1497, 2014.

[71] Jie Tan, Han Han, Darshana Wickramaratne, Wenguan Liu, Mingwen Zhao, and Ping Huai. A comparative first-principles study of the electronic, mechanical, defect and acoustic properties of Ti_2AlC and Ti_3AlC. Journal of Physics D: Applied Physics, 47(21):215301, 2014.

[72] Wai-Yim Ching, Yuxiang Mo, Sitaram Aryal, and Paul Rulis. Intrinsic mechanical properties of 20 MAX-phase compounds. Journal of the American Ceramic Society, 96(7):2292–2297, 2013.

[73] Qing-He Gao, An Du, and Ze-Jin Yang. Structural inheritance and difference between Ti_2AlC, Ti_3AlC_2 and $Ti_5Al_2C_3$ under pressure from first principles. Modern Physics Letters B, 31(03):1750016, 2017.

[74] Vo Vitek. Theory of the core structures of dislocations in body-centred-cubic metals. 1974.

[75] Sylvie Aubry and Darcy A Hughes. Reductions in stacking fault widths in fcc crystals: Semiempirical calculations. Physical Review B, 73(22):224116, 2006.

[76] Poulami Chakraborty, Aurab Chakrabarty, Amlan Dutta, and Tanusri Saha-Dasgupta. Soft MAX phases with boron substitution: A computational prediction. Physical Review Materials, 2(10):103605, 2018.

[77] B Poon, L Ponson, J Zhao, and G Ravichandran. Damage accumulation and hysteretic behavior of MAX phase materials. Journal of the Mechanics and Physics of Solids, 59(10):2238–2257, 2011.

[78] Michel W Barsoum and Miladin Radovic. Elastic and mechanical properties of the MAX phases. Annual review of materials research, 41:195–227, 2011.

[79] AG Zhou and MW Barsoum. Kinking nonlinear elastic deformation of Ti_3AlC_2, Ti_2AlC, $Ti_3Al(C_{0.5},N_{0.5})_2$ and $Ti_2Al(C_{0.5}, N_{0.5})$. Journal of alloys and compounds, 498(1):62–70, 2010.

[80] Miladin Radovic, MW Barsoum, A Ganguly, T Zhen, P Finkel, SR Kalidindi, and Edgar Lara-Curzio. On the elastic properties and mechanical damping of Ti_3SiC_2, Ti_3GeC_2, $Ti_3Si_{0.5}Al_{0.5}C_2$ and Ti2AlC in the 300-1573 K temperature range. Acta materialia, 54(10):2757–2767, 2006.

[81] Rogelio Benitez, Wen Hao Kan, Huili Gao, Morgan O'Neal, Gwénaëlle Proust, and Miladin Radovic. Room temperature stress-strain hysteresis in ti2alc revisited. Acta Materialia, 105:294–305, 2016.

[82] MW Barsoum, T Zhen, A Zhou, S Basu, and SR Kalidindi. Microscale modeling of kinking nonlinear elastic solids. Physical Review B, 71(13):134101, 2005.

[83] G Plummer, H Rathod, A Srivastava, M Radovic, T Ouisse, M Yildizhan, PO Å Persson, K Lambrinou, MW Barsoum, and GJ Tucker. On the origin of kinking in layered crystalline solids. Materials Today, 43:45–52, 2021.

[84] Debankur Das, Jürgen Horbach, Peter Sollich, Tanusri Saha-Dasgupta, and Surajit Sengupta. Wrinkles, folds, and ripplocations: Unusual deformation structures of confined elastic sheets at nonzero temperatures. Phys. Rev. Res., 2:043284, Nov 2020.

[85] Christopher J Gilbert, DR Bloyer, MW Barsoum, T El-Raghy, AP Tomsia, and RO Ritchie. Fatigue-crack growth and fracture properties of coarse and fine-grained Ti_3SiC_2. Scripta Materialia, 42(8):761–767, 2000.

[86] Andreas K Kronenberg, Stephen H Kirby, and John Pinkston. Basal slip and mechanical anisotropy of biotite. Journal of Geophysical Research: Solid Earth, 95(B12):19257–19278, 1990.

[87] Vanadis Marina Mares and AK Kronenberg. Experimental deformation of muscovite. Journal of Structural Geology, 15(9-10):1061–1075, 1993.

[88] Roy Christoffersen and Andreas K Kronenberg. Dislocation interactions in experimentally deformed biotite. Journal of Structural Geology, 15(9-10):1077–1095, 1993.

[89] Rogelio Benitez, Wen Hao Kan, Huili Gao, Morgan O'Neal, Gwénaëlle Proust, and Miladin Radovic. Room temperature stress-strain hysteresis in Ti_2AlC revisited. Acta Materialia, 105:294–305, 2016.

[90] Ai Guo Zhou and MW Barsoum. Nonlinear elastic deformation of MAX phases. Key Engineering Materials, 434:149–153, 2010.

[91] FC Frank and AN Stroh. On the theory of kinking. Proceedings of the Physical Society. Section B, 65(10):811, 1952.

[92] AG Zhou, S Basu, and MW Barsoum. Kinking nonlinear elasticity, damping and microyielding of hexagonal close-packed metals. Acta Materialia, 56(1):60–67, 2008.

[93] Xiaohui Wang and Yanchun Zhou. Solid–liquid reaction synthesis of layered machinable Ti_3AlC_2 ceramic. Journal of Materials Chemistry, 12(3):455–460, 2002.

[94] CJ Rawn, MW Barsoum, T El-Raghy, A Procipio, CM Hoffmann, and CR Hubbard.

Structure of Ti_4AlN_3—A layered $M_{n+1}AX_n$ nitride. Materials research bulletin, 35(11):1785–1796, 2000.

[95] Hui Zhang, Tao Hu, Xiaohui Wang, and Yanchun Zhou. Structural defects in MAX phases and their derivative MXenes: A look forward. Journal of Materials Science & Technology, 38:205–220, 2020.

[96] Simon C. Middleburgh, Greg R. Lumpkin, and Daniel Riley. Accommodation, Accumulation, and Migration of Defects in Ti_3SiC_2 and Ti_3AlC_2 MAX Phases. Journal of the American Ceramic Society, 96(10):3196–3201, 2013.

[97] Jiemin Wang, Bin Liu, Jingyang Wang, and Yanchun Zhou. Theoretical investigation of thermodynamic stability and mobility of the intrinsic point defects in Ti_3AC_2 (A= Si, Al). Physical Chemistry Chemical Physics, 17(14):8927–8934, 2015.

[98] B Liu, JY Wang, J Zhang, JM Wang, FZ Li, and YC Zhou. Theoretical investigation of A-element atom diffusion in Ti_2AC (A= Sn, Ga, Cd, In, and Pb). Applied Physics Letters, 94(18), 2009.

[99] Jingyang Wang, Yanchun Zhou, Ting Liao, Jie Zhang, and Zhijun Lin. A first-principles investigation of the phase stability of Ti_2AlC with Al vacancies. Scripta Materialia, 58(3):227–230, 2008.

[100] J Zhang and YC Zhou. Microstructure, mechanical, and electrical properties of Cu–Ti_3AlC_2 and in situ Cu–TiC_x composites. Journal of Materials Research, 23(4):924–932, 2008.

[101] Georgios A Tritsaris, Mehmet Gökhan Şensoy, Sharmila N Shirodkar, and Efthimios Kaxiras. First-principles study of coupled effect of ripplocations and S-vacancies in MoS_2. Journal of Applied Physics, 126(8), 2019.

[102] J Gruber, MW Barsoum, and GJ Tucker. Characterization of ripplocation mobility in graphite. Materials Research Letters, 8(2):82–87, 2020.

[103] Suman Chowdhury, Supriya Ghosal, Deep Mondal, and Debnarayan Jana. First-principles and machine-learning study of electronic and phonon transport in carbon-based AA-stacked bilayer biphenylene nanosheets. Journal of Physics and Chemistry of Solids, 170:110909, 2022.

[104] Bohayra Mortazavi, Ivan S Novikov, Evgeny V Podryabinkin, Stephan Roche, Timon Rabczuk, Alexander V Shapeev, and Xiaoying Zhuang. Exploring phononic properties of two-dimensional materials using machine learning interatomic potentials. Applied Materials Today, 20:100685, 2020.

[105] Michel W Barsoum. Ripplocations: a progress report. Frontiers in Materials, 7:146, 2020.

8

Summary and Outlook

8.1 Summary

In this thesis, we have leveraged various techniques of machine learning(ML) in investigating systems like semiconductor heterostructures, binary nanoalloys, gold atomic chains and layered crystalline MAX compounds, particularly, Ti_2AlC. We have suggested an ML-based high-throughput approach, that can substitute computationally extensive calculations, in classifying semiconductor heterostructures based on features of the individual semiconductors. In another case, we have identified the key factors and their relative importance in guiding the core-shell segregation trends in nanoscale binary alloys using an ML technique on a large database of alkali, alkaline, basic, 3d, 4d, and 5d transition metals, and p-block metals. We have also found conditions under which other morphologies,like Janus or mixed, are rather stabilized. The effect of concentration and size have been investigated using first-principles calculations on Pd-X(X= 3d,4d,5d) clusters. Additionally, we have also investigated their catalytic activity. In the next projrct, based on experimental data on formation of one-dimensional atomic gold chains, we have identified optimal values of external stimuli like breaking speed and bias voltage that support long chain formation using a supervised learning technique. Further, an unsupervised algorithm has been used on experimental trace features to recognize electrode configurations that might lead to such long chain formation. We have finally employed an ab-initio molecular dynamics simulation to reinforce our understanding. In another work, we have created a machine-learned force field based on ab-initio data for MAX compound Ti_2AlC,since the length and time scale for investigating their non-linear elastic behavior are inaccessible by first-principle calculations and classical potentials are scarce for the same. This has been employed to reconstruct the experimentally observed elastic behavior of Ti_2AlC and understand the un-

derlying micro-mechanism. Further, the effect of Al vacancies on the elastic property has also been investigated.

In the following, a summary of the key findings of our study and potential avenues for future research are highlighted.

8.1.1 Chapter 3: Machine learning classification of binary semiconductor heterostructures

In this chapter, we have tackled the problem of predicting semiconductor heterostructure types as dictated by the sign of band-edge discontinuities between the two constituent semiconductors. A combination of bandstructure information and machine learning has been used. The main findings are:

- Heterostructure types(Type-I/Type-II) can be predicted using bandstructure information of constituent semiconductors. The branch point energy can be used as zero energy to align the two semiconductors.
- The valence band offset and conduction band offset predicted using bandstructure information correlates well with experimental values.
- Combination of all elemental and binary semiconductors lead to 903 different heterostructures, out of which types have been obtained from experiments or detailed calculations for 31 instances. The bandstructure approach have exhibited perfect consensus with these. For the remaining cases, it has predicted $\approx 40\%$ as Type-I and rest as Type-II.
- A machine learning model based on instances with labeled heterostructure types and features based on elemental properties of the component semiconductors can classify heterostructure types. After subsequent feature engineering and class imbalance handling, the model have showm 89% matching with the bandstructure predictions.
- We have found that within a specific combination of semiconductors, heterostructure type can depend on the crystal structures of the semiconductors. This has been validated using first-principles calculations for the heterostructures between cubic-AlP/ZnO and cubic-GaP/GaN, between hexa-AlP/ZnO and hexa-GaP/GaN, and between cubic-AlP/ZnO and hexa-GaP/GaN.
- The established method can be extended to nanoscale heterostructures, i.e, by joining two quantum dots(QDOTs). The band alignment approach, corrected using the Brus equation[1], can reproduce experimental VBO and CBO trend between ZnSe QDOT

and CdS QDOT. By including nano-heterostructures as instances and quantum confinement correction terms as features, the classifier model could rightly classify 82% of the original learning dataset.

The approach investigated in this study can thus act as a robust computational approach for rapid materials selection in heterostructure design.

8.1.2 Chapter 4: Understanding the Trend in Core-Shell Preferences for Bimetallic Nanoclusters: A Machine Learning Approach

In this chapter, we have taken up the problem of finding the details of the driving factors behind core-shell segregation of elements in binary metal alloys. Core-shell morphology of a binary nanoalloy has been reported to be controlled by factors like cohesive energy, surface energy, atomic radii, and electronegativity of the components. It is crucial to understand the interplay of these factors and figure out their relative importance, and their dependence on the metal types. Our main findings are:

- Using a machine learning scheme to address these questions, we have found four key driving factors: cohesive energy difference, atomic radius difference, magnetic nature of the elements, and coordination number difference of the elements in their bulk phase. The relative importance of these factors depend on the metal types in the nanoalloy.
- For combination of alkali/ alkaline elements, atomic radius and coordination number are found to be more important. Similar trends are shown in TM/TM combinations. For combinations of alkali/alkaline and TM elements, magnetism and atomic radius become critical factors.
- When no specific core-shell segregation trend can be established, Janus and mixed morphologies might stabilize. We have found that when the cohesive energy difference between the constituent elements is either very small or very large, the system favors mixed and Janus structures, respectively, over the core–shell configuration.

Our comprehensive, machine-learning-driven computational study offers valuable insights to guide the design of bimetallic nanoalloys with tailored mixing patterns.

8.1.3 Chapter 5: First principles insights into the relative stability, electronic and catalytic properties of core-shell, Janus and mixed structural patterns for bimetallic Pd-X nanoalloys (X = Co, Ni, Cu, Rh, Ag, Ir, Pt, Au)

In this chapter, in extension to work done on chapter 4, we have looked at the effect of varying the composition and cluster size on stability of nanoclusters, and how it correlate to different microscopic properties of the system. The study has been done based on Pd-based binary nanoalloys for their prospects in electro-catalysis. The main findings are :

- The relative stability among the structural patterns of Pd-X nanoalloys at the two composition limits(Pd-poor/Pd-rich) are found to rely on the identity of X.
- Most stable structures are with least surface energies in either composition.
- The difference in atomic radii and cohesive energies of the constituent elements is found to correlate with stability as elucidated in Chapter 4.
- ICOHP calculations reveal that higher stability is mostly associated with an enhanced covalency.
- We have found that the three structural patterns can be distinguished in terms of their (total)orbital hybridization index. Within each composition, this value follows the order Janus> mixed>core-shell in most cases.
- To probe the catalytic activity of Pd-X nanoalloys, we have employed the d-band model[2] that proposes the position of d-band center(with respect to Fermi energy) as a descriptor of binding capacity to an absorbate. According to this model, the trend in binding of the absorbate on the surface of the catalyst is an effective indicator about the rate of the catalytic activity for the catalytic surface. Our findings have suggested that bimetallic Pd–Ni nanoalloys represent the most promising combination for developing stable and catalytically active non-Pt nanoalloys.
- We have also explored the effect of the cluster size on the studied properties. The previously done analysis have been repeated on a 55-atom sized icosahedral geometry for the bimetallic Pd–Ni nano-alloy. The trends in stability, hybridization index and catalytic activity are seen to follow the 147-atoms cluster results without any significant deviation.

8.1.4 Chapter 6: Machine-learning prediction of the formation of atomic gold wires by mechanically controlled break junctions

In this chapter, we have attempted to develop a microscopic understanding of the formation of atomic chains of gold of reasonable length. Particularly, we have investigated the cumulative effect of external stimuli(bias voltage and stretching rate) using experimental data and rationalize the optimal settings in terms of an atomistic picture. The chief findings are:

- The cumulative effect of these external stimuli has been explored under the ambit of machine learning. Our supervised learning technique has indicated that the optimal conditions for forming longer atomic chains are in the regime of low bias voltage and low stretching rate.
- The experimental traces have been clustered according to their inherent features around $1G_0$ to detect electrode configurations leading to such long chains. Three distinct types of traces could be segregated using an unsupervised learning scheme. The traces that correspond to long chains majorly belong to a particular type. Ab-initio molecular dynamics simulations have reaffirmed that the initial junction structure of this type is characterized by a double contact-like structure.

Thus, our understanding of the combined effects of bias and breaking speed in chain formation using an MCBJ setup offers useful insights in designing future experiments.

8.1.5 Chapter 7: Ab-initio trained machine learning potential for MAX compound Ti_2AlC: construction, validation, and study of non linear elasticity

In this chapter, we have developed a machine learning interatomic potential tarined on ab-initio data for MAX compound Ti_2AlC to explore its mechanical properties, specifically the non-linear elastic behavior. Layered MAX compounds show non-linear elastic behavior atypical for elastically stiff materials. This is manifested as hysteretic stress-strain response during loading and unloading of a sample. The micromechanism has long been understood in terms of basal dislocations[3, 4]. However,recently, the phenomenon of ripplocations[5, 6], has been utilized to explain the same and validated through experiments. First principle theoretical explorations are restricted by the length and time scale of the phenomenon, whereas an apt potential is scarce for classical molecular dynamics simulations. We have developed a machine learned interatomic potential based on first-principles data of force,energy and stress of various configurations of MAX phase Ti_2AlC. The chief outcomes are :

- The constructed potential has been validated against key material properties, including lattice constants, formation energy, elastic constants, and stacking fault energies. When applied in classical molecular dynamics simulations, the machine-learned potential have reliably reproduced the experimentally observed nonlinear elasticity of Ti_2AlC.
- We have found that common defects, such as Al vacancies, have a significant impact on the hysteresis behavior observed in the stress–strain curves, effectively increasing its width. This behavior has been rationalized by examining the atomic arrangements in a layer with Al vacancies vis-à-vis a defect-free system.

8.2 Outlook

1. In chapter 3, we have established a workflow to predict the type of heterostructure made by joining two dissimilar semiconductors. This presents several directions for future research.

   In our study, we have considered only combinations of elemental and binary semiconductors. It can further be expanded to include multicomponent semiconductors.

   The current study does not provide a prediction regarding whether a heterostructure's band gap is direct or indirect. To date, machine learning predictions for direct/indirect band gap classification have primarily focused on individual semiconductors. Expanding this approach to semiconductor pairs in heterostructures remains an open area for future exploration.

2. In chapter 4, we have explored the factors and their relative importance in influencing the core-shell segregation binary nanoclusters, or forming other morphologies like Janus and mixed. Building on this, there are several routes to future research.

   While core-shell, Janus or mixed are the more ubiquitous of the morphologies, certain other arrangements like the multi-shell, ball-and-cup or quasi-Janus structures are sometimes formed. Out study can be extended to accommodate these possibilities.

   The current study is based on T=0 K results. Understanding the effect of finite temperature on stability of nanoclusters using an ML analysis can help in determining their utility in high temperature environment, for example, in catalytic research.

3. In chapter 5, we have observed the effect of composition and size on stability of bimetallic nanoclusters Pd-X(X=3d/4d/5d transition metals) and concurrent trends in relevant microscopic properties. We have also examined the trend in their relative

catalytic activity. There are several avenues towards further research in this context.

The catalytic activities of bimetallic nanoclusters with doped hetero-atoms have shown promising results, and can be explored in the context of our work.

While the catalytic activity has been probed using a d-band model in our work, it might also be investigated using ML techniques. Catalytic nature can be encapsulated based on electronic and steric features.

4. In chapter 6, using ML analysis on experimental data, we have explored the formation of one-dimensional gold atomic chains which currently has immense research interest. Building on our work, there are several directions for further exploration.

   In our work, the experiments has been conducted at 77K. It would be interesting to monitor the effect of temperature on optimal conditions for long chain formation.

   To explore the effect of the element's identity in forming the chain, a similar analysis of traces over different d-block elements can be conceptualized.

   Single-molecule junctions have recently piqued interest for their possible applications in molecular electronics. Formation of such junctions for different molecules can be explored using a similar workflow as undertaken in this study.

5. In chapter 7, we have prepared a machine learned force field for MAX compound $M_{n+1}AX_n$ with n=1 and M=Ti, A=Al, X=C. Based on this work, there are several avenues for further exploration.

   Our work has considered the n=1. It can be expanded for n=2,3 case. The current potential can be also be augmented to describe MAX compounds with combinations of other M,A and X atoms.

   Nanoindentation experiments showing delamination cracks on basal plane loading, are important markers of ripplocations, the mechanism explored in this study. An atomistic simulation of nanoindentation using our force field would further confirm the reliability of our model.

6. Since the machine learning models in this thesis, and in fact, in most of the current materials science literature are developed independently, they are isolated across data modalities, material domains, and application-specific tasks. A class of AI models, called the foundation models (FMs), can be beneficial in this regard. FMs have recently shown exceptional success in tackling complex tasks across domains such as natural language processing and computer vision. These models are typically large and trained on diverse, large-scale datasets using self-supervised learning,

rather than being tailored to a single task. Once pre-trained, they can generalize and adapt to a wide range of downstream applications with minimal or no additional fine-tuning. Materials' property prediction is a crucial area to which foundation models can bring value by providing transferrable core components. Most of the foundation models currently available for this purpose are based on BERT[7, 8] or GPT architectures[9, 10]. Alternatively, some recent classes of machine learning-based potentials can also be considered as foundation models. These models are primarily designed to predict system energies and forces, having been pre-trained on extensive, high-quality reference data, typically derived from density functional theory (DFT) calculations. While the former attempt to directly predict specific properties, their effectiveness can be limited by the under representation of rare events. In contrast, machine-learned interatomic potentials (MLIPs) approximate the underlying potential energy surface, allowing conventional simulation techniques to be applied with significantly reduced computational cost. Some pre-trained model already available includes MACE[11], MEGNET[12], AIMNET[13] etc.

7. As modern datasets continue to grow in size, the time complexities of classical algorithms may become prohibitively high for practical use. In this context, quantum computing presents a promising avenue for enhancing the efficiency of these methods, potentially enabling them to scale much more effectively. Several quantum algorithms targeting linear algebra, sampling, and optimization problems theoretically promise exponential speed-ups over their classical counterparts. However, the practical deployment of current quantum machine learning (QML) techniques still faces significant hurdles—chief among them being the need for fast memory access and the use of highly specific data structures. Moreover, the adaptation of QML often involves a process of encoding classical data into quantum states, and the computational cost associated with this step plays a crucial role in determining whether quantum speed-ups in machine learning for classical data are achievable.

   Despite the nascent form of QML, latest research have shown that certain problems under the purview of machine learning can now be dealt with quantum algorithms,atleast in principle. Linear system of equations can solved using the quantum linear system algorithm (QLSA) for matrix inversion,with lesser time-complexity than classical techniques. Singular value estimation is another fundamental tool widely used in computation. Quantum singular value estimation (QSVE) offers a logarithmic time scaling as opposed to classical complexity of $O(MN^2)$ for a M $\times$N matrix (M$>$N). Recently, implementing quantum algorithms in hastening sampling techniques like Markov chain Monte Carlo (MCMC) have garnered much interest.

Algorithms have also been suggested for optimization, for eg,in certain kinds of convex hull problems. Another major diagonal of study in this domain is the quantum application of artificial neural network. The primary research directions have centered on enhancing the training speed of classical models and creating networks in which every component—from individual neurons to training algorithms—is implemented on a quantum computer.

It should be noted that the quantum techniques presently face several caveats and are quite restricted in their practical utilization. However, if application of quantum algorithm to the problems addressed in this thesis can be made possible, it would act as a proof of concept to the complexity question.

Bibliography

[1] Louis Brus. Electronic wave functions in semiconductor clusters: experiment and theory. The Journal of Physical Chemistry, 90(12):2555–2560, 1986.

[2] Jens K Nørskov, Frank Abild-Pedersen, Felix Studt, and Thomas Bligaard. Density functional theory in surface chemistry and catalysis. Proceedings of the National Academy of Sciences, 108(3):937–943, 2011.

[3] L Farber. Transmission electron microscopy study of a low-angle boundary in plastically deformed Ti3SiC2. Philosophical magazine letters, 79(4):163–170, 1999.

[4] BT Kelly. Physics of Graphite (Applied Science. New Jersey, 1981.

[5] Jacob Gruber, Andrew C Lang, Justin Griggs, Mitra L Taheri, Garritt J Tucker, and Michel W Barsoum. Evidence for bulk ripplocations in layered solids. Scientific reports, 6(1):33451, 2016.

[6] MW Barsoum and GJ Tucker. Deformation of layered solids: Ripplocations not basal dislocations. Scripta Materialia, 139:166–172, 2017.

[7] Jacob Devlin, Ming-Wei Chang, Kenton Lee, and Kristina Toutanova. Bert: Pre-training of deep bidirectional transformers for language understanding. In Proceedings of the 2019 conference of the North American chapter of the association for computational linguistics: human language technologies, volume 1 (long and short papers), pages 4171–4186, 2019.

[8] Janghoon Ock, Chakradhar Guntuboina, and Amir Barati Farimani. Catalyst energy prediction with CatBERTa: Unveiling feature exploration strategies through large language models. ACS Catalysis, 13(24):16032–16044, 2023.

[9] Kevin Maik Jablonka, Philippe Schwaller, Andres Ortega-Guerrero, and Berend Smit. Leveraging large language models for predictive chemistry. Nature Machine Intelligence, 6(2):161–169, 2024.

[10] Zequn Liu, Wei Zhang, Yingce Xia, Lijun Wu, Shufang Xie, Tao Qin, Ming Zhang, and Tie-Yan Liu. Molxpt: Wrapping molecules with text for generative pre-training. arXiv preprint arXiv:2305.10688, 2023.

[11] Ilyes Batatia, David P Kovacs, Gregor Simm, Christoph Ortner, and Gábor Csányi. MACE: Higher order equivariant message passing neural networks for fast and accurate force fields. Advances in neural information processing systems, 35:11423–11436, 2022.

[12] Chi Chen and Shyue Ping Ong. A universal graph deep learning interatomic potential for the periodic table. Nature Computational Science, 2(11):718–728, 2022.

[13] Dylan M Anstine, Roman Zubatyuk, and Olexandr Isayev. AIMNet2: a neural network potential to meet your neutral, charged, organic, and elemental-organic needs. Chemical Science, 2025.

Appendix A

List of bimetallic nanoclusters taken from literature.

System	Reference
Cu-Pt	Zhou S. et.al. Pt–Cu Core–Shell and Alloy Nanoparticles for Heterogeneous NOx Reduction: Anomalous Stability and Reactivity of a Core–Shell Nanostructure. Angew. Chem. Int. Ed. 2005, 44, 4539–4543.
Pd-Ag	Mulvaney P. Surface Plasmon Spectroscopy of Nanosized Metal Particles. Langmuir 1996, 12, 788–800.
Pd-Au	Liu H. B.; Pal U.; Medina A.; Maldonado C.; Ascencio J. A. Structural incoherency and structure reversal in bimetallic Au-Pd nanoclusters. Phys. Rev. B 2005, 71, 074503.
Ag-Pt	Doudna C. M. et.al. Radiolytic Synthesis of Bimetallic Ag-Pt Nanoparticles with a High Aspect Ratio. J. Phys. Chem. B 2003, 107, 2966–2970.
Pt-Au	Henglein A. Preparation and Optical Absorption Spectra of Au-core Pt-shell and Pt-core Au-shell Colloidal Nanoparticles in Aqueous Solution. J. Phys. Chem. B 2000, 104, 2201–2203.
Fe-Co	Zubris M.; King R.B.; Garmestani H.; Tannenbaum R. FeCo nanoalloy formation by decomposition of their carbonyl precursors. J. Mater. Chem. 2005, 15, 1277–1285.
Fe-Ni	Sahoo S.; Rollmann G.; Entel P. Segregation and ordering in binary transition metal clusters. Phase Transitions 2006, 79(9–10), 693–700.
Co-Ni	Brayner R. et.al. Algal polysaccharide capsule-templated growth of magnetic nanoparticles. New J. Chem. 2005, 29, 681–685.
Co-Cu	Lu Q.L.; Zhu L.Z.; Ma L.; Wang G.H. Magnetic properties of Co/Cu and Co/Pt bimetallic clusters. Chem. Phys. Lett. 2005, 407, 176–179.
Fe-Ag	Andrews M.P.; O'Brien S.C. Gas-Phase "Molecular Alloys" of Bulk Immiscible Elements: Fe_xAg_y. J. Phys. Chem. 1992, 96, 8233–8241.

System	Reference
Co-Pd	Carlsson A. F.; Bäumer M.; Risse T.; Freund H.J. Surface structure of Co–Pd bimetallic particles supported on thin films studied using infrared reflection absorption spectroscopy of CO. J. Chem. Phys. 2003, 119, 10885.
Co-Ag	Ferrando R. et.al. Quantum effects on the structure of pure and binary metallic nanoclusters. Phys. Rev. B 2005, 72, 085449.
Co-Rh	Fromen M.C. et.al. Structural study of bimetallic Co_xRh_{1-x} nanoparticles: Size and composition effects. Phys. Rev. B 2004, 69, 235416.
Ni-Rh	Sondón T.; Guevara J.; Saúl A. Study of the structure, segregation, and magnetic properties of Ni-Rh clusters. Phys. Rev. B 2007, 75, 104426.
Co-Pt	Park J.-I.; Cheon J. Synthesis of "Solid Solution" and "Core-Shell" Type Cobalt-Platinum Magnetic Nanoparticles via Transmetalation Reactions. J. Am. Chem. Soc. 2001, 123, 5743–5746.
Co-Au	Paulus P.M. et.al. Magnetic properties of nanosized transition metal colloids: the influence of noble metal coating. Eur. Phys. J. D 1999, 9, 501–504.
Fe-Au	Zhoua W.L.; Carpenter E.E.; Lin J.; Kumbhar A.; Sims J.; O'Connor C.J. Nanostructures of gold coated iron core-shell nanoparticles and the nanobands assembled under magnetic field. Eur. Phys. J. D 2001, 16, 289–292.
Ru-Pt	Nashner M.S. et.al. Core Shell Inversion during Nucleation and Growth of Bimetallic Pt/Ru Nanoparticles. J. Am. Chem. Soc. 1998, 120, 8093–8101.
Rh-Pt	Aguado A.; López J.M. Structural and thermal behavior of compact core-shell nanoparticles: Core instabilities and dynamic contributions to surface thermal stability. Phys. Rev. B 2005, 72, 205420.
W-Au	Li X. et.al. Experimental Observation and Confirmation of Icosahedral $W@Au_{12}$ and $Mo@Au_{12}$ Molecules. Angew. Chem. Int. Ed. 2002, 41, 24.
V-Au	Zhai H.-J.; Li J.; Wang L.S. Icosahedral gold cage clusters: $M@_{12}$ (M=V, Nb, and Ta). J. Chem. Phys. 2004, 121, 8369.

System	Reference
Cu-Zn	Hambrock J. et.al. Nano-Brass: Bimetallic Copper/Zinc Colloids by a Nonaqueous Organometallic Route Using $[Cu(OCH(Me)CH_2NMe_2)_2]$ and Et_2Zn as Precursors. Chem. Mater. 2003, 15, 4217–4222.
In-Au	Boyen H.-G. et.al. Alloy Formation of Supported Gold Nanoparticles at Their Transition from Clusters to Solids: Does Size Matter? Phys. Rev. Lett. 2005, 94, 016804.
Sn-Au	Henglein A.; Giersig M. Radiolytic Formation of Colloidal Tin and Tin-Gold Particles in Aqueous Solution. J. Phys. Chem. 1994, 98, 6931–6935.
Ag-Cd	Henglein A. Colloidal Silver Catalyzed Multi-Electron Transfer Processes in Aqueous Solution. Ber. Bunsenges. Phys. Chem. 1980, 84, 253–259.
Ag-In	Henglein A. et.al. Electrochemistry of Colloidal Silver Particles in Aqueous Solution: Deposition of Lead and Indium and Accompanying Optical Effects. Ber. Bunsenges. Phys. Chem. 1992, 96, 6.
Ag-Pb	Henglein A. et.al. Electrochemistry of Colloidal Silver Particles in Aqueous Solution: Deposition of Lead and Indium and Accompanying Optical Effects. Ber. Bunsenges. Phys. Chem. 1992, 96, 6.
Fe-Pt	Fortunelli A.; Velasco A-M. Structural and electronic properties of Pt/Fe nanoclusters from EHT calculations. J. Mol. Struct. (Theochem) 1999, 487, 251–266.
Ag-Au	Jian Z.; Caili Z. Influence of dielectric core and embedding medium on the local field enhancement for gold nanoshells. J. Appl. Phys. 2006, 100, 026104.
Ag-Au	Bruzzone S.; Arrighini G.P.; Guidotti C. Theoretical study of the optical absorption behavior of Au/Ag core–shell nanoparticles. Mater. Sci. Eng. C 2003, C23, 965–970.
Ag-Ta	Corona B.; Howard M.; Zhang L.; Henkelman G. Computational screening of core@shell nanoparticles for the hydrogen evolution and oxygen reduction reactions. J. Chem. Phys. 2016, 145, 244708.

System	Reference
Ag-W	Corona B.; Howard M.; Zhang L.; Henkelman G. Computational screening of core@shell nanoparticles for the hydrogen evolution and oxygen reduction reactions. J. Chem. Phys. 2016, 145, 244708.
Ag-Hf	Corona B.; Howard M.; Zhang L.; Henkelman G. Computational screening of core@shell nanoparticles for the hydrogen evolution and oxygen reduction reactions. J. Chem. Phys. 2016, 145, 244708.
Ag-Re	Corona B.; Howard M.; Zhang L.; Henkelman G. Computational screening of core@shell nanoparticles for the hydrogen evolution and oxygen reduction reactions. J. Chem. Phys. 2016, 145, 244708.
Co-Zn	Corona B.; Howard M.; Zhang L.; Henkelman G. Computational screening of core@shell nanoparticles for the hydrogen evolution and oxygen reduction reactions. J. Chem. Phys. 2016, 145, 244708.
Cr-Re	Corona B.; Howard M.; Zhang L.; Henkelman G. Computational screening of core@shell nanoparticles for the hydrogen evolution and oxygen reduction reactions. J. Chem. Phys. 2016, 145, 244708.
Cr-Cu	Corona B.; Howard M.; Zhang L.; Henkelman G. Computational screening of core@shell nanoparticles for the hydrogen evolution and oxygen reduction reactions. J. Chem. Phys. 2016, 145, 244708.
Cr-Nb	Corona B.; Howard M.; Zhang L.; Henkelman G. Computational screening of core@shell nanoparticles for the hydrogen evolution and oxygen reduction reactions. J. Chem. Phys. 2016, 145, 244708.
Cr-Ru	Corona B.; Howard M.; Zhang L.; Henkelman G. Computational screening of core@shell nanoparticles for the hydrogen evolution and oxygen reduction reactions. J. Chem. Phys. 2016, 145, 244708.

System	Reference
Cr-Tc	Corona B.; Howard M.; Zhang L.; Henkelman G. Computational screening of core@shell nanoparticles for the hydrogen evolution and oxygen reduction reactions. J. Chem. Phys. 2016, 145, 244708.
Cr-Zn	Corona B.; Howard M.; Zhang L.; Henkelman G. Computational screening of core@shell nanoparticles for the hydrogen evolution and oxygen reduction reactions. J. Chem. Phys. 2016, 145, 244708.
Cu-Ir	Corona B.; Howard M.; Zhang L.; Henkelman G. Computational screening of core@shell nanoparticles for the hydrogen evolution and oxygen reduction reactions. J. Chem. Phys. 2016, 145, 244708.
Cu-Tc	Corona B.; Howard M.; Zhang L.; Henkelman G. Computational screening of core@shell nanoparticles for the hydrogen evolution and oxygen reduction reactions. J. Chem. Phys. 2016, 145, 244708.
Cu-Re	Corona B.; Howard M.; Zhang L.; Henkelman G. Computational screening of core@shell nanoparticles for the hydrogen evolution and oxygen reduction reactions. J. Chem. Phys. 2016, 145, 244708.
Fe-Zn	Corona B.; Howard M.; Zhang L.; Henkelman G. Computational screening of core@shell nanoparticles for the hydrogen evolution and oxygen reduction reactions. J. Chem. Phys. 2016, 145, 244708.
Hf-Au	Corona B.; Howard M.; Zhang L.; Henkelman G. Computational screening of core@shell nanoparticles for the hydrogen evolution and oxygen reduction reactions. J. Chem. Phys. 2016, 145, 244708.
Hf-Ta	Corona B.; Howard M.; Zhang L.; Henkelman G. Computational screening of core@shell nanoparticles for the hydrogen evolution and oxygen reduction reactions. J. Chem. Phys. 2016, 145, 244708.

System	Reference
Hf-W	Corona B.; Howard M.; Zhang L.; Henkelman G. Computational screening of core@shell nanoparticles for the hydrogen evolution and oxygen reduction reactions. J. Chem. Phys. 2016, 145, 244708.
Mn-Os	Corona B.; Howard M.; Zhang L.; Henkelman G. Computational screening of core@shell nanoparticles for the hydrogen evolution and oxygen reduction reactions. J. Chem. Phys. 2016, 145, 244708.
Mn-Fe	Corona B.; Howard M.; Zhang L.; Henkelman G. Computational screening of core@shell nanoparticles for the hydrogen evolution and oxygen reduction reactions. J. Chem. Phys. 2016, 145, 244708.
Mn-Co	Corona B.; Howard M.; Zhang L.; Henkelman G. Computational screening of core@shell nanoparticles for the hydrogen evolution and oxygen reduction reactions. J. Chem. Phys. 2016, 145, 244708.
Mn-Cu	Corona B.; Howard M.; Zhang L.; Henkelman G. Computational screening of core@shell nanoparticles for the hydrogen evolution and oxygen reduction reactions. J. Chem. Phys. 2016, 145, 244708.
Mn-Ir	Corona B.; Howard M.; Zhang L.; Henkelman G. Computational screening of core@shell nanoparticles for the hydrogen evolution and oxygen reduction reactions. J. Chem. Phys. 2016, 145, 244708.
Mn-Ni	Corona B.; Howard M.; Zhang L.; Henkelman G. Computational screening of core@shell nanoparticles for the hydrogen evolution and oxygen reduction reactions. J. Chem. Phys. 2016, 145, 244708.
Mn-Ru	Corona B.; Howard M.; Zhang L.; Henkelman G. Computational screening of core@shell nanoparticles for the hydrogen evolution and oxygen reduction reactions. J. Chem. Phys. 2016, 145, 244708.

System	Reference
Mn-Tc	Corona B.; Howard M.; Zhang L.; Henkelman G. Computational screening of core@shell nanoparticles for the hydrogen evolution and oxygen reduction reactions. J. Chem. Phys. 2016, 145, 244708.
Mn-Zn	Corona B.; Howard M.; Zhang L.; Henkelman G. Computational screening of core@shell nanoparticles for the hydrogen evolution and oxygen reduction reactions. J. Chem. Phys. 2016, 145, 244708.
Mo-Os	Corona B.; Howard M.; Zhang L.; Henkelman G. Computational screening of core@shell nanoparticles for the hydrogen evolution and oxygen reduction reactions. J. Chem. Phys. 2016, 145, 244708.
Mo-Au	Corona B.; Howard M.; Zhang L.; Henkelman G. Computational screening of core@shell nanoparticles for the hydrogen evolution and oxygen reduction reactions. J. Chem. Phys. 2016, 145, 244708.
Mo-Pd	Corona B.; Howard M.; Zhang L.; Henkelman G. Computational screening of core@shell nanoparticles for the hydrogen evolution and oxygen reduction reactions. J. Chem. Phys. 2016, 145, 244708.
Mo-Hf	Corona B.; Howard M.; Zhang L.; Henkelman G. Computational screening of core@shell nanoparticles for the hydrogen evolution and oxygen reduction reactions. J. Chem. Phys. 2016, 145, 244708.
Mo-Ir	Corona B.; Howard M.; Zhang L.; Henkelman G. Computational screening of core@shell nanoparticles for the hydrogen evolution and oxygen reduction reactions. J. Chem. Phys. 2016, 145, 244708.
Nb-Au	Corona B.; Howard M.; Zhang L.; Henkelman G. Computational screening of core@shell nanoparticles for the hydrogen evolution and oxygen reduction reactions. J. Chem. Phys. 2016, 145, 244708.

System	Reference
Nb-Hf	Corona B.; Howard M.; Zhang L.; Henkelman G. Computational screening of core@shell nanoparticles for the hydrogen evolution and oxygen reduction reactions. J. Chem. Phys. 2016, 145, 244708.
Nb-Ru	Corona B.; Howard M.; Zhang L.; Henkelman G. Computational screening of core@shell nanoparticles for the hydrogen evolution and oxygen reduction reactions. J. Chem. Phys. 2016, 145, 244708.
Ni-Re	Corona B.; Howard M.; Zhang L.; Henkelman G. Computational screening of core@shell nanoparticles for the hydrogen evolution and oxygen reduction reactions. J. Chem. Phys. 2016, 145, 244708.
Pd-Ta	Corona B.; Howard M.; Zhang L.; Henkelman G. Computational screening of core@shell nanoparticles for the hydrogen evolution and oxygen reduction reactions. J. Chem. Phys. 2016, 145, 244708.
Pd-W	Corona B.; Howard M.; Zhang L.; Henkelman G. Computational screening of core@shell nanoparticles for the hydrogen evolution and oxygen reduction reactions. J. Chem. Phys. 2016, 145, 244708.
Pd-Re	Corona B.; Howard M.; Zhang L.; Henkelman G. Computational screening of core@shell nanoparticles for the hydrogen evolution and oxygen reduction reactions. J. Chem. Phys. 2016, 145, 244708.
Re-Os	Corona B.; Howard M.; Zhang L.; Henkelman G. Computational screening of core@shell nanoparticles for the hydrogen evolution and oxygen reduction reactions. J. Chem. Phys. 2016, 145, 244708.
Re-Pt	Corona B.; Howard M.; Zhang L.; Henkelman G. Computational screening of core@shell nanoparticles for the hydrogen evolution and oxygen reduction reactions. J. Chem. Phys. 2016, 145, 244708.

System	Reference
Rh-W	Corona B.; Howard M.; Zhang L.; Henkelman G. Computational screening of core@shell nanoparticles for the hydrogen evolution and oxygen reduction reactions. J. Chem. Phys. 2016, 145, 244708.
Rh-Ta	Corona B.; Howard M.; Zhang L.; Henkelman G. Computational screening of core@shell nanoparticles for the hydrogen evolution and oxygen reduction reactions. J. Chem. Phys. 2016, 145, 244708.
Rh-Re	Corona B.; Howard M.; Zhang L.; Henkelman G. Computational screening of core@shell nanoparticles for the hydrogen evolution and oxygen reduction reactions. J. Chem. Phys. 2016, 145, 244708.
Ru-Ta	Corona B.; Howard M.; Zhang L.; Henkelman G. Computational screening of core@shell nanoparticles for the hydrogen evolution and oxygen reduction reactions. J. Chem. Phys. 2016, 145, 244708.
Ru-Re	Corona B.; Howard M.; Zhang L.; Henkelman G. Computational screening of core@shell nanoparticles for the hydrogen evolution and oxygen reduction reactions. J. Chem. Phys. 2016, 145, 244708.
Ru-W	Corona B.; Howard M.; Zhang L.; Henkelman G. Computational screening of core@shell nanoparticles for the hydrogen evolution and oxygen reduction reactions. J. Chem. Phys. 2016, 145, 244708.
Sc-Ag	Corona B.; Howard M.; Zhang L.; Henkelman G. Computational screening of core@shell nanoparticles for the hydrogen evolution and oxygen reduction reactions. J. Chem. Phys. 2016, 145, 244708.
Sc-Nb	Corona B.; Howard M.; Zhang L.; Henkelman G. Computational screening of core@shell nanoparticles for the hydrogen evolution and oxygen reduction reactions. J. Chem. Phys. 2016, 145, 244708.

System	Reference
Sc-Ta	Corona B.; Howard M.; Zhang L.; Henkelman G. Computational screening of core@shell nanoparticles for the hydrogen evolution and oxygen reduction reactions. J. Chem. Phys. 2016, 145, 244708.
Sc-Hf	Corona B.; Howard M.; Zhang L.; Henkelman G. Computational screening of core@shell nanoparticles for the hydrogen evolution and oxygen reduction reactions. J. Chem. Phys. 2016, 145, 244708.
Sc-Ti	Corona B.; Howard M.; Zhang L.; Henkelman G. Computational screening of core@shell nanoparticles for the hydrogen evolution and oxygen reduction reactions. J. Chem. Phys. 2016, 145, 244708.
Sc-Zr	Corona B.; Howard M.; Zhang L.; Henkelman G. Computational screening of core@shell nanoparticles for the hydrogen evolution and oxygen reduction reactions. J. Chem. Phys. 2016, 145, 244708.
Ta-W	Corona B.; Howard M.; Zhang L.; Henkelman G. Computational screening of core@shell nanoparticles for the hydrogen evolution and oxygen reduction reactions. J. Chem. Phys. 2016, 145, 244708.
Tc-Os	Corona B.; Howard M.; Zhang L.; Henkelman G. Computational screening of core@shell nanoparticles for the hydrogen evolution and oxygen reduction reactions. J. Chem. Phys. 2016, 145, 244708.
Tc-Re	Corona B.; Howard M.; Zhang L.; Henkelman G. Computational screening of core@shell nanoparticles for the hydrogen evolution and oxygen reduction reactions. J. Chem. Phys. 2016, 145, 244708.
Tc-Ag	Corona B.; Howard M.; Zhang L.; Henkelman G. Computational screening of core@shell nanoparticles for the hydrogen evolution and oxygen reduction reactions. J. Chem. Phys. 2016, 145, 244708.

System	Reference
Tc-Au	Corona B.; Howard M.; Zhang L.; Henkelman G. Computational screening of core@shell nanoparticles for the hydrogen evolution and oxygen reduction reactions. J. Chem. Phys. 2016, 145, 244708.
Tc-Pd	Corona B.; Howard M.; Zhang L.; Henkelman G. Computational screening of core@shell nanoparticles for the hydrogen evolution and oxygen reduction reactions. J. Chem. Phys. 2016, 145, 244708.
Tc-Ru	Corona B.; Howard M.; Zhang L.; Henkelman G. Computational screening of core@shell nanoparticles for the hydrogen evolution and oxygen reduction reactions. J. Chem. Phys. 2016, 145, 244708.
Ti-Ag	Corona B.; Howard M.; Zhang L.; Henkelman G. Computational screening of core@shell nanoparticles for the hydrogen evolution and oxygen reduction reactions. J. Chem. Phys. 2016, 145, 244708.
Ti-Zr	Corona B.; Howard M.; Zhang L.; Henkelman G. Computational screening of core@shell nanoparticles for the hydrogen evolution and oxygen reduction reactions. J. Chem. Phys. 2016, 145, 244708.
Ti-Zn	Corona B.; Howard M.; Zhang L.; Henkelman G. Computational screening of core@shell nanoparticles for the hydrogen evolution and oxygen reduction reactions. J. Chem. Phys. 2016, 145, 244708.
V-Fe	Corona B.; Howard M.; Zhang L.; Henkelman G. Computational screening of core@shell nanoparticles for the hydrogen evolution and oxygen reduction reactions. J. Chem. Phys. 2016, 145, 244708.
V-Mo	Corona B.; Howard M.; Zhang L.; Henkelman G. Computational screening of core@shell nanoparticles for the hydrogen evolution and oxygen reduction reactions. J. Chem. Phys. 2016, 145, 244708.

System	Reference
V-Ta	Corona B.; Howard M.; Zhang L.; Henkelman G. Computational screening of core@shell nanoparticles for the hydrogen evolution and oxygen reduction reactions. J. Chem. Phys. 2016, 145, 244708.
V-Co	Corona B.; Howard M.; Zhang L.; Henkelman G. Computational screening of core@shell nanoparticles for the hydrogen evolution and oxygen reduction reactions. J. Chem. Phys. 2016, 145, 244708.
V-Mn	Corona B.; Howard M.; Zhang L.; Henkelman G. Computational screening of core@shell nanoparticles for the hydrogen evolution and oxygen reduction reactions. J. Chem. Phys. 2016, 145, 244708.
V-Ru	Corona B.; Howard M.; Zhang L.; Henkelman G. Computational screening of core@shell nanoparticles for the hydrogen evolution and oxygen reduction reactions. J. Chem. Phys. 2016, 145, 244708.
W-Os	Corona B.; Howard M.; Zhang L.; Henkelman G. Computational screening of core@shell nanoparticles for the hydrogen evolution and oxygen reduction reactions. J. Chem. Phys. 2016, 145, 244708.
W-Ir	Corona B.; Howard M.; Zhang L.; Henkelman G. Computational screening of core@shell nanoparticles for the hydrogen evolution and oxygen reduction reactions. J. Chem. Phys. 2016, 145, 244708.
Y-Hf	Corona B.; Howard M.; Zhang L.; Henkelman G. Computational screening of core@shell nanoparticles for the hydrogen evolution and oxygen reduction reactions. J. Chem. Phys. 2016, 145, 244708.
Y-Zr	Corona B.; Howard M.; Zhang L.; Henkelman G. Computational screening of core@shell nanoparticles for the hydrogen evolution and oxygen reduction reactions. J. Chem. Phys. 2016, 145, 244708.

System	Reference
Zn-Ru	Corona B.; Howard M.; Zhang L.; Henkelman G. Computational screening of core@shell nanoparticles for the hydrogen evolution and oxygen reduction reactions. J. Chem. Phys. 2016, 145, 244708.
Zn-Tc	Corona B.; Howard M.; Zhang L.; Henkelman G. Computational screening of core@shell nanoparticles for the hydrogen evolution and oxygen reduction reactions. J. Chem. Phys. 2016, 145, 244708.
Zn-Ir	Corona B.; Howard M.; Zhang L.; Henkelman G. Computational screening of core@shell nanoparticles for the hydrogen evolution and oxygen reduction reactions. J. Chem. Phys. 2016, 145, 244708.
Zn-Rh	Corona B.; Howard M.; Zhang L.; Henkelman G. Computational screening of core@shell nanoparticles for the hydrogen evolution and oxygen reduction reactions. J. Chem. Phys. 2016, 145, 244708.
Zn-Ag	Corona B.; Howard M.; Zhang L.; Henkelman G. Computational screening of core@shell nanoparticles for the hydrogen evolution and oxygen reduction reactions. J. Chem. Phys. 2016, 145, 244708.
Zn-Zr	Corona B.; Howard M.; Zhang L.; Henkelman G. Computational screening of core@shell nanoparticles for the hydrogen evolution and oxygen reduction reactions. J. Chem. Phys. 2016, 145, 244708.
Zr-Hf	Corona B.; Howard M.; Zhang L.; Henkelman G. Computational screening of core@shell nanoparticles for the hydrogen evolution and oxygen reduction reactions. J. Chem. Phys. 2016, 145, 244708.
Zr-Mo	Corona B.; Howard M.; Zhang L.; Henkelman G. Computational screening of core@shell nanoparticles for the hydrogen evolution and oxygen reduction reactions. J. Chem. Phys. 2016, 145, 244708.

System	Reference
Pd-Ir	Demiroglu et.al. Modelling Free and Oxide-supported Nanoalloy Catalysts: Comparison of Bulk-immiscible Pd-Ir and Au-Rh Systems and Influence of a TiO2 Support. Faraday Discussions 2018, 208, 53–66.
Ti-Ni	Hanuš J. et.al. Fabrication of Ni@Ti core–shell nanoparticles by modified gas Aggregation source. J. Phys. D: Appl. Phys. 2017, 50, 475307.
Ag-Ir	Wang L.-L.; Johnson D.D. Predicted Trends of Core–Shell Preferences for 132 Late Transition-Metal Binary-Alloy Nanoparticles. J. Am. Chem. Soc. 2009, 131(39), 14023–14029.
Ag-Os	Wang L.-L.; Johnson D.D. Predicted Trends of Core–Shell Preferences for 132 Late Transition-Metal Binary-Alloy Nanoparticles. J. Am. Chem. Soc. 2009, 131(39), 14023–14029.
Co-Ir	Wang L.-L.; Johnson D.D. Predicted Trends of Core–Shell Preferences for 132 Late Transition-Metal Binary-Alloy Nanoparticles. J. Am. Chem. Soc. 2009, 131(39), 14023–14029.
Co-Os	Wang L.-L.; Johnson D.D. Predicted Trends of Core–Shell Preferences for 132 Late Transition-Metal Binary-Alloy Nanoparticles. J. Am. Chem. Soc. 2009, 131(39), 14023–14029.
Co-Ru	Wang L.-L.; Johnson D.D. Predicted Trends of Core–Shell Preferences for 132 Late Transition-Metal Binary-Alloy Nanoparticles. J. Am. Chem. Soc. 2009, 131(39), 14023–14029.
Cu-Ru	Wang L.-L.; Johnson D.D. Predicted Trends of Core–Shell Preferences for 132 Late Transition-Metal Binary-Alloy Nanoparticles. J. Am. Chem. Soc. 2009, 131(39), 14023–14029.
Fe-Cu	Wang L.-L.; Johnson D.D. Predicted Trends of Core–Shell Preferences for 132 Late Transition-Metal Binary-Alloy Nanoparticles. J. Am. Chem. Soc. 2009, 131(39), 14023–14029.
Fe-Ir	Wang L-L; Johnson Duane D. Predicted Trends of Core–Shell Preferences for 132 Late Transition-Metal Binary-Alloy Nanoparticles. Journal of the American Chemical Society 2009, 131 (39), 14023–14029.

System	Reference
Fe-Os	Wang L-L; Johnson Duane D. Predicted Trends of Core–Shell Preferences for 132 Late Transition-Metal Binary-Alloy Nanoparticles. Journal of the American Chemical Society 2009, 131 (39), 14023–14029.
Fe-Pd	Wang L-L; Johnson Duane D. Predicted Trends of Core–Shell Preferences for 132 Late Transition-Metal Binary-Alloy Nanoparticles. Journal of the American Chemical Society 2009, 131 (39), 14023–14029.
Fe-Ru	Wang L-L; Johnson Duane D. Predicted Trends of Core–Shell Preferences for 132 Late Transition-Metal Binary-Alloy Nanoparticles. Journal of the American Chemical Society 2009, 131 (39), 14023–14029.
Ni-Os	Wang L-L; Johnson Duane D. Predicted Trends of Core–Shell Preferences for 132 Late Transition-Metal Binary-Alloy Nanoparticles. Journal of the American Chemical Society 2009, 131 (39), 14023–14029.
Ni-Ru	Wang L-L; Johnson Duane D. Predicted Trends of Core–Shell Preferences for 132 Late Transition-Metal Binary-Alloy Nanoparticles. Journal of the American Chemical Society 2009, 131 (39), 14023–14029.
Ni-Ir	Wang L-L; Johnson Duane D. Predicted Trends of Core–Shell Preferences for 132 Late Transition-Metal Binary-Alloy Nanoparticles. Journal of the American Chemical Society 2009, 131 (39), 14023–14029.
Os-Au	Wang L-L; Johnson Duane D. Predicted Trends of Core–Shell Preferences for 132 Late Transition-Metal Binary-Alloy Nanoparticles. Journal of the American Chemical Society 2009, 131 (39), 14023–14029.
Os-Ir	Wang L-L; Johnson Duane D. Predicted Trends of Core–Shell Preferences for 132 Late Transition-Metal Binary-Alloy Nanoparticles. Journal of the American Chemical Society 2009, 131 (39), 14023–14029.

System	Reference
Os-Pt	Wang L-L; Johnson Duane D. Predicted Trends of Core–Shell Preferences for 132 Late Transition-Metal Binary-Alloy Nanoparticles. Journal of the American Chemical Society 2009, 131 (39), 14023–14029.
Pd-Os	Wang L-L; Johnson Duane D. Predicted Trends of Core–Shell Preferences for 132 Late Transition-Metal Binary-Alloy Nanoparticles. Journal of the American Chemical Society 2009, 131 (39), 14023–14029.
Rh-Os	Wang L-L; Johnson Duane D. Predicted Trends of Core–Shell Preferences for 132 Late Transition-Metal Binary-Alloy Nanoparticles. Journal of the American Chemical Society 2009, 131 (39), 14023–14029.
Rh-Ag	Wang L-L; Johnson Duane D. Predicted Trends of Core–Shell Preferences for 132 Late Transition-Metal Binary-Alloy Nanoparticles. Journal of the American Chemical Society 2009, 131 (39), 14023–14029.
Rh-Ir	Wang L-L; Johnson Duane D. Predicted Trends of Core–Shell Preferences for 132 Late Transition-Metal Binary-Alloy Nanoparticles. Journal of the American Chemical Society 2009, 131 (39), 14023–14029.
Ru-Os	Wang L-L; Johnson Duane D. Predicted Trends of Core–Shell Preferences for 132 Late Transition-Metal Binary-Alloy Nanoparticles. Journal of the American Chemical Society 2009, 131 (39), 14023–14029.
Ru-Ag	Wang L-L; Johnson Duane D. Predicted Trends of Core–Shell Preferences for 132 Late Transition-Metal Binary-Alloy Nanoparticles. Journal of the American Chemical Society 2009, 131 (39), 14023–14029.
Ru-Au	Wang L-L; Johnson Duane D. Predicted Trends of Core–Shell Preferences for 132 Late Transition-Metal Binary-Alloy Nanoparticles. Journal of the American Chemical Society 2009, 131 (39), 14023–14029.

System	Reference
Ru-Ir	Wang L-L; Johnson Duane D. Predicted Trends of Core–Shell Preferences for 132 Late Transition-Metal Binary-Alloy Nanoparticles. Journal of the American Chemical Society 2009, 131 (39), 14023–14029.
Ru-Rh	Wang L-L; Johnson Duane D. Predicted Trends of Core–Shell Preferences for 132 Late Transition-Metal Binary-Alloy Nanoparticles. J. Am. Chem. Soc. 2009, 131 (39), 14023–14029.
Li-Na	Aguado A.; López J-M. Structure determination in 55-atom Li–Na and Na–K nanoalloys. J. Chem. Phys. 2010, 133, 094302.
Na-K	Aguado A.; López J-M. Structure determination in 55-atom Li–Na and Na–K nanoalloys. J. Chem. Phys. 2010, 133, 094302.
Na-Si	Sai L.; Tang L.; Zhao J.; Wang J.; Kumar V. Lowest-energy structures and electronic properties of Na–Si binary clusters from ab initio global search. J. Chem. Phys. 2011, 135, 184305.
Zn-Pt	Diego G-S. et.al. Structure, Electronic, and Magnetic Properties of Binary Pt$_n$TM$_{55-n}$ (TM = Fe, Co, Ni, Cu, Zn) Nanoclusters: A Density Functional Theory Investigation. J. Phys. Chem. C 2015, 119 (27), 15669–15679.
Al-Fe	Yang J.; Zhang Y.; Liu Y. et al. A comparative atomic simulation study of the configurations in M–Al (M = Mg, Ni, and Fe) nanoalloys: influence of alloying ability, surface energy, atomic radius, and atomic arrangement. J. Nanopart. Res. 2020, 22, 61.
Al-Ni	Yang J.; Zhang Y.; Liu Y. et al. A comparative atomic simulation study of the configurations in M–Al (M = Mg, Ni, and Fe) nanoalloys: influence of alloying ability, surface energy, atomic radius, and atomic arrangement. J. Nanopart. Res. 2020, 22, 61.
Mg-Al	Yang J.; Zhang Y.; Liu Y. et al. A comparative atomic simulation study of the configurations in M–Al (M = Mg, Ni, and Fe) nanoalloys: influence of alloying ability, surface energy, atomic radius, and atomic arrangement. J. Nanopart. Res. 2020, 22, 61.
Fe-Rh	Mokkath J-H.; Pastor G.M. Interplay between Chemical and Magnetic Order in FeRh Clusters. J. Phys. Chem. C 2012, 116 (32), 17228–17238.

System	Reference
Cu-Os	Takagi N. et.al. Core–Shell versus Other Structures in Binary $Cu_{38-n}M_n$ Nanoclusters (M = Ru, Rh, Pd, Ag, Os, Ir, Pt, and Au; n = 1, 2, and 6): Theoretical Insight into Determining Factors. J. Phys. Chem. C 2017, 121 (19), 10514–10528.
Cu-Rh	Takagi N. et.al. Core–Shell versus Other Structures in Binary $Cu_{38-n}M_n$ Nanoclusters (M = Ru, Rh, Pd, Ag, Os, Ir, Pt, and Au; n = 1, 2, and 6): Theoretical Insight into Determining Factors. J. Phys. Chem. C 2017, 121 (19), 10514–10528.
Mo-Pt	Batista K.E.A. et.al. Ab Initio Investigation of the Role of Atomic Radius in the Structural Formation of Pt_nTM_{55-n} (TM = Y, Zr, Nb, Mo, and Tc) Nanoclusters. J. Phys. Chem. C 2018, 122 (13), 7444–7454.
Nb-Pt	Batista K.E.A. et.al. Ab Initio Investigation of the Role of Atomic Radius in the Structural Formation of Pt_nTM_{55-n} (TM = Y, Zr, Nb, Mo, and Tc) Nanoclusters. J. Phys. Chem. C 2018, 122 (13), 7444–7454.
Tc-Pt	Batista K.E.A. et.al. Ab Initio Investigation of the Role of Atomic Radius in the Structural Formation of Pt_nTM_{55-n} (TM = Y, Zr, Nb, Mo, and Tc) Nanoclusters. J. Phys. Chem. C 2018, 122 (13), 7444–7454.
Y-Pt	Batista K.E.A. et.al. Ab Initio Investigation of the Role of Atomic Radius in the Structural Formation of Pt_nTM_{55-n} (TM = Y, Zr, Nb, Mo, and Tc) Nanoclusters. J. Phys. Chem. C 2018, 122 (13), 7444–7454.
Zr-Pt	Batista K.E.A. et.al. Ab Initio Investigation of the Role of Atomic Radius in the Structural Formation of Pt_nTM_{55-n} (TM = Y, Zr, Nb, Mo, and Tc) Nanoclusters. J. Phys. Chem. C 2018, 122 (13), 7444–7454.
Ti-V	Corona B.; Howard M.; Zhang L.; Henkelman G. Computational screening of core@shell nanoparticles for the hydrogen evolution and oxygen reduction reactions. J. Chem. Phys. 2016, 145, 244708.

System	Reference
Ir-Au	Akbarzadeh H.; Abbaspoura M.; Mehrjouei E. Phase transition in crown-jewel structured Au–Ir nanoalloys with different shapes: a molecular dynamics study. *Phys. Chem. Chem. Phys.* 2016, **18**, 25676–25686.
Ir-Pt	Akbarzadeh H.; Abbaspoura M.; Mehrjouei E. Phase transition in crown-jewel structured Au–Ir nanoalloys with different shapes: a molecular dynamics study. *Phys. Chem. Chem. Phys.* 2016, **18**, 25676–25686.
Ti-Au	Lia H.-F.; Wang H.-Q.; Probing the stability of neutral and anionic transition-metal-doped golden cage nanoclusters: $M@Au_{16}$ (M = Sc; Ti; V). *Phys. Chem. Chem. Phys.* 2014, **16**, 244–254.
Rh-Pd	Hung S.-H. et al. Structural investigation of ternary PdRuM (M = Pt; Rh; or Ir) nanoparticles using first-principles calculations. *RSC Adv.* 2020, **10**, 16527–16536.
Rh-Au	Piccolo L.; Li Z.; Demiroglu I. et al. Understanding and controlling the structure and segregation behaviour of AuRh nanocatalysts. *Sci Rep* 2016, **6**, 35226.
Pd-Cd	Konda S.-K. Synthesis and electrochemical study of Cd@Pd core/shell nanomaterials for hydrogen sorption and storage. *International Journal of Hydrogen Energy* 2015, **40**, 16365–16374.
Cu-Ag	Rossi G.; Rapallo A.; Mottet C.; Fortunelli A.; F. Baletto; Ferrando R. MA**g**ic Polyicosahedral Core-Shell Clusters. *Phys. Rev. Lett.* 2004, **93**, 105503.
Ni-Pd	ManAgo T.; Otani Y.; Miyajima H.; Akiba E. MA**g**netic properties and Pd–H miscibility gap in Ni/Pd composite fine particles. *J. Appl. Phys.* 1996, **79**, 5126.
Ni-Pt	ManAgo T.; Otani Y.; Miyajima H.; Akiba E. MA**g**netic properties and Pd–H miscibility gap in Ni/Pd composite fine particles. *J. Appl. Phys.* 1996, **79**, 5126.
Pd-Pt	Toshima N.; Harada A.; Yonezawa E.; Kushibashi K.; Asakurat K. Structural Analysis of Polymer-Protected Pd/Pt Bimetallic Clusters as Dispersed Catalysts by Using Extended X-ray Absorption Fine Structure Spectroscopy. *J. Phys. Chem.* 1991, **95**, 7448–7453.

System	Reference
Ni-Cu	Yang L.Q.; Depristo A.E. Surface Segregation in Bimetallic Clusters: Statistical-Mechanical Modeling Using Cluster Site Energies. *J. Catal.* 1994, **148**(2), 575–586.

Appendix B

List of calculated segregation energies.

Pair name	System of calculation	Segregation energy (eV)
Li-Be	Be54Li/Li54Be	-3.39 / 0.33
Li-Mg	Li54Mg/LiMg54	0.14 / -0.34
Li-Al	Li54Al/LiAl54	0.64 / 0.99
Li-Si	Li54Si/LiSi54	0.26 / -1.41
Li-K	Li54K/LiK54	-1.67 / 0.22
Li-Ca	Ca54Li/Li54Ca	-0.01 / 0.003
Li-Sc	Li54Sc/LiSc54	0.3 / -0.19
Li-Ti	Li54Ti/LiTi54	0.49 / 0.11
Li-V	Li54V/LiV54	-0.81 / -2.12
Li-Cr	Li54Cr/LiCr54	0.35 / -2.84
Li-Mn	Li54Mn/LiMn54	2.09 / -2.88
Li-Fe	Li54Fe/LiFe54	0.19 / -1.79
Li-Co	Li54Co/LiCo54	0.42 / -1.1
Li-Ni	Li54Ni/LiNi54	0.1 / -1.67
Li-Cu	Li54Cu/LiCu54	-0.05 / -0.59
Li-Zn	Li54Zn/LiZn54	0.22 / 0.32
Li-Ge	Ge54Li/Li54Ge	-0.95 / 0.28
Li-Rb	Rb54Li/Li54Rb	0.26 / -2.25
Li-Sr	Sr54Li/Li54Sr	-0.04 / -0.94
Li-Y	Y54Li/YLi54	-0.04 / 0.02
Li-Zr	Zr54Li/ZrLi54	0.91 / 0.62
Li-Nb	Nb54Li/NbLi54	-0.6 / 1.59
Li-Mo	Mo54Li/MoLi54	-0.37 / 1.6
Li-Tc	Tc54Li/TcLi54	-1.36 / 0.75
Li-Ru	Ru54Li/RuLi54	0.11 / 0.87
Li-Rh	Rh54Li/Li54Rh	-0.97 / 0.55
Li-Pd	Pd54Li/Li54Pd	0.22 / 0.16
Li-Ag	Ag54Li/Li54Ag	0.31 / 0.07
Li-Cd	Cd54Li/Li54Cd	0.55 / 0.24
Li-In	In54Li/Li54In	1.07 / 0.21
Li-Sn	Sn54Li/Li54Sn	-0.13 / 0.42

Pair name	System of calculation	Segregation energy (eV)
Li-Sb	Sb54Li/Li54Sb	-0.20 / 0.04
Li-Hf	Hf54Li/Li54Hf	-1.80 / 0.93
Li-Ta	Ta54Li/Li54Ta	-1.82 / 0.89
Li-W	W54Li/Li54W	-1.59 / 0.78
Li-Re	Re54Li/Li54Re	-2.05 / 1.26
Li-Os	Os54Li/Li54Os	0.55 / 0.64
Li-Ir	Ir54Li/Li54Ir	0.29 / 0.61
Li-Pt	Pt54Li/Li54Pt	0.54 / 0.67
Li-Au	Au54Li/Li54Au	0.59 / 0.24
Li-Pb	Pb54Li/Li54Pb	0.82 / 0.37
Be-Na	Na54Be/Be54Na	9.20 / 0.2
Be-Mg	Mg54Be/Be54Mg	-1.31 / 0.36
Be-Al	Al54Be/Be54Al	-2.41 / 0.04
Be-Si	Si54Be/Be54Si	-1.58 / 0.33
Be-Ca	Ca54Be/Be54Ca	-1.27 / 0.06
Be-Sc	Sc54Be/Be54Sc	-3.87 / 0.71
Be-Ti	Ti54Be/Be54Ti	-1.40 / 0.09
Be-V	V54Be/Be54V	1.74 / 0.29
Be-Cr	Cr54Be/Be54Cr	2.13 / -0.06
Be-Mn	Mn54Be/Be54Mn	2.24 / -0.24
Be-Fe	Fe54Be/Be54Fe	2.07 / -0.94
Be-Co	Co54Be/Be54Co	2.40 / -1.58
Be-Ni	Ni54Be/Be54Ni	-2.89 / 0.38
Be-Cu	Cu54Be/Be54Cu	-0.18 / 0.85
Be-Zn	Zn54Be/Be54Zn	-0.97 / 0.55
Be-Ge	Ge54Be/Be54Ge	0.22 / -0.03
Be-Ga	Ga54Be/Be54Ga	-1.52 / 0.74
Be-As	As54Be/Be54As	-0.18 / 0.34
Be-Zr	Zr54Be/Be54Zr	-0.91 / 0.62
Be-Nb	Nb54Be/Be54Nb	-0.43 / 1.32
Be-Mo	Mo54Be/Be54Mo	1.68 / -1.39
Be-Tc	Tc54Be/Be54Tc	2.09 / -1.19
Be-Ru	Ru54Be/Be54Ru	2.04 / -1.16
Be-Rh	Rh54Be/Be54Rh	0.52 / -0.17
Be-Pd	Pd54Be/Be54Pd	0.25 / -0.13
Be-Ag	Ag54Be/Be54Ag	-0.89 / 0.74

Pair name	System of calculation	Segregation energy (eV)
Be-Cd	Cd54Be/Be54Cd	1.35 / -0.46
Be-In	In54Be/Be54In	0.94 / -0.14
Be-Sb	Sb54Be/Be54Sb	-1.91 / 1.12
Be-Hf	Hf54Be/Be54Hf	2.36 / -0.33
Be-Ta	Ta54Be/Be54Ta	1.60 / -1.28
Be-W	W54Be/Be54W	-0.27 / -0.22
Be-Re	Re54Be/Be54Re	-0.29 / 0.77
Be-Os	Os54Be/Be54Os	-5.46 / 0.22
Be-Ir	Ir54Be/Be54Ir	-4.61 / 1.55
Be-Pt	Pt54Be/Be54Pt	-5.4 / 1.33
Be-Au	Be54Au/Au54Be	-5.73 / 1.3
Be-Pb	Be54Pb/Pb54Be	-0.99 / 1.27
Na-Mg	Na54Mg/Mg54Na	0.23 / -1.27
Na-Al	Na54Al/Al54Na	0.74 / -1.82
Na-Ca	Ca54Na/Na54Ca	-0.97 / -0.8
Na-Sc	Na54Sc/Sc54Na	0.5 / -2.06
Na-Ti	Na54Ti/Ti54Na	1.21 / -4.4
Na-V	Na54V/V54Na	0.77 / -4.64
Na-Cr	Na54Cr/Cr54Na	2.57 / -6.16
Na-Mn	Na54Mn/Mn54Na	0.04 / -4.61
Na-Fe	Na54Fe/Fe54Na	-0.27 / -4.96
Na-Co	Na54Co/Co54Na	-0.27 / -4.76
Na-Ni	Na54Ni/Ni54Na	0.56 / -5.39
Na-Cu	Na54Cu/Cu54Na	0.08 / -1.58
Na-Zn	Na54Zn/Zn54Na	0.82 / -1.83
Na-Ge	Ge54Na/Na54Ge	1.40 / -1.43
Na-Rb	Rb54Na/Na54Rb	-0.99 / 0.03
Na-Nb	Nb54Na/Na54Nb	-1.88 / -0.87
Na-Sr	Sr54Na/Na54Sr	0.10 / -0.43
Na-Y	Y54Na/Na54Y	-0.29 / -0.37
Na-Zr	Zr54Na/Na54Zr	-0.72 / -0.93
Na-Mo	Mo54Na/Na54Mo	-0.46 / 0.55
Na-Tc	Tc54Na/Na54Tc	-2.09 / 1.05
Na-Ru	Ru54Na/Na54Ru	-1.91 / 1.11
Na-Rh	Rh54Na/Na54Rh	-3.21 / 1.14
Na-Pd	Pd54Na/Na54Pd	-1.20 / 0.67

Pair name	System of calculation	Segregation energy (eV)
Na-Ag	Ag54Na/Na54Ag	0.42 / 0.16
Na-Cd	Cd54Na/Na54Cd	0.53 / 0.32
Na-In	In54Na/Na54In	0.14 / 0.7
Na-Sn	Sn54Na/Na54Sn	0.85 / 0.64
Na-Sb	Sb54Na/Na54Sb	-1.07 / -0.44
Na-Hf	Hf54Na/Na54Hf	-1.83 / 0.71
Na-Ta	Ta54Na/Na54Ta	-0.97 / -0.17
Na-W	W54Na/Na54W	-1.63 / -1.38
Na-Re	Re54Na/Na54Re	-6.13 / 0.92
Na-Os	Os54Na/Na54Os	-3.77 / 0.44
Na-Ir	Ir54Na/Na54Ir	-1.59 / 0.72
Na-Pt	Pt54Na/Na54Pt	-1.13 / 0.86
Na-Au	Au54Na/Na54Au	-1.10 / 0.8
Na-Pb	Pb54Na/Na54Pb	-0.78 / 0.1
Mg-Si	Mg54Si/Si54Mg	1.08 / -0.49
Mg-Mg	Mg54Mg/Mg54Mg	-1.37 / -0.14
Mg-Ca	Ca54Mg/Mg54Ca	-0.71 / 0.12
Mg-Sc	Mg54Sc/Sc54Mg	-1.39 / -0.1
Mg-Ti	Ti54Mg/Mg54Ti	0.74 / -0.21
Mg-V	V54Mg/Mg54V	1.09 / -0.64
Mg-Cr	Mg54Cr/Cr54Mg	2.24 / -1.12
Mg-Mn	Mg54Mn/Mn54Mg	0.66 / -1.78
Mg-Fe	Mg54Fe/Fe54Mg	-0.06 / -2.14
Mg-Co	Mg54Co/Co54Mg	0.96 / -2.74
Mg-Ni	Mg54Ni/Ni54Mg	1.08 / -3.03
Mg-Cu	Mg54Cu/Cu54Mg	0.77 / -1.54
Mg-Zn	Mg54Zn/Zn54Mg	0.94 / 0.31
Mg-Ge	Ge54Mg/Mg54Ge	0.87 / 0.86
Mg-Rb	Rb54Mg/Mg54Rb	0.4 / -4.36
Mg-Sr	Sr54Mg/Mg54Sr	0.01 / -2.92
Mg-Y	Y54Mg/Mg54Y	0.12 / -1.34
Mg-Zr	Zr54Mg/ZrMg54	-0.71 / -0.44
Mg-Nb	Nb54Mg/NbMg54	-0.32 / 0.24
Mg-Mo	Mo54Mg/Mg54Mo	-1.30 / 0.86
Mg-Tc	Tc54Mg/Mg54Tc	-1.64 / 1.03
Mg-Ru	Ru54Mg/Mg54Ru	-1.41 / 1.13

Pair name	System of calculation	Segregation energy (eV)
Mg-Rh	Rh54Mg/Mg54Rh	-1.81 / 1.24
Mg-Pd	Pd54Mg/Mg54Pd	0.20 / 0.77
Mg-Ag	Ag54Mg/Mg54Ag	0.44 / 0.98
Mg-Cd	Cd54Mg/Mg54Cd	0.20 / 0.71
Mg-In	In54Mg/Mg54In	1.15 / 0.44
Mg-Sn	Sn54Mg/Mg54Sn	0.4 / 0.24
Mg-Sb	Sb54Mg/Mg54Sb	0.54 / 0.06
Mg-Hf	Hf54Mg/Mg54Hf	0.78 / 0.07
Mg-Ta	Ta54Mg/Mg54Ta	-0.27 / -0.08
Mg-W	W54Mg/Mg54W	-0.99 / -0.16
Mg-Re	Re54Mg/Mg54Re	-1.38 / 1.36
Mg-Os	Os54Mg/Mg54Os	-3.17 / 0.42
Mg-Ir	Ir54Mg/Mg54Ir	-1.81 / 1.26
Mg-Pt	Pt54Mg/Mg54Pt	-0.13 / 1.16
Mg-Au	Au54Mg/Mg54Au	-0.91 / 1.36
Mg-Pb	Pb54Mg/Mg54Pb	-0.30 / 0.49
Al-K	Al54K/K54Al	-6.46 / -1.45
Al-Ca	Ca54Al/Al54Ca	0.26 / -2.39
Al-Sc	Al54Sc/Sc54Al	0.42 / 0.24
Al-Ti	Al54Ti/Ti54Al	0.7 / 1.39
Al-V	Al54V/V54Al	3.17 / -0.91
Al-Cr	Al54Cr/Cr54Al	-3.77 / 0.93
Al-Mn	Al54Mn/Mn54Al	-1.07 / -0.91
Al-Co	Al54Co/Co54Al	3.0 / -0.36
Al-Ni	Al54Ni/Ni54Al	-0.97 / -0.4
Al-Cu	Al54Cu/Cu54Al	0.3 / 0.55
Al-Ge	Ge54Al/Al54Ge	-0.3 / -2.19
Al-Rb	Rb54Al/Al54Rb	-1.91 / 0.8
Al-Sr	Sr54Al/Al54Sr	-0.72 / -1.33
Al-Y	Y54Al/Al54Y	0.72 / -1.33
Al-Zr	Zr54Al/Al54Zr	1.25 / 0.55
Al-Nb	Nb54Al/Al54Nb	-4.56 / 2.62
Al-Mo	Mo54Al/Al54Mo	0.64 / 1.51
Al-Tc	Tc54Al/Al54Tc	-3.87 / 0.75
Al-Ru	Ru54Al/Al54Ru	-0.94 / 2.67
Al-Rh	Rh54Al/Al54Rh	-0.09 / 2.6

Pair name	System of calculation	Segregation energy (eV)
Al-Pd	Pd54Al/Al54Pd	-0.09 / 1.72
Al-Ag	Ag54Al/Al54Ag	0.5 / 0.94
Al-Cd	Cd54Al/Al54Cd	1.37 / 1.08
Al-In	In54Al/Al54In	0.91 / 0.2
Al-Sn	Sn54Al/Al54Sn	-0.04 / 2.3
Al-Sb	Sb54Al/Al54Sb	-0.91 / -1.92
Al-Hf	Hf54Al/Al54Hf	1.91 / 0.6
Al-Ta	Ta54Al/Al54Ta	2.07 / 2.08
Al-W	W54Al/Al54W	1.49 / 1.78
Al-Re	Re54Al/Al54Re	-1.0 / 3.12
Al-Os	Os54Al/Al54Os	-1.06 / 3.86
Al-Ir	Ir54Al/Al54Ir	-0.14 / 2.91
Al-Pt	Pt54Al/Al54Pt	0.97 / 1.83
Al-Au	Au54Al/Al54Au	1.28 / 1.07
Al-Pb	Pb54Al/Al54Pb	0.45 / -4.69
Si-K	K54Si/Si54K	-0.84 / -0.16
Si-Ca	Ca54Si/Si54Ca	0.41 / 1.4
Si-Sc	Si54Sc/Sc54Si	1.02 / 1.22
Si-Ti	Si54Ti/Ti54Si	1.21 / 1.57
Si-V	Si54V/V54Si	1.23 / -0.21
Si-Cr	Si54Cr/Cr54Si	-0.79 / 0.52
Si-Mn	Si54Mn/Mn54Si	-0.17 / -0.04
Si-Fe	Si54Fe/Fe54Si	-0.82 / 0.17
Si-Co	Si54Co/Co54Si	-1.17 / 0.4
Si-Ni	Si54Ni/Ni54Si	-0.71 / -0.23
Si-Cu	Si54Cu/Cu54Si	-0.79 / -0.35
Si-Zn	Si54Zn/Zn54Si	-0.95 / 0.25
Si-Ge	Ge54Si/Si54Ge	0.3 / -1.07
Si-Rb	Rb54Si/Si54Rb	0.03 / -7.41
Si-Sr	Sr54Si/Si54Sr	-0.33 / 5.21
Si-Y	Y54Si/Si54Y	0.9 / 3.92
Si-Zr	Zr54Si/Si54Zr	1.11 / 2.77
Si-Nb	Nb54Si/Si54Nb	1.19 / 1.92
Si-Mo	Mo54Si/Si54Mo	-0.28 / 1.77
Si-Tc	Tc54Si/Si54Tc	-0.37 / -1.75
Si-Ru	Ru54Si/Si54Ru	-0.98 / 3.25

Pair name	System of calculation	Segregation energy (eV)
Si-Rh	Rh54Si/Si54Rh	-0.29 / -0.79
Si-Pd	Pd54Si/Si54Pd	-0.92 / -0.79
Si-Ag	Ag54Si/Si54Ag	-0.15 / 0.2
Si-Cd	Cd54Si/Si54Cd	-0.91 / -0.84
Si-In	In54Si/Si54In	-0.07 / -0.03
Si-Sn	Sn54Si/Si54Sn	0.1 / 0.84
Si-Sb	Sb54Si/Si54Sb	1.4 / -2.11
Si-Hf	Hf54Si/Si54Hf	-1.48 / 1.74
Si-Ta	Ta54Si/Si54Ta	-0.89 / 1.31
Si-W	W54Si/Si54W	-0.89 / 0.73
Si-Re	Re54Si/Si54Re	-3.17 / -0.94
Si-Os	Os54Si/Si54Os	-4.06 / 1.45
Si-Ir	Ir54Si/Si54Ir	-0.4 / -0.65
Si-Pt	Pt54Si/Si54Pt	-0.37 / -1.88
Si-Au	Au54Si/Si54Au	-0.07 / -1.48
Si-Pb	Pb54Si/Si54Pb	-4.23 / -4.92
K-Ca	Ca54K/K54Ca	-0.1 / 0.91
K-Sc	Sc54K/K54Sc	-0.41 / -2.96
K-Ti	K54Ti/Ti54K	0.42 / 0.66
K-V	V54K/K54V	-0.6 / 1.14
K-Cr	Cr54K/K54Cr	-1.46 / -10.53
K-Mn	K54Mn/Mn54K	-2.22 / -4.32
K-Fe	K54Fe/Fe54K	0.2 / -0.87
K-Co	K54Co/Co54K	2.62 / -10.17
K-Ni	K54Ni/Ni54K	0.0 / -1.8
K-Cu	K54Cu/Cu54K	-0.21 / -1.12
K-Zn	K54Zn/Zn54K	0.17 / -0.53
K-Ge	Ge54K/K54Ge	0.5 / -3.25
K-Rb	Rb54K/K54Rb	0.24 / 0.2
K-Sr	Sr54K/K54Sr	0.0 / 0.06
K-Y	Y54K/K54Y	-1.91 / 0.78
K-Zr	Zr54K/K54Zr	-4.73 / 0.99
K-Nb	Nb54K/K54Nb	-1.44 / 0.86
K-Mo	Mo54K/K54Mo	-3.05 / 3.33
K-Tc	Tc54K/K54Tc	-1.18 / -0.71
K-Ru	Ru54K/K54Ru	-9.98 / -0.45

Pair name	System of calculation	Segregation energy (eV)
K-Rh	Rh54K/K54Rh	-10.48 / 0.08
K-Pd	Pd54K/K54Pd	-4.59 / 1.12
K-Ag	Ag54K/K54Ag	-2.52 / 0.14
K-Cd	Cd54K/K54Cd	-4.25 / -0.04
K-In	In54K/K54In	-0.37 / -0.94
K-Sn	Sn54K/K54Sn	-0.91 / 3.04
K-Sb	Sb54K/K54Sb	-0.82 / -0.23
K-Hf	Hf54K/K54Hf	-1.3 / 0.5
K-Ta	Ta54K/K54Ta	-1.47 / 2.54
K-W	W54K/K54W	-12.72 / 5.22
K-Re	Re54K/K54Re	-1.02 / -0.33
K-Os	Os54K/K54Os	-10.56 / 2.93
K-Ir	Ir54K/K54Ir	-3.5 / 2.23
K-Pt	Pt54K/K54Pt	-6.41 / 0.44
K-Au	Au54K/K54Au	-8.37 / 3.24
Ca-Sc	Sc54Ca/Ca54Sc	0.55 / -0.65
Ca-Ti	Ti54Ca/Ca54Ti	-0.39 / 1.15
Ca-V	Ca54V/V54Ca	-1.31 / -1.57
Ca-Cr	Cr54Ca/Ca54Cr	2.15 / -4.68
Ca-Mn	Mn54Ca/Ca54Mn	-0.47 / -0.98
Ca-Fe	Fe54Ca/Ca54Fe	0.18 / 0.27
Ca-Co	Co54Ca/Ca54Co	-0.35 / -4.28
Ca-Ni	Ca54Ni/Ni54Ca	-0.47 / -6.15
Ca-Cu	Cu54Ca/Ca54Cu	0.01 / -0.51
Ca-Zn	Ca54Zn/Zn54Ca	-0.2 / -0.16
Ca-Ga	Ga54Ca/Ca54Ga	-0.02 / 0.18
Ca-Rb	Rb54Ca/Ca54Rb	-0.17 / -4.22
Ca-Sr	Ca54Sr/Sr54Ca	0.19 / -2.24
Ca-Y	Y54Ca/Ca54Y	-0.1 / 1.42
Ca-Zr	Zr54Ca/Ca54Zr	-2.2 / -0.08
Ca-Nb	Nb54Ca/Ca54Nb	-4.46 / 0.14
Ca-Mo	Mo54Ca/Ca54Mo	-1.6 / -0.81
Ca-Tc	Tc54Ca/Ca54Tc	-5.51 / 0.11
Ca-Ru	Ru54Ca/Ca54Ru	-1.88 / -0.21
Ca-Rh	Rh54Ca/Ca54Rh	-3.22 / -0.44
Ca-Pd	Pd54Ca/Ca54Pd	-2.82 / 0.06

Pair name	System of calculation	Segregation energy (eV)
Ca-Ag	Ag54Ca/Ca54Ag	1.3 / 0.44
Ca-Cd	Cd54Ca/Ca54Cd	0.45 / -1.32
Ca-In	In54Ca/Ca54In	-0.95 / 0.89
Ca-Sn	Sn54Ca/Ca54Sn	0.3 / 0.92
Ca-Sb	Sb54Ca/Ca54Sb	-0.67 / -0.66
Ca-Hf	Hf54Ca/Ca54Hf	-2.59 / 0.67
Ca-Ta	Ta54Ca/Ca54Ta	-4.10 / 0.44
Ca-W	W54Ca/Ca54W	-7.14 / -1.06
Ca-Re	Re54Ca/Ca54Re	5.87 / -8.13
Ca-Os	Os54Ca/Ca54Os	5.12 / -9.28
Ca-Ir	Ir54Ca/Ca54Ir	5.19 / -5.39
Ca-Pt	Pt54Ca/Ca54Pt	4.45 / -2.2
Ca-Au	Ca54Au/Au54Ca	0.97 / 0.08
Ca-Pd	Ca54Pd/Pd54Ca	0.69 / 1.25
Sc-V	Sc54V/V54Sc	0.87 / -1.33
Sc-Cr	Sc54Cr/Cr54Sc	0.15 / -2.56
Sc-Mn	Sc54Mn/Mn54Sc	0.58 / -4.18
Sc-Fe	Sc54Fe/Fe54Sc	0.03 / -2.26
Sc-Ni	Sc54Ni/Ni54Sc	-0.06 / -18.84
Sc-Cu	Sc54Cu/Cu54Sc	0.41 / -26.67
Sc-Zn	Sc54Zn/Zn54Sc	0.17 / -13.63
Sc-Ga	Sc54Ga/Ga54Sc	0.07 / -9.83
Sc-Rb	Rb54Sc/Sc54Rb	0.48 / -1.03
Sc-Y	Sc54Y/Y54Sc	-0.39 / -2.03
Sc-Mo	Sc54Mo/Mo54Sc	0.59 / -5.26
Sc-Tc	Sc54Tc/Tc54Sc	0.74 / -2.29
Sc-Ru	Sc54Ru/Ru54Sc	0.67 / -1.9
Sc-Rh	Sc54Rh/Rh54Sc	0.59 / -2.12
Sc-Pd	Sc54Pd/Pd54Sc	0.75 / -0.02
Sc-Ag	Sc54Ag/Ag54Sc	0.52 / 0.16
Sc-Cd	Sc54Cd/Cd54Sc	0.20 / 0.12
Sc-In	Sc54In/In54Sc	1.49 / 1.06
Sc-Sn	Sc54Sn/Sn54Sc	0.60 / 1.76
Sc-Sb	Sc54Sb/Sb54Sc	2.01 / 0.67
Sc-W	Sc54W/W54Sc	1.07 / -3.78
Sc-Os	Sc54Os/Os54Sc	3.67 / -0.36

Pair name	System of calculation	Segregation energy (eV)
Sc-Ir	Sc54Ir/Ir54Sc	2.09 / -0.47
Sc-Pt	Sc54Pt/Pt54Sc	2.40 / 0.73
Sc-Au	Sc54Au/Au54Sc	2.47 / 0.83
Sc-Pb	Pb54Sc/Sc54Pb	2.55 / -0.7
Ti-Co	Ti54Co/Co54Ti	2.01 / -0.34
Ti-Fe	Ti54Fe/Fe54Ti	1.85 / -1.83
Ti-Mn	Ti54Mn/Mn54Ti	1.57 / -0.68
Ti-Cr	Ti54Cr/Cr54Ti	2.55 / -0.97
Ti-Cu	Ti54Cu/Cu54Ti	2.01 / -0.34
Ti-Ga	Ga54Ti/Ti54Ga	1.57 / -1.82
Ti-Rb	Rb54Ti/Ti54Rb	0.51 / -4.93
Ti-Y	Y54Ti/Ti54Y	2.36 / -0.05
Ti-Zr	Zr54Ti/Ti54Zr	1.50 / -0.63
Ti-Nb	Ti54Nb/Nb54Ti	1.4 / 0.42
Ti-Mo	Mo54Ti/Ti54Mo	1.30 / 1.24
Ti-Tc	Tc54Ti/Ti54Tc	1.69 / -0.71
Ti-Ru	Ru54Ti/Ti54Ru	1.85 / -0.84
Ti-Rh	Rh54Ti/Ti54Rh	1.94 / -0.41
Ti-Pd	Pd54Ti/Ti54Pd	1.44 / -0.47
Ti-Ag	Ag54Ti/Ti54Ag	1.02 / -0.27
Ti-Hf	Hf54Ti/Ti54Hf	1.92 / 0.31
Ti-Ta	Ta54Ti/Ti54Ta	2.11 / -0.04
Ti-Sn	Sn54Ti/Ti54Sn	0.57 / -0.64
Ti-Hf	Hf54Ti/Ti54Hf	2.11 / -0.04
Ti-Hf	Hf54Ti/Ti54Hf	0.67 / -0.64
Ti-Au	Ta54Ti/Ti54Au	1.69 / -0.71
Ti-Re	Re54Ti/Ti54Re	-0.44 / 1.96
Ti-Os	Os54Ti/Ti54Os	-0.6 / 2.23
Ti-Ir	Ir54Ti/Ti54Ir	0.11 / 2.28
Ti-Pt	Pt54Ti/Ti54Pt	1.73 / -2.12
Ti-Pb	Pb54Ti/Ti54Pb	-2.9 / -3.7
V-Cr	V54Cr/Cr54V	0.7 / -0.7
V-Ni	V54Ni/Ni54V	-2.82 / -1.02
V-Cu	V54Cu/Cu54V	-2.94 / -0.22
V-Zn	V54Zn/Zn54V	2.8 / 0.002
V-Ge	Ge54V/V54Ge	1.19 / -0.54

Pair name	System of calculation	Segregation energy (eV)
V-Sr	Sr54V/V54Sr	-1.34 / -5.81
V-Y	Y54V/V54Y	0.67 / -1.25
V-Zr	Zr54V/V54Zr	0.41 / -1.06
V-Nb	V54Nb/Nb54V	-2.39 / 1.12
V-Tc	V54Tc/Tc54V	0.19 / 0.42
V-Rh	Rh54V/V54Rh	2.48 / 0.27
V-Pd	Pd54V/Pd54V	3.7 / 0.08
V-Ag	Ag54V/V54Ag	1.72 / 0.7
V-Cd	V54Cd/Cd54V	0.5 / 0.41
V-In	In54V/V54In	2.75 / -6.17
V-Sn	Sn54V/V54Sn	-5.82 / -5.47
V-Sb	Sb54V/V54Sb	-9.13 / -10.95
V-Hf	Hf54V/V54Hf	1.52 / -1.59
V-W	W54V/V54W	0.32 / -1.9
V-Re	Re54V/V54Re	0.5 / -0.13
V-Os	Os54V/V54Os	-0.19 / -0.91
V-Ir	Ir54V/V54Ir	0.63 / -0.55
V-Pt	Pt54V/V54Pt	2.67 / -0.57
V-Pb	Pb54V/V54Pb	2.55 / -1.05
Cr-Mn	Cr54Mn/Mn54Cr	0.6 / -14.36
Cr-Fe	Fe54Cr/Cr54Fe	1.15 / -1.87
Cr-Co	Cr54Co/Co54Cr	0.87 / -0.02
Cr-Ni	Cr54Ni/Ni54Cr	0.3 / -0.85
Cr-Ga	Ge54Cr/Cr54Ge	1.32 / -0.54
Cr-Rb	Rb54Cr/Cr54Rb	0.36 / -4.97
Cr-Sr	Sr54Cr/Cr54Sr	-0.41 / -13.55
Cr-Y	Cr54Y/Y54Cr	1.51 / -1.05
Cr-Zr	Cr54Zr/Zr54Cr	1.17 / -0.63
Cr-Mo	Cr54Mo/Mo54Cr	-0.49 / -1.7
Cr-Tc	Cr54Tc/Tc54Cr	0.19 / -0.97
Cr-Ru	Cr54Ru/Ru54Cr	0.9 / -1.43
Cr-Pd	Pd54Cr/Cr54Pd	2.25 / 0.0
Cr-Ag	Cr54Ag/Ag54Cr	3.06 / 2.65
Cr-Cd	Cr54Cd/Cd54Cr	0.3 / 2.45
Cr-In	In54Cr/Cr54In	1.19 / -5.94
Cr-Sn	Cr54Sn/Sn54Cr	1.0 / -7.92

Pair name	System of calculation	Segregation energy (eV)
Cr-Sb	Sb54Cr/Cr54Sb	-1.07 / -5.12
Cr-Ta	Hf54Cr/Cr54Ta	1.84 / -1.5
Cr-Hf	Ta54Cr/Cr54Hf	2.16 / -2.27
Cr-W	W54Cr/Cr54W	1.15 / -0.79
Cr-Os	Os54Cr/Cr54Os	2.64 / -1.04
Cr-Ir	Ir54Cr/Cr54Ir	2.1 / -0.38
Cr-Pt	Pt54Cr/Cr54Pt	1.71 / 0.56
Cr-Au	Au54Cr/Cr54Au	2.53 / -0.38
Cr-Pb	Pb54Cr/Cr54Pb	2.87 / -4.48
Mn-Ge	Ge54Mn/Mn54Ge	0.35 / -4.98
Mn-Rb	Rb54Mn/Mn54Rb	0.04 / -11.65
Mn-Sr	Sr54Mn/Mn54Sr	0.09 / -9.93
Mn-Y	Mn54Y/Y54Mn	-6.49 / -0.1
Mn-Zr	Zr54Mn/Mn54Zr	-2.41 / -7.79
Mn-Nb	Nb54Mn/Mn54Nb	-1.16 / -0.59
Mn-Mo	Mo54Mn/Mn54Mo	0.24 / -9.53
Mn-Rh	Mn54Rh/Rh54Mn	-1.22 / -0.27
Mn-Pd	Pd54Mn/Mn54Pd	-1.98 / 0.87
Mn-Cd	Mn54Cd/Cd54Mn	1.33 / -0.59
Mn-In	In54Mn/Mn54In	-2.03 / -4.44
Mn-Sn	Sn54Mn/Mn54Sn	2.31 / -4.23
Mn-Sb	Sb54Mn/Mn54Sb	-0.61 / -0.93
Mn-Hf	Hf54Mn/Mn54Hf	-2.19 / -2.42
Mn-Ta	Ta54Mn/Mn54Ta	-1.91 / -1.27
Mn-W	W54Mn/Mn54W	0.37 / -0.09
Mn-Re	Re54Mn/Mn54Re	0.18 / 0.13
Mn-Pt	Pt54Mn/Mn54Pt	-1.38 / -1.77
Mn-Au	Au54Mn/Mn54Au	-0.17 / -5.87
Mn-Pb	Pb54Mn/Mn54Pb	2.77 / -5.17
Fe-Ga	Ge54Fe/Fe54Ge	0.95 / -0.38
Fe-Rb	Rb54Fe/Fe54Rb	0.13 / -10.05
Fe-Sr	Sr54Fe/Fe54Sr	-4.65 / -5.33
Fe-Y	Y54Fe/Fe54Y	-1.36 / -7.83
Fe-Zr	Zr54Fe/Fe54Zr	-1.72 / 1.2
Fe-Nb	Nb54Fe/Fe54Nb	0.5 / -1.25
Fe-Mo	Mo54Fe/Fe54Mo	0.49 / -0.8

Pair name	System of calculation	Segregation energy (eV)
Fe-Tc	Fe54Tc/Tc54Fe	0.83 / 0.38
Fe-Cd	Cd54Fe/Fe54Cd	-3.3 / -0.91
Fe-In	In54Fe/Fe54In	0.94 / -4.36
Fe-Sn	Sn54Fe/Fe54Sn	3.04 / -6.02
Fe-Sb	Sb54Fe/Fe54Sb	1.4 / -4.5
Fe-Hf	Hf54Fe/Fe54Hf	-2.67 / -4.91
Fe-Ta	Ta54Fe/Fe54Ta	0.64 / -0.11
Fe-W	W54Fe/Fe54W	2.15 / 0.16
Fe-Re	Re54Fe/Fe54Re	0.57 / -1.9
Fe-Pb	Pb54Fe/Fe54Pb	2.57 / 1.11
Fe-Ge	Ge54Co/Co54Ge	-0.19 / -0.84
Co-Rb	Rb54Co/Co54Rb	0.37 / -4.97
Co-Y	Co54Y/Y54Co	0.92 / -18.64
Co-Zr	Co54Zr/Zr54Co	-3.03 / -3.2
Co-Nb	Co54Nb/Nb54Co	-2.81 / -2.29
Co-Mo	Mo54Co/Co54Mo	-1.2 / -0.93
Co-Tc	Co54Tc/Tc54Co	0.91 / 0.54
Co-Cd	Cd54Co/Co54Cd	0.17 / 0.41
Co-Sn	Sn54Co/Co54Sn	0.02 / -3.72
Co-In	In54Co/Co54In	-0.97 / -4.77
Co-Hf	Hf54Co/Co54Hf	-2.73 / -4.93
Co-Ta	Ta54Co/Co54Ta	-1.81 / -0.52
Co-W	W54Co/Co54W	1.14 / 0.26
Co-Os	Os54Co/Co54Os	2.64 / -1.48
Co-Ir	Ir54Co/Co54Ir	2.1 / -0.38
Co-Pt	Pt54Co/Co54Pt	1.54 / 0.77
Ni-Pb	Pb54Co/Co54Pb	0.02 / 0.47
Ni-Zn	Zn54Ni/Ni54Zn	-1.27 / -8.53
Ni-Ge	Ge54Ni/Ni54Ge	-0.37 / -1.19
Ni-Rb	Rb54Ni/Ni54Rb	0.05 / -11.96
Ni-Sr	Sr54Ni/Ni54Sr	-0.83 / 1.85
Ni-Y	Y54Ni/Ni54Y	-6.42 / -0.91
Ni-Zr	Zr54Ni/Ni54Zr	-3.96 / -2.49
Ni-Nb	Nb54Ni/Ni54Nb	-0.98 / -0.84
Ni-Mo	Mo54Ni/Ni54Mo	-1.79 / -1.22
Ni-Tc	Tc54Ni/Ni54Tc	-2.64 / -0.91

Pair name	System of calculation	Segregation energy (eV)
Ni-Cd	Cd54Ni/Ni54Cd	-1.26 / -0.97
Ni-In	In54Ni/Ni54In	-1.98 / -4.04
Ni-Sn	Sn54Ni/Ni54Sn	0.52 / -0.91
Ni-Sb	Sb54Ni/Ni54Sb	-3.18 / -2.09
Ni-Hf	Hf54Ni/Ni54Hf	-2.07 / -1.18
Ni-Ta	Ta54Ni/Ni54Ta	-0.44 / -1.12
Ni-W	W54Ni/Ni54W	-0.16 / -0.03
Ni-Pb	Pb54Ni/Ni54Pb	-1.57 / -3.83
Cu-Ge	Ge54Cu/Cu54Ge	-1.23 / -0.93
Cu-Rb	Rb54Cu/Cu54Rb	-8.43 / -7.07
Cu-Sr	Sr54Cu/Cu54Sr	-0.87 / -5.89
Cu-Y	Y54Cu/Cu54Y	-1.05 / -9.19
Cu-Zr	Zr54Cu/Cu54Zr	-0.7 / -4.35
Cu-Mo	Mo54Cu/Cu54Mo	-2.31 / -1.03
Cu-Cd	Cd54Cu/Cu54Cd	0.62 / -0.3
Cu-In	In54Cu/Cu54In	1.87 / -0.94
Cu-Sn	Sn54Cu/Cu54Sn	0.16 / -2.83
Cu-Sb	Sb54Cu/Cu54Sb	0.87 / -4.91
Cu-Hf	Hf54Cu/Cu54Hf	-2.4 / -1.46
Cu-Ta	Ta54Cu/Cu54Ta	-0.41 / -0.92
Cu-W	W54Cu/Cu54W	1.12 / 0.26
Cu-Au	Au54Cu/Cu54Au	-1.17 / -5.39
Cu-Pb	Pb54Cu/Cu54Pb	-1.3 / -3.74
Zn-Rb	Rb54Zn/Zn54Rb	-0.3 / -4.81
Zn-Sr	Sr54Zn/Zn54Sr	-0.3 / -4.42
Zn-Y	Y54Zn/Zn54Y	-2.1 / -6.99
Zn-Zr	Zr54Zn/Zn54Zr	0.47 / 0.29
Zn-Nb	Nb54Zn/Zn54Nb	-0.39 / 0.2
Zn-Mo	Mo54Zn/Zn54Mo	-1.9 / -0.52
Zn-Cd	Cd54Zn/Zn54Cd	0.11 / 0.16
Zn-In	In54Zn/Zn54In	2.1 / 0.19
Zn-Sn	Sn54Zn/Zn54Sn	2.43 / 0.69
Zn-Sb	Sb54Zn/Zn54Sb	0.05 / -0.66
Zn-Hf	Hf54Zn/Zn54Hf	-1.37 / -0.2
Zn-Ta	Ta54Zn/Zn54Ta	0.59 / -0.25
Zn-W	W54Zn/Zn54W	-0.02 / -0.87

Pair name	System of calculation	Segregation energy (eV)
Zn-Os	Os54Zn/Zn54Os	0.43 / 1.14
Zn-Pt	Pt54Zn/Zn54Pt	-0.9 / -7.76
Ge-Rb	Ge54Rb/Rb54Ge	2.7 / -0.92
Ge-Sr	Ge54Sr/Sr54Ge	2.6 / -0.04
Ge-Y	Ge54Y/Y54Ge	2.74 / -8.82
Ge-Zr	Ge54Zr/Zr54Ge	2.74 / -8.27
Ge-Nb	Nb54Ge/Ge54Nb	2.5 / -1.04
Ge-Tc	Ge54Tc/Tc54Ge	1.35 / -1.52
Ge-Ru	Ge54Ru/Ru54Ge	0.46 / -1.45
Ge-Rh	Ge54Rh/Rh54Ge	-0.97 / -1.96
Ge-Pd	Ge54Pd/Pd54Ge	-1.08 / -1.46
Ge-Ag	Ge54Ag/Ag54Ge	-0.35 / -0.3
Ge-Cd	Ge54Cd/Cd54Ge	0.07 / 0.13
Ge-In	Ge54In/In54Ge	1.0 / 0.45
Ge-Sn	Ge54Sn/Sn54Ge	0.93 / 0.46
Ge-Sb	Ge54Sb/Sb54Ge	3.17 / -0.23
Ge-Hf	Ge54Hf/Hf54Ge	3.05 / 0.5
Ge-Ta	Ge54Ta/Ta54Ge	1.12 / -2.75
Ge-W	Ge54W/W54Ge	2.31 / -0.67
Ge-Re	Ge54Re/Re54Ge	-0.82 / -5.32
Ge-Os	Ge54Os/Os54Ge	-0.49 / -1.58
Ge-Ir	Ge54Ir/Ir54Ge	-0.57 / -0.93
Ge-Pt	Ge54Pt/Pt54Ge	-0.09 / -0.94
Ge-Au	Ge54Au/Au54Ge	0.42 / -0.92
Ge-Pb	Ge54Pb/Pb54Ge	-0.1 / -0.12
Rb-Sr	Sr54Rb/Rb54Sr	0.257 / 0.92
Rb-Y	Y54Rb/Rb54Y	-2.75 / -0.92
Rb-Zr	Zr54Rb/Rb54Zr	-5.89 / -0.75
Rb-Nb	Nb54Rb/Rb54Nb	-11.10 / -5.97
Rb-Mo	Mo54Rb/Rb54Mo	-4.63 / -0.65
Rb-Tc	Tc54Rb/Rb54Tc	-11.47 / -1.07
Rb-Ru	Ru54Rb/Rb54Ru	-2.34 / -4.89
Rb-Rh	Rh54Rb/Rb54Rh	1.09 / 0.78
Rb-Pd	Pd54Rb/Rb54Pd	-8.43 / -0.12
Rb-Ag	Ag54Rb/Rb54Ag	-0.16 / 0.16
Rb-Cd	Cd54Rb/Rb54Cd	2.55 / -1.33

Pair name	System of calculation	Segregation energy (eV)
Rb-In	In54Rb/Rb54In	-2.4 / 0.53
Rb-Sn	Sn54Rb/Rb54Sn	1.25 / 0.04
Rb-Sb	Sb54Rb/Rb54Sb	-4.10 / -0.83
Rb-Hf	Hf54Rb/Rb54Hf	-6.70 / 0.98
Rb-Ta	Ta54Rb/Rb54Ta	-1.34 / 1.13
Rb-W	W54Rb/Rb54W	-13.65 / -4.93
Rb-Os	Os54Rb/Rb54Os	1.84 / -2.83
Rb-Re	Re54Rb/Rb54Re	2.25 / -4.28
Rb-Ir	Ir54Rb/Rb54Ir	2.97 / -1.64
Rb-Pt	Pt54Rb/Rb54Pt	-5.98 / -10.48
Rb-Au	Au54Rb/Rb54Au	3.53 / -5.96
Rb-Hg	Hg54Rb/Rb54Hg	1.7 / 1.01
Rb-Pb	Pb54Rb/Rb54Pb	-0.45 / -0.01
Sr-Y	Y54Sr/Sr54Y	-2.19 / 0.56
Sr-Zr	Zr54Sr/Sr54Zr	-3.05 / -0.31
Sr-Nb	Nb54Sr/Sr54Nb	-8.47 / 0.47
Sr-Mo	Mo54Sr/Sr54Mo	-1.23 / -0.2
Sr-Tc	Tc54Sr/Sr54Tc	-3.9 / -0.03
Sr-Ru	Ru54Sr/Sr54Ru	-8.65 / -0.93
Sr-Rh	Rh54Sr/Sr54Rh	-1.75 / -0.79
Sr-Pd	Pd54Sr/Sr54Pd	-4.91 / -0.02
Sr-Ag	Ag54Sr/Sr54Ag	-3.39 / -0.31
Sr-Cd	Cd54Sr/Sr54Cd	1.12 / -0.33
Sr-In	In54Sr/Sr54In	0.47 / 0.24
Sr-Sn	Sn54Sr/Sr54Sn	-0.13 / 0.91
Sr-Sb	Sb54Sr/Sr54Sb	0.0 / 0.63
Sr-Hf	Hf54Sr/Sr54Hf	-4.17 / 0.35
Sr-Ta	Ta54Sr/Sr54Ta	-5.83 / 0.44
Sr-W	W54Sr/Sr54W	-10.63 / -0.11
Sr-Re	Re54Sr/Sr54Re	1.63 / -17.59
Sr-Os	Os54Sr/Sr54Os	4.48 / -0.31
Sr-Ir	Ir54Sr/Sr54Ir	4.16 / -0.25
Sr-Pt	Pt54Sr/Sr54Pt	2.18 / -1.09
Sr-Au	Au54Sr/Sr54Au	2.36 / 1.49
Y-Nb	Nb54Y/Y54Nb	-0.11 / -0.62
Y-Mo	Mo54Y/Y54Mo	-0.01 / -7.27

Pair name	System of calculation	Segregation energy (eV)
Y-Tc	Tc54Y/Y54Tc	-1.77 / -5.2
Y-Ru	Ru54Y/Y54Ru	-0.99 / -4.56
Y-Rh	Rh54Y/Y54Rh	-0.94 / -1.79
Y-Pd	Pd54Y/Y54Pd	-0.34 / -1.96
Y-Ag	Ag54Y/Y54Ag	-0.5 / -0.92
Y-Cd	Cd54Y/Y54Cd	0.35 / 0.01
Y-In	In54Y/Y54In	0.94 / 0.69
Y-Sn	Sn54Y/Y54Sn	2.29 / 0.81
Y-Sb	Sb54Y/Y54Sb	2.29 / 0.81
Y-Hf	Hf54Y/Y54Hf	1.91 / 0.64
Y-Os	Os54Y/Y54Os	-0.96 / -6.7
Y-Re	Re54Y/Y54Re	0.05 / -6.62
Y-Ir	Ir54Y/Y54Ir	0.26 / -4.2
Y-Au	Au54Y/Y54Au	0.15 / -0.79
Y-Pb	Pb54Y/Y54Pb	0.37 / -0.67
Zr-Nb	Nb54Zr/Zr54Nb	1.17 / 3.34
Zr-Mo	Mo54Zr/Zr54Mo	1.81 / 2.23
Zr-Ru	Ru54Zr/Zr54Ru	2.41 / -0.53
Zr-Rh	Rh54Zr/Zr54Rh	2.36 / -2.83
Zr-Pd	Pd54Zr/Zr54Pd	2.80 / 0.18
Zr-Ag	Ag54Zr/Zr54Ag	0.12 / 0.91
Zr-Cd	Cd54Zr/Zr54Cd	0.52 / 0.94
Zr-In	In54Zr/Zr54In	2.50 / 0.94
Zr-Sn	Sn54Zr/Zr54Sn	-0.45 / -0.69
Zr-Sb	Sb54Zr/Zr54Sb	1.23 / -0.39
Zr-Re	Re54Zr/Zr54Re	2.17 / -0.92
Zr-Os	Os54Zr/Zr54Os	1.49 / -3.21
Zr-Ir	Ir54Zr/Zr54Ir	3.02 / -1.1
Zr-Au	Au54Zr/Zr54Au	1.87 / 1.11
Zr-Pb	Pb54Zr/Zr54Pb	2.49 / 0.43
Nb-Mo	Mo54Nb/Nb54Mo	-0.21 / -0.53
Nb-Tc	Tc54Nb/Nb54Tc	0.57 / 0.96
Nb-Ru	Ru54Nb/Nb54Ru	-0.92 / -1.53
Nb-Rh	Rh54Nb/Nb54Rh	-1.06 / -0.43
Nb-Pd	Pd54Nb/Nb54Pd	-0.65 / -1.84
Nb-In	In54Nb/Nb54In	2.25 / -1.92

Pair name	System of calculation	Segregation energy (eV)
Nb-Sn	Sn54Nb/Nb54Sn	-0.33 / -0.39
Nb-Sb	Sb54Nb/Nb54Sb	-0.47 / 1.06
Nb-Ta	Ta54Nb/Nb54Ta	-0.07 / -1.52
Nb-W	W54Nb/Nb54W	1.37 / -1.96
Nb-Re	Re54Nb/Nb54Re	0.89 / -1.45
Nb-Os	Os54Nb/Nb54Os	-1.9 / -1.95
Nb-Ir	Nb54Ir/Ir54Nb	0.03 / -1.29
Nb-Pb	Pb54Nb/Nb54Pb	-3.13 / -4.75
Mo-Tc	Tc54Mo/Mo54Tc	0.57 / 0.04
Mo-Ru	Ru54Mo/Mo54Ru	-0.81 / -0.11
Mo-Rh	Rh54Mo/Mo54Rh	0.67 / -0.01
Mo-Ag	Ag54Mo/Mo54Ag	-2.61 / 0.75
Mo-Cd	Cd54Mo/Mo54Cd	1.20 / 0.22
Mo-In	In54Mo/Mo54In	0.64 / -0.57
Mo-Sn	Sn54Mo/Mo54Sn	1.34 / -1.37
Mo-Ta	Ta54Mo/Mo54Ta	-2.09 / -0.26
Mo-W	W54Mo/Mo54W	1.02 / -0.46
Mo-Re	Re54Mo/Mo54Re	2.30 / -4.08
Mo-Pb	Pb54Mo/Mo54Pb	-0.95 / -0.12
Tc-Rh	Rh54Tc/Tc54Rh	0.89 / -0.52
Tc-Cd	Cd54Tc/Tc54Cd	1.27 / 0.37
Tc-In	In54Tc/Tc54In	2.89 / 1.52
Tc-Sn	Sn54Tc/Tc54Sn	-0.68 / -0.74
Tc-Sb	Sb54Tc/Tc54Sb	-1.94 / -7.21
Tc-Hf	Hf54Tc/Tc54Hf	-1.72 / 2.64
Tc-Ta	Ta54Tc/Tc54Ta	0.62 / 1.18
Tc-W	W54Tc/Tc54W	0.20 / -0.21
Tc-Pb	Pb54Tc/Tc54Pb	2.95 / -5.33
Ru-Cd	Cd54Ru/Ru54Cd	1.27 / 0.43
Ru-In	In54Ru/Ru54In	0.62 / -0.36
Ru-Sn	Sn54Ru/Ru54Sn	-0.25 / -4.36
Ru-Sb	Sb54Ru/Ru54Sb	-1.97 / -5.91
Ru-Hf	Hf54Ru/Ru54Hf	-2.08 / -7.88
Ru-Ta	Ta54Ru/Ru54Ta	-0.67 / -2.25
Ru-Pb	Pb54Ru/Ru54Pb	2.04 / -5.34
Rh-Cd	Cd54Rh/Rh54Cd	1.19 / -0.31

Pair name	System of calculation	Segregation energy (eV)
Rh-In	In54Rh/Rh54In	0.96 / -3.88
Rh-Sn	Sn54Rh/Rh54Sn	2.04 / -1.37
Rh-Sb	Sb54Rh/Rh54Sb	-2.23 / -4.21
Rh-Hf	Hf54Rh/Rh54Hf	-1.96 / -2.81
Rh-Pb	Pb54Rh/Rh54Pb	1.92 / -5.33
Pd-Sn	Sn54Pd/Pd54Sn	-0.63 / -1.09
Pd-Sb	Sb54Pd/Pd54Sb	1.94 / 1.17
Pd-Hf	Hf54Pd/Pd54Hf	1.09 / 1.19
Pd-Pb	Pb54Pd/Pd54Pb	-0.57 / -1.02
Pd-Ag	Ag54Pd/Pd54Ag	0.62 / 2.67
Pd-Cd	Cd54Pd/Pd54Cd	-1.04 / -0.35
Cd-In	In54Cd/Cd54In	0.79 / 0.84
Cd-Sn	Sn54Cd/Cd54Sn	-0.44 / -0.05
Cd-Sb	Sb54Cd/Cd54Sb	1.15 / 0.65
Cd-Hf	Hf54Cd/Cd54Hf	0.83 / 1.33
Cd-Ta	Ta54Cd/Cd54Ta	0.31 / -0.73
Cd-W	W54Cd/Cd54W	1.0 / -0.43
Cd-Re	Re54Cd/Cd54Re	-1.37 / -0.05
Cd-Os	Os54Cd/Cd54Os	1.35 / -0.66
Cd-Pt	Pt54Cd/Cd54Pt	-0.42 / -2.12
Cd-Au	Au54Cd/Cd54Au	0.96 / 0.45
Cd-Pb	Pb54Cd/Cd54Pb	2.17 / -0.75
In-Sn	In54Sn/Sn54In	-0.34 / -0.12
In-Sb	In54Sb/Sb54In	0.36 / 2.146
In-Hf	Hf54In/In54Hf	1.85 / 1.91
In-Ta	Ta54In/In54Ta	2.40 / 0.94
In-W	W54In/In54W	2.57 / -2.477
In-Re	Re54In/In54Re	2.65 / -5.61
In-Os	Os54In/In54Os	2.23 / -4.07
In-Ir	Ir54In/In54Ir	1.97 / -1.54
In-Pt	Pt54In/In54Pt	1.76 / -2.47
In-Pb	Pb54In/In54Pb	2.03 / -0.37
Sn-Hf	Hf54Sn/Sn54Hf	2.50 / 0.49
Sn-Ta	Ta54Sn/Sn54Ta	2.5 / 1.43
Sn-W	W54Sn/Sn54W	1.0 / -1.26
Sn-Re	Re54Sn/Sn54Re	0.96 / -5.69

Pair name	System of calculation	Segregation energy (eV)
Sn-Os	Os54Sn/Sn54Os	-0.99 / -4.52
Sn-Ir	Ir54Sn/Sn54Ir	-1.05 / -1.1
Sn-Pt	Pt54Sn/Sn54Pt	0.09 / -2.61
Sn-Pb	Pb54Sn/Sn54Pb	0.04 / -1.16
Sb-Ta	Ta54Sb/Sb54Ta	-1.83 / 0.23
Sb-Re	Re54Sb/Sb54Re	-1.77 / -5.08
Sb-Os	Os54Sb/Sb54Os	-1.66 / -6.15
Sb-Ir	Ir54Sb/Sb54Ir	-1.07 / -4.76
Sb-Pt	Pt54Sb/Sb54Pt	-2.35 / -3.61
Sb-Pb	Pb54Sb/Sb54Pb	-2.31 / -2.34
Sb-Au	Au54Sb/Sb54Au	0.30 / -0.23
Hf-Os	Os54Hf/Hf54Os	3.17 / 2.75
Hf-Ir	Ir54Hf/Hf54Ir	2.97 / 2.4
Hf-Pt	Pt54Hf/Hf54Pt	3.10 / 0.14
Hf-Pb	Pb54Hf/Hf54Pb	0.34 / -0.54
Ta-Os	Os54Ta/Ta54Os	-0.46 / -0.45
Ta-Ir	Ir54Ta/Ta54Ir	1.45 / -1.41
Ta-Pt	Pt54Ta/Ta54Pt	-2.49 / 1.6
Ta-Au	Au54Ta/Ta54Au	0.29 / 2.21
W-Pt	Pt54W/W54Pt	0.50 / -1.73
W-Re	Re54W/W54Re	-0.58 / -0.18
W-Os	Os54W/W54Os	-1.05 / -1.26
W-Pb	Pb54W/W54Pb	-0.14 / -0.04
Re-Ir	Ir54Re/Re54Ir	4.5 / 0.85
Re-Au	Au54Re/Re54Au	-1.76 / 2.11
Re-Os	Os54Re/Re54Os	-4.56 / 2.81
Os-Pb	Pb54Os/Os54Pb	-2.17 / -0.53
Pt-Pb	Pb54Pt/Pt54Pb	-2.89 / -1.35
Au-Pb	Pb54Au/Au54Pb	-2.92 / -1.35